

Copyright  
by  
Dinesh Rabindran  
2009

**The Dissertation Committee for Dinesh Rabindran Certifies that this is the approved version of the following dissertation:**

**A Differential-Based Parallel Force/Velocity Actuation Concept:  
Theory and Experiments**

**Committee:**

---

Delbert Tesar, Supervisor

---

Ronald E. Barr

---

Jeannie S. Falcon

---

Mitchell W. Pryor

---

Carolyn C. Seepersad

---

S.V. Sreenivasan

**A Differential-Based Parallel Force/Velocity Actuation Concept:  
Theory and Experiments**

**by**

**Dinesh Rabindran, B. Tech; M.S.E**

**Dissertation**

Presented to the Faculty of the Graduate School of

The University of Texas at Austin

in Partial Fulfillment

of the Requirements

for the Degree of

**Doctor of Philosophy**

**The University of Texas at Austin**

**May 2009**

## **Dedication**

In fond memory of my dear father

*Lives of great men all remind us  
We can make our lives sublime.  
And, departing, leave behind us  
Footprints on the sands of time.*

- Henry Wadsworth Longfellow (1807-1882)

## **Acknowledgments**

I would like to thank my advisor, mentor, and teacher, Prof. Del Tesar for his guidance and mentorship. I truly admire him for being a visionary in robotics, for his high regard for and his championship of the field of mechanical engineering, and for being a mechanician par excellence. Without his advice, encouragement, and support this dissertation could not have been realized. I also thank Prof. Tesar, Dr. Chetan Kapoor, and Dr. Mitch Pryor for giving me the opportunity to work on many challenging technical projects, apart from my dissertation work, during my time at the Robotics Research Group (RRG). I would like to express sincere gratitude towards my committee members, Prof. Ronald Barr, Dr. Jeannie Falcon, Dr. Mitch Pryor, Prof. Carolyn Seepersad, and Prof. S.V. Sreenivasan for their valuable suggestions and comments that have contributed a great deal to this dissertation. I am especially indebted to external reviewers for critiquing parts of this research: Prof. Jorge Angeles, McGill University; Prof. Farrokh Mistree, Georgia Tech; Prof. Robert Sturges, Virginia Tech; and Prof. Joseph Beaman, UT Austin. I would like to acknowledge the reviewers of all the conference and journal papers related to this work for volunteering their time. To several colleagues at RRG, especially Dr. Oziel Rios, Dr. Pryor, Mr. Ganesh Krishnamoorthy, Dr. Pradeep Ashok, and Mr. Amit Kulkarni, I am grateful for reviewing drafts of dissertation chapters and papers. The administrative support and assistance of the

management team at the RRG, including Dr. Kapoor, Dr. Pryor, Dr. Ashok, Ms. Janie Terrel, Ms. Betty Wilson, and Ms. Malena Pomerleau-Petersen is acknowledged.

The administrative support from the ME Graduate Office, especially by Prof. Ofodike Ezekoye, Prof. Eric Fahrenthold, Ms. Ruth Schwab, Ms. Jessica Miller, Mr. David Justh, and Ms. Prabhu Khalsa, is appreciated very much. I am appreciative of Prof. Ezekoye's continued advice and encouragement as the Graduate Advisor. Special thanks go to Ms. Cindy Raman, the area assistant for the Mechanical Systems and Design area, for advising on and assisting with many administrative tasks during my entire graduate program. To Prof. Masada and my Ph.D. qualifying examination committee I am thankful for being very considerate, accommodative, and supportive when I took the examination during a time of distress in the family. To Profs. Tesar and Sreenivasan, and Drs. Kapoor and Pryor I am thankful for giving me the great opportunity to guest lecture for ME 372J, ME 324, and ME 218.

I would like to thank Ms. Philine Donner for assistance with the set up of the Parallel Force/Velocity Actuator (PFVA) laboratory prototype, data collection and analysis, and the compilation of Appendix E. The technical assistance provided by Dr. Jagadish Janardhan, Mr. Rainer Sigwald, Mr. Krishnamoorthy, Dr. Pryor, and Dr. Ashok was valuable while designing and building this testbed. Without the selfless help of Mr. Don Artieschoufsky, Mr. Danny Jares, Mr. Curtis Johnson, Mr. Michael Slotboom, and several student assistants at the ETC Machine Shop, it would have been an uphill task to fabricate the components of the PFVA testbed.

To Prof. Barr and my friends in the student chapter of the ASEE, I am grateful for all the great team work that went into making 2005-2006 a successful year for the organization. To Ms. Tricia Berry of the Graduates Linked with Undergraduates in Engineering (GLUE) program and Ms. Debbie Mullins of the Texas Space Grant

Consortium (TSGC), I am thankful for the opportunity to be a mentor for undergraduate research projects. To all my friends and fellow musicians in Omkara, I am grateful for all the fun times, high-energy shows, and exhilarating jamming sessions which have all helped in managing the stress in graduate school. Thanks to family and friends in Austin who have helped me make this city a home away from home. Thanks to A.R. Rehman for making music that motivates and to R.W. Emerson for soul-stirring words.

I am very grateful to my partners in the ‘exciting misery’ (or, ‘miserable excitement’) of life as a doctoral student, Deepak, Sandhya, and Vandana, for being supportive and encouraging. I wish them good luck in their own pursuits of the seemingly elusive doctorate. To my buddies, Surji and Vibin, I am grateful for always being so supportive, before grad school, through grad school, and I am sure, for life! I am indebted to my lovely family for always encouraging me to challenge myself, scale new heights, and persist until I succeed; for being great role models; and for always being beside me come success come failure. To my parents, there is only one thing I can say – hats off, for everything. To my wife, Vandana, I am grateful for her unconditional love and support; for being the friend, guide, and philosopher that she is; and for sharing with me the passion for science, music, and life.

Funding from the Department of Energy (Grant# DE-FG52-06NA25591), National Aeronautics and Space Administration (Grant# NNX08BB05G), and the Mechanical Engineering Department at The University of Texas at Austin are acknowledged. The technical and hardware support by National Instruments Corporation is appreciated.

# **A Differential-Based Parallel Force/Velocity Actuation Concept: Theory and Experiments**

Publication No. \_\_\_\_\_

Dinesh Rabindran, Ph.D.

The University of Texas at Austin, 2009

Supervisor: Delbert Tesar

Robots are now moving from their conventional confined habitats such as factory floors to human environments where they assist and physically interact with people. The requirement for inherent mechanical safety is overarching in such human-robot interaction systems. We propose a dual actuator called Parallel Force/Velocity Actuator (PFVA) that combines a Force Actuator (FA) (low velocity input) and a Velocity Actuator (VA) (high velocity input) using a differential gear train. In this arrangement mechanical safety can be achieved by limiting the torque on the FA and thus making it a backdriveable input. In addition, the kinematic redundancy in the drive can be used to control output velocity while satisfying secondary operational objectives.

Our research focus was on three areas: (i) scalable parametric design of the PFVA, (ii) analytical modeling of the PFVA and experimental testing on a single-joint prototype, and (iii) generalized model formulation for PFVA-driven serial robot manipulators. In our analysis, the ratio of velocity ratios between the FA and the VA,



called the relative scale factor, emerged as a purely geometric and dominant design parameter. Based on a dimensionless parametric design of PFVAs using power-flow and load distributions between the inputs, a prototype was designed and built using commercial-off-the-shelf components. Using controlled experiments, two performance-limiting phenomena in our prototype, friction and dynamic coupling between the two inputs, were identified. Two other experiments were conducted to characterize the operational performance of the actuator in velocity-mode and in what we call ‘torque-limited’ mode (i.e. when the FA input can be backdriven). Our theoretical and experimental results showed that the PFVA can be mechanical safe to both slow collisions and impacts due to the backdriveability of the FA. Also, we show that its kinematic redundancy can be effectively utilized to mitigate low-velocity friction and backlash in geared mechanisms. The implication at the system level of our actuator level analytical and experimental work was studied using a generalized dynamic modeling framework based on kinematic influence coefficients. Based on this dynamic model, three design case studies for a PFVA-driven serial planar 3R manipulator were presented.

The major contributions of this research include (i) mathematical models and physical understanding for over six fundamental design and operational parameters of the PFVA, based on which approximately ten design and five operational guidelines were laid out, (ii) analytical and experimental proof-of-concept for the mechanical safety feature of the PFVA and the effective utilization of its kinematic redundancy, (iii) an experimental methodology to characterize the dynamic coupling between the inputs in a differential-summing mechanism, and (iv) a generalized dynamic model formulation for PFVA-driven serial robot manipulators with emphasis on distribution of output loads between the FA and VA input-sets.

# Table of Contents

List of Tables .....	xiii
List of Figures .....	xiv
<b>INTRODUCTION AND BACKGROUND .....</b>	<b>1</b>
Chapter 1. Introduction .....	1
1.1. Background .....	1
1.2. Research Objectives .....	3
1.3. Research Outline .....	5
1.4. Scope .....	6
1.5. Contributions .....	6
1.6. Report Outline .....	8
Chapter 2. Literature Review .....	11
2.1. Actuator Design and Control Influence on Physical HRI .....	11
2.1.1. Background on Design Issues .....	12
2.1.2. Background on Sensing/Control Issues .....	14
2.1.3. Implications for the Physical HRI System Designer .....	17
2.2. State of the Art in Multi-Input Actuator Concepts .....	17
2.2.1. A Taxonomy for Dual Actuators .....	18
2.2.2. Force-Summing Actuators .....	21
2.2.3. Velocity-Summing Actuators .....	25
2.2.4. Patent Literature: Prior Art in Dual Actuators .....	28
2.3. Chapter Summary and Discussion .....	29
Chapter 3. Parallel Force/Velocity Actuation: Concept .....	32
3.1. Definition of the Relative Scale Factor .....	36
3.2. Physical Meaning of RSF .....	38
3.3. PFVA Preliminary Analysis .....	40
3.4. Chapter Summary .....	42
<b>ACTUATOR LEVEL ANALYSIS AND EXPERIMENTS .....</b>	<b>44</b>
Chapter 4. Parametric Design: Power Flow Analysis .....	44
4.1. External Power Flow and Overall Mechanical Efficiency .....	44
4.2. Internal Power Flow Analysis .....	54
4.3. Effective Inertia in the PFVA .....	62
4.3.1. Practical Implication .....	66
4.4. Chapter Summary .....	68
Chapter 5. Parametric Design: Force Distribution Analysis .....	71
5.1. Candidate PFVA Designs .....	73
5.2. Parametric Accuracy Analysis .....	73
5.3. Methodology for Force Distribution Analysis .....	77
5.4. Force Distribution Analysis .....	78
5.4.1. Static Load Torques .....	78
5.4.2. Inertia Torques .....	84
5.4.3. Acceleration Responsiveness Analysis .....	90
5.5. Stiffness Distribution Analysis .....	94
5.5.1. Mechanical Stiffness .....	94
5.5.2. Discussion on Non-Mechanical Stiffness .....	101
5.6. Design Case Study: PFVA Prototype .....	103
5.7. Chapter Summary .....	104
Chapter 6. Analysis and Simulation of Dynamic Response .....	108
6.1. Velocity Controlled VA and FA .....	108
6.1.1. PFVA Operation Utilizing Kinematic Redundancy .....	109
6.2. Equations of Motion for a PFVA .....	121

6.2.1.	Note on Determining the Consolidated Damping Matrix.....	122
6.3.	<i>Preliminary Model To Study Simple Modes of Operation</i> .....	124
6.4.	<i>Generalized Model To Study Realistic Modes of Operation</i> .....	138
6.4.1.	Generalized Model Development.....	139
6.5.	<i>Chapter Summary</i> .....	144
Chapter 7.	Experiments with a PFVA Prototype.....	146
7.1.	<i>PFVA Testbed Description</i> .....	147
7.2.	<i>Experiments: Setup and Results</i> .....	149
7.2.1.	Experiment I: Identification of Friction in the FA.....	149
7.2.2.	Experiment II: Identification of Dynamic Coupling.....	160
7.2.3.	Experiment III: Utilizing Redundancy to Mitigate Low-Velocity Friction.....	171
7.2.4.	Experiment IV: Safety to Collisions Using FA's Controlled Backdriveability.....	176
7.3.	<i>Chapter Summary</i> .....	185
	<b>SYSTEM LEVEL ANALYTIC FORMULATION.....</b>	<b>187</b>
Chapter 8.	Generalized Dynamic Modeling of PFVA-Driven Serial Manipulators.....	187
8.1.	<i>Configuration Spaces</i> .....	188
8.2.	<i>Generalized Kinematics</i> .....	189
8.2.1.	Generalized Velocity Analysis.....	189
8.2.2.	Generalized Acceleration Analysis.....	196
8.3.	<i>Generalized Static Load Torques</i> .....	199
8.4.	<i>Generalized Inertial Torques</i> .....	201
8.4.1.	Input Dynamic Coupling Matrix.....	202
8.4.2.	Kinetic Energy.....	202
8.4.3.	Calculation of Generalized Inertia Torques.....	205
8.5.	<i>Controlling Equations of Motion For PFVA-driven Manipulator</i> .....	209
8.6.	<i>3R Planar PFVA-driven Manipulator Example: Parameter Study</i> .....	212
8.6.1.	Methodology.....	213
8.6.2.	Implementation.....	215
8.6.3.	Results.....	216
8.6.4.	Discussion on RSF Based Parameter Study.....	223
8.7.	<i>Introduction to PFVA-Driven Manipulator Performance Criteria</i> .....	224
8.7.1.	Partition Value of Kinetic Energy.....	225
8.7.2.	Generalized Relative Scale Factor.....	225
8.8.	<i>Chapter Summary</i> .....	227
	<b>DISSERTATION SUMMARY.....</b>	<b>229</b>
Chapter 9.	Conclusions and Discussion.....	229
9.1.	<i>Research Objectives and Contributions</i> .....	229
9.2.	<i>Literature Summary</i> .....	231
9.3.	<i>Significant Results</i> .....	233
9.3.1.	Key Analytical Results.....	233
9.3.2.	Key Experimental Results.....	237
9.4.	<i>Guidelines for the PFVA Designer</i> .....	238
9.5.	<i>Key Questions Raised</i> .....	239
9.6.	<i>Roadmap for Future Work</i> .....	241
9.6.1.	Short-Term Future Work (1-2 Years).....	241
9.6.2.	Long-Term Future Work (5 Year Roadmap).....	244
9.7.	<i>Concluding Remarks</i> .....	249
	<b>SUPPLEMENTARY MATERIAL.....</b>	<b>250</b>
Appendix A.	Differential Mechanisms: A Review.....	250
A.1.	<i>Differential Link</i> .....	251
A.2.	<i>Differential Gear</i> .....	253
A.3.	<i>Force Balance in Differentials</i> .....	254
Appendix B.	Sample PFVA Designs for Effective Inertia Analysis.....	258

Appendix C.	Calculation of Reflected Inertia Terms .....	259
Appendix D.	Simulation Parameters for 3R PFVA-Driven Robot .....	262
D.1.	<i>Kinematic and Dynamic Parameters</i> .....	262
D.2.	<i>Task Parameters</i> .....	266
Appendix E.	PFVA Testbed Details .....	268
References	.....	271
Vita	.....	283

## List of Tables

Table 2.1 Literature Summary on Force- and Velocity-Summing Actuation Concepts .....	20
Table 2.2 Summary of US Patent Literature on Dual Actuators .....	29
Table 2.3 Summary of Selected Literature and Relevance to Current Work.....	31
Table 4.1 The Six External Power-Flow Modes in a PFVA and their Physical Meaning .....	47
Table 4.2 Summary of Guidelines Suggested in this Chapter .....	70
Table 4.3 Summary of PFVA Criteria Developed in this Chapter .....	70
Table 5.1 Summary of PFVA Parameters for Candidate Designs .....	72
Table 5.2 Summary of Stiffness/Inertia Parameters in Figure 5.10.....	96
Table 5.3 Summary of PFVA design criteria based on parametric distribution analysis .....	105
Table 5.4 Summary of Guidelines Suggested in this Chapter .....	106
Table 6.1 Non-Linear Programming (NLP) Problem Statement .....	116
Table 6.2 Summary of Dynamic Parameters of the PFVA.....	122
Table 6.3 Summary of Inertial Parameters of the PFVA for Example 6.2 .....	125
Table 7.1 List of Components in the PFVA Testbed.....	148
Table 7.2 Summary of Identified Friction Parameters.....	160
Table 7.3 Conditions Imposed on PFVA in Experiment II and their Modeling Implications .....	161
Table 7.4 Speed and Frequency Combinations for Experiment II.....	163
Table 7.5 Cross-Correlation Analysis Summary .....	168
Table 7.6 Summary of Experiments and Major Results .....	186
Table 9.1 Summary of Contributions (Section 1.4).....	231
Table 9.2 Summary of Selected Literature (Section 2.2).....	232
Table 9.3 Summary of US Patent Literature on Dual Actuators (Section 2.2.4).....	233
Table 9.4 Summary of PFVA Actuator-Level Parameters, Criteria, and Models .....	234
Table 9.5 Summary of Experiments and Major Results .....	237
Table 9.6 Summary of Design Guidelines.....	238
Table 9.7 Summary of Operational Guidelines .....	239
Table 9.8 Five-Year Research Plan in Dual Actuators and Mechanical Safety.....	248
Table A.1 A List of Rotary and Linear Differential Mechanisms (Adapted from Macmillan, 1961) .....	250
Table B.1 Actuator Design Parameters used in Example 4.3 .....	258
Table D.1 D-H Parameters for the 3R Planar PFVA-Manipulator .....	262
Table D.2 Dynamic Parameters for the 3R Planar PFVA-Manipulator .....	263
Table D.3 Kinematic and Dynamic Parameters for the PFVAs of the 3R Robot.....	264
Table E.1 List of Components in the PFVA Testbed .....	269
Table E.2 List of Principal Control System Components in the PFVA Testbed .....	270

## List of Figures

Figure 1.1. A Snapshot of the Variety of Mechanical Designs for Serial Robot Manipulators. (a) Typical Industrial Manipulator from ABB that is Frequently Populated with Actuators with High Gear Ratios and High Output Inertia, (b) A Whole Arm Manipulator Based on Cable-Driven Backdriveable Joints (Barrett Technologies, Inc.), (c) A Light-Weight Humanoid with a Suite of Sensors that Enables Highly Responsive Dexterous Interaction with its Environment (DLR, Germany), and (d) An Exoskeleton-Based Rehabilitation Robot (ARMEO) Used for Stroke Therapy (Hocoma, Switzerland).....	2
Figure 1.2. Parallel Force/Velocity Actuation concept. (a) Schematic, (b) Laboratory Prototype. ....	4
Figure 2.1. A force-based teaching HRI application implemented on an off-the-shelf modular manipulator from Amtec, Germany. An admittance-type control was implemented using a 6-axis end-point force/torque sensor from ATI. The OSCAR (Kapoor and Tesar, 1996) manipulation software enabled extending this application to multiple robot platforms. ....	16
Figure 2.2. Taxonomy developed by Lauria et al. (2008) for high performance actuators. ....	18
Figure 2.3. Conceptual sketches which show simple rotary examples of velocity-summing (a) and force-summing actuators (b). This figure was adapted from (Tesar, 2003) where it was originally used to classify fault-tolerant actuators. ....	19
Figure 2.4. Antagonistic elbow module proposed by Cho, Tesar, and Freeman (1989). (a) Concept sketch of the module and (b) Concept sketch of a 3-DOF manipulator using antagonistic actuation modules. Adapted from (Cho, Tesar, and Freeman, 1989, p. 1386). ....	21
Figure 2.5. The DECMMA actuator concept from the Robotics Lab at Stanford University (Zinn, 2005, p. 48). ....	22
Figure 2.6. The PaCMMA actuator concept from MIT (Morrell and Salisbury, 1998). (a) Concept, (b) Physical Prototype .....	23
Figure 2.7. The Variable Stiffness Actuator (VSA) developed at University of Pisa, Italy (Bicchi and Tonietti, 2004). (a) Concept, (b) Physical Prototype. ....	24
Figure 2.8. Improved velocity dynamic range via layered velocity control with CHAMP (Tesar et al., 1999). Note that the larger actuator controls the gross motion (typically the desired motion for the system) and the small actuator makes finer adjustments to this baseline. ....	26
Figure 2.9. The Double Actuator Unit (DAU) from Korea University (Kim et al., 2007). (a) Concept, (b) Physical Prototype. ....	26
Figure 2.10. Differential Elastic Actuator (DEA) proposed by Lauria et al. (2008). (a) Concept diagram and implementation using a harmonic drive, (b) Lever analogue of the DEA (arrows indicate force flow) and (c) Packaged actuator prototype. Adapted from (Lauria et al., 2008; Legault et al., 2008). ....	27
Figure 3.1. A First-Generation Laboratory Prototype of the PFVA Concept Built at the University of Texas Robotics Research Lab. ....	32
Figure 3.2. A continuum of geared electro-mechanical actuators (Rabindran and Tesar, 2007b). The dynamic response of the actuator varies along the spectrum depending on the gear reduction used. ....	33
Figure 3.3. Drive trains that could be used to realize a PFVA. (a) Schematic of a simple Epicyclic Gear Train (EGT) (Rabindran and Tesar, 2007b). ....	34
Figure 3.4. Schematic showing the values of the relative scale factor $\tilde{\rho}$ for various positive-ratio drives. ....	37
Figure 3.5. Examples of PFVAs. (a) Rotational configuration where the radii of the sun, carrier, planets, and ring gears are $r_s$ , $r_c$ , $r_p$ , and $r_r$ , respectively, such that $r_r \gg r_s$ , and (b) Linear configuration such that $r_1 \gg r_2$ .....	39
Figure 3.6. Sectioned-view of the SR-20 differential (Picture Courtesy: Andantex, Inc., Wanamassa, NJ, 2007) used in the UTRRG PFVA prototype. ....	39
Figure 3.7. Nomograph representation of the velocities of the FA, VA, and the output. ....	41

Figure 3.8. Nomograph representation of two special cases, (a) kinematic redundancy, (b) coupling point. ....	41
Figure 4.1. Variation of SISO efficiencies w.r.t. the relative scale factor $\tilde{\rho}$ for the commercially available SA series differentials from Andantex Inc. [22, 18]. $\eta_{v \rightarrow o}$ is the basic efficiency of the drive train.....	49
Figure 4.2. Mechanical efficiency analysis of a DISO PFVA as the superposition of a SISO FA and VA. 50	
Figure 4.3. Variation of the overall mechanical efficiency of the PFVA w.r.t the relative scale factor and the velocity mixing ratio.....	52
Figure 4.4. Graph showing internal and external power flows in a positive-ratio PFVA: (a) No futile power and (b) futile power-flow condition.....	58
Figure 4.5. Representation of exchange of total power, rolling power, and the coupling power between the VA and the output of the PFVA for Example 4.2.....	59
Figure 4.6. Futile power ratios for varying values of relative scale factor $\tilde{\rho}$ and the inverse of velocity mixing ratio $\tilde{\lambda}$ .....	61
Figure 4.7. Variation of Effective Inertia Ratio $\tilde{I}_{eff}$ as a function of VMR for various example PFVA designs (See Appendix B). Design example 2 corresponds to the PFVA testbed being set up at the University of Texas Robotics Research Lab.....	67
Figure 5.1. Surface plot of relative accuracy factor $\tilde{\alpha}_f^j$ as a function of RSF $\tilde{\rho}$ and $\tilde{\alpha}_f^v$ . Note that $\lim_{\rho \rightarrow \infty} \tilde{\alpha}_f^j = 1$ . The relative accuracy factor corresponding to the five PFVA designs are shown. ....	75
Figure 5.2. A schematic of the PFVA with an output work function. ....	77
Figure 5.3. Schematic of the procedure for force distribution analysis of the PFVA.....	78
Figure 5.4. Mechanical efficiency analysis of a DISO PFVA as the superposition of a SISO FA and VA. 79	
Figure 5.5. Surface representing the variation of STDR with respect to the Relative Efficiency Ratio and the RSF. The circular markers represent the five PFVA designs. To demonstrate how a point on this surface should be interpreted, the square markers show two example PFVA designs with the same Relative Efficiency Ratio and different RSFs.....	82
Figure 5.6. Schematic of a single-link manipulator with lumped output inertia and reflected input inertia. The dotted lines show the parallel force paths to the two inputs from the output.....	84
Figure 5.7. Surface representing the variation of ITDR with respect to the acceleration mixing ratio and the RSF. The circular markers represent the five PFVA designs. The different surfaces correspond to various load inertia settings, namely, 2x, 1x, 0.5x, 0.25x, and 0x the output link inertia, i.e., 0.225 kg-m <sup>2</sup> . ....	88
Figure 5.8. Surface representing the variation of relative acceleration responsiveness with respect to the rated motor torque ratio and the RSF. The different surfaces correspond to various load inertia settings, namely, 2x, 1x, and 0.5x the output link inertia, i.e., 0.225 kg-m <sup>2</sup> . ....	92
Figure 5.9. (a) Schematic representation of transmission stiffness (Schempf and Yoerger, 1993) including soft and hard stiffness zones. (b) Experimental stiffness data from a 1/4-scale weapons elevator actuator using a hypocyclic gear train (Courtesy Kevin Crouchley, NAVSEA, Philadelphia). .	94
Figure 5.10. Representation of the PFVA as an in-series coupled spring system. The broken arrow on $I_j^*$ indicates that this parameter is a variable depending on the configuration of the mechanism. (a) Complete lumped spring-mass model identifying all stiffness elements on the input side of the PFVA and (b) Simplified in-series spring system model with the kinematic transformation for each input.....	95
Figure 5.11. Variation of the Relative Joint Stiffness ( $\tilde{K}_j$ ) with respect to the Relative Stiffness ( $\tilde{K}$ ) and the RSF ( $\tilde{\rho}$ ) for $\eta_{j \rightarrow v}$ varying as a function of RSF. 3D surfaces representing this data for	

various settings of $\tilde{\eta}_b$ , namely, 0.85, 1, and 1.15 (corresponding to the three surfaces in the figure) are also shown.....	98
Figure 5.12. Variation of SISO efficiencies with respect to the RSF $\tilde{\rho}$ for the commercially available SA series differentials from Andantex Inc., Wanamassa, NJ (see Chapter 4 for a detailed discussion on SISO efficiencies). The subscript $o$ refers to the output or the machine joint. Therefore, $\eta_{v \rightarrow o} = \eta_{v \rightarrow j}$ is the basic efficiency of the drive train. ....	99
Figure 5.13. Contour plot representing the data in Figure 5.11 for $\tilde{\eta}_b = 0.85$ .....	100
Figure 5.14. A 2-DOF motor drive model for a direct drive motor. The parameters shown are all lumped and referenced to the rotor shaft (Adapted from Rivin, 1980).....	102
Figure 5.15. Laboratory prototype of the PFVA built at UTRRG, Austin, TX. ....	103
Figure 6.1. Graphical representation of the null-space of the Kinematics Influence Coefficient matrix, $\mathbf{G}$ . The null-space velocities are velocities of the FA and VA for which the PFVA does not have any output motion. ....	111
Figure 6.2. Drive train used in the UTRRG PFVA lab prototype (Andantex Inc., 2007). (a) Section view of the drive train layout, and (b) N1, or the casing, is the VA and is driven by a low-torque/high-speed motor, and N2 is the FA input and is driven by a high-torque/low-speed motor (Picture Courtesy: Andantex Inc., Wanamassa, NJ). ....	113
Figure 6.3. Definition of variables in the non-linear programming problem shown graphically (see Table 6.1). This figure is similar to Figure 6.1 and is repeated here for the convenience of the reader. ....	117
Figure 6.4. The resultant joint velocity trajectory (sinusoid) when the total solutions of the VA and FA from Figure 6.5 and Figure 6.6 are commanded. ....	118
Figure 6.5. The solutions for different components of the VA's speeds. Note that the commanded solution is always positive.....	118
Figure 6.6. The solutions for different components of the FA's speeds. Note that the commanded solution is mostly negative. There are two regions (0.25-1s and 2.75-3.5s) where the total solution is positive. ....	119
Figure 6.7. The time history of the null-space scaling factor. Notice that after $k$ reaches above 12.5, it is never allowed to go below this value because of constraint 3 in the NLP problem (see Table 6.1). The value of $k$ takes a finite time to achieve this minimum value due to the limits on achievable accelerations. ....	119
Figure 6.8. Schematic of a PFVA driving a single-axis manipulator subject to a work-function $T_w$ .....	121
Figure 6.9. Definition of an acceleration-run-acceleration trapezoidal velocity profile. Note that the time intervals for each phase (constant acceleration and constant velocity) are equally spaced. The symbol $t_f$ represents the total time of travel. The symbols $V_{max}$ and $a_{max}$ represent the acceleration and velocity limits of the drive, respectively. ....	126
Figure 6.10. Simulation set-up for open-loop trapezoidal velocity response simulation.....	126
Figure 6.11. Power-flow mode corresponding to the operating conditions used in Example 6.2. The VA is actively controlled to maintain a trapezoidal velocity based on its maximum acceleration and velocity, and the FA is controlled to maintain a zero torque. ....	127
Figure 6.12. Velocity response of the FA, VA, and the PFVA (output link) when the VA is commanded to follow a trapezoidal motion profile in velocity and the FA is commanded to maintain zero torque. The FA is disturbed by the VA due to the cross-coupling inertia term $I_{vf}$ . There is no external load acting on the system. ....	128
Figure 6.13. Acceleration response of the FA, VA, and the PFVA (output link) when the VA is commanded to follow a trapezoidal motion profile in velocity and the FA is commanded to maintain zero torque. The FA is disturbed (or back-driven) by the VA due to the cross-coupling inertia term $I_{vf}$ . There is no external load acting on the system. ....	129
Figure 6.14. Simulation set up for Example 6.3. The output is connected to a load motor which is controlled at zero velocity. This is equivalent to rigidly holding the output link stationary. The conditions of the previous simulation apply to this example as well: (i) VA velocity is trapezoidal and (ii)	



FA is controlled to generate zero torque. (a) Schematic of the actuator with a load motor, (b) Power flow graph corresponding to imposed conditions, and (c) Simulation conditions shown on a 3D model. ....	130
Figure 6.15. Velocity response of the FA, VA, and the PFVA (output link) when the VA is commanded to follow a trapezoidal motion profile in velocity, the FA is commanded to maintain zero torque, and the output is connected to a load motor that holds position. The FA is disturbed by the VA due to the cross-coupling inertia term $I_{vf}$ . The velocities of FA and VA are such that $\tilde{\lambda} \approx -\tilde{\rho}$ . ....	131
Figure 6.16. Simulation set up for Example 6.4. ....	133
Figure 6.17. The velocity and torque profiles for the simulation described in Case (i) of Example 6.4. ...	134
Figure 6.18. The velocity profiles for the simulation described in Example 6.4, Case (ii). ....	136
Figure 6.19. The static torque profiles for the simulation described in Example 6.4, Case (ii). Notice that due to the programmed backdriveability of the FA, the force reduces quickly as soon as the prescribed safe force threshold is reached. ....	137
Figure 6.20. Frictional torque as a function of velocity using the continuous Stribeck model proposed by Majd and Simaan (1995). (Left) Low velocity behavior, and (Right) High velocity behavior. ....	141
Figure 6.21. Simulation set up for Example 6.5. (a) Phase I or position controlled response in free-space, (b) Phase II where collision is detected, and (c) Phase III or force controlled response to maintain a constant force between link and the object. ....	142
Figure 6.22. Positions and velocities of the FA, VA and output link during the three phases of the collision response simulation in Example 6.5. ....	143
Figure 7.1. Laboratory prototype of the Parallel Force/Velocity Actuator (PFVA) built at the Robotics Research Group at The University of Texas at Austin. ....	146
Figure 7.2. Sectioned-view of the Andantex SR-20 differential gear train used in the physical prototype of the PFVA (Courtesy: Andantex, Inc., Wanamassa, NJ). ....	148
Figure 7.3. Different types of friction effects characterized during experimental identification of friction in the FA. ....	150
Figure 7.4. Conditions imposed on the PFVA testbed during friction identification experiment. VA motor was controlled at zero velocity, FA motor was controlled at different velocities ranging from -200 to 200 rpm, and the torque reading from the torque sensor was measured. ....	151
Figure 7.5. Experimental results for velocity-dependence of friction in the FA branch. Notice the Stribeck effect in the low velocity region where average friction torque decreases with velocity. After the critical velocity, friction increases linearly (viscous damping effect). Error bars show $3\sigma$ intervals. ....	154
Figure 7.6. Results from repeatability analysis of our velocity-dependence experiments. The bars in this figure show the value of $3\sigma$ in percentage for the experiment at every speed setting. Based on this bar chart, the average $3\sigma$ for all experiments was 5.6% which indicates a relatively high repeatability. ....	156
Figure 7.7. Results from FFT analysis of friction torque data as a function of FA shaft position during the experimental determination of position-dependence of friction. Note that the frequency units are cycles/rev to directly determine torque oscillation period as a multiple of FA shaft revolution. ....	157
Figure 7.8. Torque data plotted with respect to FA shaft position for the six test speeds and for 10 revolutions. A low-pass second-order Butterworth filter was used with a cut-off frequency of 5 Hz. ....	159
Figure 7.9. Conditions imposed on the PFVA testbed during the dynamic coupling experiment. FA motor was controlled at zero velocity, VA motor was controlled to track various velocity profiles and torque reading from the torque sensor was measured. Trends in torque reading were then correlated with the velocity profiles used. ....	162
Figure 7.10. Torque sensor measurements and position, velocity, and acceleration data for Experiment II using 5.23 rad/s cycled at 0.25 Hz. ....	165
Figure 7.11. FFT of torque data for Experiment II using 5.23 rad/s cycled at 0.25 Hz. ....	165

Figure 7.12. Cross-correlation results for 50 rpm (5.23 rad/s). The first, second, and third row represent correlations of the disturbance torque with VA position, velocity, and acceleration, respectively. The first, second, and third columns represent results for 1, 0.5, and 0.25 Hz, respectively. ....	166
Figure 7.13. Cross-correlation results for 100 rpm (10.46 rad/s). The first, second, and third row represent correlations of the disturbance torque with VA position, velocity, and acceleration, respectively. The first, second, and third columns represent results for 1, 0.5, and 0.25 Hz, respectively. ....	167
Figure 7.14. Cross-correlation results for 200 rpm (20.93 rad/s). The first, second, and third row represent correlations of the disturbance torque with VA position, velocity, and acceleration, respectively. The first, second, and third columns represent results for 1, 0.5, and 0.25 Hz, respectively. ....	168
Figure 7.15. Variation of dynamic coupling factor between the FA and VA, and its derivative as a function of the RSF. Note that as $\tilde{\rho} \rightarrow \infty$ , $\tilde{\mu}, \tilde{\mu}' \rightarrow 0$ . This figure is adapted from (Rabindran and Tesar, 2007a, pp. 421). ....	169
Figure 7.16. Velocity Trajectories of the VA, FA, and the Output During a Sinusoidal Trajectory Tracking Task by Utilizing Null Space Velocities to Stay Away from Low-Velocity Zones. ....	174
Figure 7.17. Velocity Trajectories of the VA, FA, and the Output During a Sinusoidal Trajectory Tracking Task by Utilizing Null Space Velocities to Stay Away from Low-Velocity Zones. ....	175
Figure 7.18. Conditions imposed on the PFVA testbed during Experiment IV for response to slow collisions. ....	177
Figure 7.19. Results for Experiment IV when $\dot{\phi}_v = 11.42$ rad/s (link approach velocity = 0.0326 m/s). This experiment demonstrates the safety feature of the PFVA due to the backdriveability of the FA input. Three distinct phases are notable and separated by dashed-lines: (i) free space motion of the output link, (ii) introduction of the stationary obstacle ( $C_0$ line), and (iii) removal of the obstacle ( $C_n$ line). ....	179
Figure 7.20. Results for Experiment IV repeated for $\dot{\phi}_v = -15.7$ rad/s (link approach velocity = 0.0448 m/s). ....	180
Figure 7.21. Experimental results of safe response to impact loads. (Top) Time-domain trajectories of FA and VA velocities, and torque data. (Bottom) FFT of torque data to show the broad spectrum of frequencies in an impulse. ....	183
Figure 7.22. Experimental results of safe response to impact loads. (Top) Time-domain trajectories of FA and VA velocities, and torque data. (Bottom) FFT of torque data to show the broad spectrum of frequencies in an impulse. ....	184
Figure 8.1. Configuration spaces of interest in a PFVA-driven serial robot manipulator (adapted from Chen and Tsai, 1993). ....	188
Figure 8.2. Conceptual sketch of the velocity kinematics of a generalized link $jk$ on a PFVA-driven manipulator. ....	190
Figure 8.3. A PFVA-driven manipulator's output may be visualized as the velocity-summed combination of two constituent manipulators (with the same joint space and link configuration) driven by dual inputs at joints: (i) FAs, and (ii) VAs. ....	192
Figure 8.4. Conceptual picture of the null space velocities in the actuator space of the PFVA-driven manipulator that result in zero joint velocities. In addition, if the manipulator is kinematically redundant (i.e. $n > m$ ), then there are also null-space velocities in the joint space that contribute to zero EEF velocity. ....	194
Figure 8.5. Conceptual sketch of the acceleration kinematics of a generalized link $jk$ on a PFVA-driven manipulator. ....	196
Figure 8.6. Conceptual sketch of an applied static force $\mathbf{f}_p$ at point P and moment $\mathbf{m}_{jk}$ on link $jk$ of a PFVA-driven manipulator. ....	199
Figure 8.7. A PFVA-driven manipulator's EEF load may be visualized as being shared by two constituent manipulators (with the same joint space and link configuration) driven by dual inputs at joints: (i) FAs, and (ii) VAs. ....	201
Figure 8.8. Conceptual sketch of inertial loads to due to the acceleration of link $jk$ in a PFVA-driven manipulator. $C_j$ represents the Center of Gravity (COG) of the link. ....	203

Figure 8.9. Physical meaning of inertial torque terms from Eq. (8.79) explained with regard to the VA input-set. ....	208
Figure 8.10. A PFVA-driven manipulator's inertial torque demand due to an EEF motion plan may be visualized as being shared by two constituent manipulators (with the same joint space and link configuration) driven by dual inputs at joints: (i) FAs, and (ii) VAs. ....	209
Figure 8.11. A PFVA-driven manipulator's total torque demand due to an EEF motion plan and contact force may be visualized as being shared by two constituent manipulators (with the same joint space and link configuration) driven by dual inputs at joints: (i) FAs, and (ii) VAs. ....	211
Figure 8.12. Conceptual representation of a planar 3R PFVA-driven manipulator performing a finishing operation on a part surface. The centers of mass of the links are also shown. ....	212
Figure 8.13. Design space for choosing RSF values for the 3R PFVA-driven Robot. ....	214
Figure 8.14. Design cases considered in the RSF-based parameter study. ....	215
Figure 8.15. Joint torques for the finishing task performed by a 3R planar manipulator (see Appendix D for details). ....	217
Figure 8.16. Distribution of torque requirement between VA and FA input sets of the 3R manipulator for Design Case 1 ( $\tilde{\rho}_1 = \tilde{\rho}_2 = \tilde{\rho}_3 = 255.4$ ). ....	218
Figure 8.17. Distribution of torque requirement between VA and FA input sets of the 3R manipulator for Design Case 2 ( $\tilde{\rho}_1 = \tilde{\rho}_2 = \tilde{\rho}_3 = 1$ ). ....	220
Figure 8.18. Distribution of torque requirement between VA and FA input sets of the 3R manipulator for Design Case 3 ( $\tilde{\rho}_1 = 255.4, \tilde{\rho}_2 = 24.3, \tilde{\rho}_3 = 1$ ). ....	221
Figure 9.1. Parallel Force/Velocity Actuation concept. (a) Schematic, (b) Laboratory Prototype. ....	230
Figure 9.2. A PFVA-driven manipulator's total torque demand due to an EEF motion plan and contact force may be visualized as being shared by two constituent manipulators (with the same joint space and link configuration) driven by dual inputs at joints: (i) FAs, and (ii) VAs. ....	236
Figure 9.3. Conceptual picture of force- and velocity-summing actuator combinations. We studied the PFVA case in this report. ....	245
Figure 9.4. Torque-summing combinations of two inputs. (a) (Sreevijayan et al., 1994; Tesar, 2003) (b) (Chang and Tsai, 1993). ....	246
Figure A.1. Differential Link Mechanism. Note in this example $r_1 > r_2$ . ....	251
Figure A.2. Differential Gear Mechanism. The outer and inner gears have diameters $d_1$ and $d_2$ , respectively (i.e., $d_1 > d_2$ ). ....	252
Figure A.3. Differential Gear Mechanism with Mechanical Feedback. ....	253
Figure A.4. Differential Gear Mechanism without Mechanical Feedback and with Pure Static Loads. ....	254
Figure A.5. Free-Body Diagram of Differential Gear Mechanism with Mechanical Feedback. ....	255
Figure C.1. Planar four-bar linkage driven by a PFVA. ....	259
Figure C.2. Equivalent link representation of the four-bar linkage (Rabindran and Tesar, 2007a). ....	260
Figure D.1. Conceptual representation of the planar 3R PFVA-driven manipulator used in Chapter 8. The Tool Point (TP) is also shown. ....	262
Figure D.2. Conceptual representation of a planar 3R PFVA-driven manipulator performing a finishing operation on a planar part. ....	266
Figure E.1. PFVA Experimental Testbed Layout with Labeled Parts. ....	268
Figure E.2. Block Diagram Representing the System Layout of the PFVA Testbed. ....	270

# INTRODUCTION AND BACKGROUND

## Chapter 1. Introduction

### 1.1. BACKGROUND

During the early days of robotics, a major push came from the manufacturing sector and was pioneered in the United States by Joseph Engelberger and the Robot Industries Association (RIA). The field of industrial robotics has made significant progress since then and has resulted in robust mechanical hardware that outlasts (with useful life of over 100,000 hours) controller hardware; sensing platforms that can more easily be integrated with the hardware; and development in robotic tooling. However, manufacturing automation requirements, such as precise, robust, and stiff motion control, have driven the mechanical design of industrial robots and, consequently, these devices have become rugged automatons (see Figure 1.1 (a)) which can potentially injure humans in their close proximity.

The applications of robotic technologies have become more versatile since the industrial robotics revolution. For instance, the growing and fairly well-established field of service robotics is centered on assisting humans, sometimes even physically. Even in the manufacturing sector there is a new approach of cooperative robots working in unison with human operators. This new perspective has required a new approach to robot designs - safety around humans. Several interesting designs have emerged from human-centric design requirements. For example, the Barrett Arm (Figure 1.1 (b)) is a research platform that uses cable-based backdriveable joints (Townsend and Salisbury, 1988). At DLR, Germany, light-weight manipulator designs (Figure 1.1 (c)) together with robust sensing have allowed these devices to interact safely with humans even in unstructured

environments. A relatively new application area that is driving the requirements for human-safe robotics is rehabilitation and therapy (for example, ARMEO rehabilitation robot from Hocoma, Switzerland, shown in Figure 1.1 (d)).

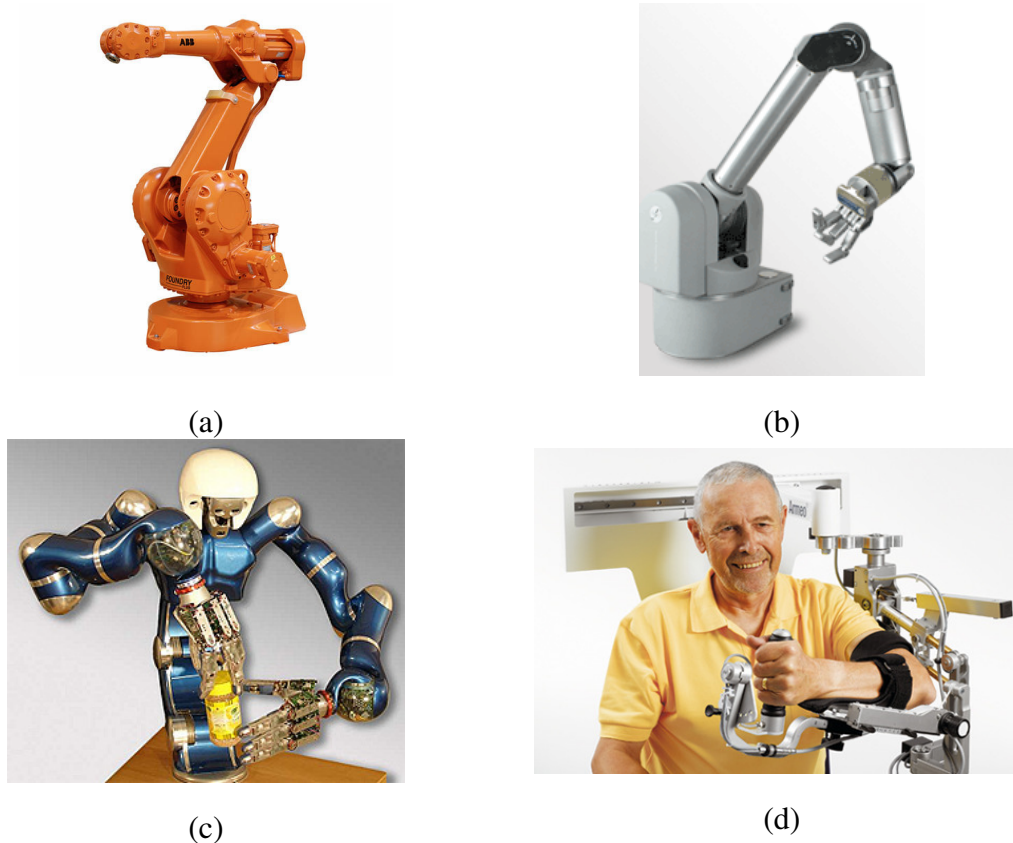


Figure 1.1.A Snapshot of the Variety of Mechanical Designs for Serial Robot Manipulators. (a) Typical Industrial Manipulator from ABB that is Frequently Populated with Actuators with High Gear Ratios and High Output Inertia, (b) A Whole Arm Manipulator Based on Cable-Driven Backdriveable Joints (Barrett Technologies, Inc.), (c) A Light-Weight Humanoid with a Suite of Sensors that Enables Highly Responsive Dexterous Interaction with its Environment (DLR, Germany), and (d) An Exoskeleton-Based Rehabilitation Robot (ARMEO) Used for Stroke Therapy (Hocoma, Switzerland)

Furthermore, to increase the cost-benefit from robots, we need to improve their functional capabilities (Tesar 1989; Tesar and Geisinger 1998; and Bekey, et al. 2006).

This translates to the need to move from conventional position or velocity controlled robots to more complex systems that can adapt their dynamic interaction with the environment. For many applications from precision light machining and intelligent fixturing in manufacturing automation, to collision detection and safe manipulation in human-robot interaction, and unstructured dexterous manipulation we need the dynamic interaction of the robot to be able to vary from a purely force controlled forgiving response to a relatively stiff velocity controlled response. For instance, dexterous applications require smooth motion planning and intricate force-profile management. The most challenging tasks are the ones in which force and motion have to be managed in the same direction, like deburring.

## **1.2. RESEARCH OBJECTIVES**

Significant actuator research effort at the University of Texas Robotics Research Group (UTRRG) has emphasized on expanding the choices in Electro-Mechanical Actuators (EMAs). A comprehensive statement of this work spanning approximately three decades is documented in the EMA architecture report (Tesar, 2003). The current research builds on past work at UTRRG in the area of differential systems (Tesar, 1972; Pennington and Tesar, 1991; McNatt and Tesar, 1993), layered control (Tesar, 1985) and fault-tolerance (Tesar et al., 1990), and investigates a new design for velocity summing dual actuators with unequal sub-systems.

Dexterous tasks can, in the limit, be classified into two mutually exclusive functional regimes, namely, force-controlled and velocity controlled. In purely force-controlled tasks, the objective is to achieve a desired interaction force (velocity management being secondary) and in purely velocity-controlled task, the goal is to adhere to a reference motion plan (force control being secondary). The EMAs that drive intelligent mechanical systems (like dexterous manipulators) can also now be classified

into “ideal” Force Actuators (FA), that are near perfect force/torque sources, and “ideal” Velocity Actuators (VA), which are near-perfect velocity sources. To a great extent, the transmission ratio used in their gear trains characterizes the response of actuators (Townsend and Salisbury, 1988; Cho, Tesar, and Freeman, 1989<sup>1</sup>; Tesar, 2006a). A high reduction gear ratio (such as 150:1) makes the actuator behave like a stiff velocity generator (or VA) in that it can manage a commanded velocity while reacting to force disturbances robustly. On the other hand, an EMA with a low reduction gear ratio (such as a direct drive actuator) acts like an ideal force generator (or a FA) and can maintain a reference force while reacting to velocity disturbances. These inverse characteristics arise due to the fact that force and velocity are power conjugate variables.

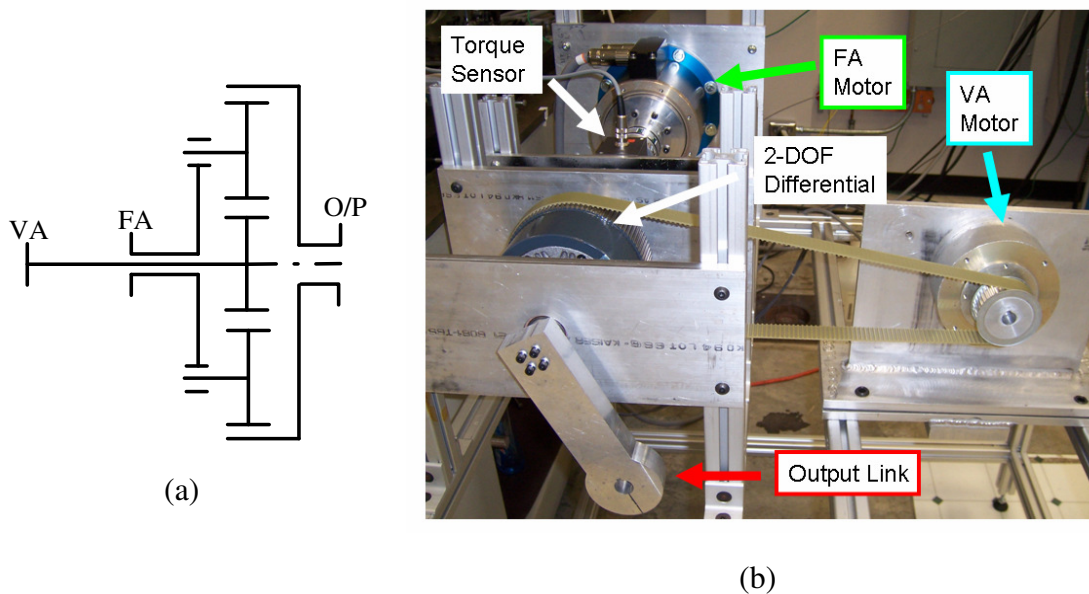


Figure 1.2. Parallel Force/Velocity Actuation concept. (a) Schematic, (b) Laboratory Prototype.

<sup>1</sup> This work on antagonistic actuation followed from a 10 year development that led to a prototype of an elbow module with antagonistic hydraulic actuation first demonstrated about 1980.

In this research we propose an approach called Parallel Force/Velocity Actuation (PFVA) in which we combine an FA and a VA using a 2-DOF differential gear train. There are primarily two goals for this design: (i) to provide at least one backdriveable input in this dual-input actuator by introducing a near direct-drive subsystem that can be responsive to output force disturbances, and (ii) to enhance the dynamic range of velocities of the combination actuator in comparison to its constituent sub-systems. The first goal translates to improved mechanical safety of a PFVA-driven manipulator and the second goal addresses the requirement to expand the choices available at the actuator-level. A review on differential mechanisms has been compiled in Appendix A for the interested reader.

### **1.3. RESEARCH OUTLINE**

In this work, our focus will primarily be at the actuator level where a significant analytical and experimental characterization of this novel PFVA design is necessary. For instance, due to its unconventional design (two inputs one of which can be backdriven), a scalable analysis of acceptable designs and operational scenarios based on relevant system parameters with good physical meaning is a challenging task. In addition, understanding the response of the actuator to various operational scenarios, such as pure velocity control based on kinematic redundancy in the drive or forgiving response to inadvertent collisions, required the development of a comprehensive dynamic model with realistic parameters. For instance, a relevant phenomenon that needs to be studied in a differentially-summed actuator such as the PFVA is the dynamic disturbance of one input due to the other. In our analysis, the ratio of velocity ratios between the FA and the VA, termed the Relative Scale Factor (RSF), emerged as a dominant parameter. Based on our parametric understanding of PFVA designs based on first principles analysis of power-flow in the device and force distributions between the inputs, a prototype and associated



testbed were designed and built using commercial-off-the-shelf components. Using controlled experiments, two important phenomena in our prototype, friction and dynamic coupling between the two inputs, were identified and characterized. Additionally, two other experiments were conducted to characterize the operational performance of the actuator in velocity-mode and in what we call ‘torque-limited’ mode (i.e. when the FA input can be backdriven). The implication of our actuator level analytical and experimental work at the robot system level was then studied using a generalized modeling framework using kinematic influence coefficients.

#### **1.4. SCOPE**

The PFVA concept, which is discussed in greater detail in Chapter 3, can be extended to include more than two actuators and multiple domain actuators as inputs, and can be implemented in both linear and rotary configurations; however in this work we will consider only electromechanical rotary PFVAs with two inputs (a high gear-ratio input and a relatively low gear-ratio input). Furthermore, most of our analysis considers the drive train in the PFVA to be a positive-ratio train (meaning that the velocity ratios of both inputs have the same sign). In the system level analytical formulation presented in Chapter 8, we will only consider the serial robot manipulator geometry, although PFVAs could be incorporated in mechanisms with other topologies.

#### **1.5. CONTRIBUTIONS**

The significant contributions of this work are in three areas: (i) parametric design of PFVA-type actuators, (ii) analytical modeling of the PFVA actuator and its experimental characterization, and (iii) extension of our actuator-level understanding of the PFVA to the robotic system using a generalized analytical formulation. Specific contributions are listed below:

- **Parametric Design of PFVAs:** In this area the main contribution of this work is a dimensionless (and therefore, scalable) parametric analysis of PFVA design and operation based on approximately six new fundamental design parameters of the actuator defined in this work. Based on parametric analysis of power distribution and force distribution between the FA and VA in the PFVA, over ten design and five operational guidelines were laid out. A sub-set of these guidelines was used to design a single-joint PFVA testbed used in our experimental work. Identification of the purely geometric RSF  $\tilde{\rho}$  as a dimensionless and dominant parameter in the PFVA-type velocity summing devices is extensible to other differential-based mechanisms (for example, differential screws).
- **Analytical and Experimental Characterization of PFVA Dynamic Response.** Analytical model and experimental demonstration was presented for a method to resolve the kinematic redundancy in the PFVA to meet a velocity specification at the output while optimizing for secondary criteria (such as reducing low-velocity friction effects by operating each input close to its maximum velocity capability). Two performance limiting physical phenomena were experimentally identified and compared either with existing models in the literature or with analytical models developed in this work: (i) friction, including position- and velocity-dependent components, and stiction, (ii) dynamic disturbance between the FA and the VA in a PFVA. The experimental methodology to measure dynamic coupling in PFVA-type actuators is an original contribution of this work. The mechanical safety aspect of the PFVA was tested using dynamic simulations based on models developed in this research, and then experimentally demonstrated using the PFVA prototype for two types of loading: (i) slow collisions and (ii) impacts. The partial experimental identification of the dynamic properties of the FA (damping ratio

and natural frequency) is a unique result which includes the servo-system dynamic properties in addition to the mechanical properties.

- **Generalized Analytic Formulation for PFVA-driven Manipulators.** The analytical formulation for serial robot manipulators using PFVA-type inputs is a new result for velocity-summing mechanisms. The development of this model with particular attention to the partitioning of manipulator work function requirements at each input is a new approach that enables the robot designer to explicitly evaluate the result of a design change. This capability was demonstrated in simulation with three simple case studies.

## **1.6. REPORT OUTLINE**

This report is organized broadly into four sections: (i) introduction and background (Chapter 1-Chapter 3), (ii) actuator level analysis and experiments (Chapter 4-Chapter 7), (iii) system level analytical formulation (Chapter 8), and (iv) dissertation summary (Chapter 9).

Chapter 2 reviews literature in the area of dual-input actuators and human-safe manipulator designs. In this chapter we first provide an overview of the design and sensing/control based research issues in physical human robot interaction. A taxonomy is developed for dual actuators based on force/velocity relationships: force-summing and velocity-summing actuators. The United States patent literature is surveyed in the area of dual actuators.

Chapter 3 introduces the PFVA concept and discusses the kinematics of the differential drive train. The definition, model, and physical meaning of RSF, a dominant design parameter for PFVAs, are developed.

Chapter 4 presents a dimensionless parametric model for designing a PFVA with the focus on power flow modes in this device. Four design and two operational guidelines

are suggested based on the models. As a representative result, the overall mechanical efficiency of the PFVA decreases as we increase the RSF and the ratio of operating velocities of the VA and FA. A model is also developed for effective inertia of PFVAs.

Chapter 5 extends the work on power flow in Chapter 4 to include a parametric understanding of different types of load distributions (i.e., static loads and inertia loads) and dynamic parameter distributions (i.e. stiffness and acceleration responsiveness) between the two inputs of a PFVA. Six design guidelines were proposed based on this force distribution analysis. An example result is that the effective compliance of the PFVA increases when the compliance of the FA increases. The system essentially behaves as a system of springs in series with different displacement influence coefficients to the output.

Chapter 6 develops an analytical model for the dynamic response of the PFVA. This model is then used to simulate the forgiving response of the actuator, due to the backdriveability of the FA, during collision scenarios. An additional mode of operation – pure velocity-based control utilizing the kinematic redundancy in the differential train – is also modeled.

Chapter 7 describes our experimental work that builds on the analytical work discussed in Chapter 6, with a single-joint PFVA prototype and testbed. Two sets of experimental results are presented: (i) parameter identification of friction model parameters and dynamic coupling between the FA and VA, and (ii) demonstration of utilization of the kinematic redundancy of the differential drive-train and experimental testing of the safety feature of the PFVA. One noteworthy result from this work was the relatively strong correlation in our testbed of the disturbance torques on the FA due to the velocity of the VA.

Chapter 8 then draws from the analytical and experimental understanding of a single-joint PFVA to develop the analytical formulation for an  $n$ -DOF PFVA-based serial robot manipulator. This development builds on already existing and well-established dynamic models for serial robots; however it focuses on expressing the equations of motion for a PFVA-robot so that the contribution of each input set (FA and VA) is explicit. This emphasis in the analysis lends better physical understanding to the designer who would potentially use this model for design optimization or dynamic response studies. A representative result from this work is the design case study of a 3-DOF PFVA-robot with decreasing values for RSF from the base to the last joint.

Chapter 9 summarizes our research results and conclusions, and lays down a roadmap for short-term and long-term future work in the area of PFVA-type actuators and systems. Based on this work, it is expected that a 3-DOF planar PFVA-based manipulator system can be demonstrated in the near future to perform complex tasks where most features of the PFVA will be evaluated.

## **Chapter 2. Literature Review**

Robots are now moving from their conventional confined habitats (such as factory floors) to human environments where they assist and physically interact with people. Consequently, the requirement for reliable, effective, and safe force control capability is overarching in such Human Robot Interaction (HRI) systems. The primary objective of the Parallel Force/Velocity Actuation (PFVA) concept, the topic of this research, is to provide inherent mechanical safety by incorporating at least one backdriveable force path to the output. Actuator designs that were motivated by similar goals (inherent safety) have been proposed in the literature. In this chapter we will review and summarize some of that work with an emphasis on multi-input actuation paradigms and systems assembled from such actuators. This literature review is focused on the following topics: (a) implication of actuator design and control to robot force control, (b) taxonomy for dual input actuators, (c) dual input actuators for improved performance and safety, and (d) patent literature in the area of dual actuators.

### **2.1. ACTUATOR DESIGN AND CONTROL INFLUENCE ON PHYSICAL HRI**

Physical HRI requires a very responsive and safe robot system (Alami et al., 2006). The efficacy of humans to perform safe and responsive manipulation at different scales is due primarily to the characteristics of muscles (Hill, 1970). Similarly, in mechanical systems, the actuator is a predominant component which principally governs the characteristics of the system at large. The impact of characteristics of actuation mechanisms on the performance of manipulator systems was recognized early on by Tesar (1989). In that forecast paper, Tesar predicted an increased thrust on mechanical manipulators with redundant prime-movers that would expand the control capability of

the inputs. There are two fundamental issues that impact the overall performance of the actuator and, therefore, of the system: (i) mechanical design of the actuator, and (ii) sensing modalities and controlled system characteristics. These are both important for the successful implementation of a HRI system. However, several approaches have been proposed in the literature to provide inherent safety by emphasizing design or control, which we will now take a closer look at.

### **2.1.1. Background on Design Issues**

Dynamic issues in system performance, especially system responsiveness, were studied by Eppinger and Seering (1992) who proposed a manipulator design guideline in their paper. That work carefully analyzed, theoretically and experimentally, the implication of compliance and its location in the machine (collocated or non-collocated actuator and sensor) to force control performance. A similar body of analytics for appropriate placement of mass and stiffness in mechanical systems was proposed by Tesar and Matthew (1976), although motivated by an entirely different goal of reducing distortion in cam systems. A common approach in the force control literature to improve impact safety deliberately includes compliance between the actuator and the load. This is called Series Elastic Actuation (SEA) and was originally proposed by Pratt and Williamson (1995a) at the MIT Leg Lab. By traditional design rules of thumb for precision systems (such as velocity-controlled industrial robots), this approach is counter-intuitive. However, for impact resistance and force control, the passive SEA approach might have some merit<sup>2</sup> although it comes at the cost of reduced bandwidth (due to the relatively low natural frequency resulting by this deliberate introduction of the series compliance). Therefore, SEAs are good candidates for applications requiring low

---

<sup>2</sup> Refer (Hyde and Cutkosky, 1994) for a discussion on the challenges of regulating force during a rigid-rigid contact of a manipulator with its environment. Addition of compliance in this system tends to reduce the power exchange during such interactions.

frequency force control such as robotic prosthesis for the lower-limb or humanoid robots. Both electromechanical and hydraulic<sup>3</sup> SEAs have been designed. Several variants of the original SEA design have since been proposed. For example, a series damper actuator includes a damper (instead of an elastic element) in-line with the actuator before the load (Zhou, et al., 2009). The notion of including compliance for force control in unstructured environments has also been used to design selectively compliant tool interfaces such as the Remote Center Compliance (RCC) (Whitney, 1982). The concept of series elasticity is found in various forms, for example, as protective compliant covering over manipulators that have high effective inertias. A recent review and comparison of passive-compliant actuation concepts was presented by Vanderborght et al. (2009).

The effect of transmission characteristics (including the transmission ratio) on force controlled performance of manipulators was studied by Townsend and Salisbury (1988). The study of actuator responsiveness as a function of the transmission ratio is especially noteworthy in that work. Results from that study were applied to the design of the commercialized Whole Arm Manipulator (WAM) from Barrett Technologies, Inc. They also studied the implication of these actuator characteristics on robotic applications. More recently, Tesar (2006a) elucidated the important role of the gear train reduction ratio for Electromechanical Actuators (EMAs) by considering six key application areas and an analysis of appropriate gear train ratios for these applications. Gear reduction allows electrical motors to operate in high speed/low torque mode (which is more efficient for them) while providing the required high output torque at low speed that are typical of robotic applications. Gear reduction increases the effective inertia at the output and, depending on the type of transmission, might increase friction and stiffness. Some

---

<sup>3</sup> In an actuator survey by Hollerbach, Hunter, and Ballantyne (1991), various types of actuator technologies, i.e. electromechanical, hydraulic, pneumatic, etc., were compared in terms of two criteria: power density and torque density.



researchers have worked with direct-drive (meaning no transmission between the motor and the load) robotic actuators (Asada and Youcef-Toumi, 1987) which have excellent force control capability<sup>4</sup> due to their sensitivity and responsiveness to forces; however, they tend to add mass due to their higher torque capability. The actuator discussed in this report uses a velocity-summing combination of the high reduction ratio actuator and a near direct-drive actuator. In Chapter 3 we will discuss this concept in greater detail.

### **2.1.2. Background on Sensing/Control Issues**

A second approach to improving force controlled performance has emphasized force control algorithms that use force/torque sensing (frequently based on strain gauge measurements). Force/torque sensing schemes can be classified based on their location on the manipulator: (i) end-point sensing includes a force transducer distally at the tool end of the manipulator (Roberts, 1984), (ii) joint-torque sensors measure loads acting at the joint (Luh et al., 1983; Pfeffer et al., 1989), (iii) a combination of (i) and (ii) or distributed load sensing such as compliant-skin tactile sensors (Russell, 1987) are useful for whole-arm manipulation applications, and (iv) base force/torque sensors are located at the manipulator's base and can be used for friction and gravity compensation (Morel et al., 2000). A platform that implements joint torque control together with a light-weight arm design is the DLR light-weight robot (Albu-Schäeffler et al., 2008).

There are two fundamentally distinct force/motion control problems: (i) control of forces and motions in mutually orthogonal directions in the task frame, and (ii) control of forces and motions not necessarily in orthogonal directions in the task frame as is required in material removal processes such as deburring or grinding. Problems of type (i) are relatively less challenging and a classical approach to deal with mutually orthogonal force and motion control requirements in the task space is called Hybrid

---

<sup>4</sup> Force control on direct-drive actuators can be done using current-control of the motor.

Force/Position Control (Raibert and Craig, 1981). For applications of type (ii), Salisbury (1980) proposed active control of the stiffness between the manipulator end-point and the environment. The concept was based on the definition of a virtual stiffness at the robot-environment interface which reduces the force control problem to a problem of controlling the deflection (i.e. position control) of the virtual spring. This is similar to explicit force control using a strain-based force sensor (where the elastic strain element acts as the spring); however the difference is that the stiffness could be virtual in active stiffness control. The concept of SEA is also similar to this approach, although the series elastic element in an SEA is a physical spring (like a force sensor). The idea of active stiffness control was later generalized by Hogan (1985) to impedance control where the virtual interface between the robot and the environment is a combination of all three dynamic elements (spring, mass, and damper) and the algorithm defines the relationship between the interface forces<sup>5</sup> and the states of this virtual interface. This relationship is frequently linear. Several variants of these two basic virtual interface approaches have been proposed in the literature. For instance, admittance control (Glosser and Newman, 1994) dictates the admittance (as opposed to the impedance) between the robot and its environment. There are two challenges associated with the virtual interface approaches. Firstly, the parametric definition of the virtual interface (for example, the spring constant in stiffness control or the mass in impedance control) based on the required robot task performance is challenging. Secondly, as for any feedback-based controlled system, the closed-loop response is maintained only as long as the frequency content in the system disturbances do not exceed the closed-loop bandwidth of the controller. In our own experience (Rabindran and Tesar, 2004) at the University of Texas Robotics Research Group (UTRRG), an admittance-type control algorithm was used to implement force-

---

<sup>5</sup> The energy-domain independent terminology for power conjugate variables is *effort* and *flow*. In mechanical systems, effort is force and flow is velocity.

based teaching of robot end-point trajectories (see Figure 2.1 for system setup). Feedback from an end-point force/torque sensor was used to command accommodative end-point motions (scaled based on measured forces). This application allows us to change the behavior of the robot end-point based on the scaling between the forces (effort) and velocities (flow); however this imposed behavior can be guaranteed only as long as the contact forces do not contain frequencies above the closed-loop bandwidth of the controlled-system (80 Hz in our case). This means that if the user, for discussion purposes, hits the end-point with a hammer (impulse forcing function or shock load), the controlled-system cannot respond. In this scenario, the user will feel the inherent dynamics of the system, which in our manipulator meant high effective inertia and stiffness because the powercubes use a reduction as high as 101:1. This explains the importance of introducing a backdriveable input in the system to make it mechanically safe. The goal of the current research is to provide sufficient input resources using a dual actuator to create a physical basis for the conceptual framework of impedance control.



Figure 2.1. A force-based teaching HRI application implemented on an off-the-shelf modular manipulator from Amtec, Germany. An admittance-type control was implemented using a 6-axis end-point force/torque sensor from ATI. The OSCAR (Kapoor and Tesar, 1996) manipulation software enabled extending this application to multiple robot platforms.

### **2.1.3. Implications for the Physical HRI System Designer**

We have discussed some design and control related issues that are significant to physical HRI. An important question can be raised at this point: where should the research emphasis be to enhance the safety of such systems? Should it be on the fundamentally different mechanical design of actuators or on leveraging improvements in control methodologies (and associated sensing technologies) to improve the system's situational awareness and responsiveness? The simple answer to this question is that a mechanical/control co-design approach is best suited as will be discussed in the next section on safe actuators. Furthermore, from the system's point of view, it is important to incorporate safety into all sub-systems (mechanics, control hardware, and software). In the current research, our emphasis is on mechanical design and our actuator has dual-inputs that are combined using a velocity-summing differential. We will now review the state of the art in dual-input actuators. This survey focuses on multi-input actuator designs primarily for mechanical safety, but also includes those proposed for other purposes (for example, fault-tolerance).

## **2.2. STATE OF THE ART IN MULTI-INPUT ACTUATOR CONCEPTS**

Studies indicate that actuators which are capable of varying their dynamic response will be beneficial for reliable and safe manipulation in human-centered environments (Bekey et al., 2006; De Santis et al., 2008). Recent conference workshops (Albu-Schäeffler et al., 2008) and journal special issues (Vanderborght et al., eds., 2008) are evidence of the growing interest in the research community in this area. The emphasis in this area is on inherently safe robot systems. Many different approaches have been proposed in the past to achieve variable response actuation capabilities. Most of these approaches are based on dual-input actuation. Some of these actuators are based on differential drives (Kim et al., 2007; Lauria et al., 2008), some others are based on

antagonistic actuation<sup>6</sup> (Bicchi and Tonietti, 2004), and some have proposed dual-input actuation frameworks based on series-elasticity (Zinn et al., 2004). Tesar (2006d) recently surveyed dual input actuators comparable to similar concepts at UTRRG. Before we discuss some dual-input actuators in detail it is important to follow a method of classification for them.

### 2.2.1. A Taxonomy for Dual Actuators

In the past a taxonomy for high-performance actuators (including single-input concepts such as joint-torque controlled actuators) has been proposed by Lauria et al. (2008) (Figure 2.2). Although that listing is up-to-date and comprehensive (surveys approximately 2 decades of work), their method of classification was not quite generalized.

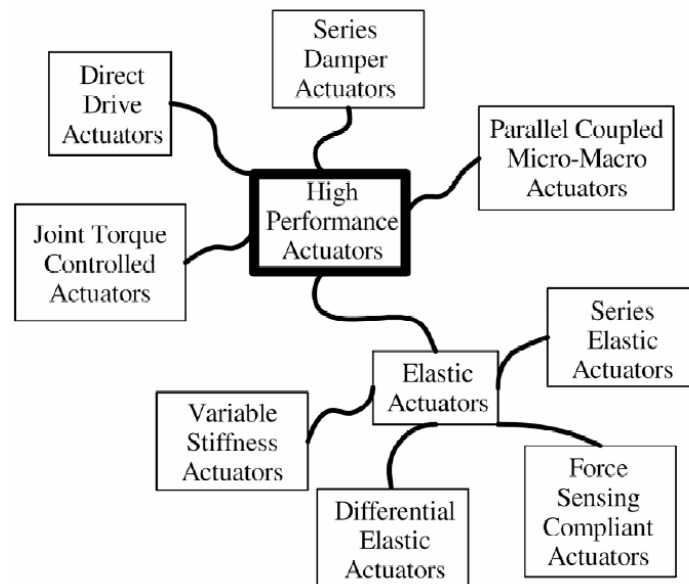


Figure 2.2. Taxonomy developed by Lauria et al. (2008) for high performance actuators.

<sup>6</sup> The concept of antagonistic actuation was earlier studied by Cho, Freeman, and Tesar (1989) which followed from a decade of work that resulted in a hydraulically actuated elbow module first demonstrated about 1980.

For instance, in Figure 2.2, direct-drive actuators could still be joint torque controlled and the authors' basis of isolating these two actuators in the classification diagram is not evident.

In the current work, our method of classification for multi-input actuators is based on the mechanics of power-conjugate variables (force<sup>7</sup> and velocity or, alternatively, effort and flow) in the device. There are two categories that result from this basis for classification: (i) force (or effort) summing and (ii) velocity (or flow) summing.

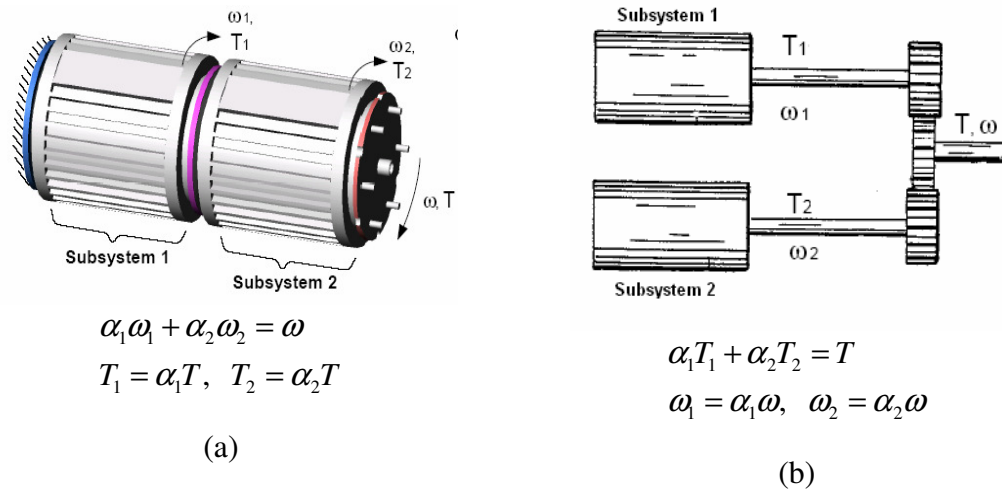


Figure 2.3. Conceptual sketches which show simple rotary examples of velocity-summing (a) and force-summing actuators (b). This figure was adapted from (Tesar, 2003) where it was originally used to classify fault-tolerant actuators.

In a linear<sup>8</sup> force-summing (velocity-summing) actuator, the output force (velocity) of the actuator is a linear combination of the input forces (velocities) while the velocities (torques) maintain a constant ratio (conceptually shown in Figure 2.3 for “equal”<sup>9</sup>

<sup>7</sup> *Force* is used in the general sense that includes forces and torques. Similarly, *velocity* includes both linear and angular velocities.

<sup>8</sup> Linear in the sense of linear superposition and not in the sense of linear motion degree of freedom.

<sup>9</sup> In “equal” subsystems  $\alpha_1 = \alpha_2 = 1$  (see Figure 2.3)

subsystems with 100% efficiency of power transfer). Force-summing configurations are commonly referred to as “parallel” and velocity-summing designs as “series”.

Table 2.1 Literature Summary on Force- and Velocity-Summing Actuation Concepts

Actuation Concept	Reference, (Institution, Country)
FORCE-SUMMING (See Section 2.2.2)	
Antagonist Joint Stiffness Control	(Migliore et al., 2005), Georgia Tech, USA
Antagonist Elbow Module	(Cho, Tesar, and Freeman, 1989), The University of Texas at Austin, USA.
Distributed Elastically Coupled Macro Mini Parallel Actuation (DECMMA)	(Zinn et al., 2004), Stanford University, USA
Moment Arm Adjustment for Induction of Net Effective Torque (MARIONET)	(Sulzer et al., 2005), Northwestern University, USA
Parallel Coupled Micro-Macro Actuator (PaCMMMA)	(Morrell and Salisbury, 1998), MIT, USA
Redundant-Drive Backlash-Free Mechanism	(Chang and Tsai, 1993), University of Maryland, College Park, USA
Torque-Summing Fault-Tolerant Actuator	(Tesar et al., 1990; Tesar, 2004), The University of Texas at Austin, USA
Variable Stiffness Actuator (VSA)	(Bicchi and Tonietti, 2004), University of Pisa, Italy
VELOCITY-SUMMING (See Section 2.2.3)	
Actuator with Mechanically Adjustable Series Compliance (AMASC)	(Hurst et al., 2007), Carnegie Mellon University, USA
Compact Hybrid Actuator for Maximum Performance (CHAMP) based on Control-in-the-Small (CITS) Concept	(Tesar et al., 1999; Tesar, 1985), The University of Texas at Austin, USA
Differential-Based Fault Tolerant Joint	(Wu et al., 1993), NASA Johnson Space Center, USA
Differential Elastic Actuator (DEA)	(Lauria et al., 2008), University of Sherbrooke, Canada
Dual Actuator Unit (DAU)	(Kim et al., 2007), Korea University, Korea
Force/Motion Control Actuator (FMCA)	(Tesar, 2003 <sup>10</sup> ; Rabindran and Tesar, 2004), The University of Texas at Austin, USA
Hybrid Actuator based on original concept of linkage-based function generators with two inputs and one output (i.e. non-linear velocity summing)	(Tokuz and Jones, 1991), Liverpool Polytechnic, UK (Mruthyunjaya, 1972), Indian Institute of Science, India
Series Elastic Actuator (SEA)	(Pratt and Williamson, 1995a), MIT, USA
Velocity-Summing Fault-Tolerant Actuator	(Tesar et al., 1990; Tesar, 2006c), The University of Texas at Austin, USA

<sup>10</sup> See the Electromechanical Actuator Architecture (EMAA) report (Tesar, 2003) on the actuator research program at UTRRG. The EMMA report is a continuously evolving document that comprehensively describes the accomplishments in actuator research within UTRRG. The conceptual origin of the parallel force/velocity actuator is the force/motion control actuator described in the 2003 version of the EMMA report.

Some dual actuators from the literature will now be classified into these categories and described in some detail. These have been summarized in Table 2.1. Some actuators listed in this list are not dual-actuators by definition, i.e. they do not have two active inputs (for example SEA and DEA); however we have included them in the list for the sake of completeness. Furthermore, although we have a comprehensive listing in Table 2.1, we will only discuss in detail the ones that are most relevant to our current research.

### 2.2.2. Force-Summing Actuators

At the University of Texas, the actuation effort has been toward maximizing the number of choices (for force and velocity control) available within the actuator (Tesar, 2003). This includes dual-level control for fault-tolerance (Tesar et al., 1990) using torque-summing actuators.

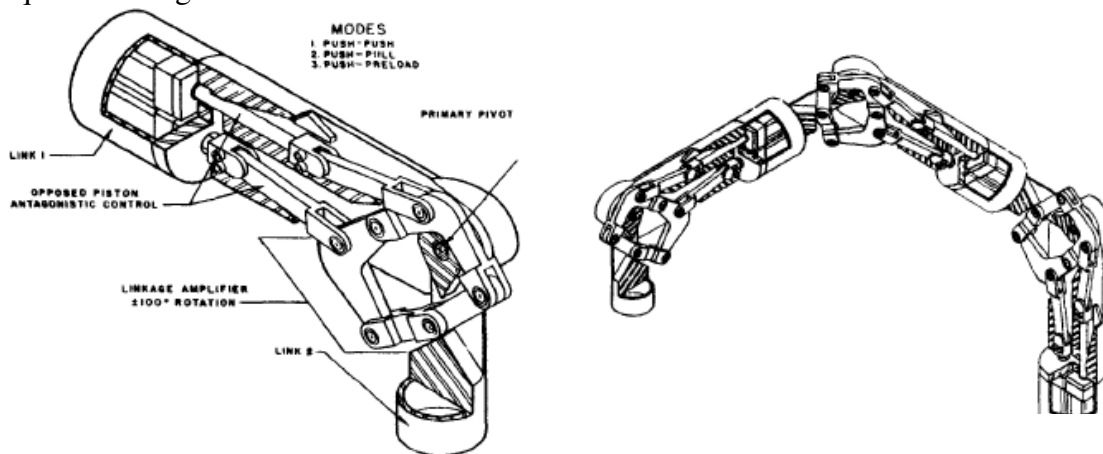


Figure 2.4. Antagonistic elbow module proposed by Cho, Tesar, and Freeman (1989)<sup>11</sup>. (a) Concept sketch of the module and (b) Concept sketch of a 3-DOF manipulator using antagonistic actuation modules. Adapted from (Cho, Tesar, and Freeman, 1989, p. 1386).

In earlier work at UTRRG, Cho, Tesar, and Freeman (1989) proposed an antagonistic actuator module and extensively modeled the dynamics of manipulators using such

<sup>11</sup> This work on antagonistic actuation followed from a 10 year development that led to a prototype of an elbow module with antagonistic hydraulic actuation.



actuators. The analytical development of manipulator stiffness as a result of inclusion of these antagonistic actuators is especially noteworthy in that work. It has been three decades since that design was proposed and demonstrated, and antagonistic actuation (another term for torque summing accomplished via opposing inputs; human muscle is a classical example of antagonistic actuation) is still a very actively researched topic (Alami et al., 2006). However in these two decades many modified variants of the classical antagonistic set up have been proposed. The level of intelligence now possible should make antagonistic actuation much more feasible.

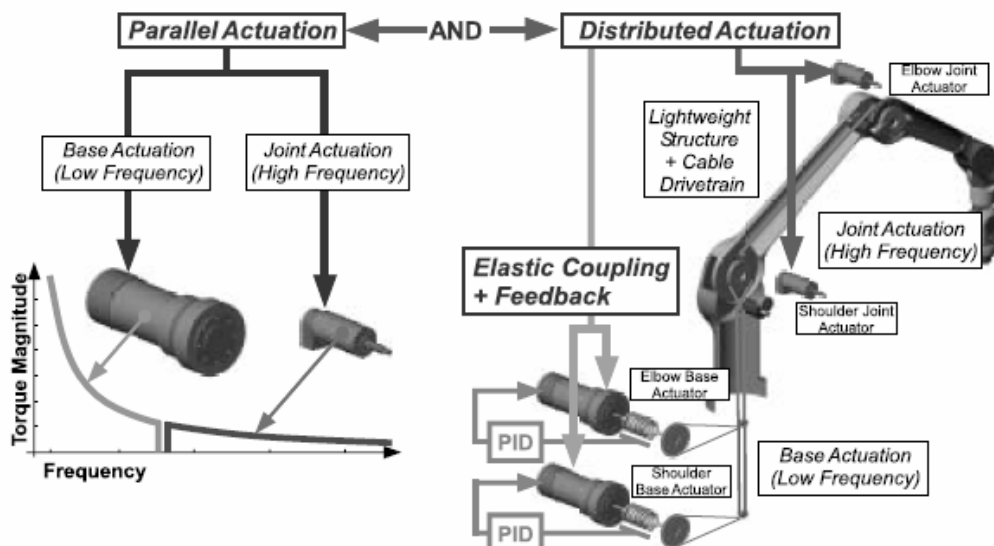


Figure 2.5. The DECMMA actuator concept from the Robotics Lab at Stanford University (Zinn, 2005, p. 48).

The Distributed Elastically Coupled Macro-Mini Parallel Actuator (DECMMA)<sup>12</sup> was proposed by Zinn *et al.* (2004) for human-centered robotic systems. That work was driven by the need to design safer as well as better performing robots that operate in close proximity around humans. The central idea of the DECMMA was to partition joint torque generation into high frequency-low magnitude and low frequency-high magnitude

<sup>12</sup> Earlier called Distributed Macro Mini (DM<sup>2</sup>) Actuator

components that sum in parallel and are appropriately located respectively at the joint and the base of the manipulator (Figure 2.5). A dual-arm testbed based on this actuation paradigm has been built at the Stanford Robotics lab.

The Parallel Coupled Micro-Macro Actuator (PaCMMMA) from MIT (Morrell and Salisbury, 1998) was motivated by, among others, the need to improve the force dynamic range (ratio of maximum and minimum applicable force) of robotic actuators. As a parallel in biological systems, the average human can lift a load as well as manipulate a small object at their fingertips. This demonstrates the large force range of human arm manipulation capability. The goal of PaCMMMA was to achieve such performance in a robotic actuator. Morrell and Salisbury used a torque-summing combination of a macro and a micro actuator using a compliant transmission as shown in Figure 2.6.

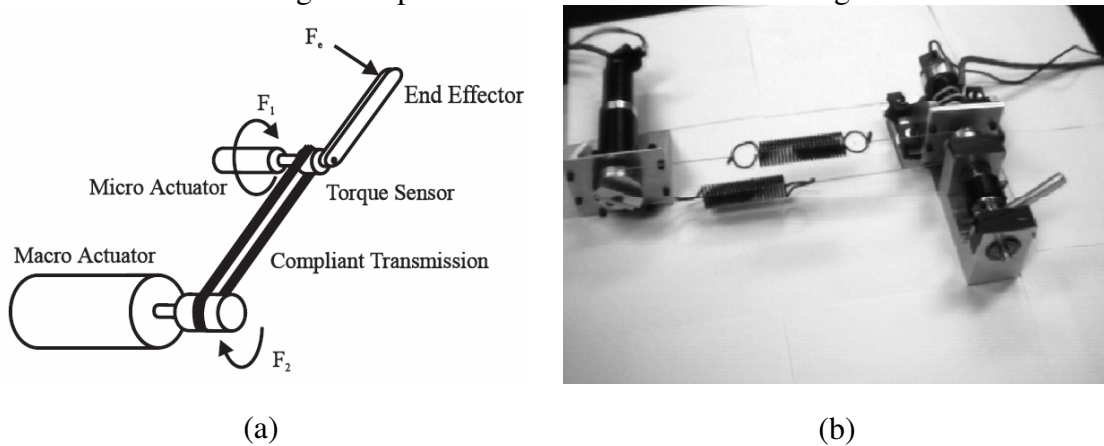


Figure 2.6. The PaCMMMA actuator concept from MIT (Morrell and Salisbury, 1998).  
 (a) Concept, (b) Physical Prototype

This can be thought of as the analogue of the Control-in-the-Small (CITS) concept (Tesar, 1985) in the force domain, i.e. layered force control. This concept is also very similar to the DECMMA approach in that the micro actuator is employed to react to high-bandwidth low magnitude forces (so that it could even be direct-drive) and the macro actuator improves the overall force range of the actuator. The compliant transmission

between the micro- and macro-actuators tends to improve, for instance, the shock safety of the system. We have discussed earlier that the inclusion of passive compliance reduces the achievable bandwidth of the actuator (approximately a third of the natural frequency of the system which in turn is reduced by the inclusion of compliance). But in the PaCMMA the macro actuator needs to control only lower bandwidth torques. Packaging of this actuator is a challenge. In addition, it uses a passive and invariable compliance which might reduce the scope of its applicability. Morrell and Salisbury (1998) proposed a set of performance measures for robotic actuators and Zinn et al. (2004) proposed a set of safety measures to assess manipulator safety around humans.

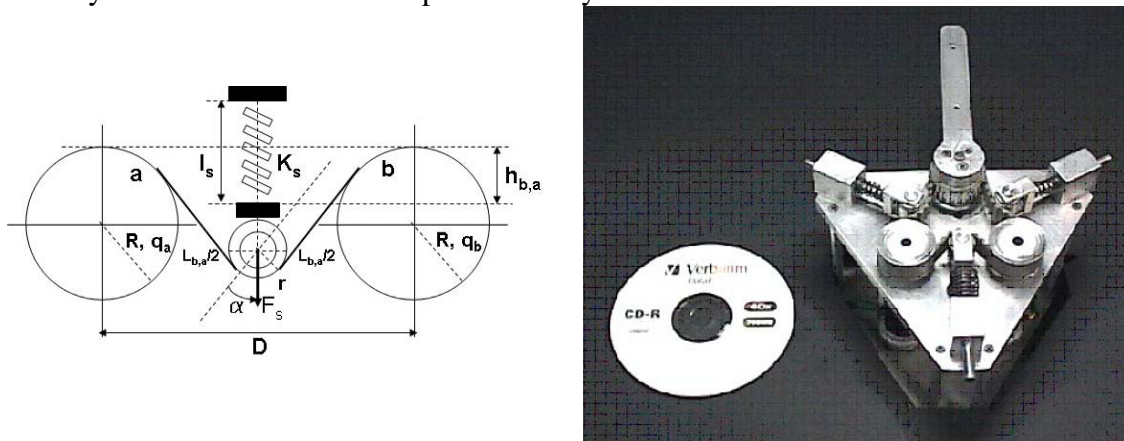


Figure 2.7. The Variable Stiffness Actuator (VSA) developed at University of Pisa, Italy (Bicchi and Tonietti, 2004). (a) Concept, (b) Physical Prototype.

Bicchi and Tonietti (2004) proposed a Variable Stiffness Actuation (VSA) paradigm for improved safety during HRI (Figure 2.7). They demonstrated this concept on a pneumatically actuated physical 3-DOF robot arm (called UNIPI Soft-Arm). This approach was a variant of the classical antagonistic set up with two opposing springs. The difference is the addition of a third spring as shown in the figure. The focus of Bicchi and Tonietti's work was to take a mechanical/control co-design approach (see our discussion on this in Section 2.1.3) to optimize the stiffness in the actuator during a point-to-point

motion trajectory while always staying below a safety index threshold in the event of an inadvertent collision. This is called the safe brachistochrone problem and the safety index they used is the Head Injury Criterion (HIC).

Other torque-summing actuators have been developed that are relevant to the current research. Cable-driven actuators and the possibility of varying the moment arm (to then vary the effective transmitted torque) were analytically and experimentally examined by Sulzer et al. (2005). From an application stand-point their motivation was to develop an inexpensive assistive device for post-stroke rehabilitation. Early work by Chang and Tsai (1993) researched the use of torque summing geared actuators to reduce the backlash in robotic mechanisms. Their design was very similar to the conceptual torque-summing actuator shown in Figure 2.3 (b). In their work, Chang and Tsai also develop an analytical modeling framework for manipulators using such gear-coupled actuators.

### **2.2.3. Velocity-Summing Actuators**

At UTRRG, the fault-tolerant actuator architecture (Tesar et al., 1990; Tesar, 2003) includes velocity summing actuators in addition to torque-summing ones. One of the seminal concepts developed in velocity-summing is that of CITS (Tesar, 1985). The work at UTRRG has not only explored torque- and velocity- summing but also this type of summing at various scales. A complete architecture has been laid out in the EMAA report (Tesar, 2003) based all these possible combinations.

As was discussed earlier, the basic concept of the PaCMMA can be reduced to a layered force control actuator. Similarly a layered velocity control actuator, called the Compact Hybrid Actuator for Maximum Performance or CHAMP (Tesar et al., 1999), was proposed for increasing the velocity dynamic range (as opposed to increasing the force dynamic range in PaCMMA) in mechanical systems. The underlying principle is

illustrated in Figure 2.8. Tesar (2003) proposed the Force/Motion Control Actuator (FMCA) design in the Electro-Mechanical Actuator Architecture (EMAA) report. The FMCA is the conceptual basis for the PFVA which is the central topic of the current work and will be discussed in depth in the following chapters.

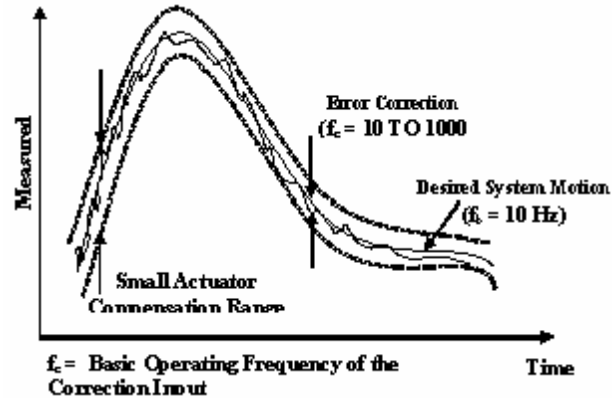


Figure 2.8. Improved velocity dynamic range via layered velocity control with CHAMP (Tesar et al., 1999). Note that the larger actuator controls the gross motion (typically the desired motion for the system) and the small actuator makes finer adjustments to this baseline.

An in-parallel actuation mechanism was proposed by Kim et al. (2007) at Korea University based on a 2-DOF planetary gear train (Figure 2.9). This is a Dual Actuator Unit (DAU) that is driven by two sub-systems, a “positioning actuator” and a “stiffness modulator”. The DAU concept bears resemblance to the Force/Motion Control Actuator proposed earlier by Tesar (2003) (Rabindran and Tesar, 2004).

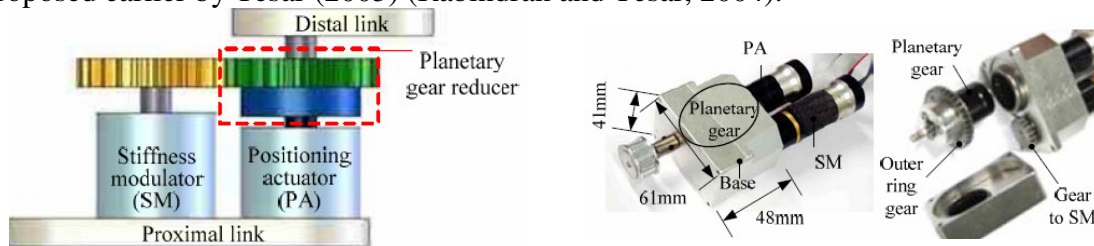


Figure 2.9. The Double Actuator Unit (DAU) from Korea University (Kim et al., 2007). (a) Concept, (b) Physical Prototype.

The DAU operates such that the “stiffness modulator” biases the position of the “positioning actuator” when a collision is detected. The DAU prototype is well-packaged; however, Kim et al. have not investigated many of the operational issues associated with multi-input gear trains (for example, the dynamic influence of one input on the other). This is especially important when the two differentially summed subsystems are unequal<sup>13</sup>. This type of analysis is one of the contributions of the current work.

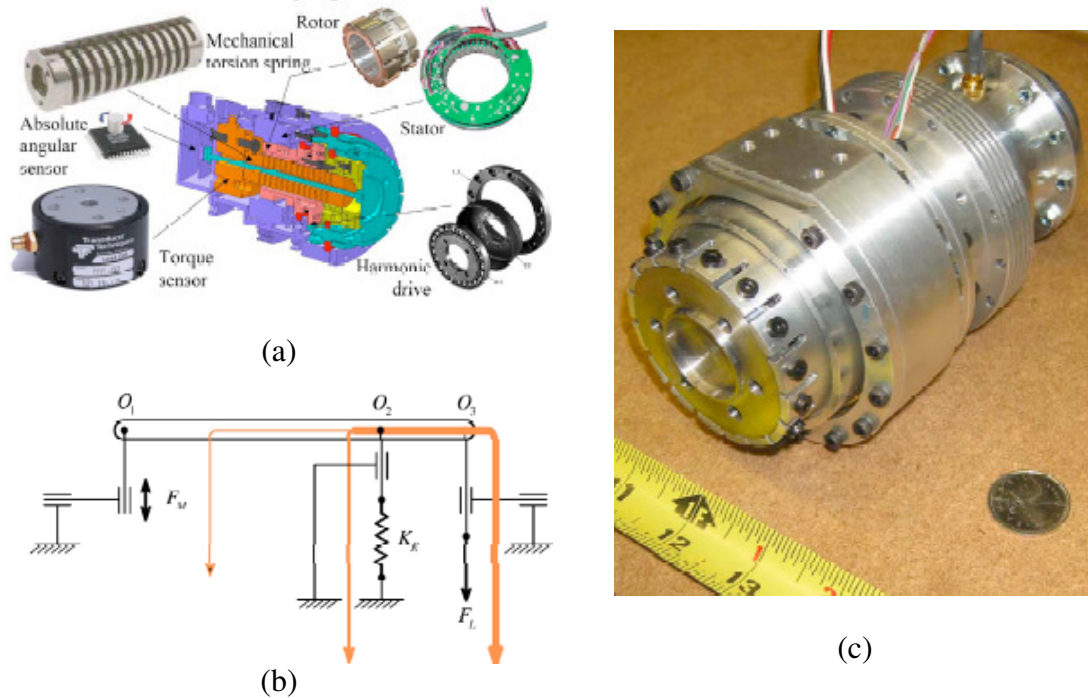


Figure 2.10. Differential Elastic Actuator (DEA) proposed by Lauria et al. (2008). (a) Concept diagram and implementation using a harmonic drive, (b) Lever analogue of the DEA (arrows indicate force flow) and (c) Packaged actuator prototype. Adapted from (Lauria et al., 2008; Legault et al., 2008).

Lauria, et al. (2008) proposed a differential-based series elastic actuator (Figure 2.10) where the motor and the series compliance are “indirectly” coupled via a differential. This concept is shown in Figure 2.10 (a) and (b), and has been developed to a

<sup>13</sup> The ratio of gear ratios between the two inputs (position input/stiffness modulator) of the DAU, i.e.  $\alpha_1 / \alpha_2$  with reference to Figure 2.3 (a), is approximately 6.69.

packaged prototype shown in Figure 2.10 (c). This actuator is similar to the PFVA proposed in the current research. The difference is that the DEA uses a passive spring element on one of the three branches of the differential, an active input on another branch, and the output to the third branch (see Figure 2.10 (b) in which this arrangement is conceptually shown). Technically, therefore, this actuator should not be classified under dual-actuators because it has only one active input. Although a passive compliance, the concept and analysis used by Lauria et al. are relevant to our research due to the similarity in the mechanics of the DEA and the PFVA.

In addition to the above discussed concepts, other velocity-summing actuators have been proposed in the literature. Hurst et al. (2007) at the Robotics Institute in Carnegie Mellon University developed an Actuator with Mechanical Adjustable Series Compliance (AMASC) for good energy storage capabilities during the running gait of a biped. Tokuz and Jones (1991) used the layered velocity control concept to develop a hybrid actuator in which one actuator maintains a constant velocity while the other introduces a secondary velocity profile on this constant motion. The difference in this concept is the non-linear velocity summing achieved by the use of a seven-bar linkage. The classical problem of non-linear function generation using a multi-input linkage was studied earlier by Mruthyunjaya (1972).

#### **2.2.4. Patent Literature: Prior Art in Dual Actuators**

In this section we include a summary of the patent literature (see Table 2.2) with a focus on United States patents in the area of dual actuators for high-performance control of robots and similar mechanical systems. Two dual actuator concepts were recently reviewed by Tesar (2006d): Solomon electric wheel drive (Pesiridis and Christian, 2006) which is a torque-summing device intended to be a wheel drive and (ii) Dual transmission by NEXXT drive (NEXXTDrive Ltd., London, UK) which is also a torque summing

device meant to provide step-less speed changes in an automobile. An early patent in hybrid drive-train technology was by Hata et al. (1999) at Toyota which was later leveraged to develop the hybrid synergy drive that mixes inputs from an Internal Combustion Engine (ICE) and an EMA. A novel continuously variable transmission was patented by Fallbrook Technologies (Miller, 2005) which uses a set of tilting balls between the input and the output. In this arrangement, the speed is varied by tilt of the balls. The advantage of this drive is a smaller number of parts and a seamless transition from under-drive to direct-drive to over-drive. Some of the actuator concepts we have discussed in Sections 2.2.2 and 2.2.3 have corresponding patents which are also listed in Table 2.2 (Pratt and Williamson, 1995b; Tesar, 1985, Tesar, 2006c; Lauria et al., 2007).

Table 2.2 Summary of US Patent Literature on Dual Actuators

Actuation Concept	Patent Number (Year), Inventor(s) (Company/Institution Lab)
Control-in-the-Small	4505166 (1985), D. Tesar (University of Florida, Gainesville)
Fault-Tolerant Rotary Actuator	7122926 (2006), D. Tesar (The University of Texas at Austin)
Force/Motion Control Actuator	Provisional Patent, D. Tesar (The University of Texas at Austin) The focus area of this report, PFVA, is based on the FMCA concept.
High Performance Differential Actuator	Patent Application 11/694123 (2007), Lauria et al. (University of Sherbrooke, Canada)
Hybrid Drive System	5875691 (1999), H. Hata, S. Kubo, Y. Taga, and R. Ibaraki (Toyota)
NEXXT Drive	UK Patent Number Unavailable (NexxtDrive Ltd., UK)
NuVinci Continuously Variable Transmission	6945903 (2005), D. Miller (Fallbrook Technologies, Inc.)
Series Elastic Actuator	5650704 (1995), G. Pratt and M. Williamson (Yobotics, Inc.)
Solomon Electric Wheel Drive	11/552207 (2006), R.A. Pesiridis and A.J. Christian (Solomon Technologies, Inc.)

### 2.3. CHAPTER SUMMARY AND DISCUSSION

The focus of this chapter was on surveying the background literature to:



- Understand the implication of actuator design and control/sensing methodologies on force-controlled performance. See Sections 2.1.1-2.1.3 for details.
- Develop a taxonomy for dual-input actuators based on their power flow mechanics. Two categories were identified: (i) force-summing and (ii) velocity-summing actuators. The distinction between these was based on the relationships between the force (or effort) and the velocity (or flow) variables of the dual-inputs and the output of the actuator. See Section 2.2.1 for details.
- Comprehensively list surveyed force-summing and velocity-summing actuators and summarize the results from work that is most relevant to the current research. See Sections 2.2.1-2.2.3 for details.
- Survey the prior art in dual actuators based on a patent literature search focused on inventions based in the United States.

The summary of our literature review is presented in Table 2.3. Based on our review we believe that, to move the science forward in the area of safe and responsive physical HRI systems, it is important to explore new mechanical designs for actuators. Furthermore, it is imperative for such actuation methodologies to be inherently safe. In Chapter 3 we will introduce the concept of PFVA which is a dual input velocity summing actuator based on a differential drive. In the PFVA, the backdriveability of the actuator (for mechanical safety) is ensured by making one input near direct-drive. This work is timely because there is a growing interest in the robotics community in the area of variable response actuators and robot safety in human environments. At the same time, current research builds on and adds to past work within UTRRG in layered control, fault-tolerance, and, most importantly, the dynamic modeling of manipulators with dual input actuators such as the PFVA.

Table 2.3 Summary of Selected Literature and Relevance to Current Work

Reference	Description	Relevance to PFVA Work
(Chang and Tsai, 1993)	<ul style="list-style-type: none"> <li>Developed a torque summing redundant drive for backlash-free robots</li> <li>Presented analytical model and design criteria for manipulators with dual torque summing actuators</li> </ul>	<ul style="list-style-type: none"> <li>Analytical model developed for dual actuators is of importance in our work on modeling of serial chains with PFVAs (Chapter 8)</li> </ul>
(Cho, Tesar, and Freeman, 1989)	<ul style="list-style-type: none"> <li>Proposed an antagonistic elbow module</li> <li>Presented an analytical framework for modeling the response of manipulators with antagonistic dual actuators</li> </ul>	<ul style="list-style-type: none"> <li>The analytical development using kinematic influence coefficients to model serial chains with dual actuators is relevant to work in Chapter 7.</li> <li>The antagonistic stiffness modeling might be relevant to analyzing the effective stiffness of a PFVA manipulator.</li> </ul>
(Hata et al., 1999)	<ul style="list-style-type: none"> <li>Invented the hybrid drive train for the Toyota hybrid vehicles</li> </ul>	<ul style="list-style-type: none"> <li>Result from an application domain distinct from ours in this report; however it demonstrates the mixing of two significantly distinct systems (ICE and EMA).</li> </ul>
(Kim et al., 2007)	<ul style="list-style-type: none"> <li>Developed a dual input actuator for simultaneous control of position and stiffness</li> <li>Used a differential gear train to mix actuator inputs</li> <li>Primary goal was to employ the drive to sense collisions and forces</li> </ul>	<ul style="list-style-type: none"> <li>Design of this actuator is very similar to the PFVA – dual inputs with differential summing.</li> </ul>
(Lauria et al., 2008)	<ul style="list-style-type: none"> <li>Proposed a differential elastic actuator based on series elasticity and differential mechanics</li> <li>Also developed a 3-DOF manipulator incorporating DEAs</li> </ul>	<ul style="list-style-type: none"> <li>Design of this actuator is very similar to the PFVA – dual inputs with differential summing.</li> <li>The difference is in the presence of a passive compliant element in the DEA.</li> </ul>
(Pratt and Williamson, 1995a)	<ul style="list-style-type: none"> <li>Introduced the idea of intentionally added compliance between actuator and load for better force control in unstructured environments</li> </ul>	<ul style="list-style-type: none"> <li>The PFVA can be regarded as an active SEA. Similarly, we can also think of the DEA as a particular case of the PFVA with one input being replaced by a passive spring.</li> </ul>
(Tesar, 1985; 1999; 2003)	<ul style="list-style-type: none"> <li>Proposed the control-in-the-small concept based on which the layered control actuator was developed</li> <li>Proposed the force/motion control actuator</li> </ul>	<ul style="list-style-type: none"> <li>Current work in PFVA builds on this past work at UTRRG.</li> <li>The original name for the PFVA was FMCA when the latter was proposed in the EMAA in 2003.</li> </ul>
(Zinn et al., 2004)	<ul style="list-style-type: none"> <li>Layered torque control with inclusion of compliance and appropriate placement of actuators near the base of the robot.</li> <li>Performed studies on a manipulator safety index to evaluate the safety of robots around humans.</li> </ul>	<ul style="list-style-type: none"> <li>The similarity between Zinn’s work and our work is the layering of two controlled inputs. In our case we layer velocity inputs.</li> </ul>

### Chapter 3. Parallel Force/Velocity Actuation: Concept

A Parallel Force/Velocity Actuator (PFVA)<sup>14</sup> mixes two distinct inputs in a parallel Dual Input Single Output (DISO) design (see Figure 3.1 for a first generation prototype of this actuator). The two distinct inputs, namely the Force Actuator (FA) and the Velocity Actuator (VA), differ in their dynamic response and have characteristics described below.

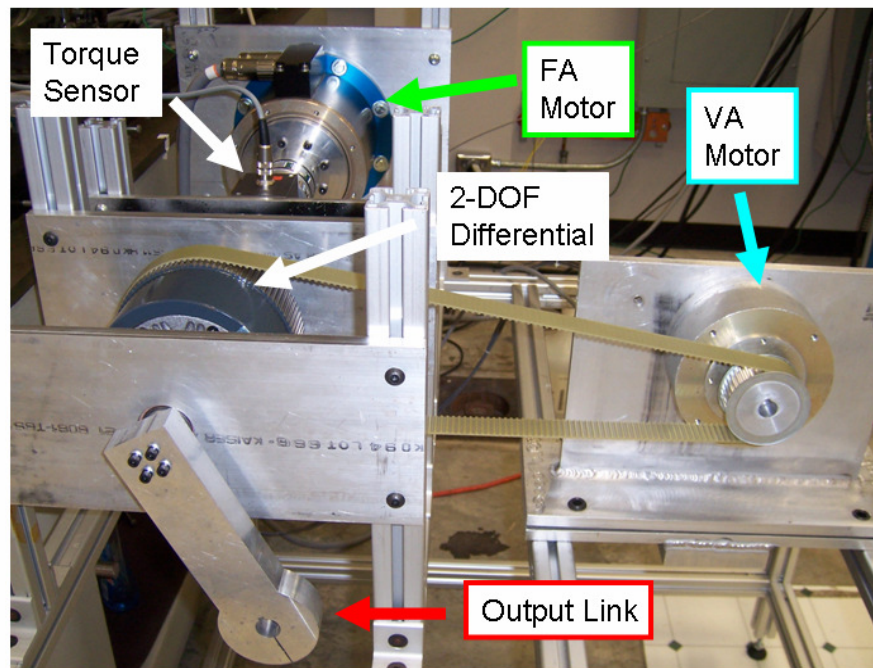


Figure 3.1. A First-Generation Laboratory Prototype of the PFVA Concept Built at the University of Texas Robotics Research Lab.

- A FA has a velocity ratio<sup>15</sup> tending to unity and is ideal for force controlled tasks that demand sensitivity to output force disturbances. In this report, this subsystem of the PFVA is also referred to as the force input.

<sup>14</sup> This concept is protected by a provisional patent in the United States.

<sup>15</sup> Velocity ratio is defined as the ratio of the output shaft velocity to the input shaft velocity.

- A VA has a relatively high gear reduction (or low velocity ratio) compared to the FA and is ideal for velocity controlled tasks that demand sensitivity to output motion disturbances. In this report, this sub-system of the PFVA is also referred to as the velocity input.

The above two classes of actuators can be regarded as the extremes of a continuum (Figure 3.2) of geared Electro-Mechanical Actuators (EMA) (Rabindran and Tesar, 2007b). The nomenclature of these inputs is based on which variables they are good at managing. A VA is an ideal candidate for precise velocity control that needs to be insensitive to output force disturbances. A FA is an ideal candidate for force control that needs to be sensitive to output force disturbances.

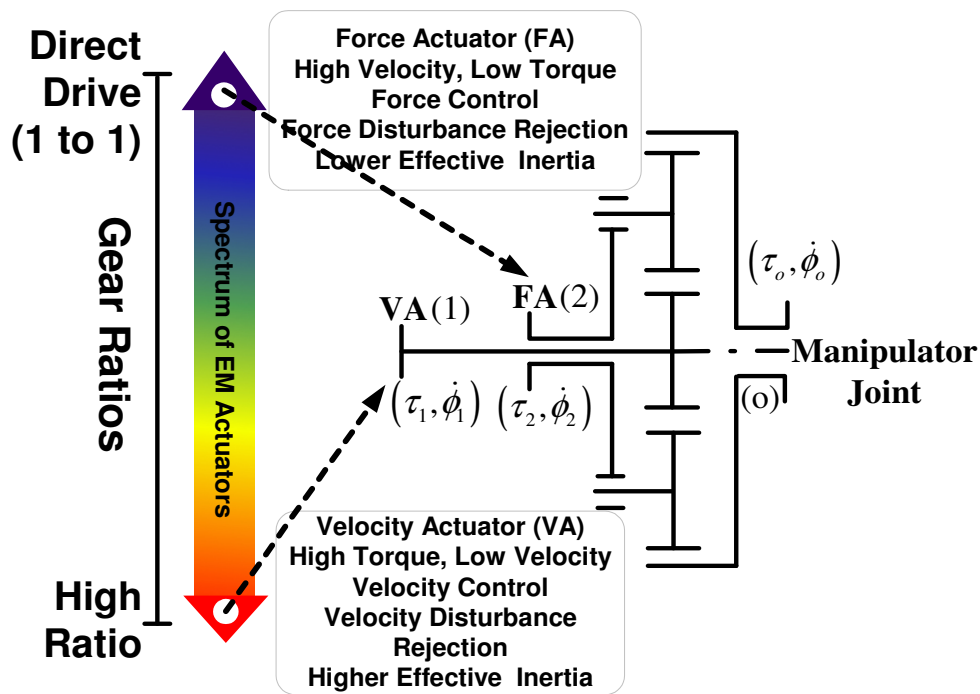


Figure 3.2. A continuum of geared electro-mechanical actuators (Rabindran and Tesar, 2007b). The dynamic response of the actuator varies along the spectrum depending on the gear reduction used.

The goal of this research thread is to provide sufficient input resources in a PFVA to create a physical basis for the conceptual framework in the literature called impedance control (Hogan, 1985). This might be made possible using a PFVA that combines an FA and a VA in parallel with the intent of expanding the range of attainable dynamic responses at the output of a system assembled from PFVAs. There are primarily two goals for this design: (i) to provide at least one backdriveable input in this dual-input actuator by introducing a near direct-drive subsystem that can be responsive to output force disturbances, and (ii) to enhance the dynamic range of velocities of the combination actuator in comparison to its constituent sub-systems. The first goal translates to improved mechanical safety of a PFVA-driven manipulator which makes this actuator relevant to human-safe robotics. The second goal addresses our requirement to expand the choices available at the actuator-level.

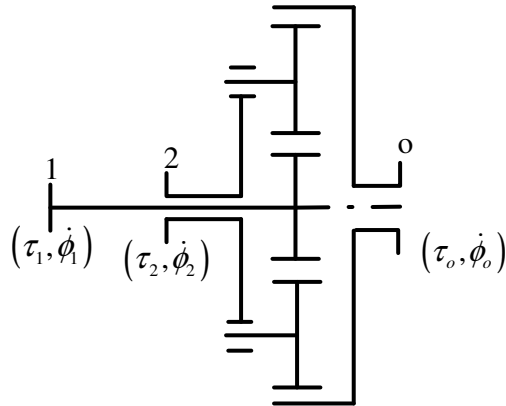


Figure 3.3. Drive trains that could be used to realize a PFVA. (a) Schematic of a simple Epicyclic Gear Train (EGT) (Rabindran and Tesar, 2007b).

The in-parallel mixing of the FA and VA in the PFVA design is realized through a 2-input-1-output EGT. The inputs and the output are configured in such a manner so that one input resembles a FA as closely as possible<sup>16</sup>, the other input has the

<sup>16</sup> Theoretically, we would like to design a PFVA with one input being an ideal force source ( $g \rightarrow 1$ , i.e., direct-drive) and the other input being an ideal velocity-source ( $g \rightarrow 0$ ), where  $g$  represents the velocity

characteristics of a VA, and the output is a manipulator joint (Figure 3.2). The schematic of such a 2-DOF gear train is shown in Figure 3.3. Note that this example is only one possible configuration for the EGT by which a PFVA can be realized. The important point is that the gear reductions of the two inputs should be disparate and, conceivably, there can be more than one EGT configuration that makes this possible. For examples of kinematic inversions of the basic EGT, refer (Müller, 1982, pp. 27-30).

There are many design and operational questions associated with the PFVA itself: what is the dynamic coupling between the two inputs; how much do the two inputs disturb each other; how do we mix the contributions from each input to best satisfy the task requirements, etc. There are similar questions we would like to answer regarding manipulator systems using PFVAs for joint actuation: how much expansion do we obtain in achievable dynamic responses; in what manner do we partition the torque and velocity requirements at the joint (or output) among the two inputs; can the PFVA-based system provide mechanical safety (via backdriveability of one input) while maintaining performance<sup>17</sup>?

To answer these questions, we need a meticulous theoretical and experimental study that progressively addresses issues with increasing complexity:

- First, the internal and external power flow phenomena in the PFVA need to be modeled. This is the focus of Chapter 4.
- The second step is a detailed study of the controlling equations of motions for the PFVA. This assists in the design of a PFVA (discussed in Chapter 5) and its operation. This latter topic of PFVA operation will be theoretically and

---

ratio. However; this is not achievable in practice using a differential drive. Consequently, we try to approximate the behavior of the two inputs as closely as possible to an FA and VA.

<sup>17</sup> Some work has been done recently to address this question of building mechanical safety into the manipulator system using novel actuation techniques, without trading off performance (Tonietti and Bicchi, 2004; Zinn et al., 2004; Kim et al., 2007).

experimentally studied in Chapters 6 and 7, respectively. At the 1-DOF level it is also important to characterize performance limiting physical phenomena in the actuator.

- Finally, we will be in a position to extend this actuator-level development to an  $n$ -DOF serial manipulator to begin to answer the system-level questions raised above. This effort will be elaborated in Chapter 8.

The overarching objective of the above steps is to develop a sound theoretical and experimental understanding of PFVA-based systems from two points of view: (i) mechanical safety, and (ii) expansion of choices at the actuator-level. Additionally, this study empowers the robot developer with the essential tools necessary to evaluate and compare the design and operation of PFVA-based systems. However, before any detailed studies, we first need to perform preliminary kinematic and static force analyses. This is the topic of discussion in the following sections. At this point, the reader might benefit from referring Appendix A where a review of differential systems is presented.

### 3.1. DEFINITION OF THE RELATIVE SCALE FACTOR

The epicyclic gear train used in the PFVA is a velocity summing mechanism, i.e., the output velocity is a linear combination of the two input velocities:

$$\dot{\phi}_o = g_1\dot{\phi}_1 + g_2\dot{\phi}_2 \quad (3.1)$$

In Eq. (3.1),  $\phi_1$ ,  $\phi_2$ , and  $\phi_o$  represent the shaft displacements of the VA, FA, and the output, respectively (see Figure 3.3). Equation. (3.1) suggests that we can independently choose the velocities of two of the three connected shafts, and the velocity of the third shaft is then fixed. In other words, there are infinitely many combinations of the input velocities,  $\phi_{1n}$  and  $\phi_{2n}$ , that result in a null-motion of the output. These input velocities are such that

$$\frac{\dot{\phi}_{1n}}{\dot{\phi}_{2n}} = -\frac{g_2}{g_1} \quad (3.2)$$

Now, let us say  $g_1 = g_v$ ,  $g_2 = g_f$ ,  $\phi_1 = \phi_v$ , and  $\phi_2 = \phi_f$ . Then by defining  $\tilde{\rho} = g_f g_v^{-1}$ , we may re-write Eq. (3.1) as

$$\dot{\phi}_o = \frac{1}{\tilde{\rho}+1} \dot{\phi}_1 + \frac{\tilde{\rho}}{\tilde{\rho}+1} \dot{\phi}_2 \quad (3.3)$$

This is due to the geometrical property of the EGT by which  $g_v + g_f = 1$ . We will call this dimensionless parameter represented by  $\tilde{\rho}$  as the *Relative Scale Factor (RSF)*.

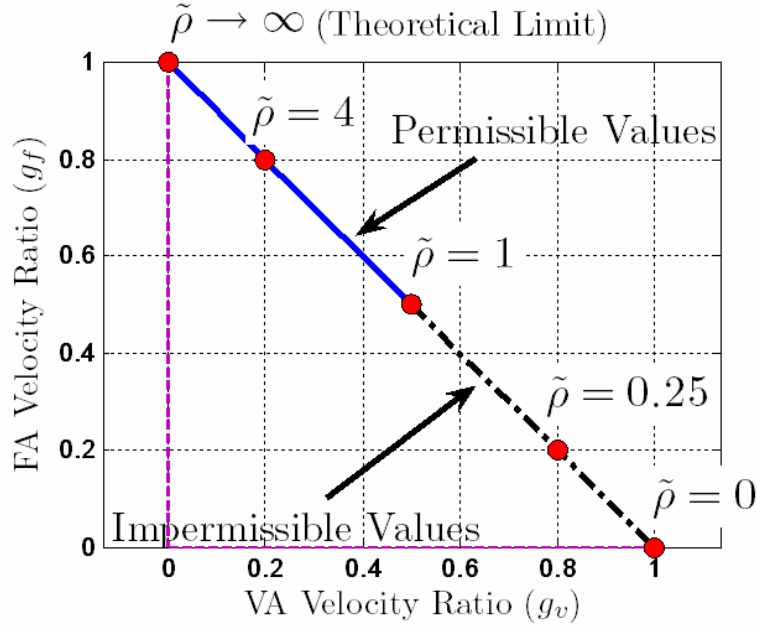


Figure 3.4. Schematic showing the values of the relative scale factor  $\tilde{\rho}$  for various positive-ratio drives.

Some observations regarding this parameter, central to the current work, are listed below.

- If  $\tilde{\rho} < 0$  ( $\tilde{\rho} > 0$ ) then the PFVA is called a negative- (positive-) ratio drive. For example, if  $\tilde{\rho} < 0$ , then the two inputs drive the output in mutually opposite senses. The values of RSF for positive-ratio drives are shown in Figure 3.4. In this



figure, positive-ratio drives occupy the first and third quadrants, and negative-ratio drives occupy the second and fourth quadrants.

- Based on the definitions of the FA and the VA,  $|\tilde{\rho}| > 1$ . In other words, the FA has a greater velocity ratio magnitude than the VA. Also, the theoretical upper limit for the magnitude of RSF is  $|\tilde{\rho}| \rightarrow \infty$ . Therefore, concisely stated  $|\tilde{\rho}| \in [1, \infty]$ . Such values are shown as permissible values in Figure 3.4 (points lying on the bold line).
- The RSF lends physical insight into how kinematically distinct the PFVA inputs are (i.e., how apart they are on the geared actuator spectrum in Figure 3.2). If  $|\tilde{\rho}| \gg 1$  the two inputs are far apart on the actuator spectrum and if  $\tilde{\rho} = 1$  the two inputs have the same velocity ratio to the output. So, evidently, the RSF is a relative measure of the velocity ratios of the two inputs.
- Choosing the values for  $g_v$  and  $g_f$  fixes  $\tilde{\rho}$  (and vice-versa).

Now, Eqs. (3.1) and (3.2) can be summarized as an operational guideline:

**OPERATIONAL GUIDELINE 3.1.** *There are always infinitely many combinations of input velocities that can meet a specified output velocity requirement for the PFVA. The infinite combinations of input velocities that result in a null output motion are such that they bear a constant ratio equal to  $-\tilde{\rho}$ .*

### 3.2. PHYSICAL MEANING OF RSF

The RSF for a PFVA is a purely geometrical quantity. It indicates the ratio of velocity ratios (and mechanical advantages) of the VA and FA. In a rotational PFVA,  $\tilde{\rho}$  is a function of the gear radii. The mechanism shown in Figure 3.5 (a) is a negative-ratio drive whose RSF is

$$|\tilde{\rho}| = 1 + \frac{r_r}{r_s} \quad (3.4)$$

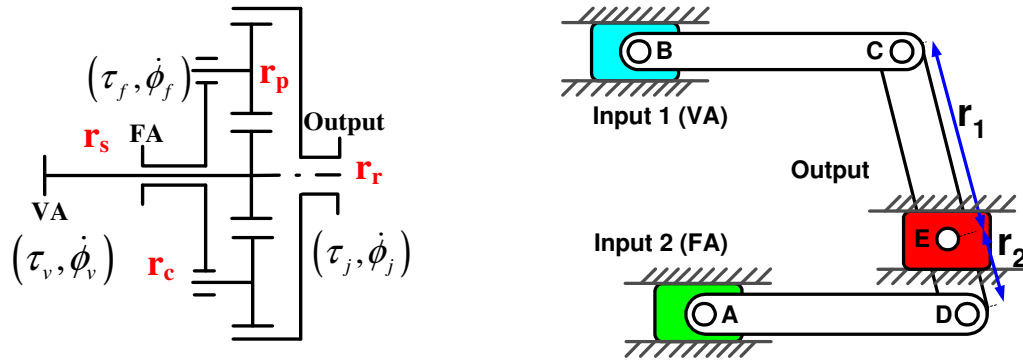


Figure 3.5. Examples of PFVAs. (a) Rotational configuration where the radii of the sun, carrier, planets, and ring gears are  $r_s$ ,  $r_c$ ,  $r_p$ , and  $r_r$ , respectively, such that  $r_r \gg r_s$ , and (b) Linear configuration such that  $r_1 \gg r_2$ .

As  $\tilde{\rho} \rightarrow \infty$ , the ring gear diameter is significantly greater than that of the sun gear. In a similar manner, in a translational PFVA,  $\tilde{\rho}$  is a function of link lengths. For example, the RSF for the mechanism shown in Figure 3.5 (b) is

$$\tilde{\rho} = \frac{r_1}{r_2} \quad (3.5)$$

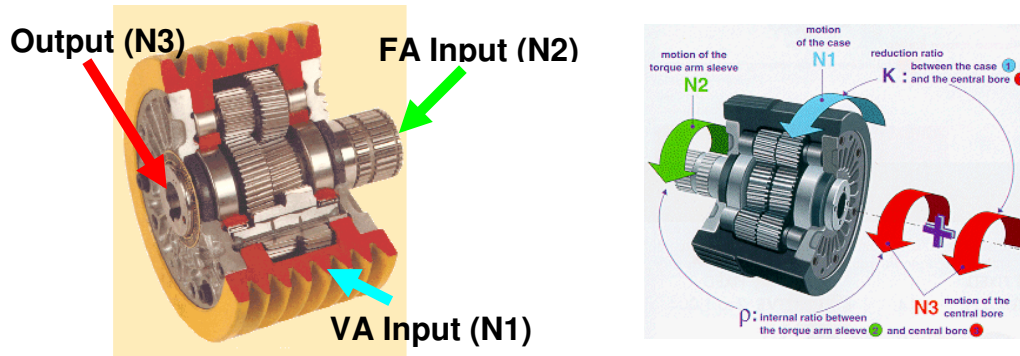


Figure 3.6. Sectioned-view of the SR-20 differential (Picture Courtesy: Andantex, Inc., Wanamassa, NJ, 2007) used in the UTRRG PFVA prototype.

In this (linear) case, as  $\tilde{\rho} \rightarrow \infty$ , the pin-joint E coincides with the pin-joint D, i.e. distance  $r_1$  is much larger than  $r_2$ . In Figure 3.6, we illustrate the physical layout of an Andantex SR-20 gear unit which is a commercially available DISO differential. This unit

was used in the PFVA prototype built by UTRRG. In this illustration, N1 is the VA, N2 is the FA, and N3 is the output of the PFVA that is attached to the machine joint. For this unit,  $\tilde{\rho} = 24.27$ .

### 3.3. PFVA PRELIMINARY ANALYSIS

In this section, we introduce the basic kinematic relationships between the inputs and the output of the PFVA. Integrating the velocity summing relationship in Eq. (3.3) we have

$$\phi_o = \frac{1}{\tilde{\rho}+1}(\phi_v - \phi_{v0}) + \frac{\tilde{\rho}}{\tilde{\rho}+1}(\phi_f - \phi_{f0}) \quad (3.6)$$

where  $\phi_{v0}$  and  $\phi_{f0}$  are the non-zero initial shaft positions for the VA and FA shafts, respectively. Similarly, differentiating Eq. (3.3), we have a relation between the input and output shafts accelerations:

$$\ddot{\phi}_o = \frac{1}{\tilde{\rho}+1}\ddot{\phi}_v + \frac{\tilde{\rho}}{\tilde{\rho}+1}\ddot{\phi}_f \quad (3.7)$$

An effective tool to visualize the absolute and relative velocities of the three connected shafts in a 2-input-1-output PFVA is the nomograph (Müller, 1982, pp. 87; Schultz, 2004). Schultz (2004) describes the construction and physical meaning of the nomograph. In the interest of brevity, we do not present it here.

In Figure 3.7 is a nomograph for the PFVA. Note that as the RSF  $\tilde{\rho}$  of the PFVA changes, the position of the ordinate corresponding to the FA velocity  $\dot{\phi}_f$  changes. As  $\tilde{\rho}$  increases (or equivalently, as the two inputs become more and more distinct), the FA-ordinate (in the nomograph) moves away (to the right in Figure 3.7) from the ordinate corresponding to the VA velocity  $\dot{\phi}_v$ . When this happens, the velocity of the FA approaches the velocity of the output shaft for any given velocity-state of the three-shaft PFVA. In other words, the FA approaches a direct-drive actuator.

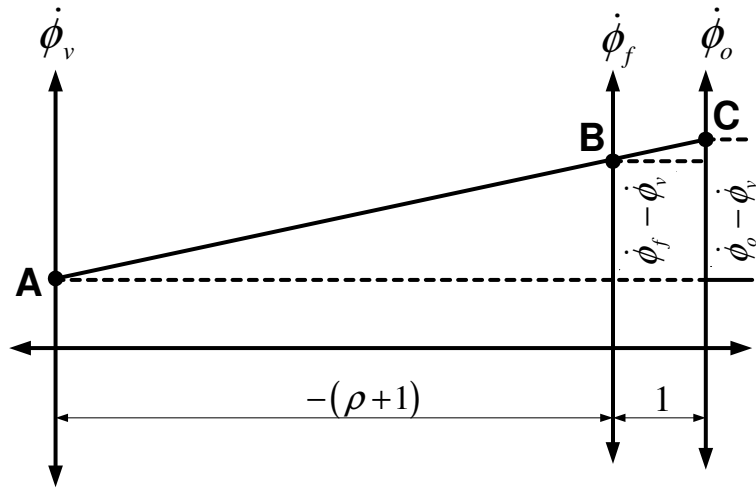


Figure 3.7. Nomograph representation of the velocities of the FA, VA, and the output.

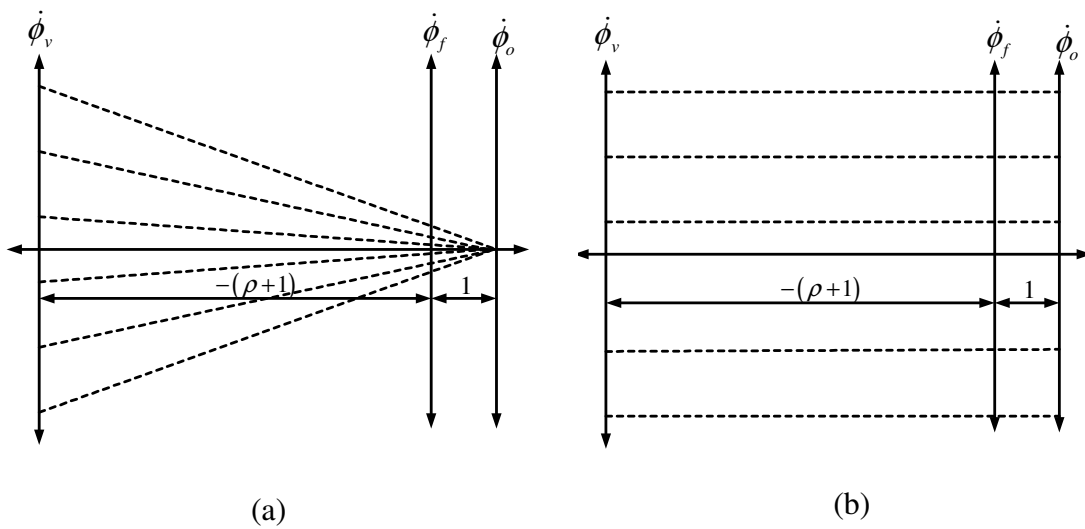


Figure 3.8. Nomograph representation of two special cases, (a) kinematic redundancy, (b) coupling point.

We presented the nomograph in this section because it is an effective tool to visualize the velocity state of the PFVA at any instant. As the velocities of the three-shafts in the PFVA change, the line ABC (in Figure 3.7) rotates and/or translates (Schultz, 2004). Any set of physically admissible values for the three shaft velocities has

to lie on a transversal line intersecting the three ordinates. From this fact we can conclude that the PFVA is kinematically redundant, i.e., there is more than one set of FA and VA velocity states  $(\dot{\phi}_v, \dot{\phi}_f)$  that can satisfy a specified output velocity  $\dot{\phi}_o$  as shown by a family of dotted lines in Figure 3.8(a) for  $\dot{\phi}_o = 0$ . Furthermore, if the line ABC is perpendicular to the three ordinates, the PFVA operates at a coupling point<sup>18</sup> as shown by a family of dotted lines in Figure 3.8(b).

Now, considering the conservation of power (if we assume no power loss due to inefficiency), we have

$$\tau_v \dot{\phi}_v + \tau_f \dot{\phi}_f + \tau_o \dot{\phi}_o = 0 \quad (3.8)$$

where  $\tau_v$ ,  $\tau_f$ , and  $\tau_o$  are the torques on the VA, FA, and output shafts, respectively, of the PFVA gear train. From Eqs. (3.1) and (3.8),

$$\begin{bmatrix} \tau_v & \tau_f \end{bmatrix}^T = - \begin{bmatrix} 1 & \tilde{\rho} \\ \tilde{\rho}+1 & \tilde{\rho}+1 \end{bmatrix}^T \tau_o \quad (3.9)$$

Equation. (3.1) suggests that the velocity of the output of a PFVA is a linear combination of the input velocities, the contribution of the inputs being in the ratio of their velocity ratios to the output. Also, Eq. (3.9) suggests that the output torque of the PFVA is distributed between the inputs in the ratio of their velocity ratios to the output. In other words, the PFVA kinematically behaves like a serial mechanism. However, we call it the *Parallel Force/Velocity Actuator* because there are two ‘parallel’ force paths from the output to the two inputs.

### 3.4. CHAPTER SUMMARY

The objective of this chapter was to introduce the concept of Parallel Force/Velocity Actuation (PFVA). A PFVA mixes two distinct inputs in a parallel Dual Input Single Output (DISO) design using a differential-type gear train. There are

---

<sup>18</sup> Coupling point is a velocity state for an EGT where all the shafts spin at the same velocity as one rigid coupling.

primarily two goals for this design: (i) to provide at least one backdriveable input in this dual-input actuator by introducing a near direct-drive subsystem that can be responsive to output force disturbances, and (ii) to enhance the dynamic range of velocities of the combination actuator in comparison to its constituent sub-systems. The first goal translates to improved mechanical safety of a PFVA-driven manipulator and the second goal addresses our requirement to expand the choices available at the actuator-level. A preliminary kinematics and statics analysis was performed as a prelude to the more detailed analyses in the following chapters. In so doing, the Relative Scale Factor ( $\tilde{\rho}$ ) or RSF was introduced and formally defined. This dimensionless parameter conveys how distinct the two inputs to the PFVA are in terms of their velocity ratios to the output. The theoretical limit for this parameter is  $\tilde{\rho} \rightarrow \infty$ . The RSF is central to the current work and is a recurring parameter in almost all the chapters in this report. The kinematic redundancy of the PFVA allows for an infinite choice of input velocities to satisfy a specified output velocity. This and other kinematic scenarios were demonstrated through the use of nomographs. In the following chapters, we will now lay out our theoretical and experimental results at the actuator-level, and investigate the implication of this 1-DOF study to an  $n$ -DOF serial robot manipulator.

## **ACTUATOR LEVEL ANALYSIS AND EXPERIMENTS**

### **Chapter 4. Parametric Design: Power Flow Analysis**

In this chapter we will consider the power flow in the Parallel Force/Velocity Actuator (PFVA). The objectives are three-fold, (i) to present a relevant model to characterize the external and internal power flow in the PFVA, (ii) to demonstrate the implications of this model by means of numerical examples, and (iii) to propose design and operational guidelines for PFVA-based systems based on our study. This analysis is important because the resulting mechanical efficiency of the 2-input PFVA can be drastically different from the individual efficiencies of the inputs (Force Actuator, FA, and Velocity Actuator, VA). This overall mechanical efficiency depends both on the external and internal power flow modes in the PFVA. Our approach will be to define design and operational criteria mathematically based on power flow models and attach physical meaning to them. The knowledge of these criteria is key to effectively designing and operating PFVA-based systems.

#### **4.1. EXTERNAL POWER FLOW AND OVERALL MECHANICAL EFFICIENCY**

In this section we will model the external power flow in the PFVA. Although some concepts about power-flow, efficiencies, and torque distribution have been obtained from several references on Epicyclic Gear Trains (EGTs) (Radzimovsky, 1956; Tuplin, 1957; Müller, 1982; Pennestri and Freudenstein, 1993; Pennestri and Valentini, 2003; Litvin *et al.*, 2004; Chen and Angeles, 2007), our focus here is to apply these concepts to the PFVA and gain physical insight into its design and operation.

The epicyclic gear train of the PFVA should be under torque equilibrium irrespective of power losses (Müller, 1982; Pennestri and Freudenstein, 1993):

$$\tau_v + \tau_f + \tau_o = 0 \quad (4.1)$$

Now, let the prime-movers driving the VA and FA of the PFVA be labeled  $M_v$  and  $M_f$  respectively. If  $\tau_{M_v}$  and  $\tau_{M_f}$  are the torques provided by the VA and FA prime-movers respectively, then the torques,  $\tau_v$  and  $\tau_f$ , available to drive the EGT are:

$$\tau_i = \tau_{M_i} - [\mathbf{I}_M + \mathbf{I}^*]_{i,:} \ddot{\boldsymbol{\phi}}, \quad i \in \{v, f\} \quad (4.2)$$

In Eqn. (4.2),  $\mathbf{I}_M$ , is the prime-mover inertia matrix lumping all inertias at the input side (see Appendix C) as seen by the prime-movers  $M_i$ ,  $\mathbf{I}^*$  is the output-to-input reflected inertia matrix, and  $\ddot{\boldsymbol{\phi}} = [\ddot{\phi}_v \quad \ddot{\phi}_f]^T$ . There are cross-coupling inertia terms in  $\mathbf{I}^*$  because this is a two-input-one-output system (Rabindran and Tesar, 2007a). Note that  $[\mathbf{X}]_{i,:}$  refers to the row of matrix  $\mathbf{X}$  corresponding to the input  $i$ .

We will now develop an expression for the operating mechanical efficiency of the PFVA. The relevant power losses in an EGT are due to the following phenomena (Radzimovsky, 1956), (a) sliding friction due to tooth meshing, (b) oil churning, and (c) bearing friction. These phenomena are important enough to be studied on their own. We will consider power loss due to meshing friction and model it using an efficiency term<sup>19</sup> as shown in the analysis that follows.

Consider a PFVA based on a simple epicyclic spur-gear train, shown as a control volume with three power-ports in Table 4.1. The three shafts connected to the PFVA in turn are connected to (a) the Velocity Actuator (VA) labeled as  $v$ , (b) the Force Actuator (FA) labeled as  $f$ , and (c) the output labeled as  $o$ . The output of the PFVA is an input to a machine, such as a manipulator joint. We choose the following sign convention for external power flow: (a) An input shaft to the epicyclic drive carries positive power and

---

<sup>19</sup> The velocity-related losses can be incorporated into this term by considering an additional ventilation/splash loss factor as suggested by Müller (1982, p. 19).



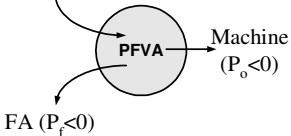
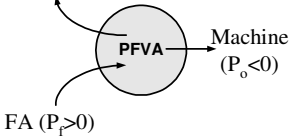
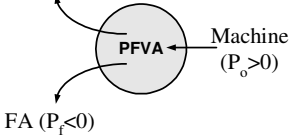
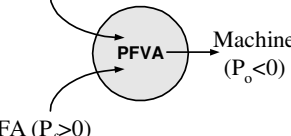
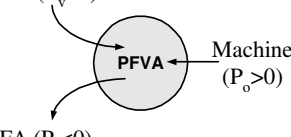
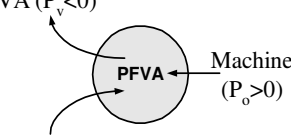
(b) an output shaft connected to the drive bears negative power. *Furthermore, each connected shaft (v, f, or o) in such an EGT can either be the only input shaft or one of the two input shafts (Müller, 1982). This results in a set of six possible power-flow modes for the PFVA as shown in Table 4.1.* The modes of flow shown in Table 4.1 (a)-(c), represent a power-division operating condition, wherein the input power from one of the three shafts is divided between the remaining two shafts. Power loss due to meshing friction, although not shown in Table 4.1 is implicitly assumed here. In the power-division scenario, any of the three shafts can be the only input shaft. On the other hand, the modes of flow shown in Table 4.1 (d)-(f), represent a power-summation operating condition, wherein the input power from two of the three shafts sum up before being transmitted to the third shaft. In the power-summation scenario, any two of the three shafts can each be the input shaft. The above mentioned six power-flow modes have been analyzed for overall mechanical efficiency  $\eta$  in the case of 2-DOF epicyclic trains by Müller (1982) and Pennestri and Freudenstein (1993). In this section our objectives are (i) to express the  $\eta$  in terms of the relative scale factor  $\tilde{\rho}$  and the ratio of operating velocities  $\tilde{\lambda}$  that will be defined shortly, and (ii) to derive physical meaning for the six possible external power-flow modes in a PFVA.

A pre-requisite for determining the overall mechanical efficiency for a PFVA in any of the six modes (shown in Table 4.1) is the knowledge of the input and output shafts. If this information is known, then the overall mechanical efficiency ( $\eta$ ) for the PFVA is as follows (Müller, 1982):

$$\eta = \frac{-P_{out}}{P_{in}} \quad (4.3)$$

where  $P_{out}$  is the total power output (which is negative according to our sign convention) and  $P_{in}$  is the total power input (which is positive). The negative sign in the numerator is used so that the efficiency value is always a positive number.

Table 4.1 The Six External Power-Flow Modes in a PFVA and their Physical Meaning

Power-Port Representation	Physical Meaning
<b>Power-Division Mode</b>	
 <p>(a)</p>	<p>The VA backdrives the FA motor while driving the machine. This is an undesirable scenario because one motor in the system is being backdriven by the other.</p>
 <p>(b)</p>	<p>The FA backdrives the VA motor while driving the machine. Like mode (a), this is an undesirable scenario too because one motor in the system is being backdriven by the other.</p>
 <p>(c)</p>	<p>The external torque from the machine backdrives the FA motor and the VA motor. This is an undesirable scenario because both motors are being backdriven. In this scenario the external power at the output shaft is significantly more than what can be supported by the two input motors. Note that this power flow configuration is similar to that in a standard automobile differential where the machine is now analogous to the IC engine input, and the FA and VA are analogous to the two wheels.</p>
<b>Power-Summation Mode</b>	
 <p>(d)</p>	<p>This is the normal operational mode. The PFVA is expected to be in this mode for the most part of its operation. The FA and VA drive the machine in the two-input-one-output mode.</p>
 <p>(e)</p>	<p>The FA motor is backdriven by the output, while the VA motor is still the input. This can happen when the output link feels a disturbance that is large enough to backdrive the FA. This mode can be used to detect collisions. Such an application has been demonstrated by Kim, <i>et al.</i> (2007).</p>
 <p>(f)</p>	<p>The VA motor is backdriven by the output, while the FA motor is still the input. By nature of its design (VA having large reduction ratios in comparison to the FA), it is significantly hard for the PFVA to operate in this mode because the VA is virtually insensitive to the torque or inertial disturbances from the output. Rabindran and Tesar (2007b) demonstrated this behavior through a slider-crank simulation to study the torque transformation and dynamic coupling issues in PFVAs.</p>

We will now illustrate the calculation of the overall mechanical efficiency for one specific operational mode, shown in Table 4.1 (d). This is the normal operational mode for the PFVA, as suggested in Table 4.1. This table also lists the physical meaning for the other five possible external power-flow modes in the Parallel Force/Velocity Actuator.

**Example 4.1: Overall Mechanical Efficiency of a Positive-Ratio PFVA**

In this example we will consider a positive ratio<sup>20</sup> PFVA and the normal operational condition, or mode (d) in Table 4.1. As suggested by Pennestri and Valentini (2003), let the Single Input Single Output (SISO) efficiency of power transfer from the FA (VA) to the output of the PFVA be  $\eta_{f \rightarrow o}$  ( $\eta_{v \rightarrow o}$ ) while the VA (FA) is held stationary.

**Note on SISO Efficiencies.** The two efficiencies  $\eta_{v \rightarrow o}$  and  $\eta_{f \rightarrow o}$  are related to one another and dependent on the kinematic-scaling. Note that  $\eta_{v \rightarrow o}$  is the efficiency of the inverted train defined by Litvin *et al.* (2004) which they use as a bound for the overall efficiency of the kinematic-inversions of the basic train. This basic efficiency, termed so by Müller with the notation  $\eta_0$ , is that of the basic train when it transmits the rated torque at low (~10 m/s) pitch-line velocities (Müller, 1982, p. 21). In our analysis, we could have chosen to assume scale-independent gear mesh loss factors as suggested by Chen and Angeles (2007, p. 107). However, in the case of the PFVA, the loss factors (which in turn are dependent on tooth numbers of the meshing gears (Tuplin, 1957)) change significantly with varying  $\tilde{\rho}$  values due to significant change in tooth numbers. So, we assume in our analysis that  $\eta_{v \rightarrow o}$  and the related  $\eta_{f \rightarrow o}$  are both known as a function of  $\tilde{\rho}$ .

---

<sup>20</sup> In negative (positive) ratio PFVAs the VA and the output have the opposite (same) sense of rotation when driven in the same direction. In other words, for negative (positive) ratio drives  $g_v < 0$  ( $g_v > 0$ ) and, consequently,  $\rho < 0$  ( $\rho > 0$ ). This terminology is from Müller (1982).

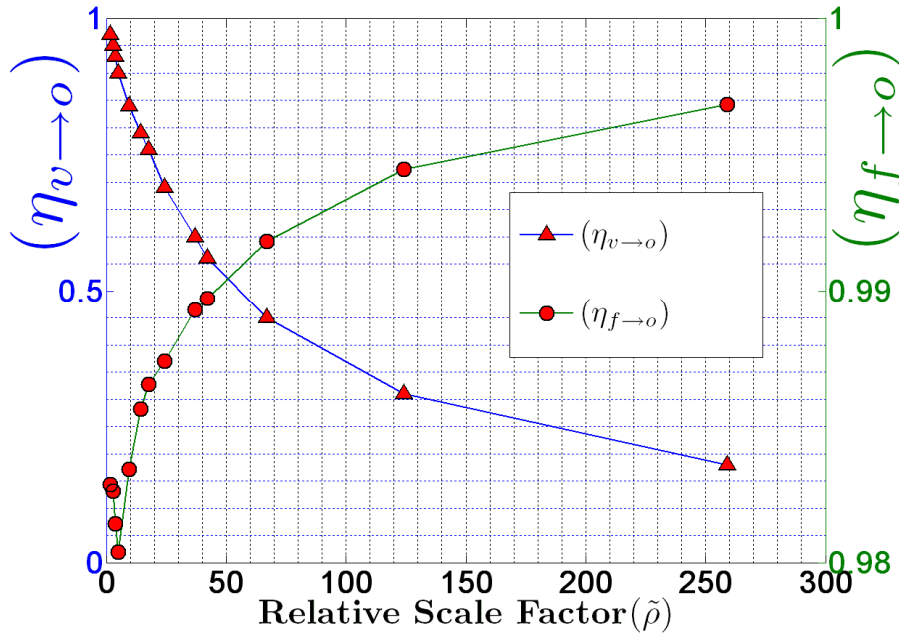


Figure 4.1. Variation of SISO efficiencies w.r.t. the relative scale factor  $\tilde{\rho}$  for the commercially available SA series differentials from Andantex Inc. [22, 18].  $\eta_{v \rightarrow o}$  is the basic efficiency of the drive train.

In Figure 4.1 we show this relation of the basic (SISO) efficiency  $\eta_{v \rightarrow o}$  with respect to the relative scale factor  $\tilde{\rho}$  of a commercially available differential gear train (SA series from Andantex Inc., Wanamassa, NJ (Andantex Inc., 2007)). These drives are compound trains and use helical gears. Although we assume our PFVA drive to be a simple EGT with spur gears, without loss of generality, we could use these data to depict a relationship between the basic efficiency of the drive  $\eta_{v \rightarrow o}$  and its relative scale factor  $\tilde{\rho}$ . Such a trend was also analytically demonstrated by Chen and Angeles (2007) (see Example 2 and Figure 9 in that work). This trend can be summarized in a design guideline.

**DESIGN GUIDELINE 4.1.** *The basic efficiency of the inverted train in a PFVA reduces as  $\tilde{\rho}$  increases, i.e., the FA and VA become more and more distinct kinematically.*

The SISO FA and VA cases are respectively shown graphically in Figure 4.2 (a) and (b). The Dual Input Single Output (DISO) PFVA is the superposition of these two SISO cases and is shown in Figure 4.2 (c). The power balance for the SISO cases in Figure 4.2 (a) and (b) can be expressed as (Pennestri and Valentini, 2003)

$$\tau_o g_v \dot{\phi}_v + \eta_{v \rightarrow o} \tau_v \dot{\phi}_v = 0 \quad (4.4)$$

$$\tau_o g_f \dot{\phi}_f + \eta_{f \rightarrow o} \tau_f \dot{\phi}_f = 0 \quad (4.5)$$

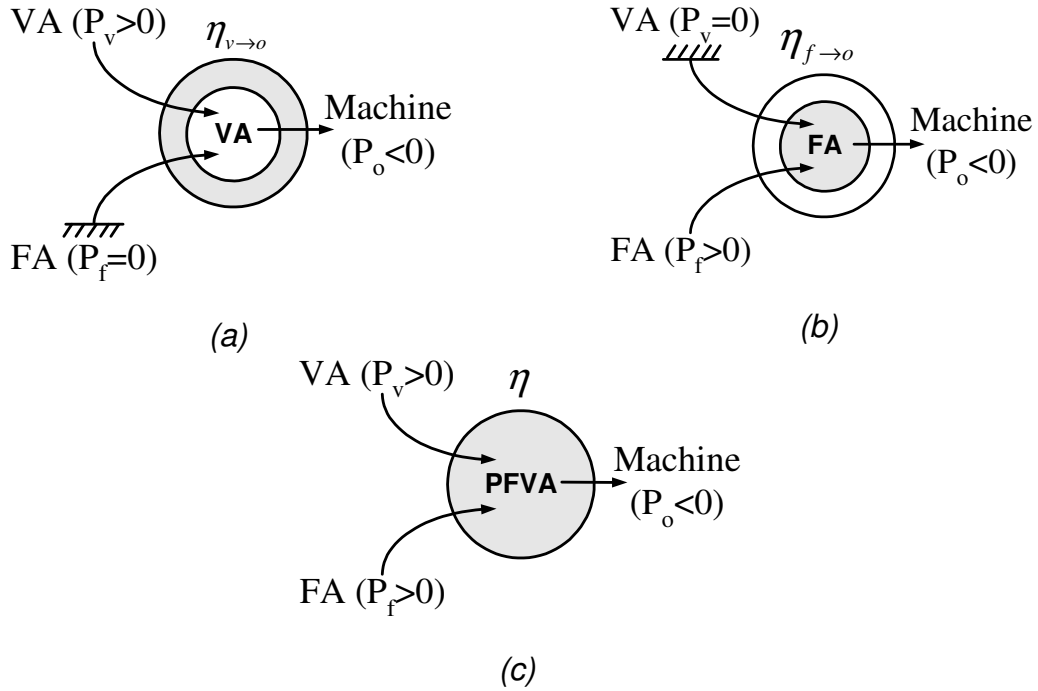


Figure 4.2. Mechanical efficiency analysis of a DISO PFVA as the superposition of a SISO FA and VA.

Adding Eqs. (4.4) and (4.5) we can now express the power balance in the PFVA (the superposition case shown in Figure 4.2 (c)) as

$$\tau_o \dot{\phi}_o + \eta_{v \rightarrow o} \tau_v \dot{\phi}_v + \eta_{f \rightarrow o} \tau_f \dot{\phi}_f = 0 \quad (4.6)$$

Now, using Eqn. (4.3), the overall mechanical efficiency of the PFVA can now be calculated as

$$\eta = -\frac{P_{out}}{P_{in}} = -\frac{\tau_o \dot{\phi}_o}{\tau_v \dot{\phi}_v + \tau_f \dot{\phi}_f} \quad (4.7)$$

From Eqs. (4.6) and (4.7) we obtain the expression originally derived by Pennestri and Valentini (2003):

$$\eta = \frac{\eta_{v \rightarrow o} \tau_v \dot{\phi}_v + \eta_{f \rightarrow o} \tau_f \dot{\phi}_f}{\tau_v \dot{\phi}_v + \tau_f \dot{\phi}_f} \quad (4.8)$$

Furthermore, from Eqs. (4.4) and (4.5) it follows that the external torques on the three shafts bear a constant ratio, i.e.,

$$\tau_o : \tau_v : \tau_f = 1 : -\frac{g_v}{\eta_{v \rightarrow o}} : -\frac{g_f}{\eta_{f \rightarrow o}} \quad (4.9)$$

Equation. (4.9) can be summarized as an operational guideline.

**OPERATIONAL GUIDELINE 4.1** *If the torque on one of the connected shafts in a PFVA is specified, then the (magnitude and direction of) torques on the other two shafts are automatically fixed based on the geometry and basic efficiency of the gear train. Consequently, a torque sensor on one of the three connected shafts suffices to reasonably estimate the magnitude and direction of the other two shaft torques.*

Using Eqn. (4.9), we can re-write  $\eta$  in Eqn. (4.8) as

$$\eta = \frac{g_v \dot{\phi}_v + g_f \dot{\phi}_f}{\frac{g_v}{\eta_{v \rightarrow o}} \dot{\phi}_v + \frac{g_f}{\eta_{f \rightarrow o}} \dot{\phi}_f} \quad (4.10)$$

We will now define the velocity mixing ratio (or the ratio of operating velocities of the two input sub-systems, FA and VA),  $\tilde{\lambda}$ , as

$$\tilde{\lambda} = \frac{\dot{\phi}_v}{\dot{\phi}_f} \quad (4.11)$$

The parameter  $\tilde{\lambda}$  characterizes only the relative nature of the two input velocities. We now have all the information required to derive a closed form expression for the overall

mechanical efficiency ( $\eta$ ) of the PFVA for power-flow mode (a) (Table 4.1) in terms of dimensionless values for RSF ( $\tilde{\rho}$ ) and the ratio of operating velocities ( $\tilde{\lambda}$ ):

$$\eta = \frac{\tilde{\lambda} + \tilde{\rho}}{\frac{\tilde{\lambda}}{\eta_{v \rightarrow o}} + \frac{\tilde{\rho}}{\eta_{f \rightarrow o}}} \quad (4.12)$$

Note that while the RSF  $\tilde{\rho}$  is a fixed design parameter depending on the gear train geometry, the Velocity Mixing Ratio (VMR)  $\tilde{\lambda}$  is a free operational choice. The basic efficiency  $\eta_{v \rightarrow o}$  is assumed to be known for the gear train and  $\eta_{f \rightarrow o}$  is related to  $\eta_{v \rightarrow o}$  as suggested by Pennestri and Valentini (2003).

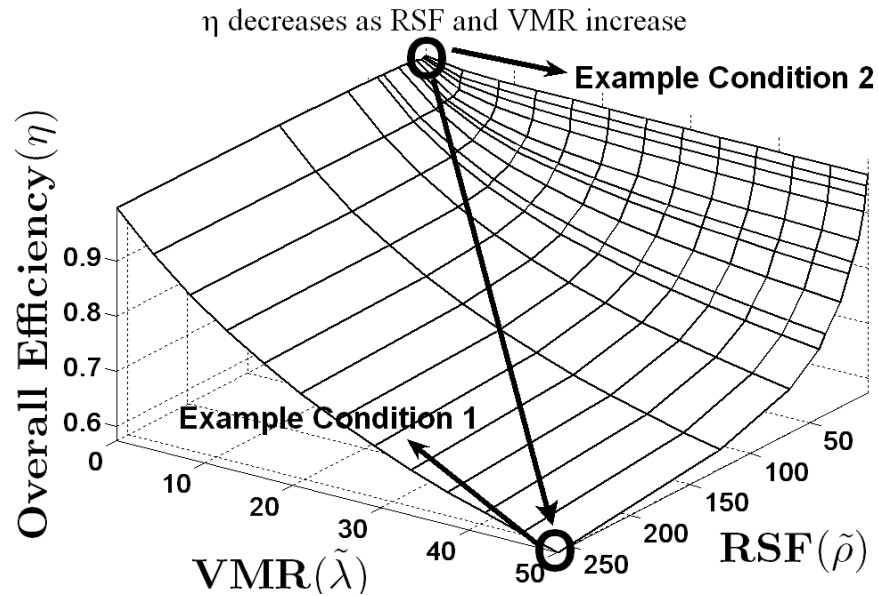


Figure 4.3. Variation of the overall mechanical efficiency of the PFVA w.r.t the relative scale factor and the velocity mixing ratio.

Now, using the information in Figure 4.1, we plot in Figure 4.3 the variation of the overall mechanical efficiency of the PFVA at various operating conditions (function of  $\tilde{\lambda}$ ) for various designs (function of  $\tilde{\rho}$ ). This result follows from Eqn. (4.12) and is based on  $\tilde{\rho}$  values of the Andantex (2007) SA-series drives. Notice that the efficiencies

decrease as  $\tilde{\lambda}$  and  $\tilde{\rho}$  increase. This places a limit on the extent to which we can make the two sub-systems in a PFVA distinct, viz., the FA and VA. In other words, the more apart the inputs are on the spectrum shown in Figure 3.2, the more the associated losses are. Rabindran and Tesar (2007a, 2007b) showed that there is a benefit in making the FA and VA as distinct as possible on the geared actuator spectrum (Figure 3.2), i.e., the two inputs are approximately decoupled in terms of inertial and static load requirements if they (inputs) are distinct. However, the above efficiency analysis shows that there are costs associated with making these inputs very distinct, i.e., making RSF large.

Some illustrative conditions from the efficiency plot in Figure 4.3 are as follows.

- *Example Condition 1:* In this condition, the VA and FA are drastically distinct in terms of the RSF; however the FA shaft is braked. The resulting efficiency is drastically lower than either of the SISO efficiencies. The theoretical limit corresponding to this condition  $\lim_{(\tilde{\lambda}, \tilde{\rho}) \rightarrow (\infty, \infty)} \eta$  does not exist; however as we approach the limit  $\tilde{\lambda} \rightarrow \infty$ , the actuator becomes a SISO velocity actuator and the resultant efficiency is that of this SISO actuator. Now, in addition to this limit if we consider the limit  $\tilde{\rho} \rightarrow \infty$ , this resulting efficiency tends to zero (see Figure 4.1).
- *Example Condition 2:* The theoretical limit corresponding to this condition is  $\lim_{(\lambda, \rho) \rightarrow (0, 1)} \eta = \eta_{f \rightarrow o}$ . In this condition, the VA is stationary and the PFVA operates as a SISO force actuator. The resulting efficiency is that of the FA input's SISO efficiency. If this condition is maintained and the RSF of the PFVA is increased then the variation of  $\eta(\tilde{\lambda} = 0, \tilde{\rho})$  is similar to the plot shown in Figure 4.1.
- The variation of efficiency with respect to  $\tilde{\rho}$  at  $\tilde{\lambda} = 0$  is identically equal to the variation of  $\eta_{f \rightarrow o}$  with respect to  $\tilde{\rho}$  in Figure 4.1.



The lessons regarding efficiency learned from this example can now be summarized into a design guideline as stated below.

**DESIGN GUIDELINE 4.2.** *In the normal operational mode, the overall mechanical efficiency of a positive-ratio PFVA decreases when two conditions simultaneously occur, viz., (i) the FA and VA become significantly distinct from each other in terms of their velocity ratios, and (ii) when the VA actuator is spinning significantly faster than the FA.*

Note that the exercise we demonstrated in this example can be repeated for the other five external power flow modes shown in Table 4.1(b)-(f). Furthermore, until this point we have considered the PFVA as a 3-port control volume, disregarding the mechanics of power flow inside the PFVA. To get a better understanding of power-losses and efficiencies in a PFVA, this internal power flow model is the topic of discussion in the next section.

#### **4.2. INTERNAL POWER FLOW ANALYSIS**

In this section, our goal is to characterize the power flow inside the PFVA for various designs (based on varying relative scale factor,  $\tilde{\rho}$ ) and for a range of operating conditions (based on changing the velocity mixing ratio,  $\tilde{\lambda}$ ). Internal circulating power is a cause for concern in multi-input differential systems with either multiple inputs or with coupled inputs forming internal feedback loops. This issue was analyzed by Tesar (1972) for differential systems with feedback (see Appendix A). In simple EGTs like the one considered in our examples in this chapter, there is another phenomenon called futile power. To understand the difference between these two phenomena, circulating power and futile power, see Müller (1982). The objective of our analysis in this section is to identify modes of operation which might give rise to futile power flow. Before we do

this, we will present two types of internal power flow in EGTs (Müller, 1982), namely, coupling and rolling power.

Consider the torque equilibrium among the three shafts of the PFVA and the power balance in a PFVA:

$$\tau_v + \tau_f + \tau_o = 0 \quad (4.13)$$

$$\tau_v \dot{\phi}_v + \tau_f \dot{\phi}_f + \tau_o \dot{\phi}_o - P_L = 0 \quad (4.14)$$

where  $P_L$  is a lumped term accounting for all the losses due to mesh friction. Multiplying either side of Eqn. (4.13) by  $\dot{\phi}_f$ ,

$$\tau_v \dot{\phi}_f + \tau_f \dot{\phi}_f + \tau_o \dot{\phi}_f = 0 \quad (4.15)$$

Now, as suggested by Chen and Angeles (2007) subtracting Eqn. (4.15) from Eqn. (4.14), we obtain

$$\tau_v (\dot{\phi}_v - \dot{\phi}_f) + \tau_o (\dot{\phi}_o - \dot{\phi}_f) - P_L = 0 \quad (4.16)$$

Each term on the left-hand side of Eqn. (4.15) is a product of a shaft torque and the angular velocity of the FA shaft (the carrier) and is called the *coupling power* associated with the corresponding shaft due to rotation of the carrier:

$$P_{Cx} = \tau_x \dot{\phi}_f, \quad x = f, v, o \quad (4.17)$$

For example, as shown in Eqn. (4.17),  $\tau_v \dot{\phi}_f$  is the coupling power associated with the VA and will be labeled  $P_{Cv}$ . As suggested by Eqn. (4.15), the coupling powers of all shafts are in equilibrium. Equation (4.16), on the other hand, represents the balance of rolling powers. The *rolling power* associated with any shaft in a 3-shaft EGT is the power measured in a reference frame rigidly attached to the carrier (Chen and Angeles, 2007)<sup>21</sup>:

$$P_{Rx} = \tau_x (\dot{\phi}_x - \dot{\phi}_f), \quad x = v, o \quad (4.18)$$

---

<sup>21</sup> The rolling power (Müller, 1982) refers to the power through a planetary gear and a sun (or ring) gear, measured by an observer fixed to the carrier driving this (planetary) gear. The virtual power (Chen and Angeles, 2007) is defined as the power through an arbitrary gear measured by an observer attached to any planetary carrier in this train. Therefore, rolling power is a special case of virtual power (when the observer is attached to the carrier connected to the planetary gear of interest).

For example, as shown in Eqn. (4.18), the rolling power associated with the VA shaft would be the product of its torque (frame-independent) and its angular velocity (frame-dependent) relative to the FA and will be labeled  $P_{Rv}$ . There is no rolling power associated with the FA shaft. The rolling power exchange is always only between the VA and the output shaft, yet the coupling power exchange could be between all three connected shafts (Müller, 1982). The power-losses due to meshing friction do not affect the coupling power balance, but these losses affect the rolling power equilibrium. This is analytically shown in Eqs. (4.15) and (4.16).

Now, from Eqs. (4.9) and (4.17), the ratio between the coupling powers of the three connected shafts are in the same ratio as their respective torques, i.e.,

$$P_{Co} : P_{Cv} : P_{Cf} = \tau_o : \tau_v : \tau_f = 1 : -\frac{g_v}{\eta_{v \rightarrow o}} : -\frac{g_f}{\eta_{f \rightarrow o}} \quad (4.19)$$

This implies that if the geometry and SISO efficiencies of the drive train are fixed then the directions of internal flow of coupling power are fixed. However, depending on the relative angular velocities of the shafts w.r.t. the carrier (or the FA shaft), the rolling power flow can change directions. The sum of the rolling power and the coupling power for a given shaft results in its total power (Müller, 1982) i.e.,

$$(P_{Rx} + P_{Cx}) = \tau_x (\dot{\phi}_x - \dot{\phi}_f) + \tau_x \dot{\phi}_f = \tau_x \dot{\phi}_x = P_x \quad (4.20)$$

where  $x = f, v, o$  is a subscript for to identify the shaft.

Tesar (1972) defines a criterion, labeled  $\gamma = \frac{P_{cir}}{P_{TR}}$ , for differential systems based on circulating power in them, where  $P_{cir}$  is the circulating power in the differential system and  $P_{TR}$  is the total power transmitted to the output of the system. This ratio is related to the operational mechanical efficiency of the differential system.

The above two generalized concepts are important to our study of internal power flow in the PFVA:

- Müller's (1982) concept of partitioning of the total power into two partial powers, viz., coupling power and rolling power throws light on the modes of power flow inside the PFVA that could lead to undesirable (or substantially inefficient) operating conditions. Furthermore, Müller provided a very powerful technique to visualize internal power flow modes using directed graphs.
- Tesar's (1972) concept of the ratio of circulating power to total transmitted power provides a useful operational criterion in a dimensionless form.

We will now use an example to demonstrate the implication of these ideas.

***Example 4.2: Analysis of Futile Power in a Positive Ratio PFVA***

Consider the PFVA drive that we analyzed for external power flow in Example 4.1. This was a positive ratio drive, i.e.,

$$\tilde{\rho} > 0, \quad 0 < g_v < 1, \quad \text{and} \quad 0 < g_f < 1 \quad (4.21)$$

Furthermore, the external power flow direction in this drive was assumed to be in the normal operating mode shown in Table 4.1 (d), i.e., the VA and FA are both inputs while the machine is the output. Now, from Eqn. (4.9):

$$\begin{aligned} \frac{\tau_v}{\tau_0} &= -\frac{g_v}{\eta_{v \rightarrow o}} = -\frac{1}{(\tilde{\rho} + 1)\eta_{v \rightarrow o}} \\ \frac{\tau_f}{\tau_0} &= -\frac{g_f}{\eta_{f \rightarrow o}} = -\frac{\tilde{\rho}}{(\tilde{\rho} + 1)\eta_{f \rightarrow o}} \end{aligned} \quad (4.22)$$

From Eqs. (4.21) and (4.22):

$$-\frac{1}{\eta_{v \rightarrow o}} < \frac{\tau_v}{\tau_0} < 0, \quad -\frac{1}{\eta_{f \rightarrow o}} < \frac{\tau_f}{\tau_0} < 0 \quad (4.23)$$

This implies that the torques on the VA (and the FA) shaft and the output (or joint) shaft have opposite signs. Furthermore, because the VA, by its definition, has a large reduction, the magnitude of the output torque is invariably larger than that of the VA shaft torque from Eqn. (4.22).

The above analysis (for a positive ratio drive) has been mentioned by Müller (1982) by assuming 100% efficiency. However, we have included an efficiency term in this example. In the power-flow mode considered in this example, the FA shaft is an input shaft. Hence, from our sign convention for power flow, its coupling power is positive. Now, this fact together with Eqn. (4.9) tells us that the coupling power in the drive flows from the VA shaft and FA shaft to the output shaft. The rolling power flows only between the VA shaft and the output shaft, and can flow in either direction. All of this information can be shown on a directed power flow graph (a tool used by Müller) as shown in Figure 4.4.

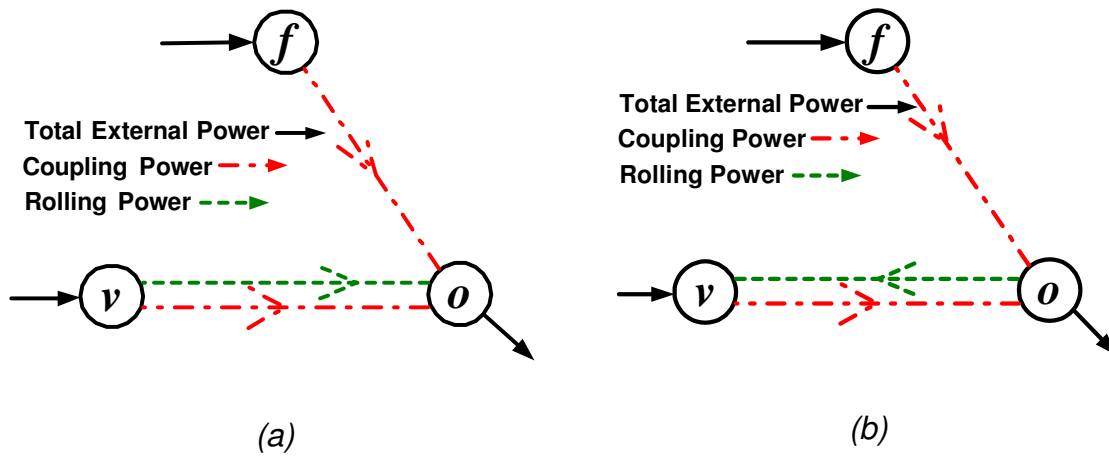


Figure 4.4. Graph showing internal and external power flows in a positive-ratio PFVA: (a) No futile power and (b) futile power-flow condition

We will now simulate an operational scenario for the PFVA considered in this example. In this scenario the torque at the output is assumed to be constant and equal to -100 N-m. At the same time, the velocity at the VA is assumed to be constant and equal to  $15 \text{ rads}^{-1}$  (~150 rpm). Under these conditions, we now vary the velocity state of the FA from being stationary to rotating at twice the speed of the VA. When we specify the magnitude and direction of the torque on the output shaft, by Eqn. (4.9), the magnitude

and direction of the torques on the other two shafts are automatically fixed. In our scenario, therefore, the VA and FA shaft torques are fixed and they are positive. This implies that as long as we impose a positive velocity on the FA and VA shafts in our simulation, they will be input shafts because they will hold positive power. Under these conditions, the drive being a positive ratio drive, the output shaft velocity is always positive and this shaft will hold negative power.

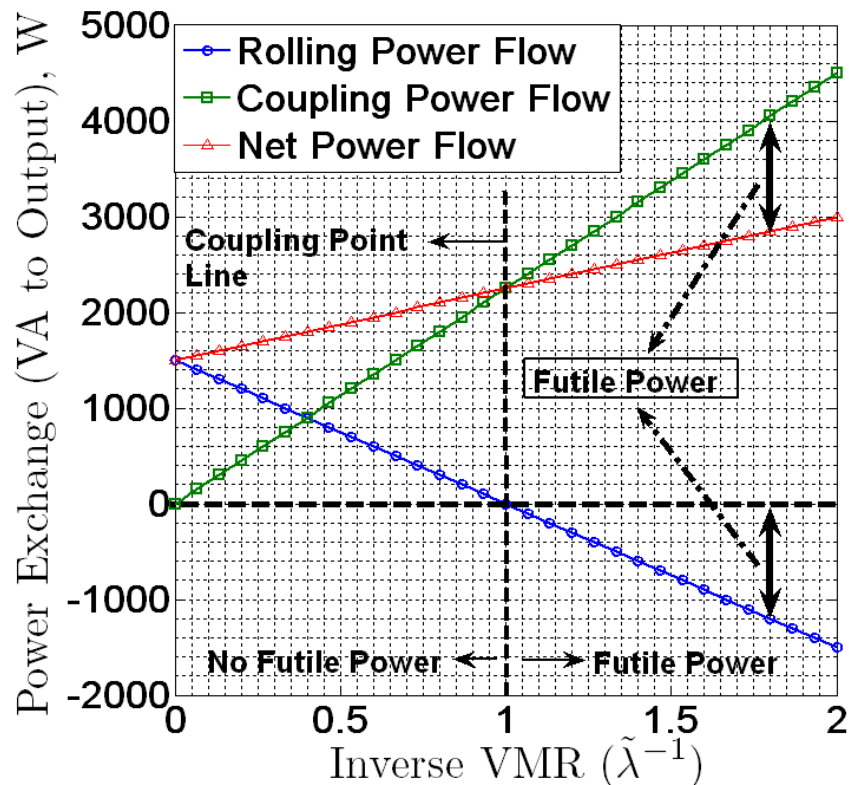


Figure 4.5. Representation of exchange of total power, rolling power, and the coupling power between the VA and the output of the PFVA for Example 4.2

The objective of this example is to demonstrate the phenomenon of futile power in the PFVA. See Figure 4.5 for a graphical representation of power exchange in the direction from the VA to the output for a positive-ratio drive with  $\tilde{\rho} = 1$ . The condition

$\tilde{\lambda} = \tilde{\lambda}_c$  (say) = 1 represents the coupling point for the drive (both inputs and the output all moving at the same velocity). As concluded before, the net coupling power exchange is in the direction from the VA to the output (this is fixed by  $\tilde{\rho}$ ,  $\eta_{v \rightarrow o}$ , and  $\eta_{f \rightarrow o}$ ). On the other hand, the rolling power exchange between these two shafts can be in either direction (dependent on  $\tilde{\lambda}$ ). For operation in the range  $0 \leq \tilde{\lambda} \leq \tilde{\lambda}_c$  the exchange of coupling, rolling, and total powers between VA and the output are all in the same direction as shown in Figure 4.5 to the left of the coupling point line and in Figure 4.4(a). For operation in  $\tilde{\lambda} > \tilde{\lambda}_c$ , the rolling power exchange is in the direction from the output to the VA (opposed to the coupling and total power flow direction) as shown in Figure 4.5 to the right of the coupling point line and in Figure 4.4(b). For example, consider  $\tilde{\lambda} = 1.8$  as shown in Figure 4.5. For this condition, the net rolling power flow between the VA and the output is approximately -1 kW, the net power flow is about 2.8 kW, and the coupling power flow is about 3.8 kW. The absolute value of the lower partial power (rolling power of -1 kW) can be considered as a futile power flow<sup>22</sup>.

Note that the coupling power exchange exceeds the net power flow by this same amount (1 kW). As the name suggests, futile power flow results in inefficiency and generates heat in the gear train (Müller, 1982). As demonstrated in this example, such ineffective (or futile) internal power flow (Figure 4.4(b)) can occur even in the normal external power flow mode (Table 4.1(d)) of the PFVA. Consequently, it is important for us to consider it as an operational criterion for controlling a PFVA. Now in a more complex compound EGT with inner loops, there is a similar phenomenon called circulating power (Müller, 1982). For a PFVA using a simple EGT, we will now define a criterion similar to Tesar's (1972) circulating power ratio ( $\gamma$ ).

---

<sup>22</sup> We base our argument about futile power on Müller's work (1982, p. 61) who originally presented it. However, the futile power term might be fictitious because it is measured by an observer attached to the planet carrier (FA shaft in our case). Greater clarity on the physical meaning of this term is needed.

For the simple EGT case we will call this criterion the *Futile Power Ratio (FPR)*, labeled  $\tilde{\nu}$ , defined as the dimensionless ratio between the futile power in the EGT,  $P_{futile}$ , and the total power,  $P_o$ , transmitted to the output shaft, i.e.,  $\tilde{\nu} = P_{futile} P_o^{-1}$ . Note that a futile power flow exists only when either of the rolling power flow,  $P_{R,v \rightarrow o}$ , or the coupling power flow,  $P_{C,v \rightarrow o}$ , between the VA and the output is in the opposite direction of the effective power-flow between the same two shafts. As long as this condition is not met, there is no futile power exchange. Mathematically, there is no futile power flow between the VA and the output if all of the following conditions are simultaneously met:

$$P_{R,v \rightarrow o} P_{C,v \rightarrow o} > 0, P_{R,v \rightarrow o} P_{v \rightarrow o} > 0, P_{C,v \rightarrow o} P_{v \rightarrow o} > 0 \quad (4.24)$$

When there is futile power flow, it is defined as

$$P_{futile} = \min \left\{ \left| P_{R,v \rightarrow o} \right|, \left| P_{C,v \rightarrow o} \right| \right\} \quad (4.25)$$

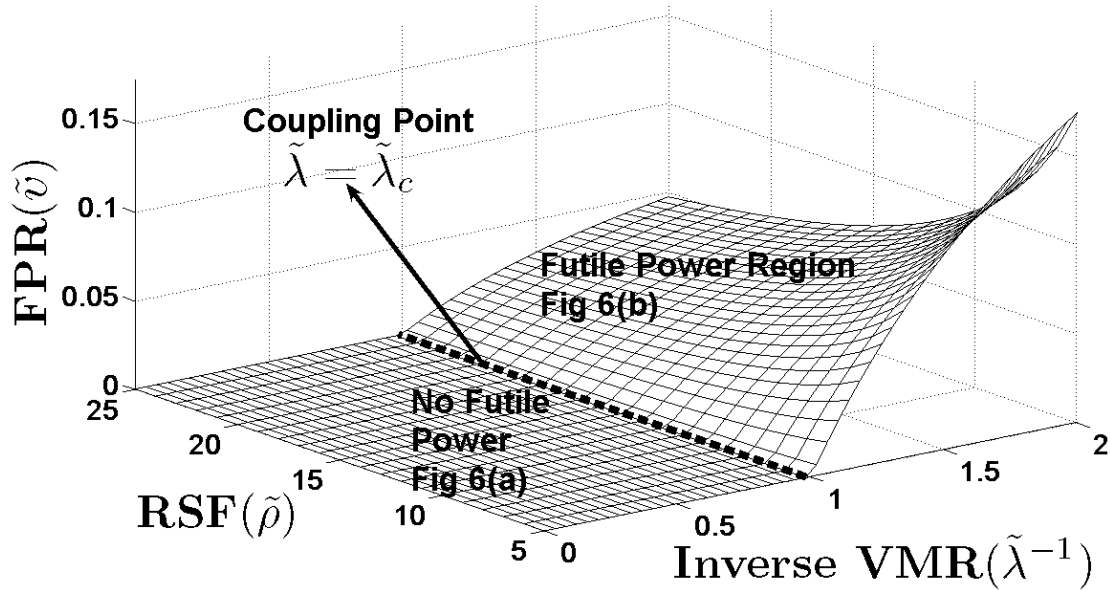


Figure 4.6. Futile power ratios for varying values of relative scale factor  $\tilde{\rho}$  and the inverse of velocity mixing ratio  $\tilde{\lambda}$

Now we will vary the relative scale factor  $\tilde{\rho}$  in the above example to study how the FPR  $\tilde{\nu}$  varies w.r.t. various designs. These results have been plotted in Figure 4.6.



The objective of Figure 4.6 is to demonstrate the two internal power flow modes shown in Figure 4.4 (a) and (b) for normal external power flow conditions as shown in Table 4.1(d), and also the transition between these two internal power flow modes. The difference between the internal power flow modes in Figure 4.4(a) and (b) is that there is no futile power exchange between the VA and the output in mode (a), while such a futile power does exist in mode (b). This distinction between these two modes exists due to a change in the direction of the rolling power exchange alone which in turn is effected by a change in the relative velocities between the three shafts. This analysis on futile power can be summarized in an operational guideline.

**OPERATIONAL GUIDELINE 4.2.** *FPR becomes a relevant dimensionless operational criterion for PFVAs based on positive velocity ratio simple revolving epicyclic drives. Futile power flow exists only when one of the partial power flows between the VA and the machine (or PFVA output) is in the opposite direction of the effective power flow between the same two shafts.*

The result of our analysis of futile power is presented as an operational guideline because this phenomenon can occur in almost all positive-ratio design configurations and depends only on the relative velocities of the inputs. In the next section, we will present another phenomenon that is a function of the relative scale factor  $\tilde{\rho}$  and the velocity mixing ratio  $\tilde{\lambda}$ , i.e., effective inertia.

### **4.3. EFFECTIVE INERTIA IN THE PFVA**

In this section, our focus is on determining the input-to-output reflected inertia of a PFVA as a function of the velocity mixing ratio  $\tilde{\lambda}$ , the relative scale factor  $\tilde{\rho}$ , and other inertia-dependent dimensionless parameters that will be defined in this section. This study on the effective inertia is important for applications where forces of interaction between a PFVA-based machine and a human operator are of concern. For example, in a

PFVA-based manipulator used as a rehabilitation robot, the backdriveability of the FA, owing to its near direct-drive velocity ratio, offers mechanical safety. However, the operational condition (in terms of  $\tilde{\lambda}$ ) might determine how much effective inertia the human operator feels while interacting with the robot. Such applications are the motivation behind this study on the input to output effective inertia in PFVA systems.

Let  $I_{eff}$  be the effective inertia of the PFVA system reflected from the input to the output. Also, let the total inertia seen by the force and velocity prime-movers be represented by  $\mathbf{I}_M$ , the prime-mover inertia matrix as introduced in Eqn. (4.2). Then from the equivalence of kinetic energy,

$$\frac{1}{2} I_{eff} \dot{\phi}_o^2 = \frac{1}{2} \dot{\boldsymbol{\phi}}^T \mathbf{I}_M \dot{\boldsymbol{\phi}} \quad (4.26)$$

where  $\dot{\boldsymbol{\phi}} = [\dot{\phi}_v \quad \dot{\phi}_f]^T$  is the vector of operating velocities of the VA and FA and  $\dot{\phi}_o$  is the angular velocity of the output shaft connected to the machine. Now, the output velocity of the PFVA can be expressed as a linear combination of the VA and FA velocities:

$$\dot{\phi}_o = g_v \dot{\phi}_v + g_f \dot{\phi}_f \quad (4.27)$$

From Eqs. (4.26) and (4.27), the effective inertia  $I_{eff}$  can now be expressed as

$$I_{eff} = \frac{\dot{\boldsymbol{\phi}}^T \mathbf{I}_M \dot{\boldsymbol{\phi}}}{(g_v \dot{\phi}_v + g_f \dot{\phi}_f)^2} \quad (4.28)$$

This expression is true for any general differential mechanism with two inputs and one output.<sup>23</sup> The prime-mover inertia matrix  $\mathbf{I}_M$  is symmetric and positive definite and can be represented in the form

$$\mathbf{I}_M = \begin{bmatrix} I_{M_v} & I_{vf} \\ I_{vf} & I_{M_f} \end{bmatrix} \quad (4.29)$$

---

<sup>23</sup> In a differential mechanism such as the PFVA, the output velocity is a weighted sum of the input velocities and the torques on all components bear a constant ratio. See Figure 1 (Macmillan, 1961) for some multi-domain examples of differential mechanisms.

The diagonal terms  $I_{M_v}$  and  $I_{M_f}$  are the principal decoupled inertias seen by each prime-mover and  $I_{vf}$  is the dynamic coupling term between the two inputs. The determination of this matrix is based on Kinematics Influence Coefficients (KICs) (Benedict and Tesar, 1978) as discussed for output inertia reflection in (Rabindran and Tesar, 2007a) (see Appendix C). For example, any component  $g$  in the gear train with an inertia  $I_g$  reflects to the prime-movers as  $\mathbf{G}_g^T I_g \mathbf{G}_g$  where  $\mathbf{G}_g = \begin{bmatrix} g_v^g & g_f^g \end{bmatrix}$  is the matrix of KICs (constant gear ratios in the PFVA) from the prime-movers to the component  $g$ . We will now define three dimensionless parameters based on our inertia variables

$$\tilde{I}_{eff} = \frac{I_{eff}}{I_{M_v}}, \tilde{I}_M = \frac{I_{M_f}}{I_{M_v}}, \tilde{I}_{vf} = \frac{I_{vf}}{I_{M_v}} \quad (4.30)$$

where  $\tilde{I}_{eff}$  is called the Effective Inertia Ratio (EIR) and characterizes the effective inertia relative to the VA inertia.  $\tilde{I}_M$  is called the Prime-Mover Inertia Ratio (PMIR) and conveys the relative nature (or distribution) of the inertia content in each input subsystem;  $\tilde{I}_{vf}$  is called the Coupling Inertia Ratio (CIR) and represents the inertial coupling between the two subsystems as expressed relative to the VA inertia. To define these dimensionless quantities, the comparison has been done to the VA system because the VA, or the SISO actuator resulting from the PFVA by locking the FA or the carrier, has been regarded as a baseline actuator throughout this chapter. For example, the basic efficiency (Müller, 1982) and the basic ratio are defined for this baseline SISO actuator.

Expressing the effective inertia in Eqn. (4.28) using the dimensionless parameters defined in Eqn. (4.30), we have

$$\tilde{I}_{eff} = \frac{(\tilde{\lambda}^2 + 2\tilde{I}_{vf}\tilde{\lambda} + \tilde{I}_M)(\tilde{\rho} + 1)^2}{(\tilde{\lambda} + \tilde{\rho})^2} \quad (4.31)$$

At this point, it is important to review the physical meaning of VMR and RSF. The velocity mixing ratio  $\tilde{\lambda}$  is a control parameter that can be chosen during the PFVA

operation and it conveys the relative nature of the two prime-mover velocities. The relative scale factor  $\tilde{\rho}$  tells us how distinct the two inputs are in terms of their velocity ratios to the output. It is interesting to note that  $\tilde{I}_{eff}$  is a function of the velocity state of the two inputs in addition to the inertia content. However,  $\tilde{I}_{eff}$  is always positive for non-zero velocities of the inputs. This follows from the fact that  $\mathbf{I}_M$  is always positive-definite (see Eqn. (4.29)). We will now present some properties of the effective inertia ratio expression in Eqn. (4.31).

*Property 1.* The effective inertia ratio of the PFVA becomes unbounded as  $\tilde{\lambda} \rightarrow -\tilde{\rho}$ .

When  $\tilde{\lambda} \rightarrow -\tilde{\rho}$ , the FA and VA bias each other to result in a null-motion at the output. Under this condition, the expression in Eqn. (4.31) becomes indeterminate, indicating a very large effective inertia. Physically, this means that it is impossible to move the output. Mathematically,

$$\lim_{\tilde{\lambda} \rightarrow -\tilde{\rho}} \tilde{I}_{eff} \rightarrow \infty \quad (4.32)$$

*Property 2.* The effective inertia ratio of the PFVA (dual inputs)  $[\tilde{I}_{eff}]_{PFVA}$  is bounded by the effective inertia ratios of FA and VA (single input),  $[\tilde{I}_{eff}]_{FA}$  and  $[\tilde{I}_{eff}]_{VA}$  respectively.

As  $|\tilde{\lambda}| \rightarrow \infty$ , the FA is stationary and the PFVA is reduced to a SISO velocity actuator resulting in a relatively high effective inertia ratio,  $[\tilde{I}_{eff}]_{VA}$ :

$$\lim_{|\tilde{\lambda}| \rightarrow \infty} \tilde{I}_{eff} = [\tilde{I}_{eff}]_{VA} = (1 + \tilde{\rho})^2 \quad (4.33)$$

Similarly as  $\tilde{\lambda} \rightarrow 0$ , the VA is stationary and the PFVA is reduced to a SISO force actuator with a relatively low effective inertia,  $[\tilde{I}_{eff}]_{FA}$ :

$$\lim_{\tilde{\lambda} \rightarrow 0} \tilde{I}_{eff} = [\tilde{I}_{eff}]_{FA} = \tilde{I}_M \left( \frac{1 + \tilde{\rho}}{\tilde{\rho}} \right)^2 \quad (4.34)$$

In a traditional actuator with motor inertia  $I_m$  and a gear ratio  $N$ , the input to output effective inertia is  $I_m N^2$ . For such a SISO actuator the EIR  $\tilde{I}_{eff} = N^2$ . The bounds for  $\tilde{I}_{eff}$  of a PFVA discussed above in Eqs. (4.33) and (4.34) are scaling factors for the FA and VA similar to  $N^2$ :

$$\tilde{I}_M \left( \frac{1 + \tilde{\rho}}{\tilde{\rho}} \right)^2 \leq \tilde{I}_{eff} \leq (1 + \tilde{\rho})^2 \quad (4.35)$$

#### 4.3.1. Practical Implication

We will now demonstrate the value of the functional relationship in Eqn. (4.31) through a numerical example considering 3 sample PFVA designs as shown in Appendix B. The function in Eq. (4.31) contains four dimensionless parameters on the right hand side, viz.,  $\tilde{\rho}$ ,  $\tilde{\lambda}$ ,  $\tilde{I}_M$ , and  $\tilde{I}_{vf}$ . In reality, we do not have the freedom to independently pick and choose all of these parameters. The PFVA is designed based on task requirements at its output in terms of a required torque, and a required velocity. These requirements then translate to motor and gear train selections. Choosing a gear train fixes  $\tilde{\rho}$  and the dynamic coupling term  $\tilde{I}_{vf}$ . Choosing motors for the FA and VA, and the gearing inertia terms fixes  $\tilde{I}_M$  and the coupling inertia ratio  $\tilde{I}_{vf}$ . Therefore, given a set of task requirements, once we have chosen a design (by choosing  $\tilde{\rho}$ ), we can independently choose only  $\tilde{\lambda}$  (which is an operational parameter). We now present a practical example.

#### ***Example 4.3: Effective Inertia in a Positive Ratio PFVA***

In this example, we again consider only positive ratio drives. We have considered three different PFVA designs based on a task requirement of 100 Nm nominal torque and 40 rpm nominal speed (Appendix B). The results of this example are plotted in Figure 4.7. This figure shows the variation of EIR as a function of VMR  $\tilde{\lambda}$  for various values of RSF  $\tilde{\rho}$  (which fixes  $\tilde{I}_M$  and  $\tilde{I}_{vf}$ ).

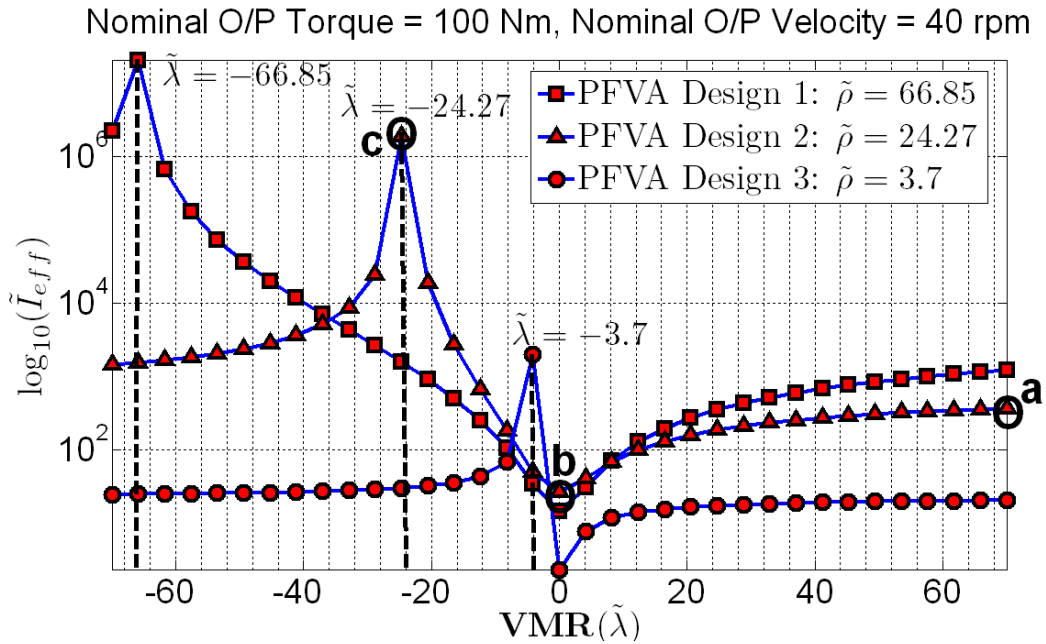


Figure 4.7. Variation of Effective Inertia Ratio  $\tilde{I}_{eff}$  as a function of VMR for various example PFVA designs (See Appendix B). Design example 2 corresponds to the PFVA testbed being set up at the University of Texas Robotics Research Lab.

To illustrate the properties discussed earlier in this section, we will consider the PFVA Design 2 shown in Figure 4.7 (using triangular markers). This design corresponds to the components in the PFVA testbed being setup in the UT Robotics Research Lab. Given the relative scale factor for this design  $\tilde{\rho} = 24.27$ , the velocity ratios of the FA and VA are respectively  $g_f = 0.9604$  and  $g_v = 0.0396$ . At  $\tilde{\lambda} = 70$  (VA rotating 70x faster than the FA) for this design (point ‘a’ in Figure 4.7) the effective inertia ratio is approx.  $\tilde{I}_{eff} = 366$ . This value is approximately  $0.6 \left[ \tilde{I}_{eff} \right]_{VA}$  for this design. Similarly, for  $\tilde{\lambda} = 0$  (single input FA case) the effective inertia ratio is approx.  $\tilde{I}_{eff} = 26.5$  (point ‘b’ in Figure 4.7). This means that the effective inertia of the FA is approximately 26 times the principal inertia content seen by the VA. The point ‘c’ represents property 1 for design 2.

Here  $\tilde{\lambda} = -24.27 = -\tilde{\rho}$  and  $\tilde{I}_{eff}$  is unbounded. Our analysis of input to output effective inertias in PFVA-based systems can be summarized in a design guideline as follows.

**DESIGN GUIDELINE 4.3.**

- (i) *The input to output inertia of a PFVA system is bounded by the VA and FA SISO effective inertias,  $[I_{eff}]_{FA} \leq [I_{eff}]_{PFVA} \leq [I_{eff}]_{VA}$ , if we exclude the special case of  $\tilde{\lambda} \rightarrow -\tilde{\rho}$ , which corresponds to an unbounded effective inertia.*
- (ii) *To reduce the effective inertia of a PFVA system it is thus necessary to drive it as closely as possible to a SISO FA, i.e.,  $\tilde{\lambda} \rightarrow 0$ .*

**4.4. CHAPTER SUMMARY**

Our focus in this chapter was to develop a parametric model for external and internal power flow, and effective inertia in PFVAs. The objective of this work was to develop key criteria that influence the design and operation of PFVAs. To facilitate scalability of our solutions we chose these criteria to be dimensionless. Based on the three phenomena we studied, i.e., external power flow, internal power flow, and effective inertia, we developed three dimensionless criteria, namely, overall mechanical efficiency  $\eta$ , futile power ratio  $\tilde{\nu}$ , and the effective inertia ratio  $\tilde{I}_{eff}$ . The dependence of these criteria on the operational state and the kinematic design of the PFVA were captured using two other fundamental parameters of the PFVA, viz., the relative scale factor  $\tilde{\rho}$  and velocity mixing ratio  $\tilde{\lambda}$ , respectively. We considered example PFVA designs based on positive-ratio epicyclic drive trains with 2-DOF for our analysis to numerically illustrate the practical implication of the models that we developed. Representative results from our study are as follows:

- The relative scale factor  $\tilde{\rho}$  and the velocity mixing ratio  $\tilde{\lambda}$  were identified as two fundamental parameters for a PFVA. The former is a fixed design criterion that says how kinematically distinct the two inputs are w.r.t. their velocity ratios and the latter is a free operational choice by means of which the velocity contributions from the two inputs can be mixed. See Section 4.1 for details.
- The overall mechanical efficiency of the PFVA decreases as we increase the relative scale factor and the ratio of operating velocities of the VA and FA. It was observed that the efficiency decreases approx. 19% from the basic efficiency when the  $\tilde{\rho}$  was increased approx. 6.5x (from 4.7 to 25.27) and the  $\tilde{\lambda}$  was increased 10x (from 4.16 to 41.6). See Section 4.1 for details.
- Futile power in PFVAs was identified as a critical operational criterion. Futile power is a function of the relative velocities between the FA and the VA. For a specified torque of -100 Nm at the output of a positive-ratio PFVA and a fixed VA angular velocity of 15 rads<sup>-1</sup> (approx. 150 rpm), the futile power ratio  $\tilde{\nu}$  was observed to occur at velocity states of the two inputs such that  $\tilde{\lambda} > 1$ . For example, futile power ratio  $\tilde{\nu} = 0.4$  when  $\tilde{\lambda} = 0.55$  (velocity of FA is approx. 1.8x that of VA). See Section 4.2 for details.
- Effective input to output inertia of a PFVA system was characterized by a dimensionless variable called the effective inertia ratio  $\tilde{I}_{eff}$  which depends on three dimensionless design parameters, i.e. (i) coupling inertia ratio  $\tilde{I}_{vf}$ , (ii) prime-mover inertia ratio  $\tilde{I}_M$ , and (iii) the relative scale factor  $\tilde{\rho}$ . In addition,  $\tilde{I}_{eff}$  depends on a fourth operational parameter which is the velocity mixing ratio  $\tilde{\lambda}$ . The effective inertia ratio is always non-zero and positive, and is unbounded when  $\tilde{\lambda} \rightarrow -\tilde{\rho}$ . As an example,  $\tilde{I}_{eff} = 366$  for a PFVA design with  $\tilde{\rho} = 24.27$  and inertia properties as shown in Appendix B. See Section 4.3 for details.



Table 4.2 Summary of Guidelines Suggested in this Chapter

Design Guidelines
<ul style="list-style-type: none"> <li>The basic efficiency of the inverted train in a PFVA reduces as <math>\tilde{\lambda}</math> increases, i.e., the FA and VA become more and more distinct kinematically.</li> <li>In the normal operational mode, the overall mechanical efficiency of a positive-ratio PFVA decreases when two conditions simultaneously occur, viz., (i) the FA and VA become significantly distinct from each other in terms of their velocity ratios, and (ii) when the VA actuator is spinning significantly faster than the FA.</li> <li>The input to output inertia of a PFVA system is bounded by the VA and FA SISO effective inertias, <math>[I_{eff}]_{FA} \leq [I_{eff}]_{PFVA} \leq [I_{eff}]_{VA}</math>, if we exclude the special case of <math>\tilde{\lambda} \rightarrow -\tilde{\rho}</math>, which corresponds to an unbounded effective inertia.</li> <li>To reduce the effective inertia of a PFVA system it is thus necessary to drive it as closely as possible to a SISO FA, i.e., <math>\tilde{\lambda} \rightarrow 0</math>.</li> </ul>
Operational Guidelines
<ul style="list-style-type: none"> <li>If the torque on one of the connected shafts in a PFVA is specified, then the (magnitude and direction of) torques on the other two shafts are automatically fixed based on the geometry and basic efficiency of the gear train. Consequently, a torque sensor on one of the three connected shafts suffices to reasonably estimate the magnitude and direction of the other two shaft torques.</li> <li>FPR becomes a relevant dimensionless operational criterion for PFVAs based on positive velocity ratio simple revolving epicyclic drives. Futile power flow exists only when one of the partial power flows between the VA and the machine (or PFVA output) is in the opposite direction of the effective power flow between the same two shafts.</li> </ul>

Table 4.3 Summary of PFVA Criteria Developed in this Chapter

PFVA Criteria	Dependencies	Mathematical Model
Overall Mechanical Efficiency, $\eta$	Relative Scale Factor, $\tilde{\rho}$ FA and VA Efficiencies, $\eta_{f \rightarrow o}$ and $\eta_{v \rightarrow o}$ (and) Velocity Mixing Ratio, $\tilde{\lambda}$	$\eta = \frac{\tilde{\lambda} + \tilde{\rho}}{\frac{\tilde{\lambda}}{\eta_{v \rightarrow o}} + \frac{\tilde{\rho}}{\eta_{f \rightarrow o}}}$
Futile Power Ratio, $\tilde{\nu}$	Relative Scale Factor, $\tilde{\rho}$ Velocity Mixing Ratio, $\tilde{\lambda}$	$\tilde{\nu} = P_{futile} P_o^{-1}, \text{ where}$ $P_{futile} = \min \{  P_{R,v \rightarrow o} ,  P_{C,v \rightarrow o}  \}$
Effective Inertia Ratio, $\tilde{I}_{eff}$	Relative Scale Factor, $\tilde{\rho}$ Velocity Mixing Ratio, $\tilde{\lambda}$ Coupling Inertia Ratio, $\tilde{I}_{vf}$ Prime-Mover Inertia Ratio, $\tilde{I}_M$	$\tilde{I}_{eff} = \frac{(\tilde{\lambda}^2 + 2\tilde{I}_{vf}\tilde{\lambda} + \tilde{I}_M)(\tilde{\rho} + 1)^2}{(\tilde{\lambda} + \tilde{\rho})^2}$

## **Chapter 5. Parametric Design: Force Distribution Analysis**

This chapter presents the force distribution analysis for PFVAs, and extends the work done in the previous chapter where internal and external power flow was analyzed. The overall goal in this chapter is to present a parametric model to analyze the effect of various design- and operation-based parameters of the PFVA on the distribution of forces between the two inputs. This analysis aids the designer in choosing an optimal kinematic scaling between the PFVA inputs. In addition, we have followed a dimensionless approach so that design decisions can be made regardless of the scale of the actuator. This helps the designer, for example, to use the same set of design guidelines for both the shoulder and wrist actuators of a serial robot manipulator which experience drastically different loading conditions.

The following topics are discussed in this chapter: (i) mixing of position uncertainties from the two inputs in the PFVA, (ii) distribution of static torques between the inputs for a given load at the output, (iii) distribution of inertia torques between the inputs and comparison of their acceleration responsiveness, and lastly (iv) a discussion on the effective stiffness of the PFVA given the individual stiffness of each input. To illustrate the use of our modeling framework and design guidelines, a design case study is presented based on the laboratory prototype of the PFVA built at the University of Texas Robotics Research Group (UTRRG).

We present five physical quantities that are relevant to the design and operation of PFVA-based systems. For each of them we (i) follow a first principles approach to develop a model, (ii) define dimensionless parameters and criteria that indicate the relative distribution of the quantity between the two inputs of the PFVA, (iii) express the basic model in terms of these dimensionless parameters, (iv) provide numerical examples

using five candidate designs using commercial off-the-shelf components, (v) investigate the limiting case as the two inputs become more and more distinct ( $\tilde{\rho} \rightarrow \infty$ ), and (vi) suggest design guidelines based on our analysis. It will be our continuing goal in this chapter to study the coupling between the two inputs in terms of dimensionless parameters.

Table 5.1 Summary of PFVA Parameters for Candidate Designs

	Design 1	Design 2	Design 3	Design 4	Design 5
GEAR TRAIN DATA					
Relative Scale Factor $\tilde{\rho}$	66.85	37	24.27	17.61	3.7
VA Forward Efficiency % ( $\eta_{v \rightarrow o}$ )	45	60	69	76	95
VA Backdriving Efficiency % ( $\eta_{o \rightarrow v}$ )	22	33	55	73	94
PARAMETERS RELEVANT TO VA					
Motor Model (With Frame)	Emoteq HT07000	Kollmorgen AKM44G	Kollmorgen RBE-03001-A50	Emoteq HT07004	Danaher DH063M-22-1310
Position Accuracy (arc-min)	1.5	2.5	0.6	2.0	0.45
Motor Inertia (kg-m <sup>2</sup> )	1.6 x 10 <sup>-3</sup>	2.73 x 10 <sup>-4</sup>	7.8 x 10 <sup>-4</sup>	1.1 x 10 <sup>-2</sup>	8.6 x 10 <sup>-3</sup>
Rated Speed (rpm)	820	2000	650	281	800
Cont. Torque (Nm)	6.3	4.9	5.1	28.9	17.7
Peak Torque (Nm)	57.2	16.1	28.2	327.2	64.4
PARAMETERS RELEVANT TO PFVA (WHOLE ACTUATOR)					
Relative Accuracy Factor ( $\alpha_j^v$ )	1.11	7.111	1.33	4	1
Prime-Mover Inertia Ratio ( $\tilde{I}_M$ )	0.2900	0.3031	0.2980	0.2218	0.2360
Output-to-VA Inertia Ratio ( $\tilde{I}_j^*$ )	7.3529	7.6863	7.5554	5.6250	5.9840
Rated Motor Torque Ratio (Continuous)	2.8095	3.6122	3.4706	0.6125	1.0

## 5.1. CANDIDATE PFVA DESIGNS

In this section we will describe the five candidate rotary PFVA designs used in this chapter. The analysis in this chapter enables the designer to choose optimal RSF values based on various physical requirements such as accuracy, static and inertial load distribution, and stiffness. Therefore the objective was to choose PFVA designs with varying RSF values. The output loading requirements for all five designs were similar: peak torque and peak speed of 150 N-m and 40 rpm, respectively. The differential gear trains considered for all designs were from Andantex Inc., Wanamassa, NJ. The parameters for these designs are listed in Table 5.1. Some parameters were common to all designs: forward and backward efficiencies of the FA were both 98%; VA- and FA-side gear train inertias were  $2.9 \times 10^{-2}$  and  $2.74 \times 10^{-4}$  kg-m<sup>2</sup>, respectively; FA motor was Danaher Motion DH063M-22-1310 with inertia of  $8.6 \times 10^{-3}$  kg-m<sup>2</sup>, rated speed of 800 rpm, and continuous and peak torques of 17.7 and 64.4 N-m, respectively; and the FA position accuracy was 0.45 arc-min. The output link inertia was 0.225 kg-m<sup>2</sup> with a mass of 7 kg. The candidate designs utilize off-the-shelf components and will be used throughout this chapter in the examples for every section.

## 5.2. PARAMETRIC ACCURACY ANALYSIS

In this section, we will study the resulting position uncertainty  $\Delta\tilde{\phi}_j$  at the joint given the position uncertainty of the FA and VA motor encoders. Waldron and Kumar (1979) obtained reasonable approximations for end-effector position uncertainty based on the assumption that joint angle errors are normally distributed. In the following discussion we will use a similar approach – assuming that sensor uncertainties follow a normal distribution. This assumption is based on the Central Limit Theorem (Devore, 1999, pp. 235).

Let the normal distribution corresponding to the estimates for the VA and FA shaft positions be  $N(\tilde{\phi}_v, \Delta\tilde{\phi}_v)$  and  $N(\tilde{\phi}_f, \Delta\tilde{\phi}_f)$ , where  $\tilde{\phi}_v$  and  $\tilde{\phi}_f$  are respectively the shaft position estimates (or mean) for the VA and FA, and  $\Delta\tilde{\phi}_v$  and  $\Delta\tilde{\phi}_f$  are the uncertainties (or standard deviations) associated with these estimates respectively. Such norms were used by Hill and Tesar (1997) to model inaccuracies in the manipulator EEF position due to inaccuracies in the joint sensors. Considering that the output position of the PFVA (i.e. the manipulator joint) is a weighted linear combination of the input shaft positions as shown in Eq. (3.6), the output position estimate is also a normal distribution<sup>24</sup>  $N(\tilde{\phi}_j, \Delta\tilde{\phi}_j)$ :

$$\tilde{\phi}_j = \left( \frac{1}{\tilde{\rho}+1} \right) (\tilde{\phi}_v - \phi_{v0}) + \left( \frac{\tilde{\rho}}{\tilde{\rho}+1} \right) (\tilde{\phi}_f - \phi_{f0}) \quad (5.1)$$

Also,

$$\Delta\tilde{\phi}_j^2 = \left[ \frac{1}{\tilde{\rho}+1} \Delta\tilde{\phi}_v \right]^2 + \left[ \frac{\tilde{\rho}}{\tilde{\rho}+1} \Delta\tilde{\phi}_f \right]^2 \quad (5.2)$$

The relationships in Eqs. (5.1)-(5.2) follow from the properties<sup>25</sup> of normal distributions (Welch and Bishop, 2001). We will now define a dimensionless scalar called *relative accuracy factor* between the two inputs  $\tilde{\alpha}_v^f$  that indicates the relative nature of the position uncertainties in the two inputs:

$$\tilde{\alpha}_v^f = \frac{\Delta\tilde{\phi}_f}{\Delta\tilde{\phi}_v} \quad (5.3)$$

For example, if the encoder accuracies of the motors driving the VA and the FA are respectively  $\pm 2.5$  arc-min and  $\pm 0.45$  arc-min, then  $\tilde{\alpha}_v^f = \frac{0.45}{2.5}$  ( $= 0.18$ ). In this

example, the FA is more accurate than the VA. Now, we will compute the relative

---

<sup>24</sup> The linear weighted sum of two normally distributed variables is a normal distribution (Welch and Bishop, 2001, p. 11).

<sup>25</sup> Note that the correlation between  $\tilde{\phi}_v$  and  $\tilde{\phi}_f$  is zero because the encoder uncertainties in the FA and VA inputs are independent of each other.

accuracy factor  $\tilde{\alpha}_f^j$  between the output and the FA which is defined as the ratio of the output position uncertainty to that of the FA:

$$\Delta\tilde{\phi}_j = \sqrt{\left[\frac{1}{26.1}(2.5)\right]^2 + \left[\frac{25.1}{26.1}(0.45)\right]^2} = 0.44 \text{ arc-min} \quad (5.4)$$

In this example,  $\tilde{\alpha}_f^j = \frac{0.44}{0.45} (\cong 0.98)$ , i.e. the output position uncertainty is approximately

the equal to that of the FA position uncertainty. For this example, it is evident that the output position uncertainty is predominantly influenced by that of the FA. For completeness, we can now also define the relative accuracy  $\tilde{\alpha}_f^j$  in terms of  $\tilde{\alpha}_v^f$  and  $\tilde{\alpha}_f^j$ :

$$\tilde{\alpha}_f^j = \sqrt{\left[\frac{\tilde{\alpha}_v^f}{\tilde{\rho}+1}\right]^2 + \left[\frac{\tilde{\rho}}{\tilde{\rho}+1}\right]^2} \quad (5.5)$$

The importance of Eq. (5.5) is that it characterizes the relative nature of the output position uncertainty with respect to that of the FA. This is expressed in terms of the relative accuracy factor between the inputs  $\tilde{\alpha}_f^v = 1/\tilde{\alpha}_v^f$  and the RSF  $\tilde{\rho}$ .

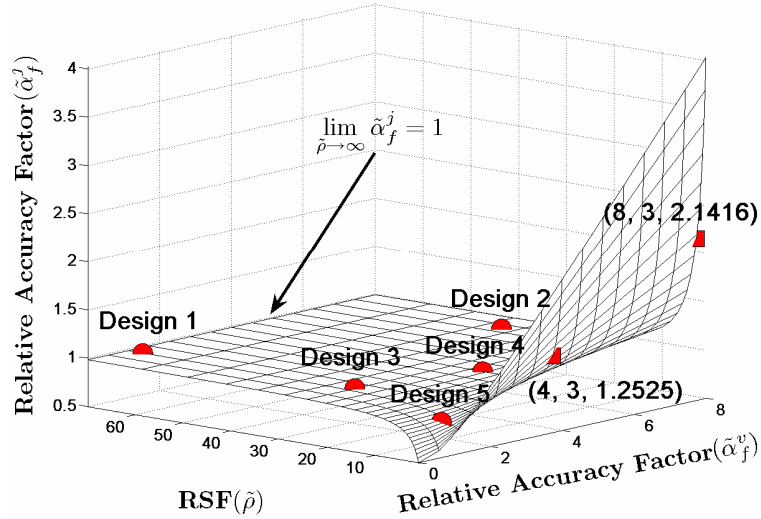


Figure 5.1. Surface plot of relative accuracy factor  $\tilde{\alpha}_f^j$  as a function of RSF  $\tilde{\rho}$  and  $\tilde{\alpha}_f^v$ . Note that  $\lim_{\tilde{\rho} \rightarrow \infty} \tilde{\alpha}_f^j = 1$ . The relative accuracy factor corresponding to the five PFVA designs are shown.

### ***Example 5.1: Parametric Analysis of Accuracy in the PFVA***

We will now illustrate the concept developed in this section. For this example, we use the five candidate PFVA designs. We will graphically show the variation of the relative accuracy factor  $\tilde{\alpha}_f^j$  with respect to the two dimensionless design variables: (a) RSF  $\tilde{\rho}$  and (b) the relative accuracy factor between the two inputs  $\tilde{\alpha}_f^v$ , and derive physical meaning for this relation. The expression in Eq. (5.5) is plotted in Figure 5.1.

In this same plot are shown the values for the five discrete designs we have considered. The fundamental distinction among these five designs is their RSF which varies from 3.7 (indicates significantly coupled inputs) to 66.85 (indicates relatively uncoupled inputs). We would like to make some observations regarding the above plot:

- Two example designs for the same value of RSF = 3 are shown with square markers on the plot. We considered two different  $\tilde{\alpha}_f^v$  values for the same value of RSF in these two example designs because most motor suppliers can include different encoders for the same motor. It was observed that when  $\tilde{\alpha}_f^v$  was increased 2x (from 4 to 8), then  $\tilde{\alpha}_f^j$  increased by approximately 1.7x.
- The two axes corresponding to relative accuracy factor and RSF are dependent on the design of the PFVA. The circular markers in Figure 5.1 show the five designs, considered in this chapter, on the relative accuracy factor  $\tilde{\alpha}_f^j$  surface. It can be observed from the plot that for designs 1, 2, 3, and 4 the output position uncertainty is predominantly influenced by that of the FA.
- In design 3 which corresponds to the laboratory prototype of the PFVA built at UTRRG, the values for RSF,  $\tilde{\alpha}_f^v$  and  $\tilde{\alpha}_f^j$  are respectively 24.27, 1.33, and 0.9619.
- The theoretical limit for the RSF  $\tilde{\rho}$  in a PFVA is infinity. As this limit is approached, the accuracy transformation in Eq. (5.5) takes the form

$$\lim_{\tilde{\rho} \rightarrow \infty} \tilde{\alpha}_f^j = 1 \quad (5.6)$$

This is also observed in the plot in Figure 5.1. This observation can be summarized as a design guideline.

**DESIGN GUIDELINE 5.1.** *In considering the influence of the input accuracies on the output joint accuracy, as the gear ratios in a PFVA approach their theoretical limit ( $\tilde{\rho} \rightarrow \infty$ ), the output position accuracy will be entirely dictated by the accuracy of the FA.*

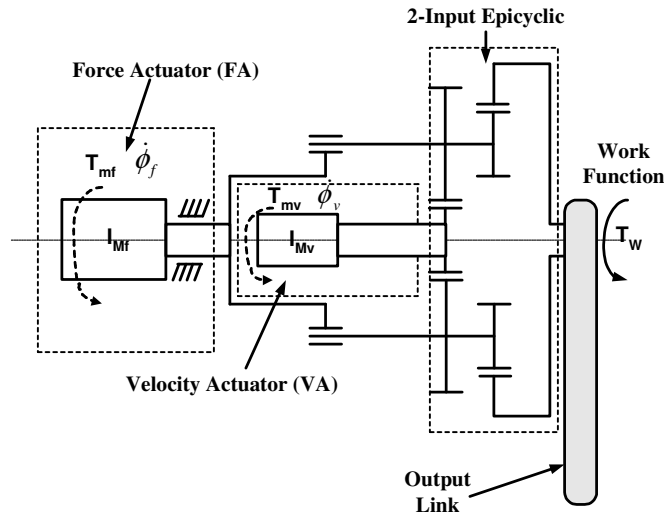


Figure 5.2. A schematic of the PFVA with an output work function.

### 5.3. METHODOLOGY FOR FORCE DISTRIBUTION ANALYSIS

Our intention in performing the force distribution analysis of the PFVA is to determine the distribution of the force and acceleration requirements due to an output work function  $T_w$  (Figure 5.2), between the two inputs of the PFVA. We investigate the variation of these effects as the VA and FA become increasingly distinct from each other, or mathematically, as  $\tilde{\rho} \rightarrow \infty$ . In the following sections, we will parametrically analyze the force distribution in PFVAs in order to aid the design of PFVA driven systems.



Although the models used in this chapter are relatively straightforward, our objective is to characterize the coupling between the two inputs of the PFVA in terms of dimensionless numbers. The notion of coupling needs clarification here (Figure 5.3).

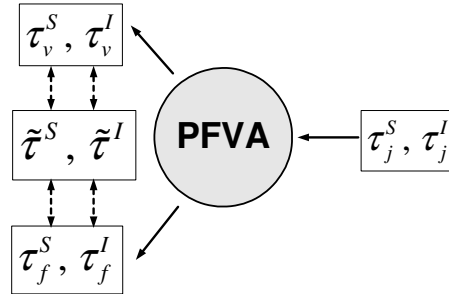


Figure 5.3. Schematic of the procedure for force distribution analysis of the PFVA.

In this figure, the subscript  $j$  represents the joint which is connected to the output of the PFVA. We analyze the coupling between the two inputs for two types of loads at the output of the PFVA (i) static load torques ( $\tau_j^S$ ), and (ii) inertial torques ( $\tau_j^I$ ). For each of these we determine (from inverse dynamics) the static and inertial torque requirement at each input ( $\tau_v^S, \tau_v^I, \tau_f^S$ , and  $\tau_f^I$ ) to be able to support these loads. After this we define a ratio between the determined torque requirements at the inputs which represent the coupling (or distribution) of the static ( $\tilde{\tau}^S$ ) or inertial ( $\tilde{\tau}^I$ ) load requirement between the two inputs. The objective is to study how this distribution ratio changes with respect to  $\tilde{\rho}$ . We will also present numerical examples considering the five candidate PFVA designs described in Section 5.1. In conducting the force distribution analysis, we will derive physical insight into the operation of a PFVA through some design guidelines.

## 5.4. FORCE DISTRIBUTION ANALYSIS

### 5.4.1. Static Load Torques

A study of static torque transformation in PFVA driven systems was done in (Rabindran and Tesar, 2007b). However that work did not consider the effect of

efficiency on torques. A more refined development of static torque transformation is presented in Chapter 4. We will briefly review this analysis here with the goal of determining the static load torque distribution between the VA and FA. For considering the efficiencies it is necessary to know the direction of power flow in the PFVA. Chapter 4 lists six possible power flow modes for a PFVA and their physical meanings in Table 4.1. One of these modes is the normal operational mode wherein, the FA and VA are inputs<sup>26</sup> to the PFVA and the machine is the output (Figure 5.4). We will consider this mode of power flow for the following analysis.

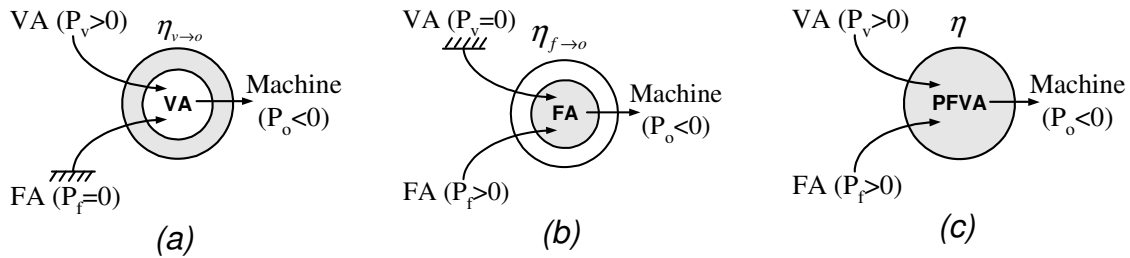


Figure 5.4. Mechanical efficiency analysis of a DISO PFVA as the superposition of a SISO FA and VA.

Pennestri and Valentini (2003) used the principle of virtual work to determine the torque transformation for the Single Input Single Output (SISO) modes shown in Figure 5.4 (a) and (b). Assume a non-zero, physically permissible, and infinitesimal virtual displacement  $\delta\phi_v$  and  $\delta\phi_f$  associated with the VA and FA shafts, respectively. Then, applying the principle of virtual work to the two SISO modes shown in Figure 5.4 (a):

$$\tau_j^S \left[ \delta\phi_j \right]_{\delta\phi_f=0} + \eta_{v \rightarrow j} \tau_v^S \delta\phi_v = 0 \quad (5.7)$$

<sup>26</sup> Our sign convention is such that an input shaft has positive power associated with it. In other words, the torque and angular velocity of an input shaft have the same sign. This is similar to the convention in Section 4.1.

where  $[\delta\phi_j]_{\delta\phi_f=0} = \left(\frac{1}{\tilde{\rho}+1}\right)\delta\phi_v$  is the velocity of the PFVA output in the SISO case from

Figure 5.4(a). Hence this relation may be re-written in terms of  $\delta\phi_v$ :

$$\tau_j^s \left(\frac{1}{\tilde{\rho}+1}\right) \delta\phi_v + \eta_{v \rightarrow j} \tau_v^s \delta\phi_v = 0 \quad (5.8)$$

Similarly, for static torque transformation in mode (b) of Figure 5.4:

$$\tau_j^s \left(\frac{\tilde{\rho}}{\tilde{\rho}+1}\right) \delta\phi_f + \eta_{f \rightarrow j} \tau_f^s \delta\phi_f = 0 \quad (5.9)$$

Since we have imposed non-zero virtual displacements on the input shafts, we can conclude from Eqs. (5.8)-(5.9) that:

$$\tau_v^s = -\tau_j^s \frac{1}{\eta_{v \rightarrow j}} \left(\frac{1}{\tilde{\rho}+1}\right) \quad (5.10)$$

$$\tau_f^s = -\tau_j^s \frac{1}{\eta_{f \rightarrow j}} \left(\frac{\tilde{\rho}}{\tilde{\rho}+1}\right) \quad (5.11)$$

From Eqs. (5.10)-(5.11) we recognize that the shaft torques bear a constant ratio:

$$\tau_j^s : \tau_v^s : \tau_f^s = 1 : -\left[\frac{1}{\eta_{v \rightarrow j}(\tilde{\rho}+1)}\right] : -\left[\frac{\tilde{\rho}}{\eta_{f \rightarrow j}(\tilde{\rho}+1)}\right] \quad (5.12)$$

If we represent the velocity transformation in Eq. (3.1) as:

$$\dot{\phi}_j = [\mathbf{G}^j] \begin{bmatrix} \dot{\phi}_v \\ \dot{\phi}_f \end{bmatrix} \quad (5.13)$$

where

$$[\mathbf{G}^j] = \begin{bmatrix} 1 & \tilde{\rho} \\ \tilde{\rho}+1 & \tilde{\rho}+1 \end{bmatrix} \quad (5.14)$$

is a matrix of Kinematic Influence Coefficients (KICs). See (Benedict and Tesar, 1971; Hall, 1992) for the definition and use of KICs for mechanism analysis. In our case, the KICs are constant gear ratios. We may now rewrite the static torque transformation as:

$$\boldsymbol{\tau}^s = -\boldsymbol{\eta} [\mathbf{G}^j]^T \boldsymbol{\tau}_j^s \quad (5.15)$$

where

$$\boldsymbol{\tau}^S = \begin{bmatrix} \tau_v^S & \tau_f^S \end{bmatrix}^T \quad (5.16)$$

represents the vector of static torques required at each input (VA and FA) to support a net static torque  $\tau_j^S$  at the machine. In Eq. (5.15),  $\boldsymbol{\eta} \in R^{2 \times 2}$  is a diagonal matrix of efficiencies:

$$\boldsymbol{\eta} = \begin{bmatrix} \eta_{v \rightarrow j} & 0 \\ 0 & \eta_{f \rightarrow j} \end{bmatrix} \quad (5.17)$$

In a PFVA the two inputs are very distinct from each other in terms of their velocity ratios. The theoretical limits for the velocity ratios of an FA and VA respectively approach 1 and 0. Consequently, the theoretical limit of the RSF  $\tilde{\rho}$  approaches  $\infty$ . We will now determine the limiting static torques at the two inputs as the limit of  $\tilde{\rho}$  approaches  $\infty$ :

$$\lim_{\rho \rightarrow \infty} \tau_v^S = 0 \quad (5.18)$$

$$\lim_{\rho \rightarrow \infty} \tau_f^S = \frac{-\tau_j^S}{\eta_{f \rightarrow j}} \quad (5.19)$$

We can now introduce a dimensionless parameter, called Static Torque Distribution Ratio (STDR) labeled  $\tilde{\tau}^S$ , as the ratio of the static torque on the FA shaft to that on the VA shaft. Note that the STDR should be a constant (equal to the RSF  $\tilde{\rho}$ ), for given PFVA geometry, in order to assure steady operation:

$$\lim_{\rho \rightarrow \infty} \tau_f^S = \frac{-\tau_j^S}{\eta_{f \rightarrow j}} \quad (5.20)$$

Substituting the expressions from Eqs. (5.10) and (5.11) in (5.20):

$$\tilde{\tau}^S = \frac{-\tau_j^S \frac{1}{\eta_{f \rightarrow j}} \left( \frac{\tilde{\rho}}{\tilde{\rho} + 1} \right)}{-\tau_j^S \frac{1}{\eta_{v \rightarrow j}} \left( \frac{1}{\tilde{\rho} + 1} \right)} \quad (5.21)$$

Simplifying this expression for STDR in terms of two dimensionless parameters, (i) the RSF  $\tilde{\rho}$  that has already been defined and (ii) the *relative efficiency ratio*  $\tilde{\eta}$  or the ratio of the FA input's efficiency to that of the VA input's efficiency:

$$\tilde{\tau}^S = \frac{\tilde{\rho}}{\tilde{\eta}} \quad (5.22)$$

where

$$\tilde{\eta} = \frac{\eta_{f \rightarrow j}}{\eta_{v \rightarrow j}} \quad (5.23)$$

We will now use an example to demonstrate the ideas in this section.

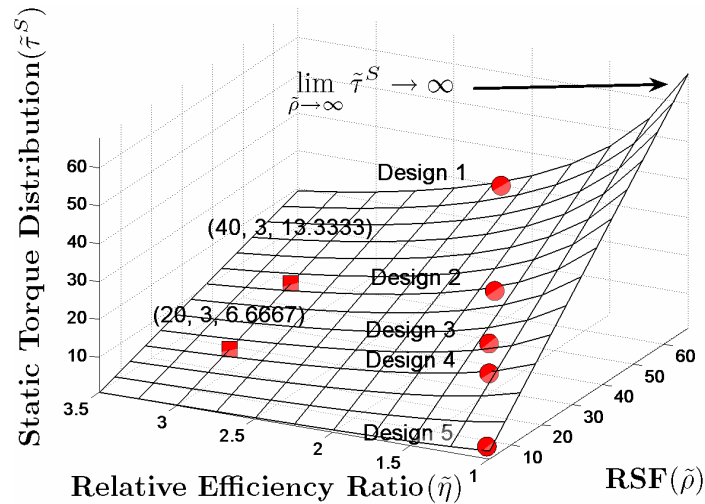


Figure 5.5. Surface representing the variation of STDR with respect to the Relative Efficiency Ratio and the RSF. The circular markers represent the five PFVA designs. To demonstrate how a point on this surface should be interpreted, the square markers show two example PFVA designs with the same Relative Efficiency Ratio and different RSFs.

### ***Example 5.2: Static Load Torque Distribution***

In this example we will plot the surface for the analytical relation in Eq. (5.22), i.e. the variation of STDR with respect to two parameters, namely the RSF  $\tilde{\rho}$  and the relative efficiency ratio  $\tilde{\eta}$ . We will consider multiple points on this surface

corresponding to the five candidate designs. Some observations from the plot in Figure 5.5 were made:

- Two example designs for the same value of  $\tilde{\eta} = 3$  are shown with square markers on the surface. This indicates that the FA is 3x more efficient than the VA. It can be observed that when  $\tilde{\rho}$  was increased 2x (from 20 to 40) for the given value of  $\tilde{\eta}$ , the STDR increases by approximately 2x. It should be emphasized here that the STDR is an invariant with respect to the applied load due to Eq. (5.12).
- The two axes corresponding to the relative efficiency ratio and RSF are dependent on the design of the PFVA. The circular markers in Figure 5.5 show the five designs, considered in this chapter, on the STDR surface. As we go from Design 1 through 5 the two inputs get more and more coupled (due to decreasing RSF values). Consequently, the distribution of static torques between the two inputs becomes increasingly even. For the UTRRG PFVA design (#3), the values for RSF  $\tilde{\rho}$ , the relative efficiency ratio  $\tilde{\eta}$  and STDR  $\tilde{\tau}^S$  are respectively 24.27, 1.42, and 17.08.
- The theoretical limit for the RSF  $\tilde{\rho}$  in a PFVA is infinity. As this limit is approached, STDR  $\tilde{\tau}^S$  in Eq. (5.22) takes the following form:

$$\lim_{\tilde{\rho} \rightarrow \infty} \tilde{\tau}^S \rightarrow \infty \quad (5.24)$$

This observation can be summarized as a design guideline.

**DESIGN GUIDELINE 5.2.** *As the two inputs in a PFVA become more and more distinct, and approach their theoretical limits ( $\tilde{\rho} \rightarrow \infty$ ), the entire output static load requirement is only on the FA. Consequently, in this scenario, the two inputs are decoupled in terms of static torque demand.*

### 5.4.2. Inertia Torques

In this section, our goal is to determine the inertial torque demand on the inputs (FA and VA) based on the lumped inertias in the system. Let the inertia of the output mechanism be lumped at the PFVA output (or the mechanism's active joint) and be labeled  $I_j^*$  as shown in Figure 5.6.

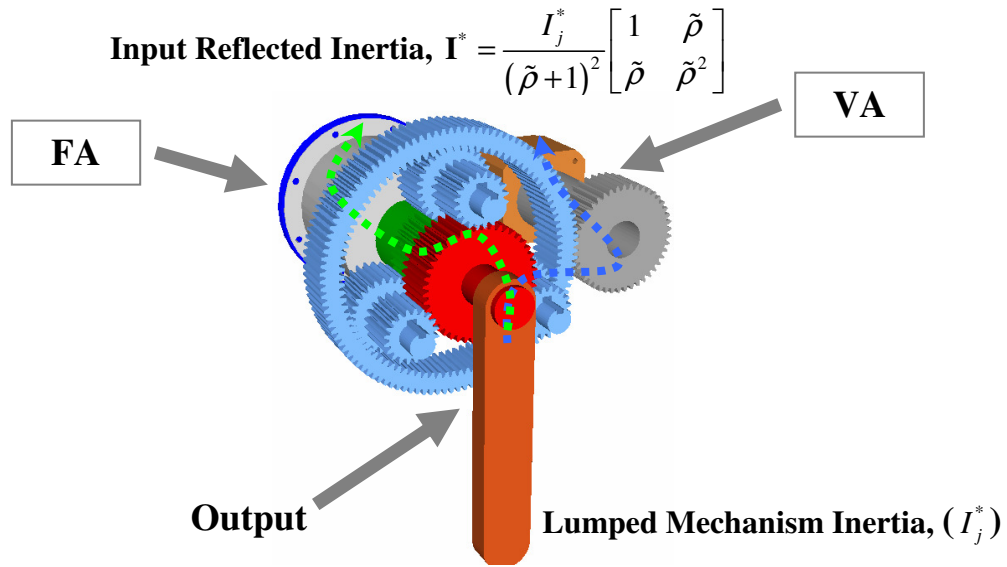


Figure 5.6. Schematic of a single-link manipulator with lumped output inertia and reflected input inertia. The dotted lines show the parallel force paths to the two inputs from the output.

To look at the torque demand at the two inputs due to an inertial load  $I_j^*$  at the joint, we will reflect this inertia to the input side using equivalence of kinetic energy. This output to input inertia transformation for a PFVA was first presented by Rabindran and Tesar (2007a):

$$\frac{1}{2} \dot{\phi}_j^T I_j^* \dot{\phi}_j = \frac{1}{2} \dot{\phi}^T \mathbf{I}^* \dot{\phi} \quad (5.25)$$

where  $\dot{\phi}_j$  is the velocity of the output,  $I_j^*$  is the lumped inertia at the output,  $\mathbf{I}^* \in \mathbb{R}^{2 \times 2}$  is the input reflected inertia matrix, and  $\dot{\boldsymbol{\phi}} = [\dot{\phi}_v \quad \dot{\phi}_f]^T$  is the vector of input velocities.

Now Eq. (5.25) can be combined with Eq. (5.13):

$$\mathbf{I}^* = I_j^* [\mathbf{G}^j]^T [\mathbf{G}^j] \quad (5.26)$$

Note that the output inertial load  $I_j^*$  has been factored out from the matrix part of Eq. (5.26) because it is a scalar quantity in this example<sup>27</sup>. Expanding this expression in terms of the RSF  $\tilde{\rho}$  yields:

$$\mathbf{I}^* = I_j^* \begin{bmatrix} \left(\frac{1}{\tilde{\rho}+1}\right)^2 & \frac{\tilde{\rho}}{(\tilde{\rho}+1)^2} \\ \frac{\tilde{\rho}}{(\tilde{\rho}+1)^2} & \left(\frac{\tilde{\rho}}{\tilde{\rho}+1}\right)^2 \end{bmatrix} = \frac{I_j^*}{(\tilde{\rho}+1)^2} \begin{bmatrix} 1 & \tilde{\rho} \\ \tilde{\rho} & \tilde{\rho}^2 \end{bmatrix} \quad (5.27)$$

Two observations regarding the inertia transformation matrix  $\mathbf{I}^*$  are as follows:

- $[\mathbf{G}^j]^T [\mathbf{G}^j]$  in Eq. (5.26) represents an outer product of the vector  $[\mathbf{G}^j]^T$  with itself. The rank of such an outer product is always 1. The second row of this matrix is a scalar multiple of the first row. Equivalently, the second column of this matrix is a scalar multiple of the first column. The physical interpretation of this mathematical observation is that we are expressing the inertia of a single DOF system using a higher dimensional inertia matrix, and hence such a matrix should be singular. Our interest in determining this matrix is to quantify the inertial demands on the PFVA inputs due to an external inertial load.
- We will define a dimensionless design parameter called the dynamic coupling factor  $\tilde{\mu}$  that represents the off-diagonal term in the matrix  $[\mathbf{G}^j]^T [\mathbf{G}^j]$ , i.e.:

$$\tilde{\mu} = \frac{\tilde{\rho}}{(\tilde{\rho}+1)^2} \quad (5.28)$$

Initial study of this term was carried out in (Rabindran and Tesar, 2007a).

<sup>27</sup> Note that for multi-input-multi-output systems this is not a scalar.



The torque demand  $\boldsymbol{\tau}^I$  at the VA and FA due to an inertial load at the machine can now be expressed as:

$$\boldsymbol{\tau}^I = (\mathbf{I}^* + \mathbf{I}_M) \begin{bmatrix} \ddot{\phi}_v \\ \ddot{\phi}_f \end{bmatrix} \quad (5.29)$$

In the above equation  $\mathbf{I}_M$  is the prime-mover inertia matrix that lumps all the motor and gear train component inertias of the VA and FA (see Appendix C):

$$\mathbf{I}_M = \begin{bmatrix} I_{M_v} & I_{vf} \\ I_{vf} & I_{M_f} \end{bmatrix} \quad (5.30)$$

To look at the components of the inertia torque vector, we could expand the expression in Eq. (5.29):

$$\tau_v^I = \left( I_{M_v} + I_j^* \frac{1}{(\tilde{\rho} + 1)^2} \right) \ddot{\phi}_v + \left( I_{vf} + I_j^* \frac{\tilde{\rho}}{(\tilde{\rho} + 1)^2} \right) \ddot{\phi}_f \quad (5.31)$$

$$\tau_f^I = \left( I_{vf} + I_j^* \frac{\tilde{\rho}}{(\tilde{\rho} + 1)^2} \right) \ddot{\phi}_v + \left( I_{M_f} + I_j^* \frac{\tilde{\rho}^2}{(\tilde{\rho} + 1)^2} \right) \ddot{\phi}_f \quad (5.32)$$

The limiting inertial torque demand in the inverse dynamics equation of a PFVA driven 1-DOF system (as  $\tilde{\rho} \rightarrow \infty$ ) was discussed by Rabindran and Tesar (2007a):

$$\lim_{\tilde{\rho} \rightarrow \infty} \tau_v^I = I_{M_v} \ddot{\phi}_v \quad (5.33)$$

$$\lim_{\tilde{\rho} \rightarrow \infty} \tau_f^I = (I_{M_f} + I_j^*) \ddot{\phi}_f \quad (5.34)$$

As in the case of static torques (in the previous section), we will define a dimensionless parameter to signify the distribution of inertia torques between the two inputs. This parameter will be called Inertia Torque Distribution Ratio (ITDR) and labeled  $\tilde{\tau}^I$ :

$$\tilde{\tau}^I = \frac{\tau_f^I}{\tau_v^I} \quad (5.35)$$

Substituting the expressions from Eqs. (5.31) and (5.32) in Eq. (5.35) we have

$$\tilde{\tau}^I = \frac{\left( I_{vf} + I_j^* \frac{\tilde{\rho}}{(\tilde{\rho}+1)^2} \right) \ddot{\phi}_v + \left( I_{Mf} + I_j^* \frac{\tilde{\rho}^2}{(\tilde{\rho}+1)^2} \right) \ddot{\phi}_f}{\left( I_{Mv} + I_j^* \frac{1}{(\tilde{\rho}+1)^2} \right) \ddot{\phi}_v + \left( I_{vf} + I_j^* \frac{\tilde{\rho}}{(\tilde{\rho}+1)^2} \right) \ddot{\phi}_f} \quad (5.36)$$

We will now determine an expression for ITDR in terms of other dimensionless parameters based on the design and operation of the PFVA:

$$\tilde{\phi} = \frac{\ddot{\phi}_f}{\ddot{\phi}_v}, \quad \tilde{I}_M = \frac{I_{Mf}}{I_{Mv}}, \quad \tilde{I}_{vf} = \frac{I_{vf}}{I_{Mv}}, \quad \text{and} \quad \tilde{I}_j^* = \frac{I_j^*}{I_{Mv}} \quad (5.37)$$

In Eq. (5.37),  $\tilde{\phi}$  refers to the *acceleration mixing ratio* or the ratio of accelerations of the two inputs;  $\tilde{I}_M$  refers to the *prime-mover inertia ratio* or the ratio between the principal inertias seen by the two prime-movers;  $\tilde{I}_{vf}$  is the *coupling inertia ratio* or the ratio of the lumped gear train coupling inertias to the VA-side inertia;  $\tilde{I}_j^*$  is the *output-to-VA inertia ratio* or the ratio of the output inertia and the VA-side principal inertia. Combining Eqs. (5.36) and (5.37):

$$\tilde{\tau}^I = \frac{\left( \tilde{I}_{vf} + \tilde{I}_j^* \frac{\tilde{\rho}}{(\tilde{\rho}+1)^2} \right) + \left( \tilde{I}_M + \tilde{I}_j^* \frac{\tilde{\rho}^2}{(\tilde{\rho}+1)^2} \right) \tilde{\phi}}{\left( 1 + \tilde{I}_j^* \frac{1}{(\tilde{\rho}+1)^2} \right) + \left( \tilde{I}_{vf} + \tilde{I}_j^* \frac{\tilde{\rho}}{(\tilde{\rho}+1)^2} \right) \tilde{\phi}} \quad (5.38)$$

It should be recognized here that the RSF  $\tilde{\rho}$ , prime-mover inertia ratio  $\tilde{I}_M$ , coupling inertia ratio  $\tilde{I}_{vf}$ , and out-to-VA inertia ratio  $\tilde{I}_j^*$  are not entirely independent of each other. For a given load, the  $\tilde{I}_M$ ,  $\tilde{I}_{vf}$ , and  $\tilde{I}_j^*$  all depend on the RSF<sup>28</sup>  $\tilde{\rho}$ . This relationship has not been explicitly accounted for in Eqs. (5.37) and (5.38). This is because such a relation (among the dimensionless design parameters defined above) depends on the type of gear train and prime-mover considered during the design process.

---

<sup>28</sup> For a given load, the selected motor's size and inertia depends on the gear ratio and gear train type.

With this caveat, we will now use a numerical example to demonstrate the ideas presented in this section.

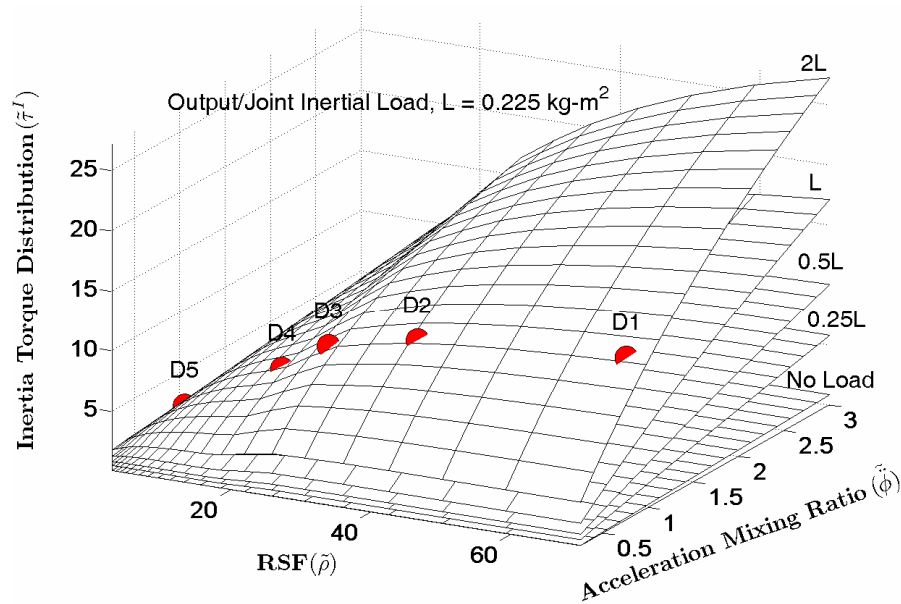


Figure 5.7. Surface representing the variation of ITDR with respect to the acceleration mixing ratio and the RSF. The circular markers represent the five PFVA designs. The different surfaces correspond to various load inertia settings, namely, 2x, 1x, 0.5x, 0.25x, and 0x the output link inertia, i.e.,  $0.225 \text{ kg-m}^2$ .

### ***Example 5.3: Inertia Torque Distribution***

In this example we will plot the surface for the analytical relation in Eq. (5.38), i.e. the variation of ITDR  $\tilde{\tau}^I$  with respect to two of the four dimensionless parameters in this equation, namely the RSF  $\tilde{\rho}$  and the acceleration mixing ratio  $\tilde{\phi}$ . To account for the dependence of  $\tilde{I}_M$  on  $\tilde{\rho}$ , we determined the prime-mover inertias for a given RSF by interpolating between the five candidate designs. As we are considering the gear trains from the same manufacturer (Andantex SA Series gear trains, 2007) and the motors we are considering are approximately similar in construction (permanent magnet brushless DC motors from Danaher Motion), this assumption is justified. We now plot multiple

surfaces for ITDR for varying inertial loads. The link inertia at the output is considered to be  $0.225 \text{ kg-m}^2$ . However, we plot surfaces for 2x, 1x, 0.5x, 0.25x of this inertial load and for no-load conditions. These five different load settings correspond to the five different surfaces in Figure 5.7. Some observations from this figure are:

- The axis corresponding to RSF is design-dependent and the one corresponding to acceleration mixing ratio is dependent on the motion-state (in terms of input accelerations) of the system. The circular markers show the location of the five candidate designs on the surface when the two inputs for each design are accelerated at the same rate ( $\tilde{\phi} = 1$ ). These points have been shown on the surface corresponding to load inertia  $I_j^* = 0.45 \text{ kg-m}^2$  (labeled 2L in the Figure 5.7).
- With a unit acceleration mixing ratio ( $\tilde{\phi} = 1$ ), it was observed that the ITDR  $\tilde{\tau}^I$  increased by approximately 5x when RSF ( $\tilde{\rho}$ ) was increased by approximately 66x.
- Note that for the no-load condition  $\tilde{I}_j^* = 0$ , the ITDR will be

$$\left(\tilde{\tau}^I\right)_{No-Load} = \frac{\tilde{I}_{vf} + \tilde{I}_M \tilde{\phi}}{1 + \tilde{I}_{vf} \tilde{\phi}} \quad (5.39)$$

- The theoretical limit for the RSF ( $\tilde{\rho}$ ) in a PFVA is infinity. As this limit is approached, ITDR ( $\tilde{\tau}^I$ ) in Eq. (5.38) takes the form

$$\lim_{\tilde{\rho} \rightarrow \infty} \tilde{\tau}^I = \frac{\tilde{I}_{vf} + (\tilde{I}_M + \tilde{I}_j^*) \tilde{\phi}}{1 + \tilde{I}_{vf} \tilde{\phi}} \quad (5.40)$$

Using the same approach that was used to obtain Eqs. (5.33)-(5.34),  $\lim_{\tilde{\rho} \rightarrow \infty} \tilde{I}_{vf} = 0$  is

inserted into Eq. (5.40) to give

$$\lim_{\tilde{\rho} \rightarrow \infty} \tilde{\tau}^I = \frac{\tilde{I}_{vf} + (\tilde{I}_M + \tilde{I}_j^*) \tilde{\phi}}{1 + \tilde{I}_{vf} \tilde{\phi}} \quad (5.41)$$

This observation can be summarized as a design guideline.

**DESIGN GUIDELINE 5.3.** *As the two inputs in a PFVA become more and more distinct, and approach their theoretical limits ( $\tilde{\rho} \rightarrow \infty$ ), the entire output inertial load demand acts on the FA. Consequently, in this scenario, the two inputs are decoupled in terms of inertial torque demand.*

### 5.4.3. Acceleration Responsiveness Analysis

In this section we will look at the model developed in Eqs. (5.31) and (5.32) from the point of view of acceleration capability of the two inputs, namely the FA and VA, in the PFVA. We define *acceleration responsiveness* (labeled  $\xi$ ) for an input as the ratio of the maximum torque capability of the input to the total inertia of the system reflected to the input. This criterion is an acceleration threshold. As a simplified example of the concept, we studied the relation  $F = ma$  for the PFVA inputs in the previous section on inertial torque demands. In this section we will study the relation  $a_{\max} = F_{\max} / m$ , the limiting acceleration, for the PFVA inputs. Although not called acceleration responsiveness<sup>29</sup>, this criterion has been addressed in the literature (West and Leonard, 1955; Tal and Kahne, 1972) in the context of prime-mover selection for servo-systems. Vaculik and Tesar (2007) have considered this as one of the criteria for the parametric design of electro-mechanical actuators. Rios and Tesar (2008) have considered acceleration responsiveness as a design criterion for serial chain manipulators that use single input joints (unlike the PFVA which has two inputs per joint). Acceleration Responsiveness is a design criterion and tells us how fast the input can accelerate or decelerate.

In our case of the dual input PFVA, we are interested in studying the effect of the RSF  $\tilde{\rho}$  on the acceleration responsiveness of the force and velocity inputs. To do this,

---

<sup>29</sup> This criterion has sometimes been called torque-to-inertia ratio by motor manufacturers (Kollmorgen, 2007, p. 2).

we have to consider the ratio of the prime-mover torques to the sum of all inertias reflected to each input. The *input*<sup>30</sup> acceleration responsiveness of the PFVA can be determined by re-arranging the terms in Eq. (5.29). In the dual input case, the acceleration responsiveness is not a simple ratio. If  $\xi_v$  and  $\xi_f$  are respectively the acceleration responsiveness of the VA and FA and  $\boldsymbol{\tau}_{rated}$  is a vector of rated torques of the motors driving these inputs, then:

$$\begin{bmatrix} \xi_v \\ \xi_f \end{bmatrix} = (\mathbf{I}^* + \mathbf{I}_M)^{-1} \boldsymbol{\tau}_{rated} \quad (5.42)$$

It has been our continuing goal in this chapter to study the distinction between the two inputs (FA and VA) for every criterion that we have identified, in terms of dimensionless design (or operational parameters). In the same spirit, we define a dimensionless ratio called the relative acceleration responsiveness labeled  $\tilde{\xi}$  between the two inputs as:

$$\tilde{\xi} = \frac{\xi_f}{\xi_v} \quad (5.43)$$

This criterion indicates how responsive (in terms of accelerations) the two inputs are with respect to each other. Using the relation in Eq. (5.42) and the dimensionless quantities defined in Eq. (5.37), we can determine<sup>31</sup>  $\tilde{\xi}$ :

$$\tilde{\xi} = \frac{-\left[ I_{vf} + I_j^* \frac{\tilde{\rho}}{(\tilde{\rho}+1)^2} \right] (\tau_{M_v})_{rated} + \left[ I_{M_v} + I_j^* \frac{1}{(\tilde{\rho}+1)^2} \right] (\tau_{M_f})_{rated}}{\left[ I_{M_f} + I_j^* \frac{\tilde{\rho}^2}{(\tilde{\rho}+1)^2} \right] (\tau_{M_v})_{rated} - \left[ I_{vf} + I_j^* \frac{\tilde{\rho}}{(\tilde{\rho}+1)^2} \right] (\tau_{M_f})_{rated}} \quad (5.44)$$

or

---

<sup>30</sup> It is important to make a distinction between the acceleration responsiveness at the input vs. that at the output. In the former (latter) case, we are looking at the rate at which the motor (output) shaft can be accelerated or decelerated by the motor, given the machine and actuator parameters.

<sup>31</sup> Closed-form inverse for a 2x2 matrix was used.

$$\xi_{\tilde{\rho}} = \frac{-\left[\tilde{I}_{vf} + \tilde{I}_j^* \frac{\tilde{\rho}}{(\tilde{\rho}+1)^2}\right] + \left[1 + \tilde{I}_j^* \frac{1}{(\tilde{\rho}+1)^2}\right] \tilde{\tau}_{Mr}}{\left[\tilde{I}_M + \tilde{I}_j^* \frac{\tilde{\rho}^2}{(\tilde{\rho}+1)^2}\right] - \left[\tilde{I}_{vf} + \tilde{I}_j^* \frac{\tilde{\rho}}{(\tilde{\rho}+1)^2}\right] \tilde{\tau}_{Mr}} \quad (5.45)$$

where  $\tilde{\tau}_{Mr}$  is a dimensionless ratio between the rated (continuous or peak)<sup>32</sup> torques for the FA and VA motors or the rated motor torque ratio given by

$$\tilde{\tau}_{Mr} = \left( \frac{\tau_{Mf}}{\tau_{Mv}} \right)_{rated} \quad (5.46)$$

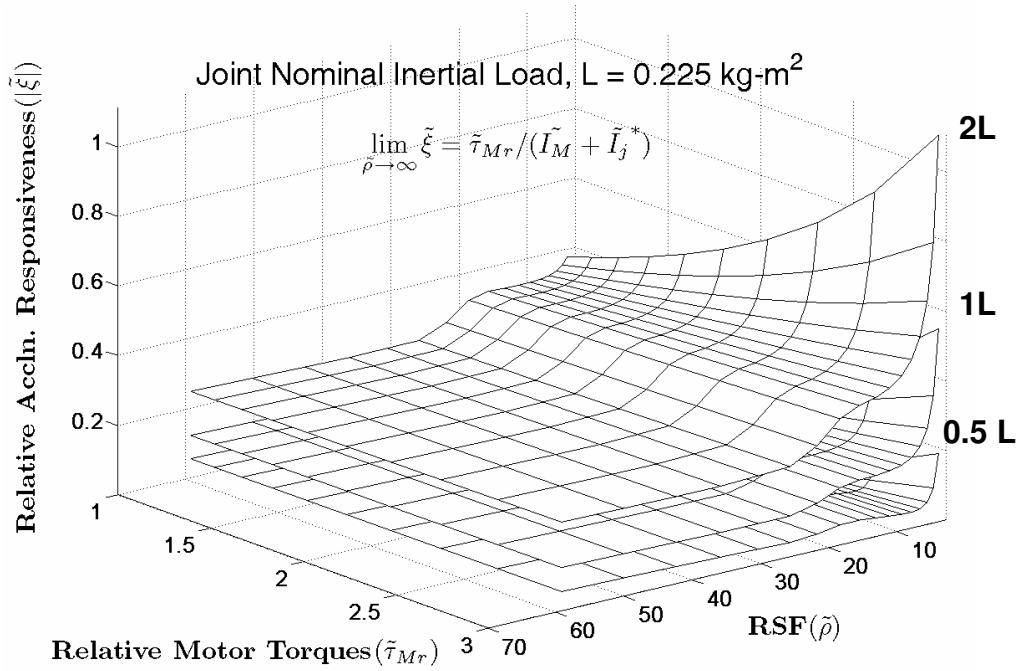


Figure 5.8. Surface representing the variation of relative acceleration responsiveness with respect to the rated motor torque ratio and the RSF. The different surfaces correspond to various load inertia settings, namely, 2x, 1x, and 0.5x the output link inertia, i.e., 0.225 kg-m<sup>2</sup>.

<sup>32</sup> Acceleration responsiveness can be calculated using either the continuous or the peak torque rating of the motor. The former (latter) calculation signifies how much maximum acceleration can be achieved for continuous (peak) operation.

**Note on Output-to-VA-Inertia Ratio.** There is literature (West and Leonard, 1955; Tal and Kahne, 1972) that suggests that the optimal gear ratio  $g_{opt}$  (that maximizes load acceleration capability for a given output load inertia) for a SISO geared actuator is equal to  $\sqrt{\tilde{I}_j^*}$ . For example, if the output (or load) inertia is  $2.1 \times 10^{-3} \text{ kg-m}^2$  and the motor side inertia is  $9.6 \times 10^{-5} \text{ kg-m}^2$ , then the optimal gear ratio which maximizes acceleration capability of this actuator is  $g_{opt} = \sqrt{\frac{2.1 \times 10^{-3}}{9.6 \times 10^{-5}}} = 4.68$ .

**Example 5.4: Acceleration Responsiveness Distribution**

We will now illustrate the ideas in this section using a numerical example. In this example we will plot the surface for the analytical relation in Eq. (5.45), i.e. the variation of relative acceleration responsiveness  $\tilde{\xi}$  with respect to two of the four dimensionless parameters in this equation, namely the RSF  $\tilde{\rho}$  and the acceleration mixing ratio  $\tilde{\phi}$ . To account for the dependence of  $\tilde{I}_M$  and  $\tilde{I}_{vf}$  on  $\tilde{\rho}$ , we determined the prime-mover and gear train inertias for a given RSF by interpolating between the five candidate designs. Multiple surfaces for relative acceleration responsiveness for varying inertial loads are plotted in Figure 5.8. The link inertia at the output is considered to be  $0.225 \text{ kg-m}^2$ . However, we plot surfaces for 2x, 1x, and 0.5x of this inertial load. These three different load settings correspond to the three different surfaces in Figure 5.8. Some observations regarding the above plot are listed below.

- Both the axes, RSF and the rated motor torque ratio, are design-dependent.
- The theoretical limit for the RSF  $\tilde{\rho}$  in a PFVA is infinity. As this limit is approached, the relative acceleration responsiveness  $\tilde{\xi}$  in Eq. (5.45) takes the form

$$\lim_{\tilde{\rho} \rightarrow \infty} \tilde{\xi} = \frac{\tilde{\tau}_{Mr}}{\tilde{I}_M + \tilde{I}_j^*} \quad (5.47)$$

This observation can be summarized as a design guideline.



**DESIGN GUIDELINE 5.4.** As the two inputs in a PFVA become more and more distinct, and approach their theoretical limits ( $\tilde{\rho} \rightarrow \infty$ ), the FA has much more acceleration capability than the VA.

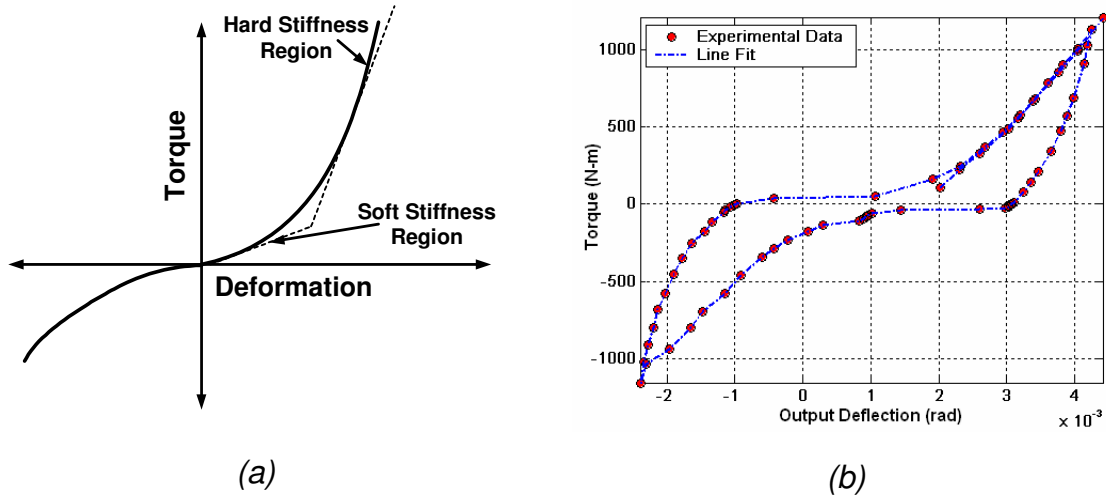


Figure 5.9. (a) Schematic representation of transmission stiffness (Schempf and Yoerger, 1993) including soft and hard stiffness zones. (b) Experimental stiffness data from a 1/4-scale weapons elevator actuator using a hypocyclic gear train (Courtesy Kevin Crouchley, NAVSEA, Philadelphia).

## 5.5. STIFFNESS DISTRIBUTION ANALYSIS

In this section we will study the stiffness characteristics of PFVAs. Our objective here is to characterize the mechanical and non-mechanical stiffness on the input side of the PFVA and determine their influence at the output of the system. For the mechanical stiffness, such a characterization has to consider the effect the RSF  $\tilde{\rho}$  on the overall stiffness of the PFVA. Stiffness analysis is important for studying the dynamic response of the PFVA. In addition, stiffness influences the backdriveability of the PFVA.

### 5.5.1. Mechanical Stiffness

In an actuator, there can be mechanical compliances in the shafts, the couplings, the transmission, and the bearings. The nature (linear or non-linear) and the magnitude

(significant or insignificant) of these compliances depend on the type of transmission and the gear ratio. Schempf and Yoerger (1993) studied the performance characteristics in robot transmissions and suggested models for various types of transmissions including a planetary gear head. They suggest a combined model for soft-zone and stiff zones of a typical robotic transmission as shown in Figure 5.9 (a). Beside this schematic, in Figure 5.9 (b) we show the experimental results<sup>33</sup> for the  $\alpha$ -prototype of a quarter-scale rugged electromechanical actuator (designed for an automated weapons elevator) that uses a hypocyclic gear train.

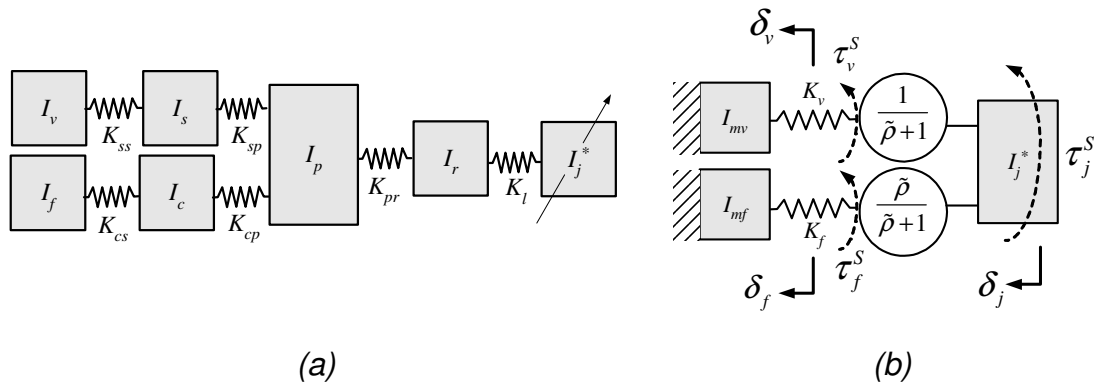


Figure 5.10. Representation of the PFVA as an in-series coupled spring system. The broken arrow on  $I_j^*$  indicates that this parameter is a variable depending on the configuration of the mechanism. (a) Complete lumped spring-mass model identifying all stiffness elements on the input side of the PFVA and (b) Simplified in-series spring system model with the kinematic transformation for each input.

The actuators in the above two examples are Single-Input-Single-Output (SISO) actuators. On the other hand, the PFVA is a DISO system, and we would like to do a similar analysis of the output stiffness of this actuator in terms of its relevant design parameters.

<sup>33</sup> Testing done by Kevin Crouchley at the Naval Sea Systems Command (NAVSEA), Philadelphia.

The sources of stiffness on the input side of the PFVA are shown in Figure 5.10(a). This figure includes only the mechanical stiffness elements (and the connecting inertia elements). The physical meaning of these lumped stiffness elements have been described in Table 5.2. Refer (Kahraman, 1994) for a more detailed description of compliances in a planetary gear train. Our intention is to first delineate all the parameters that contribute to the overall stiffness as shown in Figure 5.10(a) at the output and then simplify the system into a coupled-spring system as shown in Figure 5.10(b).

Table 5.2 Summary of Stiffness/Inertia Parameters in Figure 5.10

Parameter	Units	Physical Meaning
$I_v, I_f$	kg-m <sup>2</sup>	Rotational inertias of VA and FA prime-movers, respectively.
$K_{ss}$	Nm <sup>-1</sup>	Stiffness for VA shaft
$K_{sp}$	Nm <sup>-1</sup>	Stiffness for sun-planet meshing
$I_p$	kg-m <sup>2</sup>	Rotational inertia of the planet
$I_s$	kg-m <sup>2</sup>	Rotational inertia of the sun
$K_{cs}$	Nm <sup>-1</sup>	Stiffness coefficient for carrier shaft
$K_{cp}$	Nm <sup>-1</sup>	Stiffness coefficient for carrier-planet meshing
$K_{pr}$	Nm <sup>-1</sup>	Stiffness coefficient for planet-ring meshing
$I_r$	kg-m <sup>2</sup>	Rotational inertia of the ring
$K_l$	Nm <sup>-1</sup>	Stiffness coefficient for carrier-planet meshing
$I_{Mv}$	kg-m <sup>2</sup>	Rotational inertia of the VA lumped at its prime-mover
$I_{Mf}$	kg-m <sup>2</sup>	Rotational inertia of the FA lumped at its prime-mover
$I_j^*$	kg-m <sup>2</sup>	(Variable) load rotational inertia

In the following analytical development our goal is to determine the effective stiffness of the PFVA at its output, given the individual stiffness parameters for the mechanical elements as shown in Figure 5.10. In other words, considering the simplified

coupled spring system in Figure 5.10(b), we are trying to determine the effective stiffness  $K_j$  at the manipulator joint (PFVA output) such that

$$\tau_j^s = K_j \delta_j, \tau_v^s = K_v \delta_v, \text{ and } \tau_f^s = K_f \delta_f \quad (5.48)$$

From the velocity/displacement equation for a PFVA

$$\delta_j = \frac{1}{\tilde{\rho}+1} \delta_v + \frac{\tilde{\rho}}{\tilde{\rho}+1} \delta_f \quad (5.49)$$

Now if  $\eta_{j \rightarrow v}$  and  $\eta_{j \rightarrow f}$  are the backdriving efficiencies for the VA and FA force/power pathways in the PFVA, then as shown in Figure 5.10(b)

$$\tau_v^s = -\tau_j^s \eta_{j \rightarrow v} \left( \frac{1}{\tilde{\rho}+1} \right) \text{ and } \tau_f^s = -\tau_j^s \eta_{j \rightarrow f} \left( \frac{\tilde{\rho}}{\tilde{\rho}+1} \right) \quad (5.50)$$

Using Eqs. (5.48)-(5.49), we have

$$\frac{\tau_j^s}{K_j} = \frac{1}{\tilde{\rho}+1} \frac{\tau_v^s}{K_v} + \frac{\tilde{\rho}}{\tilde{\rho}+1} \frac{\tau_f^s}{K_f} \quad (5.51)$$

Substituting Eq. (5.50) in Eq. (5.51) and neglecting the sign of the torques,

$$\frac{1}{K_j} = \eta_{j \rightarrow v} \left( \frac{1}{\tilde{\rho}+1} \right)^2 \frac{1}{K_v} + \eta_{j \rightarrow f} \left( \frac{\tilde{\rho}}{\tilde{\rho}+1} \right)^2 \frac{1}{K_f} \quad (5.52)$$

We will define two dimensionless ratios based on the parameters in Eq. (5.52): (i)  $\tilde{K} = K_f / K_v$ , called the relative stiffness and (ii)  $\tilde{K}_j = K_j / K_v$ , called the relative joint stiffness. Using these ratios, Eq. (5.52) can be rewritten as

$$\tilde{K}_j = \frac{1}{\eta_{j \rightarrow v}} \left( \frac{\tilde{K} (\tilde{\rho}+1)^2}{\tilde{K} + \tilde{\eta}_b \tilde{\rho}^2} \right) \quad (5.53)$$

In Eq. (5.53)  $\tilde{\eta}_b = \eta_{j \rightarrow f} / \eta_{j \rightarrow v}$  is the relative backdriving efficiency. We will now study the relationship in this equation using a numerical example.

### ***Example 5.5: Stiffness Distribution***

In this example we will plot the surface for the analytical relation in Eq. (5.53), i.e. the variation of relative joint stiffness  $\tilde{K}_j$  with respect to the RSF  $\tilde{\rho}$ , the relative stiffness  $\tilde{K}$ , and discrete values of the relative backdriving efficiency  $\tilde{\eta}_b$ .

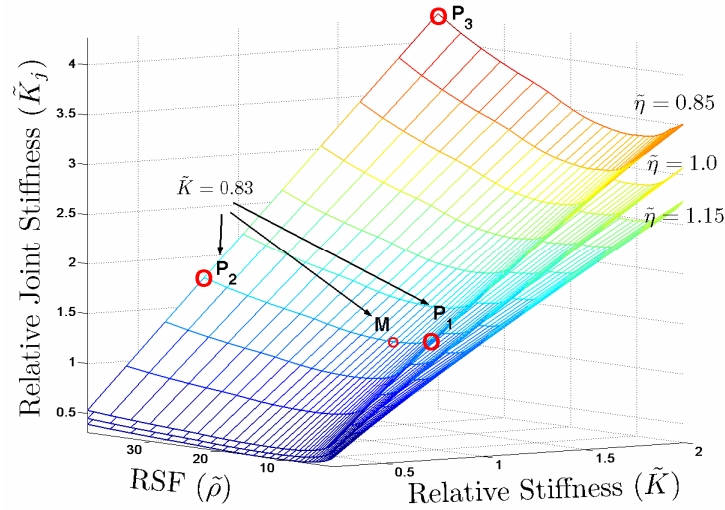


Figure 5.11. Variation of the Relative Joint Stiffness ( $\tilde{K}_j$ ) with respect to the Relative Stiffness ( $\tilde{K}$ ) and the RSF ( $\tilde{\rho}$ ) for  $\eta_{j \rightarrow v}$  varying as a function of RSF. 3D surfaces representing this data for various settings of  $\tilde{\eta}_b$ , namely, 0.85, 1, and 1.15 (corresponding to the three surfaces in the figure) are also shown.

Figure 5.11 represents the variation of the relative joint stiffness  $\tilde{K}_j$  with the RSF  $\tilde{\rho}$  and the relative stiffness  $\tilde{K}$ . Each of the three different plotted 3D surfaces corresponds to a different value of relative backdriving efficiency  $\tilde{\eta}_b$ . For all three surfaces shown in Figure 5.11, the VA efficiency is assumed to be a function of the RSF,  $\eta_{j \rightarrow v} = f(\tilde{\rho})$ . This relation can be determined from the SISO efficiencies of the two inputs as shown in Figure 5.12. Some observations from this example are listed below.

- The contour plot in Figure 5.13 shows the variation of  $\tilde{K}_j$  for various values of  $\tilde{K}$  and a constant value of relative backdriving efficiency  $\tilde{\eta}_b = 0.85$ . It can be observed that the value of relative joint stiffness  $\tilde{K}_j$  initially decreases. This is because as the RSF increases, the FA tends towards a direct-drive system thus having a tendency to be backdriven. On the contrary,  $\tilde{K}_j$  increases as  $\tilde{\rho}$  increases significantly. This is because the backdriving efficiency reduces

significantly for these values of  $\tilde{\rho}$ , thus making it harder to backdrive the joint. Hence, there is a minimum relative joint stiffness value  $\tilde{K}_j^{\min}$  such that

$$\frac{\partial \tilde{K}_j}{\partial \tilde{\rho}} = 0, \text{ if } \tilde{K}_j = \tilde{K}_j^{\min} \quad (5.54)$$

Point M on Figure 5.11 and Figure 5.13 shows this minimum point,  $\tilde{K}_j^{\min}=1.4$  (joint is approximately 40% more stiff than the VA), for  $\tilde{\eta}_b = 0.85$  and  $\tilde{K} = 0.83$ . This occurs when the RSF  $\tilde{\rho} = 11.5$ . Physically, this means that the joint stiffness will be at least 40% greater than that of the VA, if (i) the FA is 85% as efficient as the VA, and (ii) the FA is 17% less stiff than the VA).

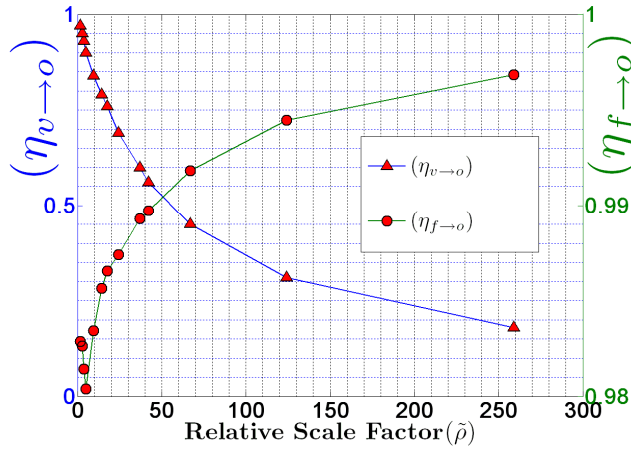


Figure 5.12. Variation of SISO efficiencies with respect to the RSF  $\tilde{\rho}$  for the commercially available SA series differentials from Andantex Inc., Wanamassa, NJ (see Chapter 4 for a detailed discussion on SISO efficiencies). The subscript  $o$  refers to the output or the machine joint. Therefore,  $\eta_{v \rightarrow o} = \eta_{v \rightarrow j}$  is the basic efficiency of the drive train.

- Three example design points P1, P2, and P3 are shown on the surfaces in Figure 5.11. Points P1, P2, and P3 all lie on the (topmost) surface corresponding to  $\tilde{\eta}_b = 0.85$ . Further, points P1, P2, and M correspond to a PFVA design such that  $\tilde{K} = 0.83$ . For this value of  $\tilde{K}$ , with a 3x increase in the RSF  $\tilde{\rho}$  (going from point P1 to M), the relative joint stiffness  $\tilde{K}_j$  decreases by approximately 18%. In

a similar manner, with a 2.5x increase in the RSF  $\tilde{\rho}$  (going from point M to P2),  $\tilde{K}_j$  increases by approximately 20%.

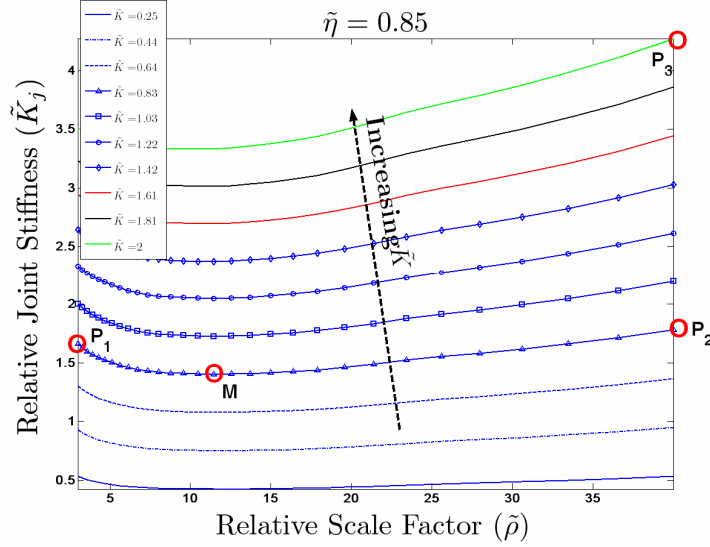


Figure 5.13. Contour plot representing the data in Figure 5.11 for  $\tilde{\eta}_b = 0.85$ .

- Two important design questions can now be raised: what is the limiting value of  $\tilde{K}_j$  as (i) the two inputs become distinct ( $\tilde{\rho} \rightarrow \infty$ ) and (ii) as the FA becomes increasingly softer than the VA ( $\tilde{K} \rightarrow 0$ ). These may be answered by considering the limiting value of the expression in Eq. (5.53):

$$\lim_{\tilde{\rho} \rightarrow \infty} \tilde{K}_j = \frac{\tilde{K}}{\eta_{j \rightarrow f}} \quad (5.55)$$

$$\lim_{\tilde{K} \rightarrow 0} \tilde{K}_j = 0 \quad (5.56)$$

To answer question (i), considering Eq. (5.55), the relative joint stiffness is entirely governed by the relative stiffness and the backdriving efficiency of the FA  $\eta_{j \rightarrow f}$ . If  $\eta_{j \rightarrow f}$  approaches zero as  $\tilde{\rho} \rightarrow \infty$ , then the PFVA is infinitely stiff (meaning not backdriveable) in this limit. Similarly to answer question (ii), considering Eq. (5.56) the PFVA becomes very compliant with respect to the VA when the FA (also) becomes very compliant with respect to the VA.

These two observations can be summarized as a design guideline as follows.

**DESIGN GUIDELINE 5.5.**

*(i) When the two inputs to the PFVA approach an ideal FA and VA, the relative joint stiffness of the actuator is entirely governed by the relative stiffness and the backdriving efficiency of the FA alone. When the backdriving efficiency of the FA approaches zero as the two inputs become very distinct, the PFVA stiffness approaches infinity (i.e. a very large stiffness which usually will lead to non-backdriveability).*

*(ii) The effective compliance of the PFVA increases when the compliance of the FA increases. The system essentially behaves as a system of series spring with different displacement influence coefficients to the output.*

This completes our analysis of mechanical stiffness in the PFVA as seen at its output. Now, we will look at the effects of the non-mechanical stiffness of the PFVA prime-movers.

**5.5.2. Discussion on Non-Mechanical Stiffness**

The PFVA contains two inputs connected through a differential of which one is kinematically approximately equivalent to a direct-drive source (FA). It has been argued in the literature that the electromagnetic damping and stiffness characteristics of the electric motor become dominant for a direct drive source (Rivin, 1980; Asada et al., 1983; Rivin, 1999). Rivin (1980) proposed a 2-DOF spring-mass oscillator model that combines the electromagnetic motor “dynamics” and the mechanical system connected to this drive.

The calculation of the mechanical parameters  $I_o$ ,  $B_o$ , and  $K_o$  is well-understood. Asada et al. (1983) showed that  $B_m = K_t^2 / R_m$  where  $K_t$  and  $R_m$  are the motor torque constant and winding resistance, respectively. Rivin (1980) determined  $K_m$  for induction



motors which can be extended to DC motors as well.  $I_m$  lumps the rotor inertia of the motor. Apart from the electromagnetic damping and stiffness between the rotor and the stator, the control approach and kinematic scaling also contribute to the motor “dynamics.” For instance, it was shown by Rivin (1999) that a velocity feedback controlled motor drive offers relatively higher damping. Another reference that discusses servo stiffness is (Younkin, 2003). A rigorous electro-mechanical modeling effort is necessary to completely characterize servo stiffness of an electrical drive.

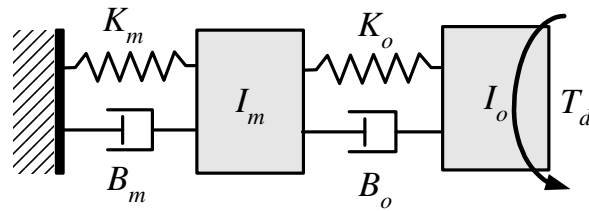


Figure 5.14. A 2-DOF motor drive model for a direct drive motor. The parameters shown are all lumped and referenced to the rotor shaft (Adapted from Rivin, 1980).

Permanent magnet Brushless DC (BLDC) motors are commonly used for robotic applications. The electromagnetic torque delivered at the output of a BLDC motor has a ripple effect. Two reasons for torque ripple in electro-mechanical prime-movers are (Aydin et al., 2006): (i) variation of air-gap permeance that results in a cogging torque, (ii) interaction between the magneto-motive force of the stator and the rotor. Torque ripple is quantitatively characterized by a criterion known as the *torque ripple factor*  $T_{RF}$  (Sun et al., 2002). This is defined as the ratio of the peak-to-peak ripple  $\Delta T_{pp}$  to the average torque  $T_{avg}$  expressed in percentage:

$$T_{RF} = \frac{\Delta T_{pp}}{T_{avg}} \times 100\% \quad (5.57)$$

The frequency of the ripple effect is a function of the geometry of the prime-mover and the angular velocity of the motor shaft (Aydin et al., 2006). Torque ripple is

sometimes available in the motor manufacturer's data sheet. The effect of torque ripple on the FA and VA sub-systems can be different. If used for direct-drive applications (the limit case for a FA), the effect of torque ripple might be more pronounced than if used for a non-direct drive application. This is because the inertia and friction in the gear train would filter out the ripple in the electromagnetic torque generated by the VA subsystem's prime-mover because a typical spring-mass-damper system has a second order low pass filter response. This concludes our discussion of the stiffness analysis in PFVAs. The utility of this study is in the design of these actuators for better response and backdriveability.

## 5.6. DESIGN CASE STUDY: PFVA PROTOTYPE

In this section we present a design case study based on our analysis of the force distributions in a PFVA in this chapter and our study of power flow in the previous chapter. A physical prototype of the PFVA was built and tested at UTRRG. The modeling framework and design guidelines presented in these chapters were useful in the initial stages of the design of this prototype.

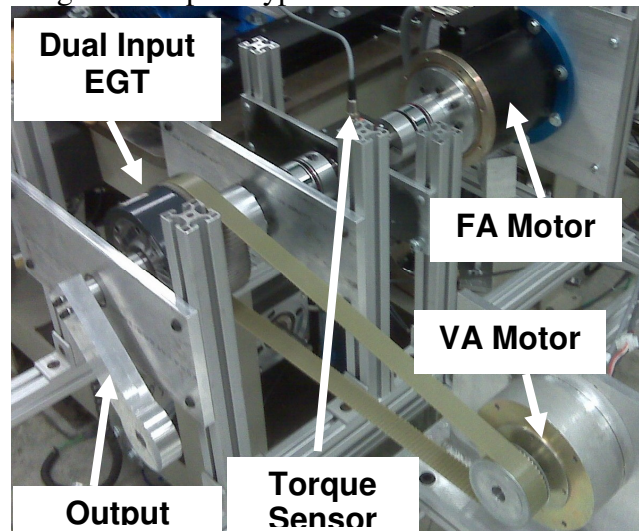


Figure 5.15. Laboratory prototype of the PFVA built at UTRRG, Austin, TX.

The principal design requirements for this testbed at the output were 150 N-m of peak torque and 40 rpm of peak speed. The objective was to maximize overall mechanical efficiency and maintain some dynamic coupling between the two inputs because we wanted to study the disturbances between the two inputs. Additionally, we desired the acceleration responsiveness of the FA to be relatively high to be able to quickly react to external disturbances in a contact task performed using indirect force control on the FA. Also, we were designing and sizing our components against some constraints:

- Due to the cost of a BLDC motor we were constrained to using an older motor in the laboratory as the VA input. This fixed most of the VA side parameters.
- Due to time and cost concerns we decided to buy a commercial-off-the-shelf dual input differential gear train. This restricted our choice of the RSF  $\tilde{\rho}$ .

According to Design Guideline 4, the acceleration responsiveness requirement for the FA drives the design toward  $\tilde{\rho} \rightarrow \infty$ . At the same time, requirements on the dynamic coupling and overall mechanical efficiency of the PFVA drive the design toward  $\tilde{\rho} \rightarrow 1$ , based on Eq. (5.28) and Design Guideline 4.2 in Chapter 4, respectively. Considering these suggested trends and the available gear ratios for the Andantex differential drives, we chose the SR-20 module which has a RSF  $\tilde{\rho} = 24.27$ . The main components used in this prototype are listed in Appendix E.

## 5.7. CHAPTER SUMMARY

The objective of this chapter was to extend the parametric design framework for PFVAs, presented in the previous chapter, with a focus on force distribution between the two inputs (FA and VA). Four issues were addressed: (i) overall actuator position uncertainty, (ii) static and inertia torque distribution between the FA and VA for a given

load, (iii) acceleration responsiveness of the two inputs of the actuator, and (iv) effective stiffness of the PFVA.

Table 5.3 Summary of PFVA design criteria based on parametric distribution analysis

Design Issue	Parameter Dependencies	Physical Dependencies	Criteria and Mathematical Model
Position Uncertainty. (Section 5.2)	Relative Accuracy Factor ( $\tilde{\alpha}_f^v$ ), RSF ( $\tilde{\rho}$ )	FA and VA prime-mover position inaccuracies FA- and VA-side lost motion and backlash	Relative Accuracy Factor ( $\tilde{\alpha}_f^j$ ), $\tilde{\alpha}_f^j = \sqrt{\left[ \frac{\tilde{\alpha}_f^v}{\tilde{\rho}+1} \right]^2 + \left[ \frac{\tilde{\rho}}{\tilde{\rho}+1} \right]^2}$
Static Torque Distribution. (Section 5.4.1)	Relative Efficiency Ratio ( $\tilde{\eta}$ ), RSF ( $\tilde{\rho}$ )	Meshing friction losses	Static Torque Distribution Ratio ( $\tilde{\tau}^s$ ), $\tilde{\tau}^s = \frac{\tilde{\rho}}{\tilde{\eta}}$
Inertial Torque Distribution (Section 5.4.2)	Output-to-VA Inertia Ratio ( $\tilde{I}_j^*$ ) Acceleration Mixing Ratio ( $\tilde{\phi}$ ) Prime-Mover Inertia Ratio ( $\tilde{I}_M$ ) RSF ( $\tilde{\rho}$ )	Inertia content in the output machine, the gear train, and the actuator components on FA- and VA-sides of the PFVA	Inertia Torque Distribution Ratio ( $\tilde{\tau}^l$ ) $\tilde{\tau}^l = \frac{\left( \tilde{I}_{vf} + \tilde{I}_j^* \frac{\tilde{\rho}}{(\tilde{\rho}+1)^2} \right) + \left( \tilde{I}_M + \tilde{I}_j^* \frac{\tilde{\rho}^2}{(\tilde{\rho}+1)^2} \right) \tilde{\phi}}{\left( 1 + \tilde{I}_j^* \frac{1}{(\tilde{\rho}+1)^2} \right) + \left( \tilde{I}_{vf} + \tilde{I}_j^* \frac{\tilde{\rho}}{(\tilde{\rho}+1)^2} \right) \tilde{\phi}}$ Dynamic Coupling Factor ( $\tilde{\mu}$ ), $\tilde{\mu} = \frac{\tilde{\rho}}{(\tilde{\rho}+1)^2}$
Acceleration Responsiveness (Section 5.4.3)	Relative Motor Torque Ratio ( $\tilde{\tau}_{Mr}$ ) Prime-Mover Inertia Ratio ( $\tilde{I}_M$ ), and Output-to-VA Inertia Ratio ( $\tilde{I}_j^*$ ), RSF ( $\tilde{\rho}$ )	Torque capacities of the FA and VA prime-movers Inertia content in the output machine, the gear train, and the actuator components on FA- and VA-sides of the PFVA Type of prime-movers (electro-mechanical, hydraulic, etc.) used for VA and FA and torque density of these prime-movers	Relative Acceleration Responsiveness ( $\tilde{\xi}$ ) $\tilde{\xi} = \frac{-\left[ \tilde{I}_{vf} + \tilde{I}_j^* \frac{\tilde{\rho}}{(\tilde{\rho}+1)^2} \right] + \left[ 1 + \tilde{I}_j^* \frac{1}{(\tilde{\rho}+1)^2} \right] \tilde{\tau}_{Mr}}{\left[ \tilde{I}_M + \tilde{I}_j^* \frac{\tilde{\rho}^2}{(\tilde{\rho}+1)^2} \right] - \left[ \tilde{I}_{vf} + \tilde{I}_j^* \frac{\tilde{\rho}}{(\tilde{\rho}+1)^2} \right] \tilde{\tau}_{Mr}}$
Effective Mechanical Stiffness (Section 5.5.1)	Relative Stiffness ( $\tilde{K}$ ), Relative Backdriving Efficiency ( $\tilde{\eta}_b$ ), RSF ( $\tilde{\rho}$ )	Meshing friction losses for reverse power-flow (output to input), <i>Mechanical</i> compliances of VA and FA actuator components, and that of the differential's gear meshes	Relative Joint Stiffness ( $\tilde{K}_j$ ), $\tilde{K}_j = \frac{1}{\eta_{j \rightarrow v}} \left( \frac{\tilde{K} (\tilde{\rho}+1)^2}{\tilde{K} + \tilde{\eta}_b \tilde{\rho}^2} \right)$

Table 5.4 Summary of Guidelines Suggested in this Chapter

Design Guidelines
<ul style="list-style-type: none"> <li>• In considering the influence of the input motor accuracies on the output (or ) joint accuracy, as the gear ratios in a PFVA approach their theoretical limit (<math>\tilde{\rho} \rightarrow \infty</math>), the output position accuracy will be entirely dictated by the accuracy of the FA actuator's prime-mover.</li> <li>• As the two inputs in a PFVA become more and more distinct, and approach their theoretical limits (<math>\tilde{\rho} \rightarrow \infty</math>), the entire static load requirement is only on the FA. Consequently, in this scenario, the two inputs are decoupled in terms of static torque demand.</li> <li>• As the two inputs in a PFVA become more and more distinct, and approach their theoretical limits (<math>\tilde{\rho} \rightarrow \infty</math>), the entire output inertial load requirement is only on the FA. Consequently, in this scenario, the two inputs are decoupled in terms of inertial torque demand.</li> <li>• As the two inputs in a PFVA become more and more distinct, and approach their theoretical limits (<math>\tilde{\rho} \rightarrow \infty</math>), the FA has much more acceleration capability than the VA.</li> <li>• When the two inputs to the PFVA approach an ideal FA and VA, the relative joint stiffness of the actuator is entirely governed by the relative stiffness and the backdriving efficiency of the FA alone. When the backdriving efficiency of the FA approaches zero as the two inputs become very distinct, the PFVA stiffness approaches infinity (i.e. a very large stiffness which usually will lead to non-backdriveability).</li> <li>• The effective compliance of the PFVA increases when the compliance of the FA increases. The system essentially behaves as a system of series spring with different displacement influence coefficients to the output.</li> </ul>

The design guidelines developed in this chapter are listed in Table 5.4. These guidelines lend physical insight to the design process:

- To optimize the position uncertainty at the output of a PFVA, the FA should be chosen such that its accuracy increases as RSF increases.
- To decouple the PFVA inputs in terms of the static and inertial torque demand, a relatively large RSF should be chosen.
- To optimize the acceleration capability of the FA relative to the VA, a large RSF should be chosen.
- When the RSF is increased, the overall stiffness of the PFVA is predominantly governed by the stiffness and backdriving efficiency of the FA.

The utility of the design guidelines was demonstrated through a design case study and PFVA prototype developed at the UTRRG laboratory. A dimensionless approach was followed to define the relevant design parameters of the PFVA so that our results are scalable. For example, the guidelines from this analysis can be identically applied to the design of a shoulder joint and a wrist joint in a serial robot manipulator which experience drastically different loading conditions.

## Chapter 6. Analysis and Simulation of Dynamic Response

In Chapter 4, we analyzed the power flow modes in a PFVA that might lead to inefficient designs or operating conditions. In Chapter 5, we studied the force balance between the two inputs in a PFVA with the intent of developing criteria for the design of PFVAs. In both those chapters the primary objective was PFVA design. Going one step further, in this chapter, we will analyze the dynamic response of the PFVA under various settings. This chapter is organized as follows. We will first examine the most elementary mode in which a PFVA can be operated – utilizing the kinematic redundancy in this dual input actuator to operate as a velocity source. Following this, we will simulate the dynamic response of the PFVA using two models: (i) a simplified model to study special modes of operation and (ii) a generalized model to show realistic modes of operation.

### 6.1. VELOCITY CONTROLLED VA AND FA

In this section our objective is to analyze the mode of operation of the PFVA wherein both the inputs are controlled as velocity sources. Most frequently differential systems are controlled in this (velocity-controlled) mode. Studies have been done before where such operation was considered: use of redundant actuators to control various scales of motion, also called Control-in-the-Small or CITS (Tesar, 1985); use of a multi-input actuator for backlash-free operation (Chang and Tsai, 1993); use of a fault-tolerant robotic joint for a space shuttle remote manipulator system (Wu et al., 1993); use of a dual drive to mitigate the effects of low-velocity friction in robotic actuators (Ontañón-Ruiz et al., 1998); use of a dual drive for fault-tolerance (Tesar, 2004). The kinematic redundancy in a dual-drive such as the one used in the PFVA can be utilized to maximize or minimize a primary criterion<sup>34</sup> and satisfy a secondary operational choice. In the

---

<sup>34</sup> Minimum velocity norm is a frequently used criterion for the inversion of under-constrained systems.

following sub-section, we will investigate this utilization of the PFVA drive's redundancy. The current work on redundancy resolution is motivated by previous work from the Robotics Research Group in this area (Hooper and Tesar, 1994; Kapoor et al., 1998), from Chang and Tsai (1993) in the area of backlash-free redundantly actuated drives, and from Ontañón-Ruiz et al. (1998) in the area of redundancy resolution for differential systems.

### 6.1.1. PFVA Operation Utilizing Kinematic Redundancy

The focus in this sub-section is to study the null-space of the parallel force/velocity actuator and determine its relation to the relative scale factor  $\tilde{\rho}$ . In Chapter 3 we described the kinematics of a PFVA drive and showed that the epicyclic gear train used in the PFVA is a kinematically redundant velocity summing mechanism. If the output of the PFVA is connected to joint  $j$  in a machine (such as a manipulator), then the joint velocity is a linear combination of the two input velocities:

$$\dot{\phi}_j = \frac{1}{\tilde{\rho}+1} \dot{\phi}_v + \frac{\tilde{\rho}}{\tilde{\rho}+1} \dot{\phi}_f \quad (6.1)$$

Furthermore, there is an infinite set of input velocity combinations that can be used to achieve a given velocity state at the joint. This extra choice can be used to appropriately manage the inputs to optimize a secondary criterion. Let us further explore this possibility. Re-writing Eq. (6.1) in the matrix form we have

$$\dot{\phi}_j = \mathbf{G} \begin{bmatrix} \dot{\phi}_v \\ \dot{\phi}_f \end{bmatrix} \quad (6.2)$$

where  $\mathbf{G} = \begin{bmatrix} 1 & \tilde{\rho} \\ \tilde{\rho}+1 & \tilde{\rho}+1 \end{bmatrix}$  is the Kinematic Influence Coefficient (KIC) matrix which, in this case, is a matrix of constant velocity ratios of the two inputs. Now, to invert Eq.



(6.1), using the pseudo-inverse<sup>35</sup>  $\mathbf{G}^\# = \mathbf{G}^T (\mathbf{G}\mathbf{G}^T)^{-1} \in R^{2 \times 1}$  and the null-space of  $\mathbf{G}$  we have

$$\begin{bmatrix} \dot{\phi}_v \\ \dot{\phi}_f \end{bmatrix} = \mathbf{G}^\# \dot{\phi}_j + \dot{\phi}_n \quad (6.3)$$

where  $\dot{\phi}_j$  is the specified joint velocity we are trying to satisfy and  $\dot{\phi}_n = \begin{bmatrix} \dot{\phi}_{vn} & \dot{\phi}_{fn} \end{bmatrix}^T$  is a vector belonging to the null-space<sup>36</sup> of the operator  $\mathbf{G}$ . It can be shown that

$$\mathbf{G}^\# = \begin{bmatrix} \left( \frac{\tilde{\rho} + 1}{\tilde{\rho}^2 + 1} \right) \\ \tilde{\rho} \left( \frac{\tilde{\rho} + 1}{\tilde{\rho}^2 + 1} \right) \end{bmatrix} \quad (6.4)$$

Also, by examining Eq. (6.1), we can show that the null-space vector  $\dot{\phi}_n = \begin{bmatrix} \dot{\phi}_{vn} & \dot{\phi}_{fn} \end{bmatrix}^T$  is such that

$$\frac{\dot{\phi}_{fn}}{\dot{\phi}_{vn}} = -\frac{1}{\tilde{\rho}} \quad (6.5)$$

It is interesting to note that the null-space can be specified purely as a function of the relative scale factor  $\tilde{\rho}$ . We can now graphically represent all the information in Eqs. (6.1)-(6.5) as shown in Figure 6.1.

We would like to make some observations about this figure. For a specified joint velocity  $\dot{\phi}_j$ , the velocity inverse solution in Eq. (6.3) consists of two terms:

- $\dot{\phi}_n$  which represents the projected null-space velocities shown at an angle  $\theta = \tan^{-1} \left( \frac{-1}{\tilde{\rho}} \right)$  from the  $\dot{\phi}_v$ -axis. This term results in a null joint velocity.

---

<sup>35</sup> For a detailed derivation of the pseudo-inverse, refer (Sciavicco and Siciliano, 1996, pp. 91-94). Also, the Robotics Research Group at the University of Texas has produced many research reports in the area of criteria-based redundancy resolution for manipulator systems.

<sup>36</sup> The null-space velocities of the VA and FA are those that result in a zero joint velocity.

Therefore, the null-space velocity vector  $\dot{\phi}_n$  can be used to maximize or minimize a secondary criterion.

- $\mathbf{G}^\# \dot{\phi}_j$  is the pseudo-inverse based solution which is transformed into the specified joint velocity. This solution space is orthogonal to the null-space as shown in Figure 6.1.

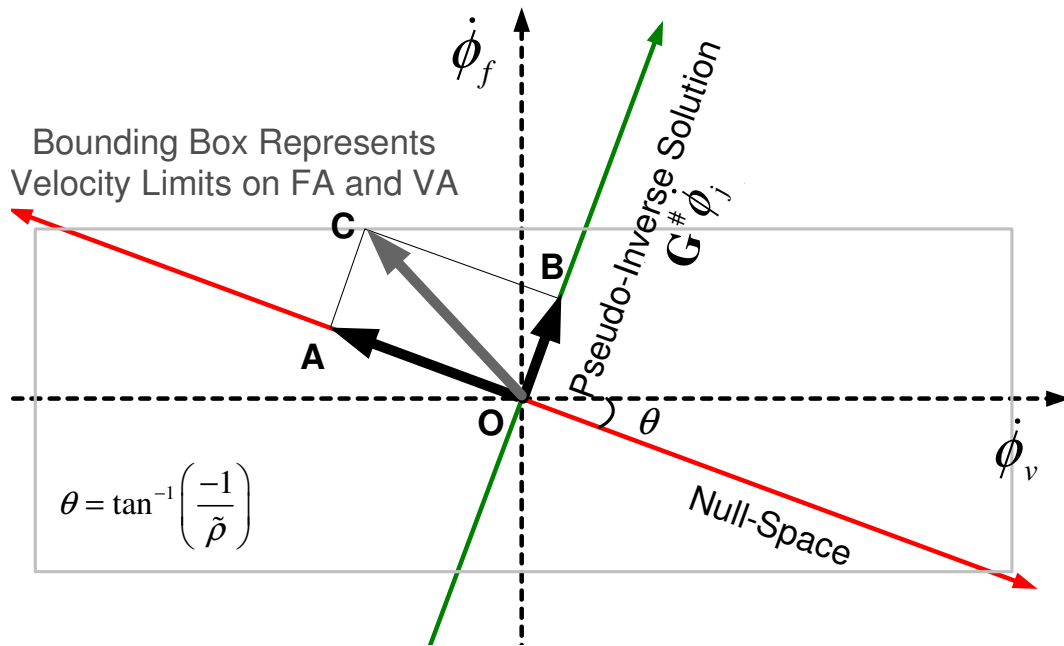


Figure 6.1. Graphical representation of the null-space of the Kinematics Influence Coefficient matrix,  $\mathbf{G}$ . The null-space velocities are velocities of the FA and VA for which the PFVA does not have any output motion.

The bounding box represents the velocities achievable by the prime-movers driving the FA and the VA, i.e. all achievable velocities  $\dot{\phi} = [\dot{\phi}_v \quad \dot{\phi}_f]^T$  lie within this bounding box. Now for a given output velocity, say  $\dot{\phi}_{jd}$ , the pseudo-inverse solution is  $\mathbf{G}^\# \dot{\phi}_{jd}$  shown as the vector  $\overline{\mathbf{OB}}$  in Figure 6.1. Given the limitation of bounded velocities at the FA and VA inputs, the choice of null-space velocities is now limited. Let us assume, for discussion purposes, that we would like to run the FA with a positive velocity and the VA

with a negative velocity throughout the operation of the PFVA. Therefore we are now restricted to the second quadrant of the  $\dot{\phi}_v - \dot{\phi}_f$  space. It is therefore evident from Figure 6.1 that, for this scenario, we cannot choose a null-space velocity vector greater than  $\overline{\mathbf{OA}}$  because  $\overline{\mathbf{OA}}$  (i.e. the resultant input velocities commanded to the motors) has to lie within the velocity bounding box.

Our motivation for the null-space analysis of the PFVA was to determine the choices available to us when the VA and FA tend towards an ideal velocity source and an ideal force generator, respectively, i.e. the dual-input actuator approaches an ideal PFVA. We have shown in Chapter 3 that this theoretical limit is approached as  $\tilde{\rho} \rightarrow \infty$ . Therefore, we will now examine the null-space velocities and the pseudo-inverse solution as this limit is approached:

$$\lim_{\tilde{\rho} \rightarrow \infty} \begin{bmatrix} \dot{\phi}_v \\ \dot{\phi}_f \end{bmatrix} = \left( \lim_{\tilde{\rho} \rightarrow \infty} \mathbf{G}^\# \right) \dot{\phi}_j + \lim_{\tilde{\rho} \rightarrow \infty} \dot{\phi}_n \quad (6.6)$$

Using Eqs. (6.3)-(6.5), it can be shown that

$$\lim_{\tilde{\rho} \rightarrow \infty} \begin{bmatrix} \dot{\phi}_v \\ \dot{\phi}_f \end{bmatrix} = \begin{bmatrix} 0 \\ 1 \end{bmatrix} \dot{\phi}_j + \begin{bmatrix} 1 \\ 0 \end{bmatrix} \quad (6.7)$$

This means that as the theoretical limit  $\tilde{\rho} \rightarrow \infty$  is approached, the PFVA becomes a direct drive actuator. This is because the VA does not contribute to the velocity at the output. From Eq. (5.12), we also know that as this limit is approached, the VA does not feel any of the static torque disturbances occurring at the output. In Figure 6.1, as  $\tilde{\rho} \rightarrow \infty$  the null-space approaches the  $\dot{\phi}_v$  axis and  $\dot{\phi}_f$  entirely influences the output velocity. We will now illustrate some of the concepts introduced in this section using a numerical example.

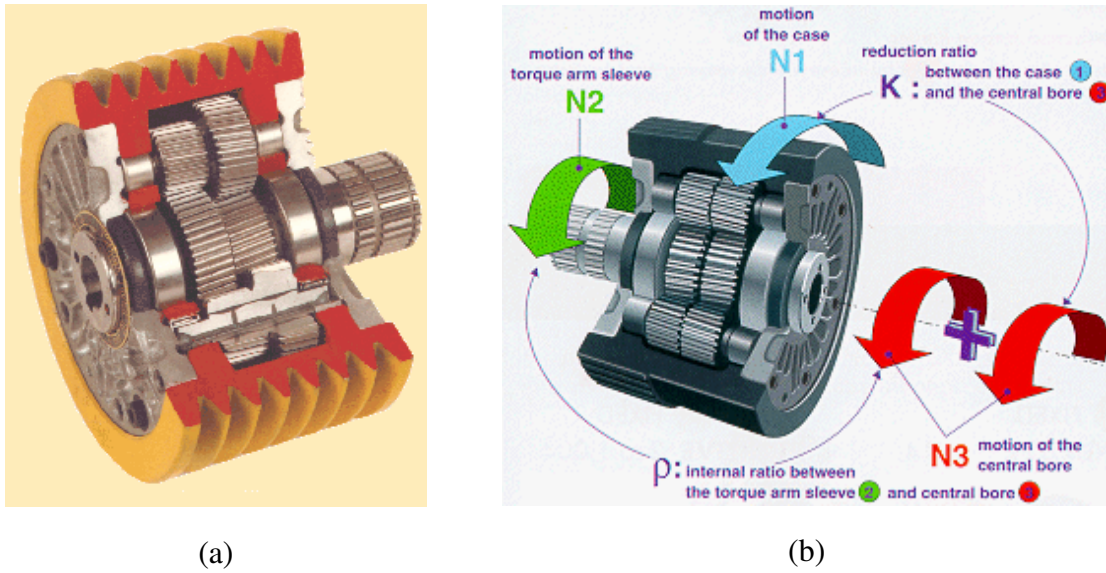


Figure 6.2. Drive train used in the UTRRG PFVA lab prototype (Andantex Inc., 2007). (a) Section view of the drive train layout, and (b) N1, or the casing, is the VA and is driven by a low-torque/high-speed motor, and N2 is the FA input and is driven by a high-torque/low-speed motor (Picture Courtesy: Andantex Inc., Wanamassa, NJ).

### ***Example 6.1: PFVA Operation Utilizing Null-Space Velocities***

In this example, we will consider the PFVA Design #3, the specifications for which are listed in Table 5.1. This design corresponds to the PFVA lab prototype at The University of Texas Robotics Research Group. In this design,  $\tilde{\rho} = 24.27$ ,  $(\dot{\phi}_v)_{\max} = 250\text{rpm}$ , and  $(\dot{\phi}_f)_{\max} = 400\text{rpm}$ . Figure 6.2 shows the drive train used in this design. In this design, N1 (or the motion of the casing) is the VA input (driven by a low torque motor via a stiff timing belt), N2 is the FA input, and N3 is a linear combination of these two inputs.

The objective, in this example, is to drive the inputs of the PFVA such that the joint follows a specified velocity trajectory subject to secondary constraints imposed on

the velocities of VA and FA. Let us say, for discussion purposes, that the desired joint velocity has to follow a sinusoidal trajectory<sup>37</sup> defined as

$$\dot{\phi}_{jd}(t) = \omega_{\max} \sin\left(2\pi \frac{t}{T}\right) \quad (6.8)$$

where  $\dot{\phi}_{jd}(t)$  is the time-varying desired joint velocity,  $\omega_{\max} = 10\text{rpm}$ , and the time period  $T = 5\text{s}$ . Now, the inverse velocity solution takes the form shown in Eq. (6.3):

$$\begin{bmatrix} \dot{\phi}_{vd} \\ \dot{\phi}_{fd} \end{bmatrix} = \mathbf{G}^{\#} \dot{\phi}_{jd} + \dot{\phi}_n \quad (6.9)$$

i.e., from Eq. (6.4)

$$\begin{bmatrix} \dot{\phi}_{vd} \\ \dot{\phi}_{fd} \end{bmatrix} = \begin{bmatrix} \left(\frac{\tilde{\rho}+1}{\tilde{\rho}^2+1}\right) \\ \tilde{\rho} \left(\frac{\tilde{\rho}+1}{\tilde{\rho}^2+1}\right) \end{bmatrix} \omega_{\max} \sin\left(2\pi \frac{t}{T}\right) + \dot{\phi}_n \quad (6.10)$$

As can be concluded from Eq. (6.10), the pseudo-inverse based solution is now fixed by the output (or joint) velocity specification; however we have a freedom of choice in the null-space represented by the second term in the above equation,  $\dot{\phi}_n$ . This can also be visualized in Figure 6.1. The magnitude and direction of  $\overline{\mathbf{OB}}$  are both fixed by the first term in Eq. (6.10). The direction of  $\overline{\mathbf{OA}}$  is fixed by the fact that the second term in Eq. (6.10) should lie in the null-space. The freedom we have is in the choice of the magnitude of  $\overline{\mathbf{OA}}$ . In other words, if  $\dot{\phi}_n = k\hat{\phi}_n$ , where  $\hat{\phi}_n$  is the unit vector representing the null-space and  $k$  is a scaling factor, then we can choose an appropriate  $k$  to satisfy secondary

---

<sup>37</sup> The phase of this sinusoid is an arbitrary choice because it does not affect our results in this section. It is assumed to be zero in Eq. (6.7).

constraints on the velocities  $\dot{\phi}_f$  and  $\dot{\phi}_v$ , respectively, of the FA and VA. For this example, these secondary constraints are defined as follows.

Two significant physical concerns in operating robotic actuators are backlash and stiction phenomena at low velocities. We will now define the secondary constraints based on two requirements: (i) to reduce backlash by avoiding the switching of velocity directions for the FA and VA and (ii) to maintain a minimum magnitude of input velocities even at very low joint velocities. Requirement (i) above mathematically means that the input velocity vector  $\dot{\phi} = [\dot{\phi}_v \quad \dot{\phi}_f]^T$  should lie in one of the four quadrants for all joint velocities  $\dot{\phi}_{jd}(t)$ , i.e.,

$$\left. \begin{array}{l} \dot{\phi}_v \geq 0 \\ \text{or} \\ \dot{\phi}_v \leq 0 \end{array} \right\} \text{ and } \left\{ \begin{array}{l} \dot{\phi}_f \geq 0 \\ \text{or} \\ \dot{\phi}_f \leq 0 \end{array} \right. \quad (6.11)$$

Requirement (ii) can very simplistically be expressed mathematically as

$$\|\dot{\phi}\| \geq \omega_{\min} \quad (6.12)$$

In addition, the input velocities should not violate the maximum achievable velocities and accelerations, i.e.,

$$\left[ \left| \dot{\phi}_v \right| \quad \left| \dot{\phi}_f \right| \right]^T \leq \left[ \left| \dot{\phi}_v \right|_{\max} \quad \left| \dot{\phi}_f \right|_{\max} \right]^T \quad (6.13)$$

$$\left[ \left| \ddot{\phi}_v \right| \quad \left| \ddot{\phi}_f \right| \right]^T \leq \left[ \left| \ddot{\phi}_v \right|_{\max} \quad \left| \ddot{\phi}_f \right|_{\max} \right]^T \quad (6.14)$$

Table 6.1 Non-Linear Programming (NLP) Problem Statement

Mathematical Model	Graphical Meaning (Refer Figure 6.3)	Physical Meaning
<b>OBJECTIVE FUNCTION</b>		
$\max \ \dot{\phi}_n\  =  k $	Maximize the length of vector $\overline{\text{OA}}$ .	The objective is to maximize the magnitude of the null-space velocity to stay away from low-velocity friction in the PFVA drive. Note that maximizing the null-space velocities will in turn maximize the velocities of the VA and FA.
<b>CONSTRAINTS</b>		
1	$\dot{\phi}_v \geq 0$	Point C lies in the fourth quadrant of the $\dot{\phi}_v - \dot{\phi}_f$ plane.
2	$\dot{\phi}_f \leq 0$	
3	$\ \dot{\phi}\  \geq \omega_{\min}$	Point C should lie <i>outside</i> the hashed circle. This circle has a radius equal to $\omega_{\min} = 12.5$ rpm in our example.
4	$\begin{bmatrix}  \dot{\phi}_v  &  \dot{\phi}_f  \end{bmatrix}^T \leq \begin{bmatrix}  \dot{\phi}_v _{\max} &  \dot{\phi}_f _{\max} \end{bmatrix}^T$	Point C should lie within the bounding box that represents the velocity limits of the FA and the VA. For this example, $(\dot{\phi}_v)_{\max} = 250$ rpm and $(\dot{\phi}_f)_{\max} = 400$ rpm.
5	$\begin{bmatrix}  \ddot{\phi}_v  &  \ddot{\phi}_f  \end{bmatrix}^T \leq \begin{bmatrix}  \ddot{\phi}_v _{\max} &  \ddot{\phi}_f _{\max} \end{bmatrix}^T$	$\frac{d\overline{\text{OC}}}{dt}$ is limited by the acceleration limits of the drives. For this example, $(\ddot{\phi}_v)_{\max} = (\ddot{\phi}_f)_{\max} = 10$ rads <sup>-2</sup> .

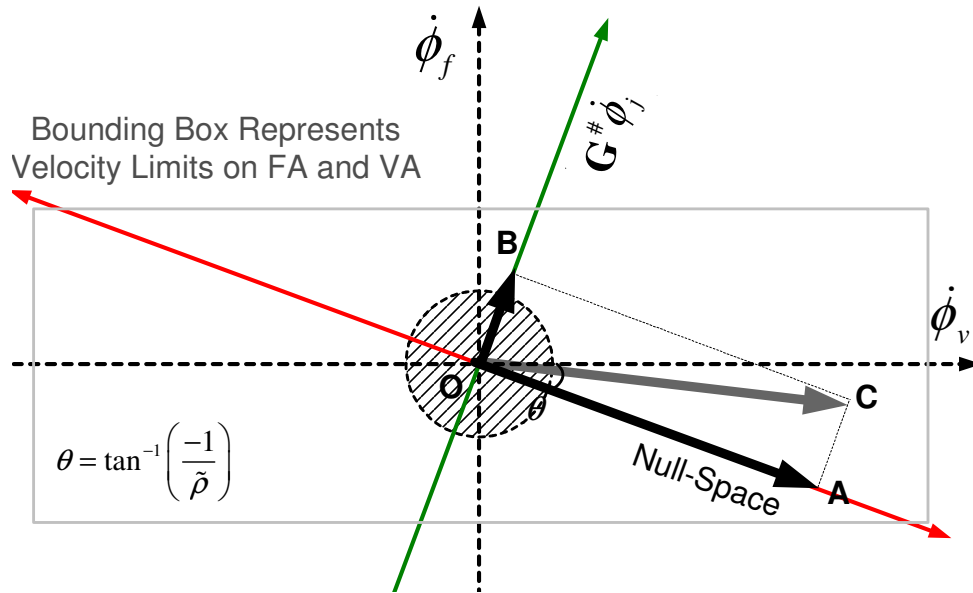


Figure 6.3. Definition of variables in the non-linear programming problem shown graphically (see Table 6.1). This figure is similar to Figure 6.1 and is repeated here for the convenience of the reader.

Our objective is to now determine the maximal null-space scaling  $k$  that will satisfy the constraints defined in Eqs. (6.11)-(6.14). This can be posed as a Non-Linear Programming (NLP) problem. We will not cover the methodology to solve this NLP problem because it is not our focus here. Also, commercial tools are available to determine feasible solutions for appropriately posed NLP problems. In our solution we used the `fmincon()` function in MATLAB<sup>®</sup> with a medium-scale optimization setting (MATLAB<sup>®</sup> Help<sup>38</sup>). The results are shown in Figure 6.5-Figure 6.7. In Figure 6.5 are shown the components of the VA velocities. As specified, the commanded solution is

<sup>38</sup> See <http://www.mathworks.com/access/helpdesk/help/helpdesk.html>



always positive. Notice that the pseudo-inverse solution is a scaled form of the desired joint velocity trajectory.

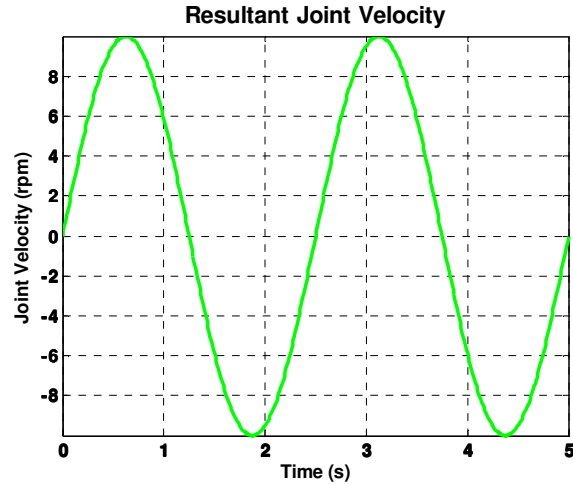


Figure 6.4. The resultant joint velocity trajectory (sinusoid) when the total solutions of the VA and FA from Figure 6.5 and Figure 6.6 are commanded.

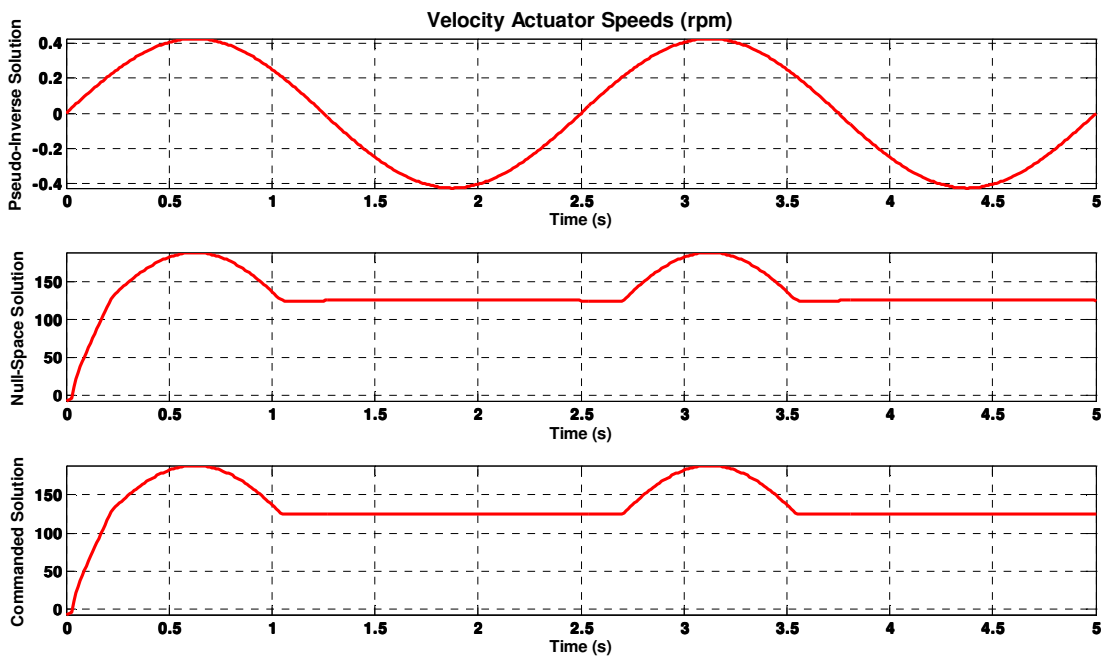


Figure 6.5. The solutions for different components of the VA's speeds. Note that the commanded solution is always positive.

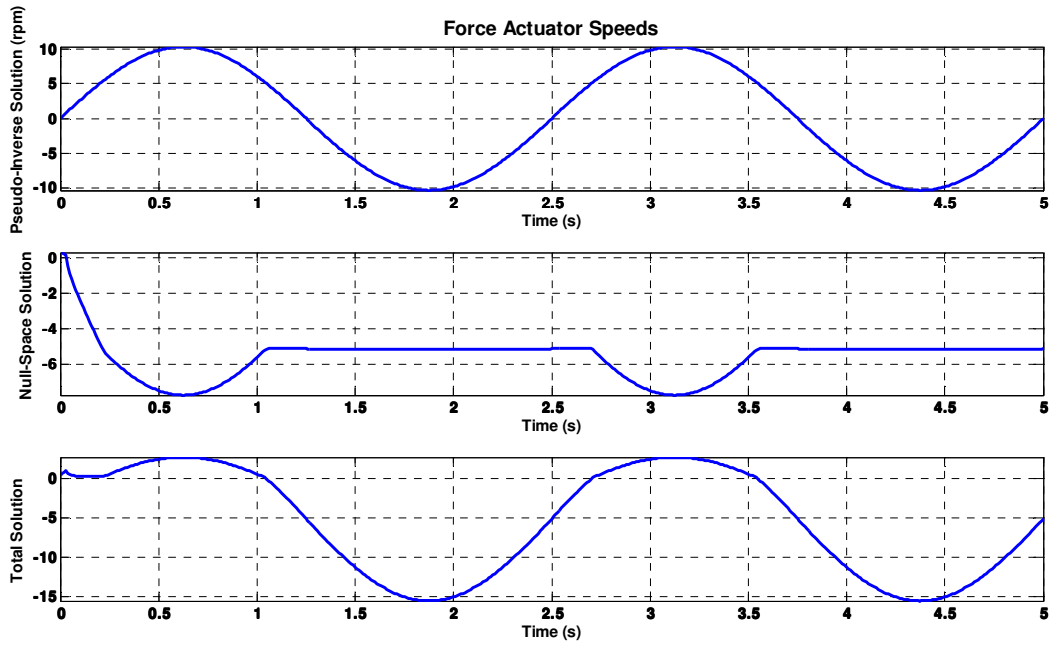


Figure 6.6. The solutions for different components of the FA's speeds. Note that the commanded solution is mostly negative. There are two regions (0.25-1s and 2.75-3.5s) where the total solution is positive.

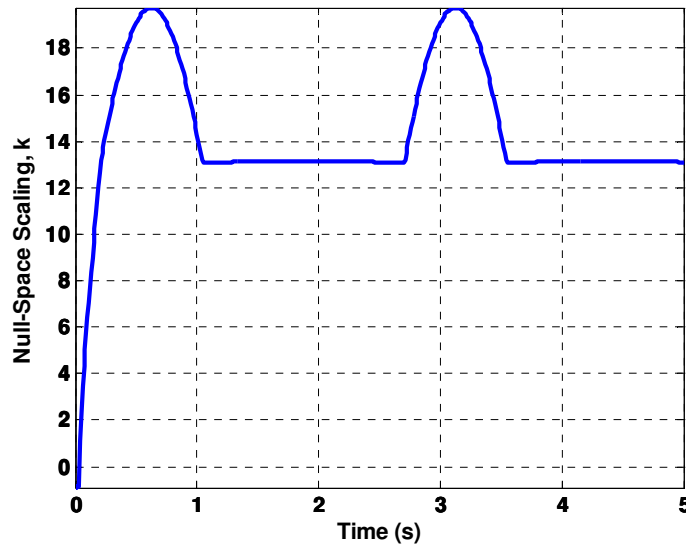


Figure 6.7. The time history of the null-space scaling factor. Notice that after  $k$  reaches above 12.5, it is never allowed to go below this value because of constraint 3 in the NLP problem (see Table 6.1). The value of  $k$  takes a finite time to achieve this minimum value due to the limits on achievable accelerations.

For the force actuator solution (see Figure 6.6), the NLP solver does not determine a feasible solution in the time periods 0-1.1s and 2.6-3.6s. In Figure 6.6, the commanded FA velocity is positive during these time periods. The accelerations of the FA and VA are within the specified limit of  $10 \text{ rad/s}^2$ . The joint velocity resulting from the commanded input velocities shown in Figure 6.5-Figure 6.6 is plotted in Figure 6.4. Notice that the joint velocity is unaffected by the variations in the null-space velocities. In the time-period of the simulation, the values of the null-space scaling factor  $k$  determined by the NLP solver is shown in Figure 6.7. Notice that the solver does not allow the scaling factor to dip below 12.5 after it has accelerated above this value. This is because the minimum velocity magnitude is  $\omega_{\min} = 12.5 \text{ rpm}$ .

In this section we have shown how to utilize the kinematic redundancy of the PFVA drive to optimize a secondary criterion. The secondary criterion is used to determine appropriate null-space velocities which do not directly contribute to output motion. Note that kinematic redundancy resolution can be done only when the PFVA is operated in the most elementary mode of a velocity summing actuator, i.e. the VA and FA are both controlled in velocity mode and the output (or joint) velocity is a linear combination of these commanded input velocities. To this point, we have not factored in the dynamics of the PFVA drive into our analysis. The following sections develop models to analyze the response of a PFVA by considering the dynamics of the system.

## 6.2. EQUATIONS OF MOTION FOR A PFVA

In this section we will develop a generalized model for a PFVA and identify the different dynamic parameters together with their physical sources. A schematic of the PFVA driving an output link is shown in Figure 6.8. The generalized dynamic model of the PFVA can be represented as

$$\mathbf{I}\ddot{\phi} + \mathbf{B}\dot{\phi} + \boldsymbol{\tau}_{st} + \mathbf{G}^T \boldsymbol{\tau}_o = \boldsymbol{\tau}_M \quad (6.15)$$

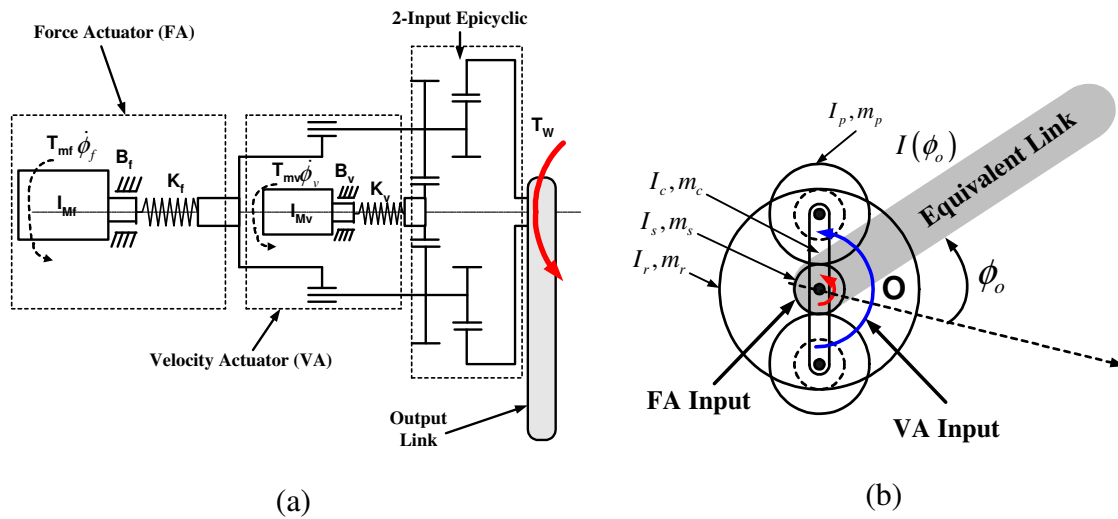


Figure 6.8. Schematic of a PFVA driving a single-axis manipulator subject to a work-function  $T_w$ .

The parameters in Eq. (6.15) and their physical sources are tabulated in Table 6.2. Note that the stiffness in the system is not considered in this model in order to first establish a simplified model for mixed control of the VA and FA. Moreover, the gear train of the PFVA is reasonably stiff. However, the servo stiffness of the FA (introduced in Section 5.5.2) might become dominant due to the electromechanical dynamics in this almost direct-drive branch (Rivin, 1980; Asada et al., 1983; Asada and Youcef-Toumi, 1987; Rivin, 1999; Younkin, 2003). The natural frequency of the FA's dynamics was

experimentally determined and will be presented in Section 7.2.4. The analysis and experimental characterization of stiffness in the PFVA is a topic that should be seriously considered in future work.

Table 6.2 Summary of Dynamic Parameters of the PFVA

Mathematical Symbol/Model	Parameter Description	Physical Source(s) and/or Remarks
$\mathbf{I} \in R^{2 \times 2}$	Matrix representing the consolidated inertia of the entire system reflected to the input prime-movers	There are three sources of inertia in the single-axis PFVA shown in Figure 6.8: (i) Output link inertia, (ii) Gear-train inertia, and (iii) Prime-mover inertia which includes inertias of all the components on each prime-mover side. The determination of the terms in this inertia matrix is shown in Appendix C.
$\ddot{\boldsymbol{\phi}} = \begin{bmatrix} \ddot{\phi}_v & \ddot{\phi}_f \end{bmatrix}^T$	Vector of prime-mover accelerations	These are limited by the acceleration capability (or limits) of each prime-mover.
$\mathbf{B} \in R^{2 \times 2}$	Matrix representing the consolidated damping in the entire system reflected to the input prime-movers	The primary source of viscous damping in this actuator is the fluid friction inside the gear train. For example, the gear train (Andantex SR-20 unit) used in the UT Robotics Research Group laboratory prototype of the PFVA is oil lubricated.
$\dot{\boldsymbol{\phi}} = \begin{bmatrix} \dot{\phi}_v & \dot{\phi}_f \end{bmatrix}^T$	Vector of prime-mover velocities	These are limited by the velocity capability (or limits) of each prime-mover.
$\boldsymbol{\tau}_{st} \in R^2$	Vector of stiction torques on the input side	There could be several stiction sources in the single-axis PFVA system: (i) the motor stiction, (ii) gear train stiction, (iii) coupler stiction, and (iv) other stiction sources such as structural stresses due to imperfect assembly.
$\mathbf{G} \in R^{1 \times 2}$	Matrix of velocity ratios of the VA and FA	Note that $\mathbf{G} = \begin{bmatrix} g_v & g_f \end{bmatrix}$ where $g_v$ and $g_f$ are the velocity ratios of the VA and FA, respectively.
$\tau_o$	Static torque acting on the output link	Sources of static torque might be (i) external forces/torques acting on the output link and (ii) presence of a force-field, such as gravity.
$\boldsymbol{\tau}_M \in R^2$	Vector of control torques exerted by the prime-movers	These are the controls available in the system.

### 6.2.1. Note on Determining the Consolidated Damping Matrix

In Appendix C we show how to calculate the different terms in the consolidated inertia matrix reflected to the prime-mover side ( $\mathbf{I}$ ). Similarly, here we show how to determine the consolidated damping matrix at the prime-mover side. This derivation has been adapted from Benedict and Tesar (1978). In this discussion, we assume that viscous

damping is primarily concentrated in the gear train because it uses oil for lubrication. Consider a component  $k$  in the gear train (say, a planet) with a velocity  $\dot{\phi}_k$  and an associated viscous damping coefficient  $b_k$ . Also, consider the velocity ratio from each input (VA and FA) to this component to be  $g_v^k = \frac{\dot{\phi}_k}{\dot{\phi}_v}$  and  $g_f^k = \frac{\dot{\phi}_k}{\dot{\phi}_f}$ . In other words,  $g_v^k$  and  $g_f^k$  are the kinematic influence coefficients relating the velocities of component  $k$  in the gear train and inputs VA and FA, respectively. If the viscous damping force acting on component  $k$ ,  $\tau_k^d$ , is

$$\tau_k^d = b_k \dot{\phi}_k \quad (6.16)$$

This damping force can be reflected to the input side as

$$\tau^d = \begin{bmatrix} g_v^k \\ g_f^k \end{bmatrix} b_k \dot{\phi}_k \quad (6.17)$$

where  $\tau^d$  is the damping torque vector at the input side. Eq. (6.17) can be re-written as follows.

$$\mathbf{B}_k \dot{\phi} = \begin{bmatrix} g_v^k \\ g_f^k \end{bmatrix} b_k \dot{\phi}_k \quad (6.18)$$

The PFVA being a velocity-summing mechanism (as discussed in Chapter 3), Eq. (6.18) can now be expressed in the form

$$\mathbf{B}_k \dot{\phi} = \begin{bmatrix} g_v^k \\ g_f^k \end{bmatrix} b_k \begin{bmatrix} g_v^k & g_f^k \end{bmatrix} \dot{\phi} \quad (6.19)$$

or,

$$\left\{ \mathbf{B}_k - \begin{bmatrix} g_v^k \\ g_f^k \end{bmatrix} b_k \begin{bmatrix} g_v^k & g_f^k \end{bmatrix} \right\} \dot{\phi} = \mathbf{0} \quad (6.20)$$

Considering the non-trivial solution ( $\dot{\phi} \neq \mathbf{0}$ ), we have

$$\mathbf{B}_k = b_k \begin{bmatrix} (g_v^k)^2 & g_v^k g_f^k \\ g_v^k g_f^k & (g_f^k)^2 \end{bmatrix} \quad (6.21)$$

Note that the reflected damping coefficient matrix has the same form as the reflected inertia matrix derived in Appendix C. Now considering all the  $D$  dampers, i.e.  $k \in \{1, 2, \dots, D\}$ , in the system:

$$\mathbf{B} = \sum_{k=1}^{k=D} \mathbf{B}_k \quad (6.22)$$

### 6.3. PRELIMINARY MODEL TO STUDY SIMPLE MODES OF OPERATION

In this section we will consider a simplified model of the PFVA-based single link robot shown in Figure 6.8. It is assumed in this section that there is no friction (viscous damping or stiction) in the system. This assumption is made to study the response of the PFVA to inertial and static loads. The system model after making this assumption can be represented as

$$\mathbf{I}\ddot{\boldsymbol{\phi}} + \mathbf{G}^T \boldsymbol{\tau}_o = \boldsymbol{\tau}_M \quad (6.23)$$

We can re-write the components in the input-space for the FA and VA separately as

$$\begin{aligned} I_{vv} \ddot{\phi}_v + I_{vf} \ddot{\phi}_f + \frac{1}{\tilde{\rho} + 1} \tau_o &= \tau_{Mv} \\ I_{vf} \ddot{\phi}_v + I_{ff} \ddot{\phi}_f + \frac{\tilde{\rho}}{\tilde{\rho} + 1} \tau_o &= \tau_{Mf} \end{aligned} \quad (6.24)$$

where  $I_{vv}$ ,  $I_{vf}$ , and  $I_{ff}$  are the total inertia seen by the VA, the total coupled inertia, and the total inertia seen by the FA, respectively. It is clear from Eqs. (6.23)-(6.24) that the two sub-systems of the PFVA are inertially coupled<sup>39</sup> due to the  $I_{vf}$  term. In other words,

---

<sup>39</sup> In the general case, the two sub-systems are also coupled in terms of frictional torques as evidenced in Eq. (6.15).

when one sub-system (FA or VA) accelerates, it disturbs the other sub-system. In an  $n$ -DOF manipulator system that uses a 2-input PFVA at every joint, the system is similarly described by  $2n$  coupled equations of motion.

***Example 6.2: Open-Loop Response of the FA and VA to Trapezoidal Velocity***

We will now simulate the open-loop response (no feedback) for a trapezoidal acceleration-run-deceleration input on the velocity sub-system (VA). Our goal is to study the response of the output and the FA in this case. The inertial and motion parameters of the PFVA used for this example are listed in Table 6.3. The velocity limits are provided in the motor catalogues. The acceleration limits were determined by evaluating the ratio between the continuous torque of each drive and the inertia content seen by it. In this example, the system is operated in a zero-gravity environment. In addition, there are no external or dissipative (friction) forces.

Table 6.3 Summary of Inertial Parameters of the PFVA for Example 6.2

System Parameter	Value	Units
Inertia Seen by VA, $I_{vv}$	$3.83 \times 10^{-2}$	Kg-m <sup>2</sup>
Inertia Seen by FA, $I_{ff}$	$3.83 \times 10^{-2}$	Kg-m <sup>2</sup>
Coupling Inertia between FA and VA, $I_{vf}$	1.1585	Kg-m <sup>2</sup>
Output Link Inertia	1.25 (mass of 5 Kg and radius of gyration of 0.5m)	Kg-m <sup>2</sup>
Relative Scale Factor, $\tilde{\rho}$	24.27	-
VA Velocity Limit	29.42	rad/s
FA Velocity Limit	83.77	rad/s
VA Acceleration Limit	70.2	rad/s <sup>2</sup>
FA Acceleration Limit	1626.1	rad/s <sup>2</sup>



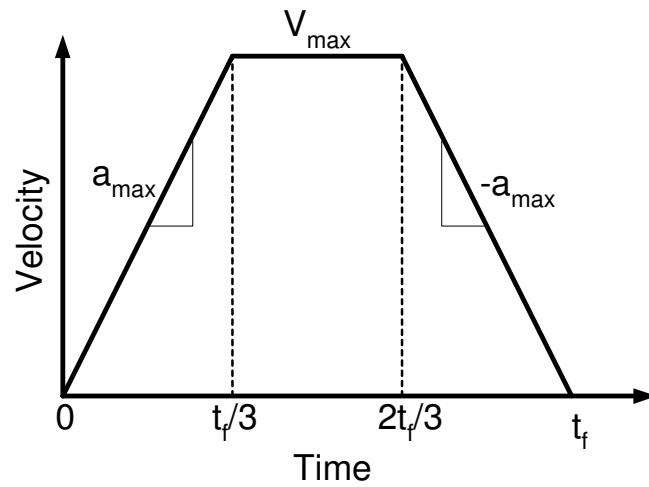


Figure 6.9. Definition of an acceleration-run-acceleration trapezoidal velocity profile. Note that the time intervals for each phase (constant acceleration and constant velocity) are equally spaced. The symbol  $t_f$  represents the total time of travel. The symbols  $V_{max}$  and  $a_{max}$  represent the acceleration and velocity limits of the drive, respectively.

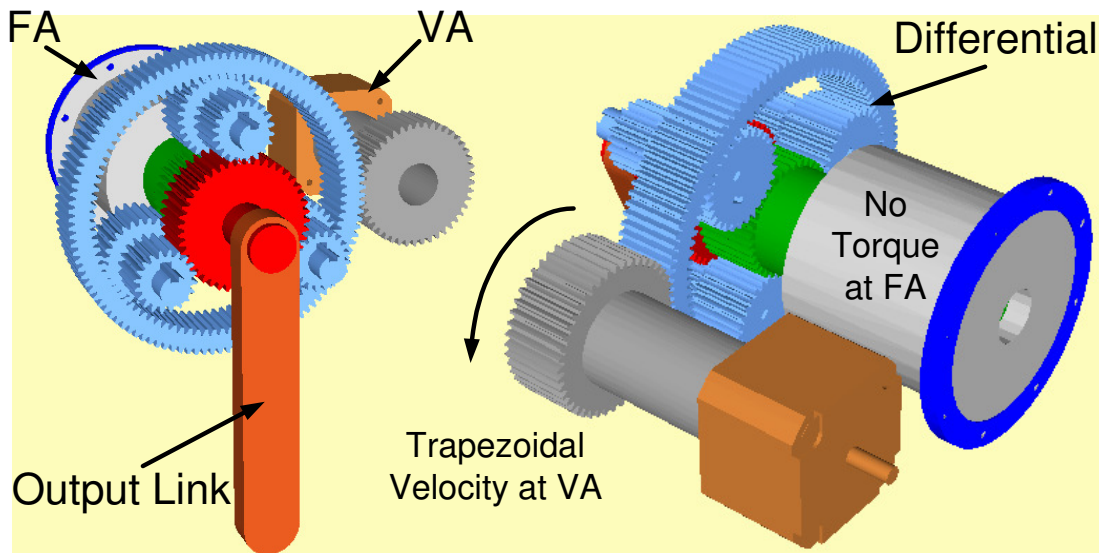


Figure 6.10. Simulation set-up for open-loop trapezoidal velocity response simulation.

The definition of the acceleration-run-deceleration trapezoidal motion program used for this simulation is shown in Figure 6.9. An example of a PFVA and the conditions imposed on it in this simulation are also shown in Figure 6.10. This simulation assumes that an acceleration-run-deceleration velocity profile is commanded at the VA based on its maximum acceleration and velocity. Concurrently, there is no torque acting on the FA motor. In other words, the PFVA operates in a power-flow mode represented by the graph in Table 4.1 (a) which is reproduced in Figure 6.11. In solving the forward dynamics (i.e. integrating the equations of motion), the limits on velocity and acceleration are imposed. To understand the results, we re-write the equation of motion of the PFVA system, considering the conditions in this simulation:

$$\begin{aligned} I_{vv}\ddot{\phi}_v + I_{vf}\ddot{\phi}_f &= \tau_{Mv} \\ I_{vf}\ddot{\phi}_v + I_{ff}\ddot{\phi}_f &= 0 \end{aligned} \quad (6.25)$$

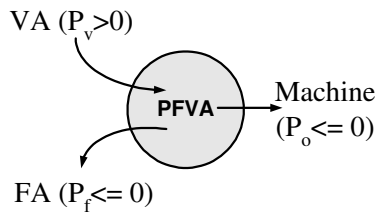


Figure 6.11. Power-flow mode corresponding to the operating conditions used in Example 6.2. The VA is actively controlled to maintain a trapezoidal velocity based on its maximum acceleration and velocity, and the FA is controlled to maintain a zero torque.

The actual velocity and acceleration of the VA, FA, and the output link of the PFVA are shown in Figure 6.12 (velocities) and Figure 6.13 (accelerations).

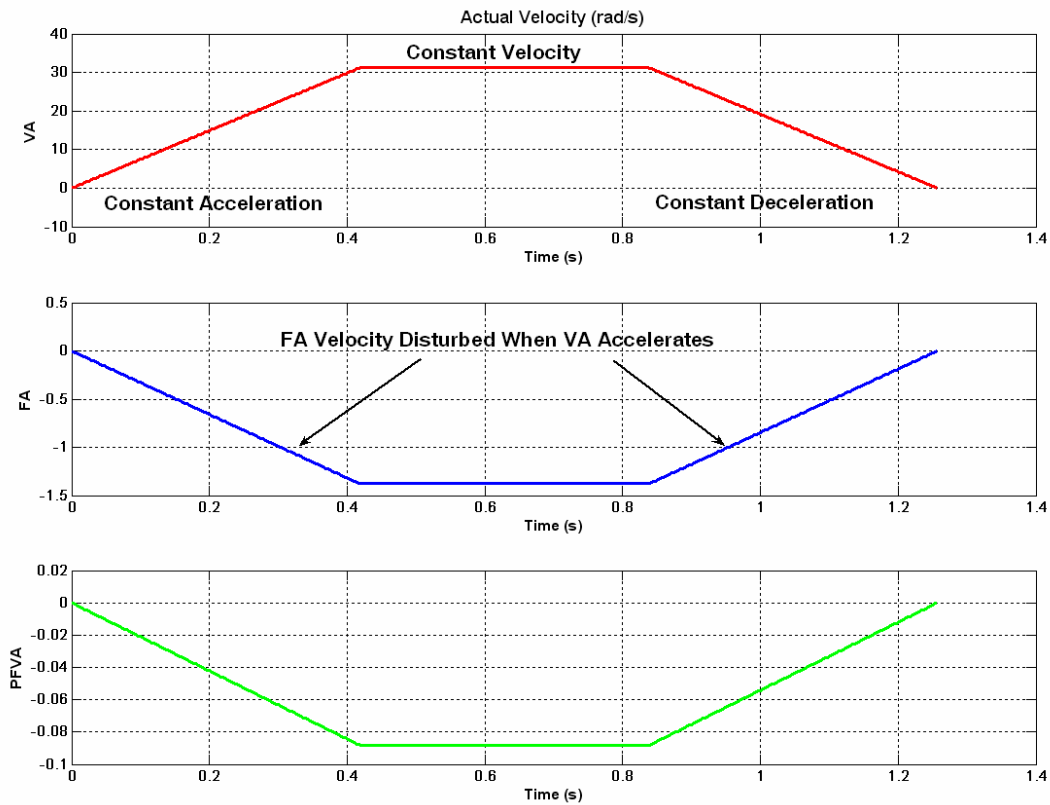


Figure 6.12. Velocity response of the FA, VA, and the PFVA (output link) when the VA is commanded to follow a trapezoidal motion profile in velocity and the FA is commanded to maintain zero torque. The FA is disturbed by the VA due to the cross-coupling inertia term  $I_{vf}$ . There is no external load acting on the system.

In the velocity responses shown in Figure 6.12, the VA follows the commanded trapezoidal trajectory; the FA is disturbed due to the cross-coupled inertia term  $I_{vf}$  during the accelerated phases; the output motion is a linear combination of the VA and FA motion trajectories based on their velocity ratios to the output,  $g_v$  and  $g_f$ , respectively. In the constant velocity phase, the FA velocity is not disturbed as evidenced in Figure 6.13.

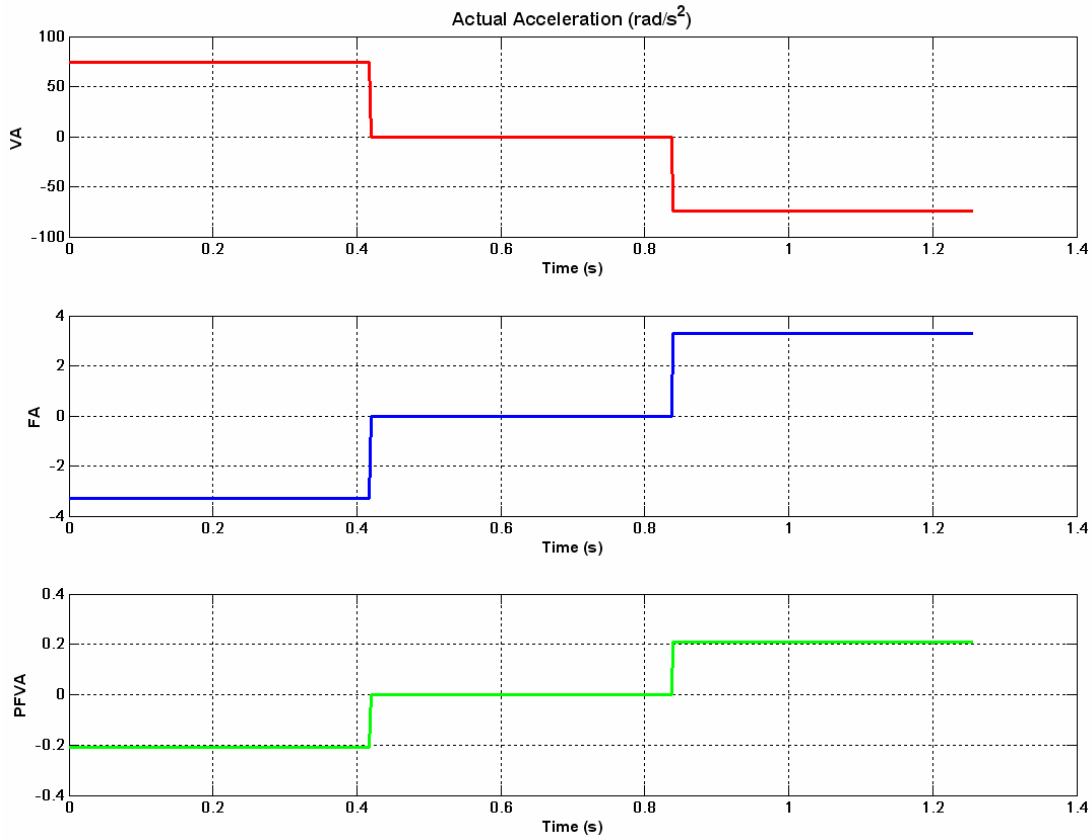


Figure 6.13. Acceleration response of the FA, VA, and the PFVA (output link) when the VA is commanded to follow a trapezoidal motion profile in velocity and the FA is commanded to maintain zero torque. The FA is disturbed (or back-driven) by the VA due to the cross-coupling inertia term  $I_{vf}$ . There is no external load acting on the system.

***Example 6.3: Open-Loop Response to Trapezoidal Velocity with Programmed Load***

In this example we will also consider a programmed load acting at the output of the system. The conditions of simulation in this example are similar to the previous example:

- The velocity actuator is velocity-controlled to execute a trapezoidal motion profile.
- The force actuator is torque-controlled to generate zero torque.

- The output is connected to a load motor that is programmed to hold position. This is equivalent to rigidly holding the output link in place.

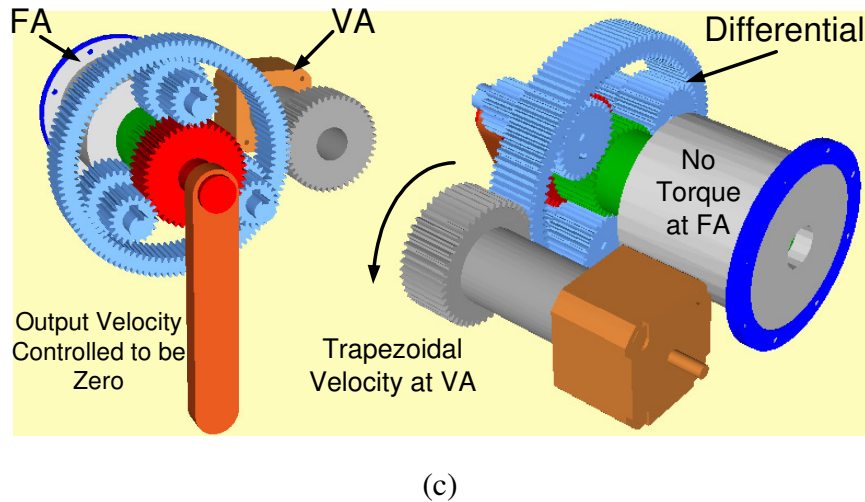
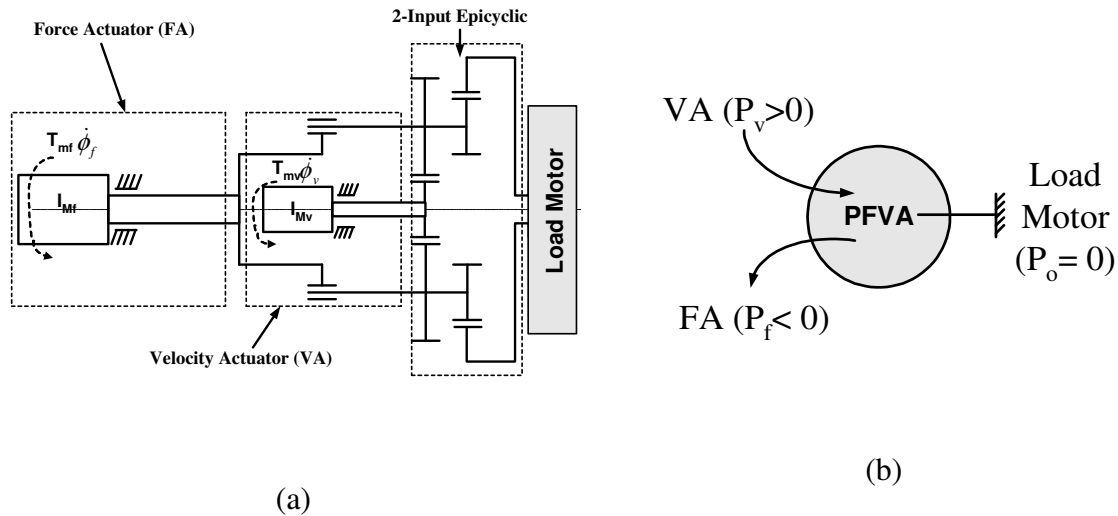


Figure 6.14. Simulation set up for Example 6.3. The output is connected to a load motor which is controlled at zero velocity. This is equivalent to rigidly holding the output link stationary. The conditions of the previous simulation apply to this example as well: (i) VA velocity is trapezoidal and (ii) FA is controlled to generate zero torque. (a) Schematic of the actuator with a load motor, (b) Power flow graph corresponding to imposed conditions, and (c) Simulation conditions shown on a 3D model.

Note that the additional condition imposed in this example is the external programmed load applied by a load-motor as shown in Figure 6.14. Considering the conditions in this simulation, the equations of motion of the PFVA system take the form

$$\begin{aligned} I_{vv}\ddot{\phi}_v + I_{vf}\ddot{\phi}_f + \frac{1}{\tilde{\rho}+1}\tau_H &= \tau_{Mv} \\ I_{vf}\ddot{\phi}_v + I_{ff}\ddot{\phi}_f + \frac{\tilde{\rho}}{\tilde{\rho}+1}\tau_H &= 0 \end{aligned} \quad (6.26)$$

where  $\tau_H$  is the holding torque of the load motor (controlled to maintain position) and  $\tau_{Mv}$  is the torque required for the VA to follow a trapezoidal trajectory.

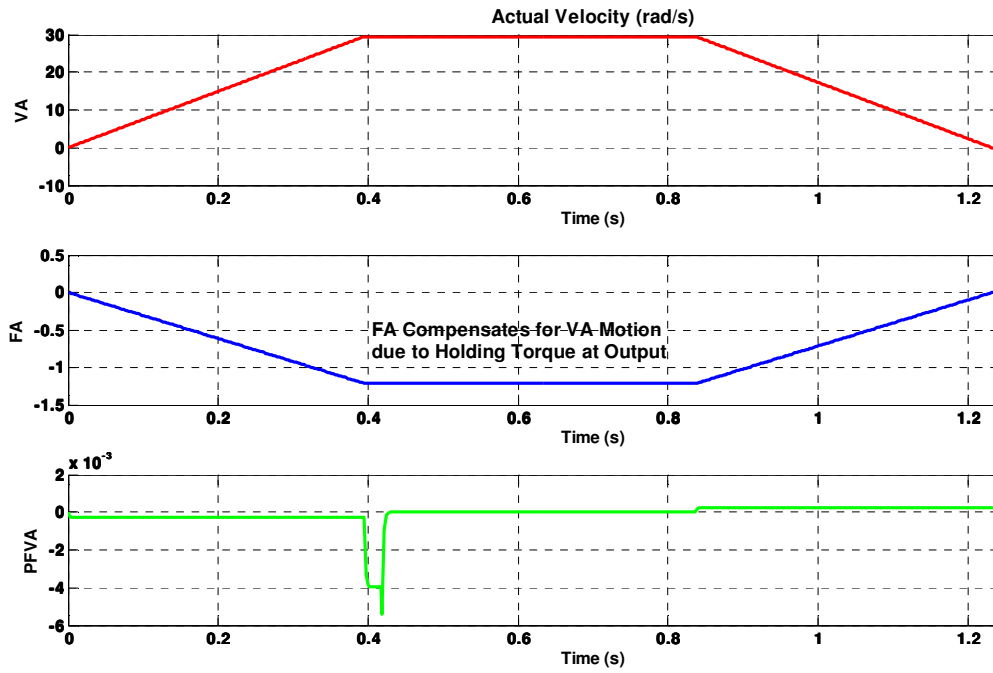


Figure 6.15. Velocity response of the FA, VA, and the PFVA (output link) when the VA is commanded to follow a trapezoidal motion profile in velocity, the FA is commanded to maintain zero torque, and the output is connected to a load motor that holds position. The FA is disturbed by the VA due to the cross-coupling inertia term  $I_{vf}$ . The velocities of FA and VA are such that  $\tilde{\lambda} \approx -\tilde{\rho}$ .

The velocity response of the FA, VA, and the output in this simulation are shown in Figure 6.15. As expected, the velocity of the PFVA output is approximately equal to zero

because the load motor is being controlled to hold position. Due to the holding torque at the output, the FA moves to compensate for the zero velocity of the output (notice that the scale of PFVA is  $10^{-3}$  rad/s although there is a sharp change at approximately 0.4s). In other words, the ratio of the VA speed to the FA speed at any instant is approximately equal to the relative scale factor  $\tilde{\rho}$ .

***Example 6.4: Velocity Controlled VA and Torque Limited FA for Collision Detection***

In this example we will use the simplified PFVA model from Eq. (6.23) to simulate a scenario where the VA is being controlled in position mode and the FA is used as a torque limiter to detect a collision of the output link with an obstacle. Re-writing the model presented in Eq. (6.24),

$$\begin{aligned} I_{vv}\ddot{\phi}_v + I_{vf}\ddot{\phi}_f + \frac{1}{\tilde{\rho}+1}\tau_o &= \tau_{M_v} \\ I_{vf}\ddot{\phi}_v + I_{ff}\ddot{\phi}_f + \frac{\tilde{\rho}}{\tilde{\rho}+1}\tau_o &= \tau_{M_f} \end{aligned} \tag{6.27}$$

We will now provide a torque at the VA such that the VA follows a trapezoidal trajectory, i.e.  $\tau_{M_v} = I_{vv}\ddot{\phi}_v$ . At the same time, we will apply a torque at the FA to compensate for the disturbance torque coming from the VA, i.e.,  $\tau_{M_f} = I_{vf}\ddot{\phi}_v$ . External forces are assumed to be zero, i.e.  $\tau_o = 0$ . Note that this does not mean external forces do not exist. They might exist, but their effects are not modeled in the above model-based control. Also, the as-designed and as-built systems are assumed to be identical. In other words, there are no modeling errors. Such a simplistic approach is first taken to demonstrate the operation of the PFVA. In a later section, a more realistic representation of the PFVA will be simulated by dropping some of the above restrictions. In this

example, we model an obstacle at  $\phi_{ob} = 50^\circ$ . An external torque  $\tau_{ob}$  is applied by the obstacle on the output link according to the following model.

$$\tau_{ob} = K_{ob} (\phi_o - \phi_{ob}) \quad (6.28)$$

We will now present the results of this simulation. In doing so, we will consider two cases: (i) the obstacle is not present, and (ii) the obstacle is present. The conditions of cases (i) and (ii) are shown in.

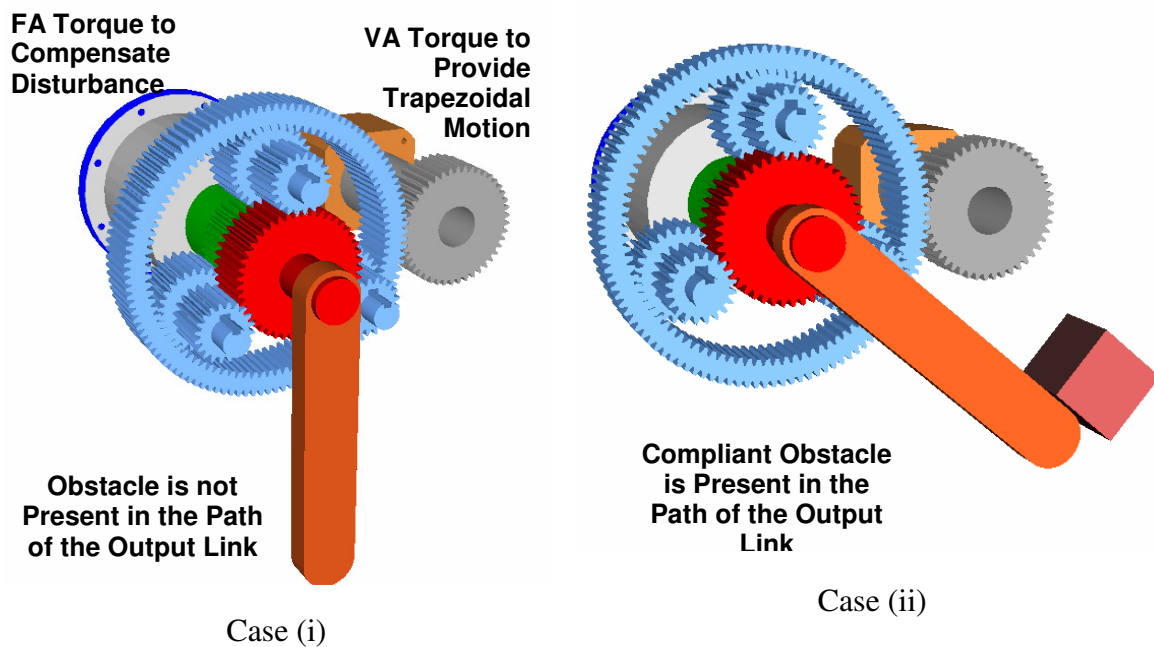


Figure 6.16. Simulation set up for Example 6.4.

**Case (i). Obstacle is not Present.** In this case, we do not expect the FA shaft to have any displacement because the FA motor applies a balancing torque to compensate for the inertial disturbance torque coming from the VA. The velocity and torque profiles of the FA and VA are shown in the following plots (Figure 6.17).



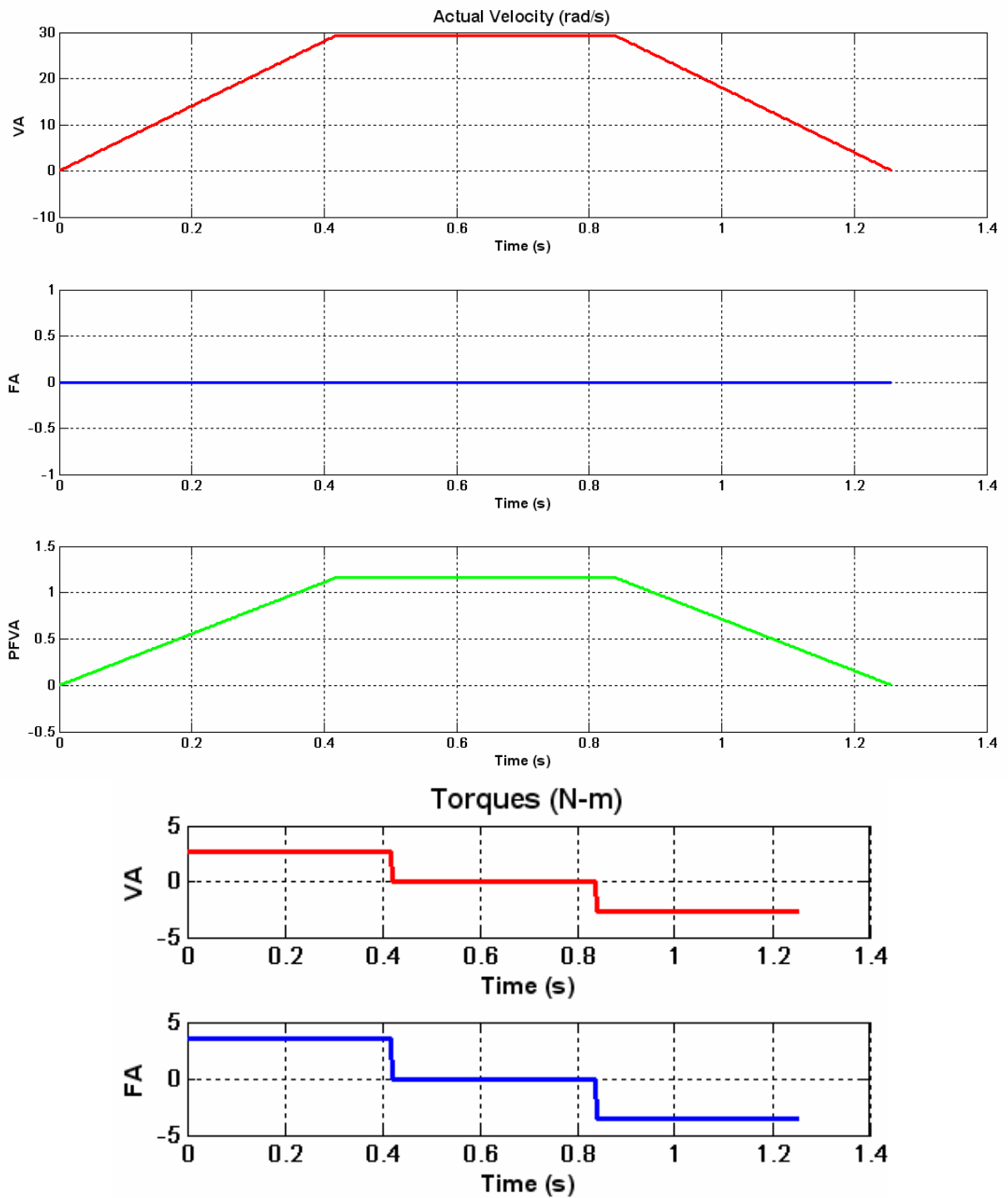


Figure 6.17. The velocity and torque profiles for the simulation described in Case (i) of Example 6.4.

The velocity profiles shown in Figure 6.17 suggest that the FA does not move if the FA motor torque balances the cross-coupling inertia torque due to the VA shaft's acceleration. This compensation torque needs to be provided because the PFVA is essentially a serial mechanism. Also, this compensation torque is the product of two parameters: (i) cross-coupling inertia,  $I_{vf}$ , and (ii) acceleration of the VA shaft,  $\ddot{\phi}_v$ . Therefore, this cross-coupling torque requirement increases when either or both of these parameters increase. In the simulation above, the cross-coupling inertia is  $I_{vf} = 0.0511$  Kg-m<sup>2</sup> (this includes cross-coupling link inertia and gear-train inertia). The acceleration of the VA during the variable velocity phases is  $\ddot{\phi}_v = 70.219$  rad/s<sup>2</sup>. Consequently, the compensation torque that the FA needs to provide, to prevent the FA shaft from being back-driven, is  $I_{vf}\ddot{\phi}_v = 3.591$  N-m. The inertia torque distribution ratio  $\tilde{\tau}^l = \tau_f^l / \tau_v^l = 1.3362$ . In other words the torque requirement on the FA is approximately 33% greater than that on the VA.

Now, the torque on each branch of the PFVA mechanism (i.e. the VA, FA, and the output link) is limited by the lowest torque among the three branches. This was mathematically shown in Eq. (4.9) and is reproduced here:

$$\tau_o : \tau_v : \tau_f = 1 : -\frac{g_v}{\eta_{v \rightarrow o}} : -\frac{g_f}{\eta_{f \rightarrow o}} \quad (6.29)$$

Therefore we can operate the FA in the system as a torque limiter. In this simulation, external torques acting on the output link are not modeled and they are not introduced in the simulation either. However, if such torques do exist, they will produce an unbalanced torque on the FA shaft which will then be backdriven. Therefore, using the FA as a torque limiter can improve the mechanical safety of the PFVA, as will be demonstrated in the next case.

**Case (ii). Obstacle is Present.** In the simulation set-up for Case (i) above, we will now introduce an obstacle which behaves like a linear spring with a spring constant<sup>40</sup>  $K_{ob} = 94,000$  N-m/rad. The simulation parameters of Case (ii) are identical to those in Case (i) except for the presence of an obstacle. The velocity profiles of the three shafts in the PFVA are shown in Figure 6.18.

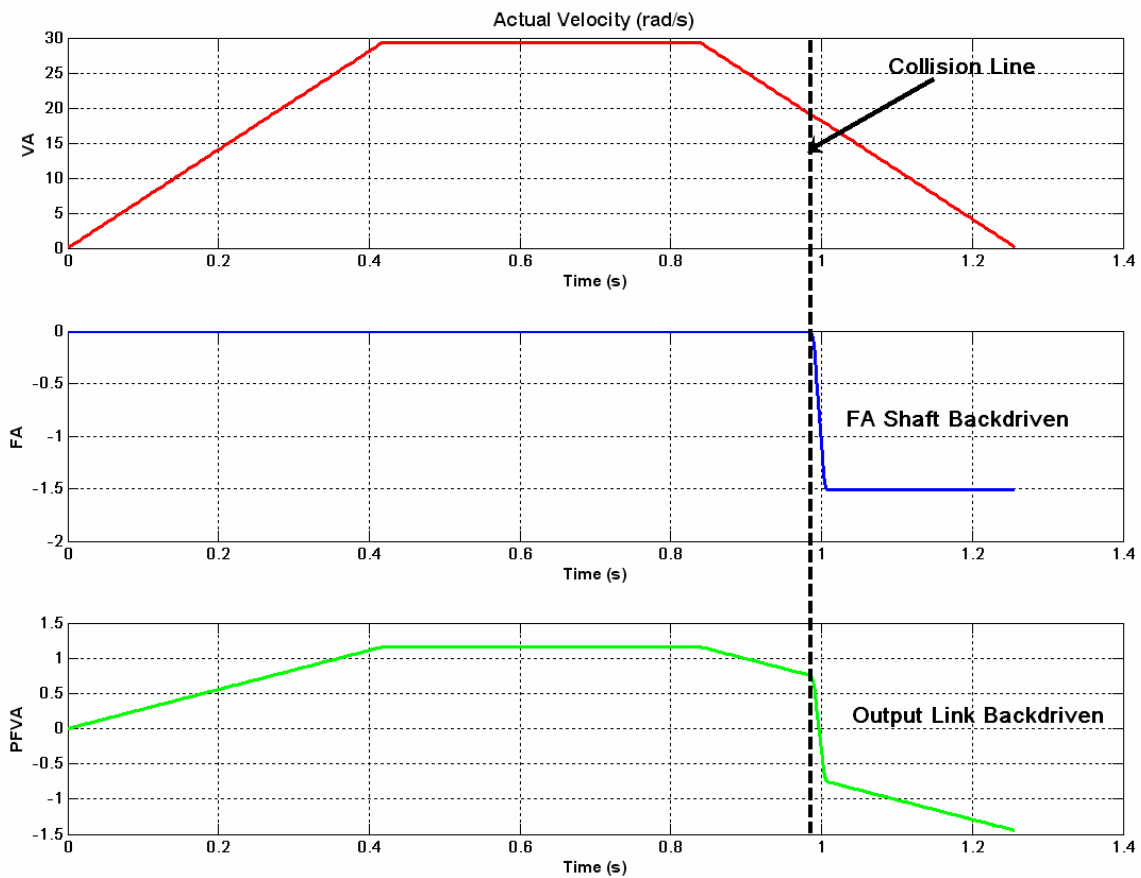


Figure 6.18. The velocity profiles for the simulation described in Example 6.4, Case (ii).

In this figure, the dotted vertical line indicates the instant the collision occurs. At this instant the output link is at  $50^\circ$  to the vertical, the instant shown in Figure 6.16 (ii) when

<sup>40</sup> This corresponds to the compliance of the ATI Gamma Force/Torque (F/T) sensor. We have used this value to simulate an F/T sensor as the obstacle.

the link makes initial contact with the obstacle. Note that after the collision the FA is backdriven, thus forcing the output link to move away from the obstacle. The FA continues to move at  $-1.5$  rad/s without stopping because there is no dissipative force in this branch at this time (due to the simplifying assumption in our model). The PFVA output also continues to move because the VA is still trying to maintain the trapezoidal motion plan. During this event, the static torques acting on the shafts are shown in Figure 6.19.

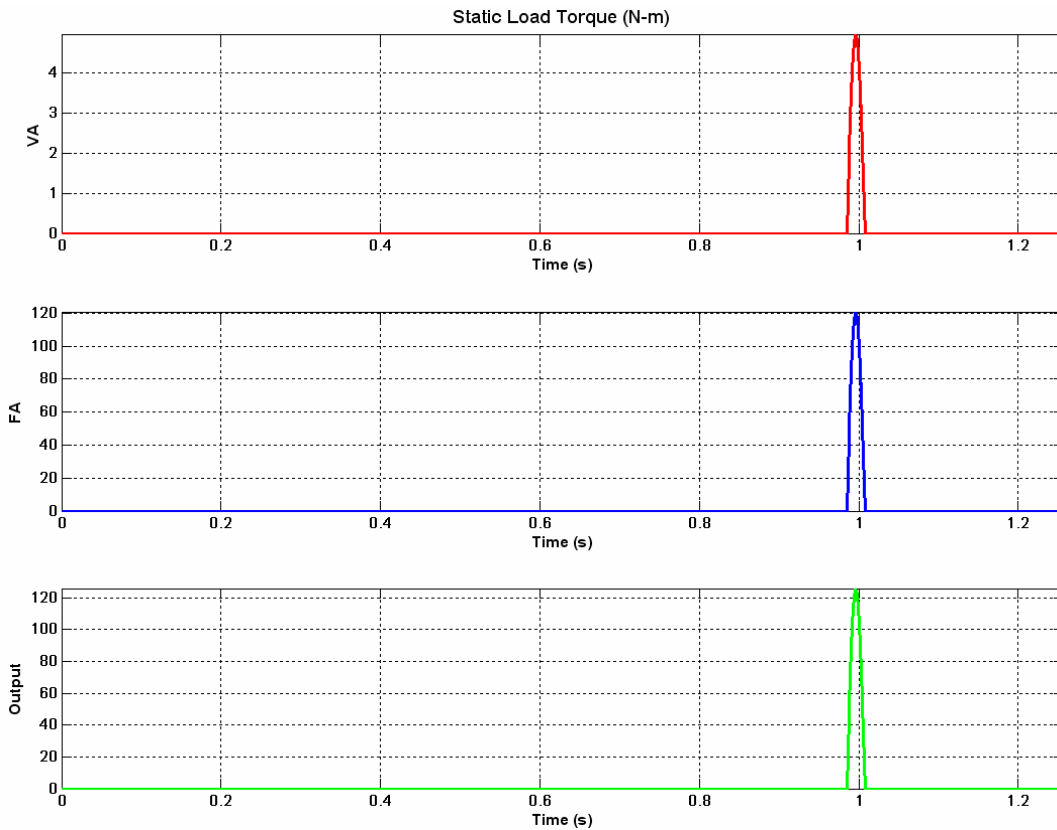


Figure 6.19. The static torque profiles for the simulation described in Example 6.4, Case (ii). Notice that due to the programmed backdriveability of the FA, the force reduces quickly as soon as the prescribed safe force threshold is reached.

The maximum output torque is 125.757 N-m which when translated to the force acting at the end-point of the link<sup>41</sup> is 251.514 N (or 56.543 lbf). When reflected to the input side, the torque on the FA and VA shafts are 120.8 N-m and 4.98 N-m, respectively. As the active torque provided by the FA motor is only 3.591 N-m ( $\ll 120.8$  N-m), the FA shaft is back-driven and this forces the output link to move away from the obstacle (see velocity profile in Figure 6.18 to the right of the dotted collision line), thus reducing the contact force almost instantaneously. The approach velocity of the output link (the velocity with which the link tip moves towards the obstacle) right before collision is approximately 0.375 m/s. In this simulation we have shown that the PFVA drive can be used to detect a collision and behave in an inherently safe manner (due to its backdriveability).

There are two successively important aspects of manipulation in both structured and unstructured environments: (i) obstacle avoidance to prevent collisions and (ii) safe and forgiving response in the event of an inadvertent collision. Our discussion of mechanical safety using the FA in the PFVA as a torque-limiter has focused on item (ii) above. However, several approaches have been proposed in the past for (both model-based and sensor-based) obstacle avoidance (Harden and Tesar, 2002; Swint and Tesar, 2005; Spencer et al., 2008). Current work at UTRRG is exploring stopping criteria for collision avoidance in serial manipulators (Steinfeld and Tesar, 2009).

#### **6.4. GENERALIZED MODEL TO STUDY REALISTIC MODES OF OPERATION**

The objectives of this section are listed below.

---

<sup>41</sup> We use the moment arm for the force acting at the end-point to determine the force at the end-point,

$$F_o = \frac{\tau_o}{l_{link}}. \text{ The link length is 0.5m.}$$

- We will develop a generalized model for the PFVA and develop extensive parametric representations of each of its terms. The motivation behind developing such a rigorous model is to characterize the actual dynamics of the PFVA system. For instance, in the previous section we assumed that there is no friction; however in this section we will include frictional effects in the model. Another complexity we will add in this section is a gravitational field.
- We will then use this model to simulate the response of the 1-DOF PFVA introduced in the previous section for three scenarios: (i) free space motion (primarily an inertia management issue), (ii) transition from free-space motion to constrained-space motion (requires collision detection and safe forgiving response as demonstrated in Case (ii) of Example 6.4 above), and (iii) force-controlled response in constrained space.

#### 6.4.1. Generalized Model Development

The governing equations of motion of the PFVA can be expressed as a set of kinematic transformations and a matrix differential equation:

$$\phi_o = \mathbf{G}\phi, \quad \dot{\phi}_o = \mathbf{G}\dot{\phi}, \quad \text{and} \quad \ddot{\phi}_o = \mathbf{G}\ddot{\phi} \quad (6.30)$$

$$\mathbf{I}\ddot{\phi} + \boldsymbol{\tau}_F(\dot{\phi}) + \boldsymbol{\tau}_G(\phi) + \boldsymbol{\tau}_S = \boldsymbol{\tau}_M \quad (6.31)$$

where  $\mathbf{G} = \begin{bmatrix} g_v & g_f \end{bmatrix}$  is a matrix of velocity ratios for the two inputs,  $\dot{\phi} \in \begin{bmatrix} \dot{\phi}_v & \dot{\phi}_f \end{bmatrix}^T$  is a vector of input velocities,  $\mathbf{I} \in \mathbb{R}^{2 \times 2}$  is the consolidated inertia matrix in the input space,  $\boldsymbol{\tau}_F(\dot{\phi}) \in \mathbb{R}^2$  is a vector of frictional torques that are dependent on stiction and the velocities of the input shafts,  $\boldsymbol{\tau}_G \in \mathbb{R}^2$  is a vector of gravitational loads (reflected to the inputs) that are functions of the input shaft positions,  $\boldsymbol{\tau}_S \in \mathbb{R}^2$ , that is a vector of static loads seen by the inputs. The inertia matrix includes the output inertia, gear train component inertias, and the motor-side inertias of the FA and VA (see Appendix C). The frictional load is represented using a continuous-model for Stribeck friction (Majd and Simaan, 1995). The gravitational load due to the external link alone is considered in the

simulation section. The static load vector can be determined if the static load acting on the output is known:

$$\boldsymbol{\tau}_s = \mathbf{G}^T \boldsymbol{\tau}_o \quad (6.32)$$

where the external torque acting on the link is modeled as

$$\boldsymbol{\tau}_o = K_{env} (\boldsymbol{\phi}_o - \boldsymbol{\phi}_{env}) + B_{env} (\dot{\boldsymbol{\phi}}_o - \dot{\boldsymbol{\phi}}_{env}) \quad (6.33)$$

The environment interaction model in Eq. (6.33) is that of a linear spring-damper system.

In our simulations and experiments we consider a stationary obstacle, i.e.  $\dot{\boldsymbol{\phi}}_{env} = 0$ .

**Note on Friction Modeling.** We have used the Stribeck model (Armstrong-Hélouvy, 1991) for frictional effects in the PFVA. This is a static discontinuous model and one representation of this effect was presented by Armstrong-Hélouvy:

$$\boldsymbol{\tau}_F(\dot{\boldsymbol{\phi}}) = \begin{cases} b\dot{\boldsymbol{\phi}} + (\tau_s - \tau_c) e^{-\frac{|\dot{\boldsymbol{\phi}}|}{|\dot{\boldsymbol{\phi}}_c|} \sigma} + \tau_c, & \text{if } \dot{\boldsymbol{\phi}} \neq 0 \\ \tau_e, & \text{if } \dot{\boldsymbol{\phi}} = 0 \text{ and } |\tau_e| < \tau_s \\ \tau_s \operatorname{sgn}(\tau_e), & \text{otherwise} \end{cases} \quad (6.34)$$

This model is discontinuous at  $\dot{\boldsymbol{\phi}} \neq 0$  and, consequently, substituting this value in Eq. (6.31) results in a set of stiff differential equations that are computationally expensive to integrate. Therefore, we have used a continuous model for Stribeck effect proposed by Majd and Simaan (1995):

$$\boldsymbol{\tau}_F(\dot{\boldsymbol{\phi}}) = b\dot{\boldsymbol{\phi}} + \left[ \tau_c + \sigma e^{-\frac{|\dot{\boldsymbol{\phi}}|}{|\dot{\boldsymbol{\phi}}_c|} \sigma} - (\sigma + \tau_c) e^{-\frac{|n\dot{\boldsymbol{\phi}}|}{|\dot{\boldsymbol{\phi}}_c|} \sigma} \right] \operatorname{sgn}(\dot{\boldsymbol{\phi}}) \quad (6.35)$$

In this continuous model,  $b$  is the damping coefficient for viscous friction,  $\tau_c$  is the coulomb friction term,  $\sigma$  is a scalar parameter with units of N-m, that is numerically determined,  $n$  is an integer constant which dictates the sharpness of the friction curve,  $\dot{\boldsymbol{\phi}}_c$  is the critical velocity (limit for Stribeck effect), and  $\operatorname{sgn}(\dot{\boldsymbol{\phi}})$  is the sign of the velocity variable  $\dot{\boldsymbol{\phi}}$ . The low and high velocity behaviors of this model are shown in Figure 6.20.

The parameters used for this representation are  $b = 0.05$  N-m/(rad/s),  $\tau_c = 0.5$  N-m,  $\sigma = 0.6858$ ,  $n = 10$ , and  $\dot{\phi}_c = 0.006$  rad/s.

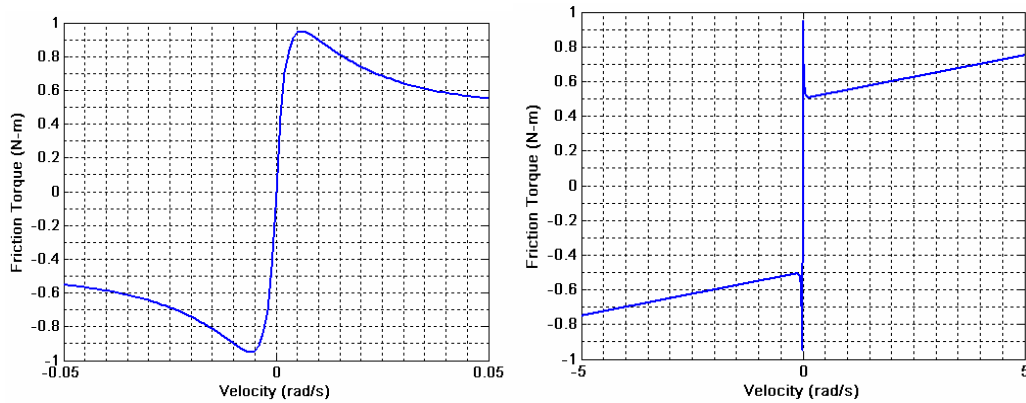


Figure 6.20. Frictional torque as a function of velocity using the continuous Stribeck model proposed by Majd and Simaan (1995). (Left) Low velocity behavior, and (Right) High velocity behavior.

**Example 6.5: PFVA Response for an Approach-Collision-Force Control Scenario**

In this example, we will use the generalized model presented in this section and simulate its dynamic response to an impact scenario. We will simulate three phases of operation of the PFVA: (i) free-space motion, (ii) backdriveability during collision, and (iii) force-control. The conditions of the simulation during these phases are shown in Figure 6.21 and described below. The specified output velocity was a polynomial motion program. Stribeck friction effects are present in both the inputs and the system is in a gravity field.

- **Free-space Motion.** In this phase, the FA was controlled at zero position and the VA was position controlled to support the polynomial motion at the output link. The torque commanded to the FA motor was limited to a threshold based on a safe contact force between the link end-point and the environment (75 N). Such a threshold was not imposed on the VA motor torque which was limited to its maximum rated torque.



The position and velocity errors in the two inputs were used as evaluation metrics for the PID position control.

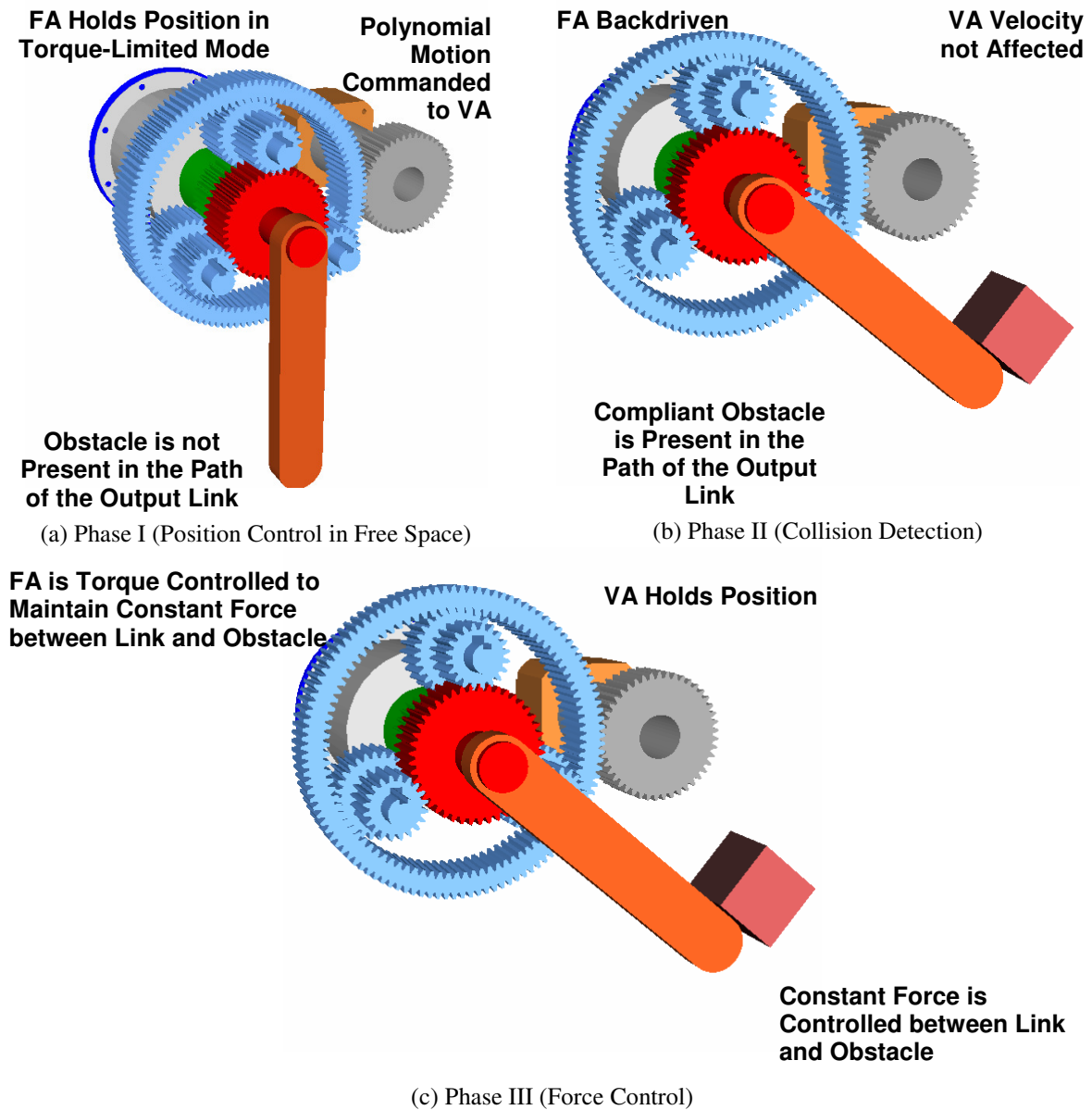


Figure 6.21. Simulation set up for Example 6.5. (a) Phase I or position controlled response in free-space, (b) Phase II where collision is detected, and (c) Phase III or force controlled response to maintain a constant force between link and the object.

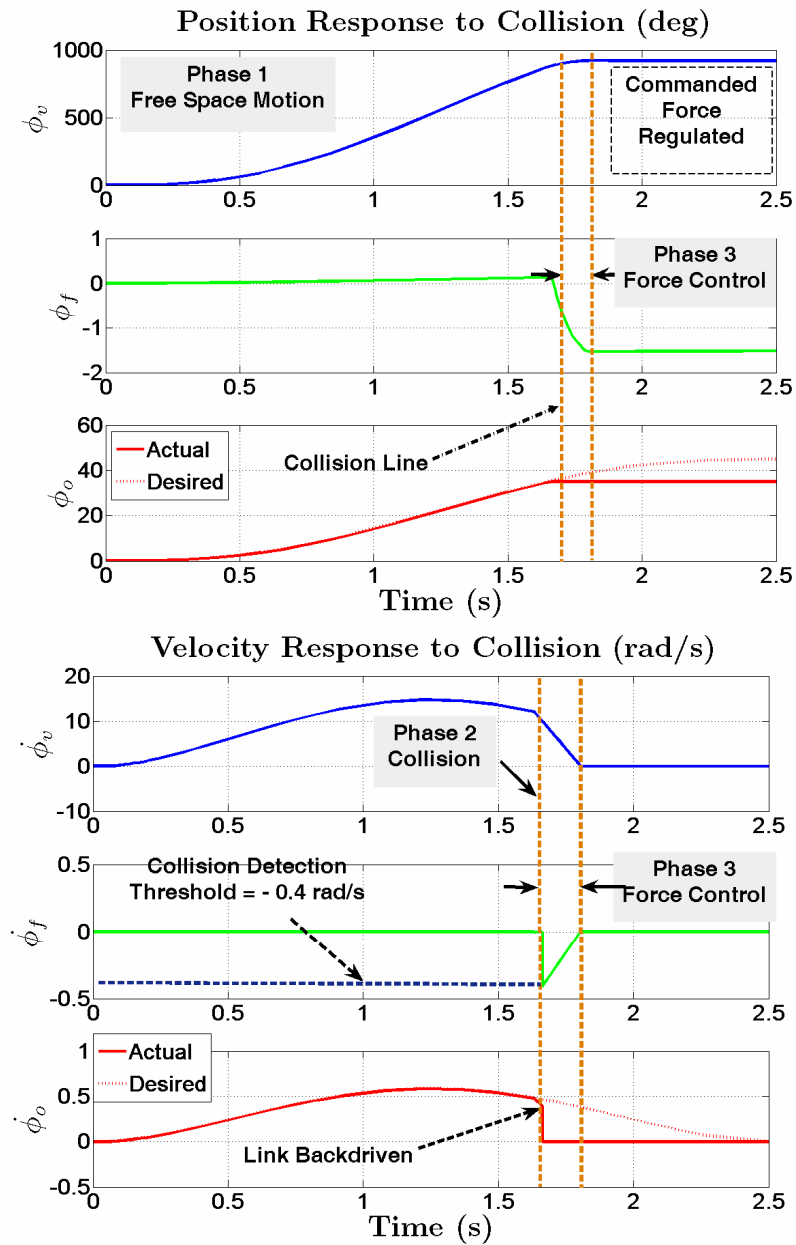


Figure 6.22. Positions and velocities of the FA, VA and output link during the three phases of the collision response simulation in Example 6.5.

- **Collision Phase.** This is a short phase relative to the other two phases. When the output link encounters an obstacle and the contact force with the environment exceeds

75 N, the FA motor (due to its threshold torque) is backdriven. When the backdriving speed of the FA motor exceeded 0.4 rad/s, the system enters the force control phase.

- **Force Control Phase.** In this phase, the torque on the FA motor is explicitly controlled using the feedback from the torque sensor in this branch. The VA motor continues to be position controlled; however at zero velocity. The overall objective in this phase is to maintain a specified constant force between the link tip and the encountered obstacle. The VA position and velocity error were metrics for VA control, and the error between the specified force (15 N) and the measured force (measured through the torque sensor) between the link and the obstacle was the evaluation metric for force control of the FA.

**Simulation Results.** The positions of the various shafts of the PFVA are shown in Figure 6.22. Note that the collision occurs at approximately 1.65s. Until this point the two inputs are position controlled and the output position error is approximately zero. During collision, after the backdriving velocity of the FA motor exceeds the specified value (0.4 rad/s), the system's objective is to maintain a constant force of 15 N on the obstacle.

## 6.5. CHAPTER SUMMARY

The main objective of this chapter was to present the dynamic response of the PFVA when the VA and FA are controlled in different operational modes. Broadly, we have considered two main modes of control: (i) VA and FA both being controlled in velocity mode (kinematic control) and (ii) VA being torque controlled to track a motion trajectory while the FA is torque controlled to either act as a torque-limited input or as a force-controlled actuator (dynamic control). The kinematic control mode entails resolving the kinematic redundancy in the dual-input drive to satisfy a velocity demand at the PFVA output while optimizing a set of secondary criteria. In an example, a pseudo-

inverse based non-linear programming problem was formulated to track a sinusoidal motion trajectory at the output of the PFVA while maintaining constant directionality of rotation for the FA and VA (to minimize backlash) and spinning them at higher rates (to mitigate low-velocity stiction).

We developed a simplified model for the coupled PFVA system to demonstrate some ideal modes of operation. Following this we developed a generalized model to incorporate realistic dynamic effects such as friction and gravity. A dynamic simulation was presented where the generalized model was utilized to study the response of the controlled PFVA in three phases of a manipulation task: (i) free-space motion, (ii) inadvertent collision, and (iii) force-controlled motion. Numerical examples were presented for both the simplified and the generalized PFVA model.

## Chapter 7. Experiments with a PFVA Prototype

In Chapter 4 through Chapter 6, we have presented analytical formulations to study the design and dynamic response of PFVAs. In this chapter we will build on that analytical understanding and perform controlled experiments with a PFVA prototype and associated testbed that was assembled at the robotics laboratory at UT (Figure 7.1).

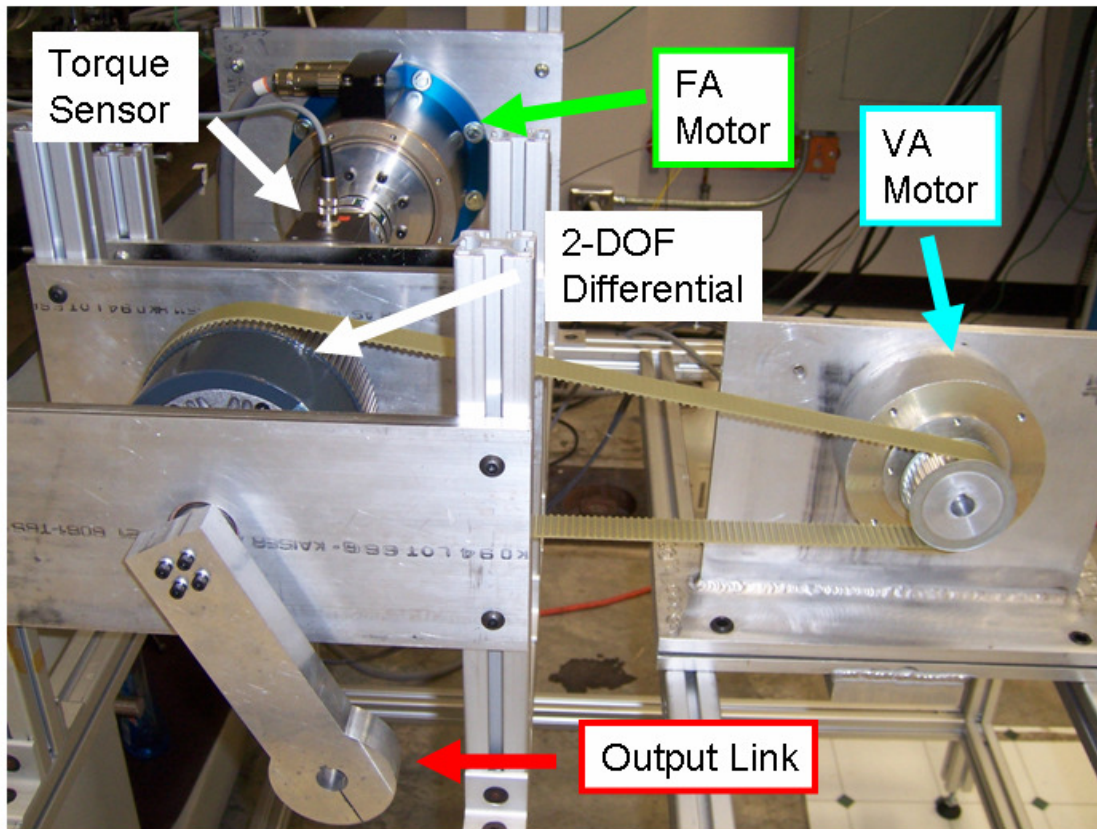


Figure 7.1. Laboratory prototype of the Parallel Force/Velocity Actuator (PFVA) built at the Robotics Research Group at The University of Texas at Austin.

The focus of this experimental work was as follows:

- To identify two physical phenomena that could significantly limit the performance of the actuator: (i) friction, and (ii) dynamic coupling (manifested as

disturbance torques) between the FA and the VA and its relation to the RSF parameter.

- To demonstrate two modes of operation of the PFVA: (i) velocity controlled performance by utilizing the kinematic redundancy in this dual actuator to mitigate low-velocity friction effects and (ii) safe response of the PFVA, via the controlled backdriveability of the FA, to collision and impact scenarios. These modes of operation were theoretically discussed in Chapter 6 and will be experimentally demonstrated in this chapter.

Apart from the above goals pertinent to the central theme of this report, a secondary objective was to build a dual actuator testbed that can potentially be used to study actuator criteria such as acceleration response, servo-stiffness (we partially characterize this behavior in this chapter), control-in-the-small performance (Tesar, 1985), fault-tolerance capability, etc.

### **7.1. PFVA TESTBED DESCRIPTION**

Figure 7.2 shows the testbed setup of the PFVA prototype. The principal components of this system are the VA motor, the FA motor, the torque sensor, the 2-DOF differential drive-train, and the output link (see Table 7.1). The differential drive consists of three input/output branches labeled N1, N2, and N3 in Figure 7.2. In our set-up (see Figure 7.2), the VA motor is connected to the casing (carrier) of the differential via a pulley and a steel-reinforced T32 timing belt, and is the *velocity input* (labeled N1 in the figure) to the PFVA. The *force input* comprises the FA motor and the in-line torque sensor. The force input (labeled N2 in the figure) drives the sun gear of the differential. The output (labeled N3 in the figure) is connected to the internal ring gear and is labeled N3. Since all three shafts of this gear train are either driving or driven, mounting the differential was a challenge.

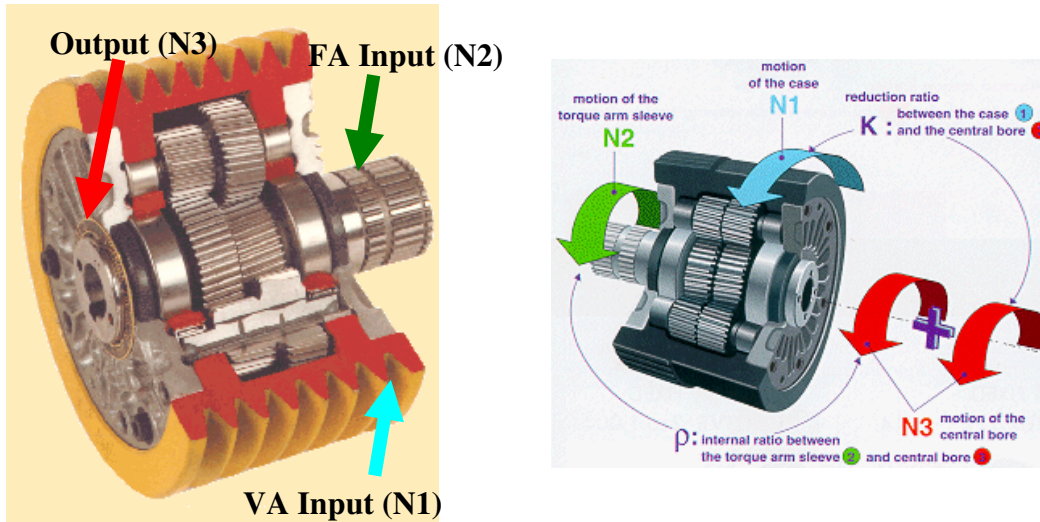


Figure 7.2. Sectioned-view of the Andantex SR-20 differential gear train used in the physical prototype of the PFVA (Courtesy: Andantex, Inc., Wanamassa, NJ).

The differential is supported by two bearings, one attached to the FA input shaft and the other attached to the output shaft. The output link was designed to have 360° rotation and to have weights attached to simulate external loads. See Appendix E for details regarding the testbed.

Table 7.1 List of Components in the PFVA Testbed

Components	Manufacturer and Model	Relevant Specifications
FA Motor (Framed)	Kollmorgen Goldline DDR DH063M-22-1310	Peak Torque = 150 N-m, Max. Speed = 800 rpm, Rotor Inertia = $8.6 \times 10^{-3}$ kg-m <sup>2</sup>
Torque Sensor	Honeywell Sensotec 1703	Torque Range = $\pm 200$ N-m, Noise = $\pm 0.4\%$
VA Motor (Framed)	Kollmorgen RBE-03001-A50	Peak Torque = 28.9 N-m. Max. Speed = 281 rpm, Rotor Inertia = $7.8 \times 10^{-4}$ kg-m <sup>2</sup>
2-DOF Differential (Oil Lubricated)	Andantex SR-20 Unit	Rated Torque = 150 N-m, Relative Scaling Factor = 24.27, VA Efficiency = 69%, FA Efficiency = 98%
Output Link	Fabricated In-house	Material = Aluminum, Length = 0.158 m

The velocity ratios of the differential used for this testbed are  $g_f = 0.9604$  for the FA and  $g_v = 0.0396$  for the VA (note that they sum to unity), resulting in a relative scale factor of  $\tilde{\rho} = 24.72$ . The timing belt introduces an additional velocity ratio (approximately 0.4383) on the velocity input resulting in a total relative scaling between the FA input and the VA input of 55.367. The differential used in our experiments is a positive-ratio epicyclic drive. In other words, the velocity ratios of the two inputs are of the same sign. Therefore, the relative scaling between the two inputs is a positive scalar.

## **7.2. EXPERIMENTS: SETUP AND RESULTS**

In this section we will report four experiments performed as part of this research: (i) identification of friction phenomena, (ii) identification of dynamic coupling, (iii) utilization of kinematic redundancy of the PFVA, and (iv) demonstration of the safe response of the PFVA to collision and impact scenarios.

### **7.2.1. Experiment I: Identification of Friction in the FA**

The goal of this experiment was to measure the frictional effects on the FA branch for various operating conditions. In Chapter 6 we showed using simulations that the FA can be torque controlled to maintain a specified force between the output link and its environment. However, while controlling the FA in torque mode, identification of friction in this branch of the PFVA is essential. Friction can be classified into velocity-dependent and position-dependent friction (see Figure 7.3).



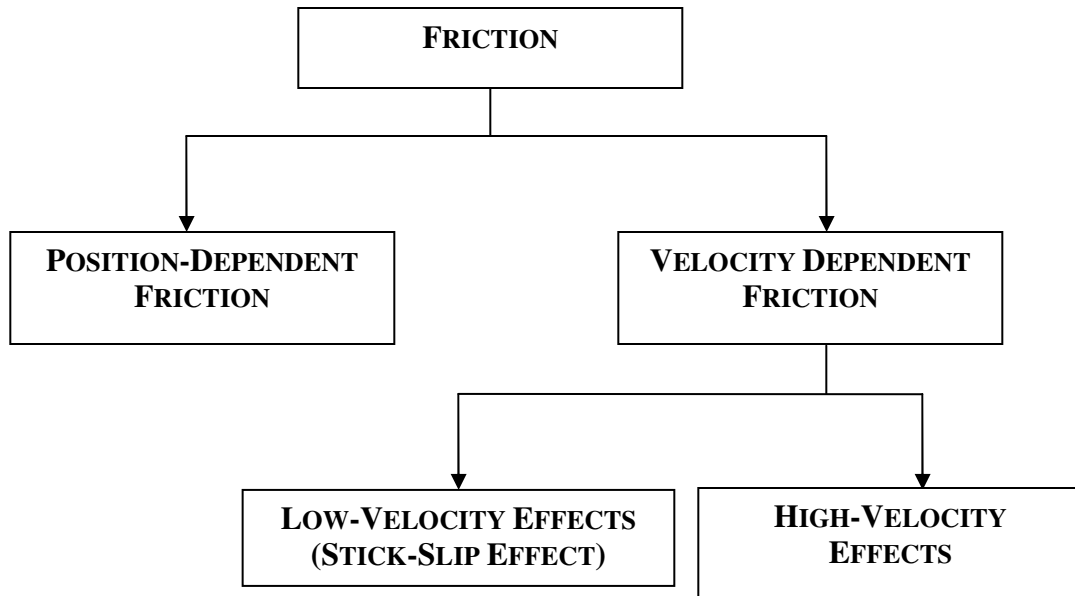


Figure 7.3. Different types of friction effects characterized during experimental identification of friction in the FA.

Furthermore, the velocity-dependent friction effects are different in low- and high-velocity zones. In the high-velocity region, viscous damping is predominant and in the low-velocity region, the Stribeck effect (Armstrong-Hélouvy, 1991; Majd and Simaan, 1995) is present. Position-dependent friction (Garcia et al., 2002) arises due to inaccuracies in the assembly of the testbed and the resulting loading on the FA shaft as a function of the angular position. Our goal was to systematically lay out an experimental procedure to identify these friction effects and, based on this procedure, to also estimate their magnitudes in the FA branch.

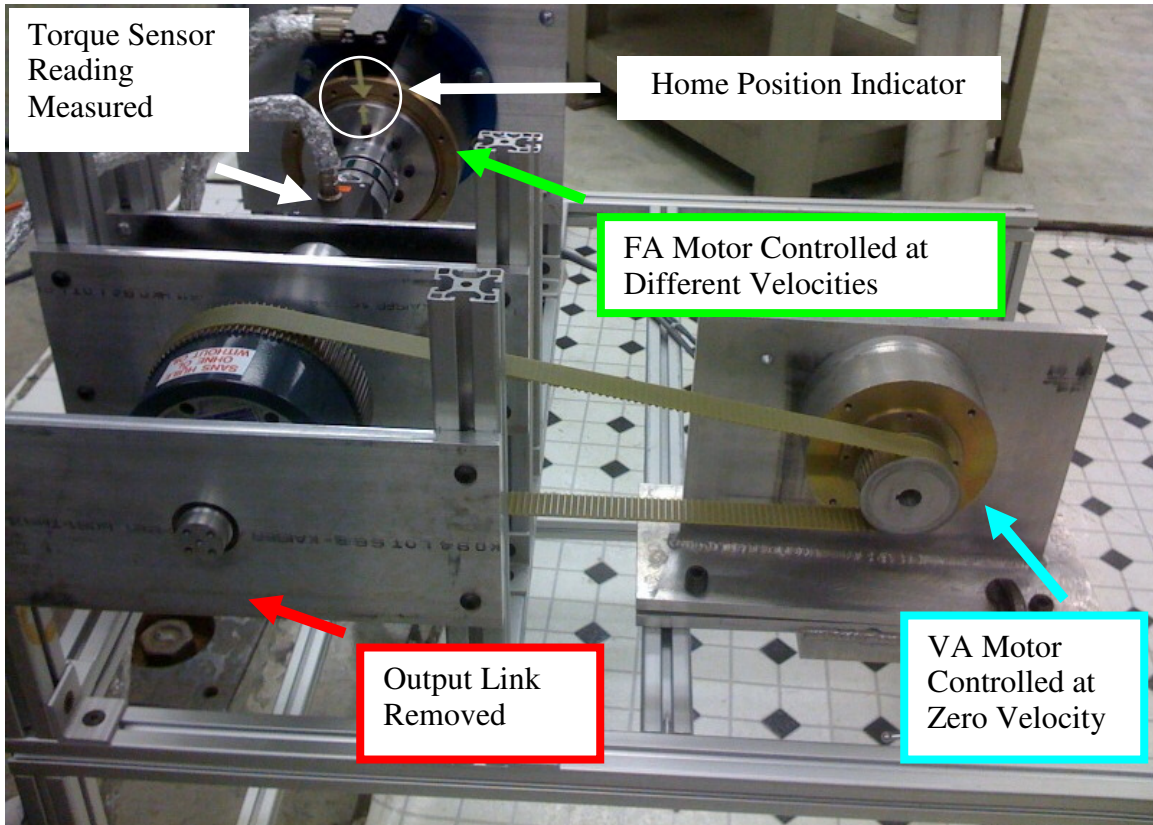


Figure 7.4. Conditions imposed on the PFVA testbed during friction identification experiment. VA motor was controlled at zero velocity, FA motor was controlled at different velocities ranging from -200 to 200 rpm, and the torque reading from the torque sensor was measured.

The theory behind this procedure is the Stribeck friction model which was discussed earlier in Section 6.4.1 in Eq. (6.34). The testing procedure itself is from previous work by Garcia et al (2002, p.762). The difference between their procedure and ours is that they indirectly compute the friction torque by measuring the motor current; however we directly measure the torque using a torque sensor.

#### ***PROCEDURE***

To determine the velocity-dependent friction, the VA motor was controlled at zero velocity (holding position), the FA motor was controlled at different velocities in the

range [-200 200] rpm. The lowest non-zero velocity experimented with was  $\pm 5$  rpm. For each FA velocity value, 10 runs were performed and the mean torque measurement was determined. For each run the torque sampled for 15 revolutions of the FA shaft. Torque was sampled at 20 Hz and a second-order low-pass forward-backward Butterworth filter (Barr and Chan, 1986) with a cut-off frequency of 5 Hz was used. To eliminate the artifacts in the filtered signal due to forward-backward filtering, the torque data from the first two and the last two periods of the shaft revolution were ignored for averaging. This process also eliminates transients in the torque measurements due to the PID action of the motor controller. For every speed setting the average and variance of torque measurements from all 10 runs were, respectively, used as an estimate of the frictional torque and its repeatability at that speed. Before this experiment, a ‘warm up’ routine was used where the FA was run for approximately 2 minutes at 200 rpm in both directions to eliminate error due to temperature variation. The significance of ‘warming up’ is that friction decreases rapidly after a short period (1-2 mins) of activity across the whole range of velocities. This is explained in detail in (Armstrong-Hélouvry, 1991, Chapter 5). The output link was removed for this experiment to eliminate gravity loading due to its weight. The FA velocity values selected for different runs were randomized<sup>42</sup> to eliminate experimental bias. To determine the stiction torque, the current on the FA motor was gradually increased while monitoring for the movement of the FA shaft. The torque measurement at the instant when the FA shaft starts moving (break-away torque) was used as an estimate of stiction. This stiction experiment was conducted for 8 runs each for both positive- and negative- torque regions to determine the variance (or repeatability) of the stiction estimate.

---

<sup>42</sup> The function `randperm()` in Matlab can be used to select a randomized sample from a set of values.

To measure position-dependent friction, it was important to choose a reference to count rotations of the FA shaft in addition to characterizing the friction torque as a function of angular shaft position. Therefore, a home position for the FA was arbitrarily chosen as a reference and marked on the testbed as shown in Figure 7.3. The procedure followed for this experiment was similar to the one for measuring velocity dependent friction. The VA was controlled at zero velocity. The FA was controlled at different velocities chosen from the set  $\{\pm 5, \pm 10, \pm 25\}$  rpm and was controlled to repeatably move for exactly 12 revolutions during every experiment. Torque data was sampled at 20 Hz<sup>43</sup> and a low-pass second-order butterworth forward-backward filter (Barr and Chan, 1986) with a cut-off frequency of 5 Hz was used for data analysis. To verify that the friction torque is dependent on the angular position, the spatial frequency spectrum, or Fast Fourier Transform (FFT), of the torque data was plotted to compare the frequency content in the torque data and the angular frequency of rotation of the FA shaft. The unit used for spatial frequency was cycles/rev (as opposed to cycles/second for temporal frequency). This change of units allows us to focus on the torque oscillations as a function of angular position (in terms of revolutions) rather than angular velocity. The procedure described above was laid down in a monograph by (Armstrong-Hélouvy, 1991) and used by (Garcia et al., 2002) to determine the position-dependent friction in the joint of a legged robot.

### ***DATA ANALYSIS AND RESULTS***

The results from our velocity-dependent friction estimation experiments are shown in Figure 7.5 (friction torque vs. speed range) and Figure 7.6 (repeatability of velocity-dependent friction experiment). From our break-away experiments, the positive

---

<sup>43</sup> Our experiments were not performed on a real-time computing platform and therefore we did some benchmarking tests and determined that the actually attained bandwidth was only approximately 18 Hz (an error of 10%).

and negative stiction torque measurements were 1.008 and -0.9705 N-m, respectively, with a repeatability of approximately  $3\sigma = 7\%$  (based on the variance across the 8 runs performed).

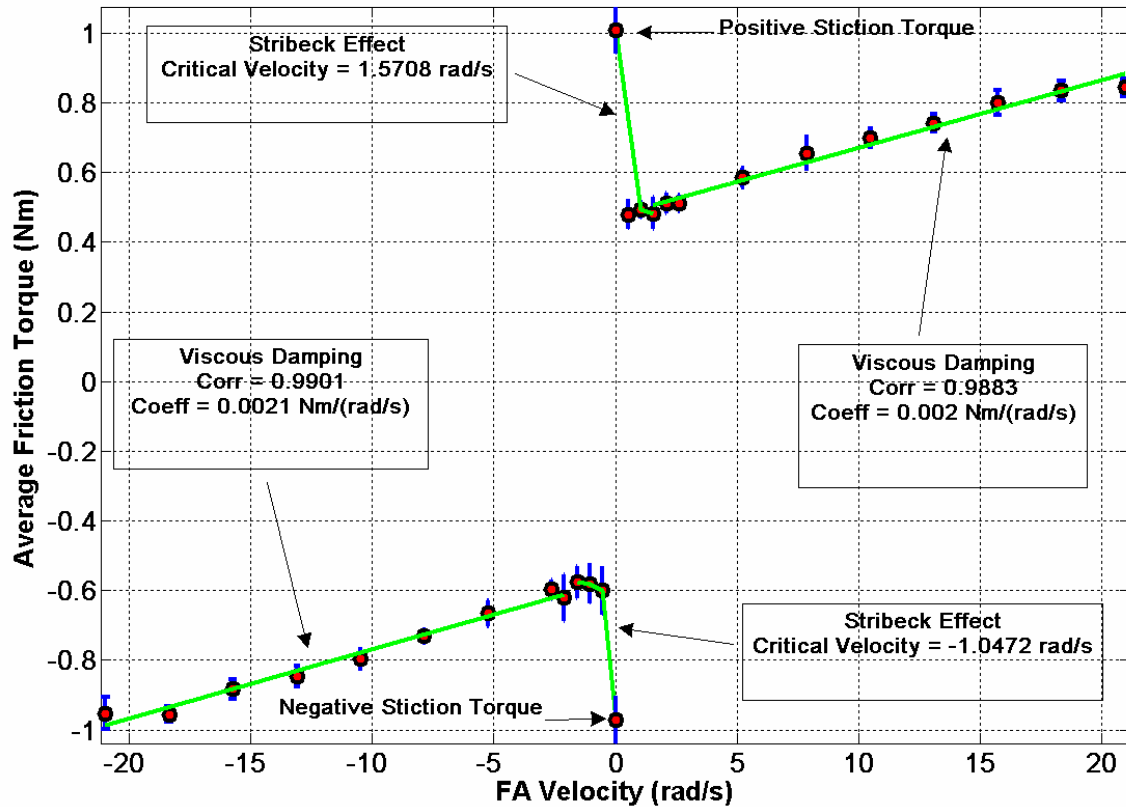


Figure 7.5. Experimental results for velocity-dependence of friction in the FA branch. Notice the Stribeck effect in the low velocity region where average friction torque decreases with velocity. After the critical velocity, friction increases linearly (viscous damping effect). Error bars show  $3\sigma$  intervals.

The error bar in this figure shows the repeatability of torque measurement at a speed (based on the  $3\sigma$  computation across the 10 runs performed). There are three noteworthy observations from the first quadrant in Figure 7.5:

- The segment from approximately 2.0944 to 20.93 rad/s shows a linear viscous damping trend with correlation coefficient of 0.9883. The viscous damping coefficient in this region is 0.002 N-m/rad/s.

- The Stribeck effect was observed with an estimated critical velocity of 1.5708 rad/s.
- After break-away the friction torque decreases from its stiction value ( $1.008 \pm 7\%$ ) to approximately  $0.4792 \pm 4\%$ . This rate of decrease is approximately  $-0.33$  N-m/rad/s.

Correspondingly, in the third quadrant the following observations were made:

- The segment from approximately  $-1.5708$  to  $-20.93$  rad/s shows a linear viscous damping trend with correlation coefficient of 0.9901. The viscous damping coefficient in this region is  $0.0021$  N-m/rad/s.
- The Stribeck effect was observed with an estimated critical velocity of  $-1.0472$  rad/s.
- After break-away the friction torque decreases from its stiction value ( $-0.9705 \pm 7\%$ ) to approximately  $-0.5804 \pm 9\%$ . This rate of decrease is approximately  $-0.372$  N-m/rad/s.

We also performed a repeatability analysis for our experiment at various speeds (see Figure 7.6). The variance in the low velocity region ( $< 5$  rad/s in both positive and negative directions) was on an average approximately 2 times lower than that for higher velocities ( $\geq 5$  rad/s).

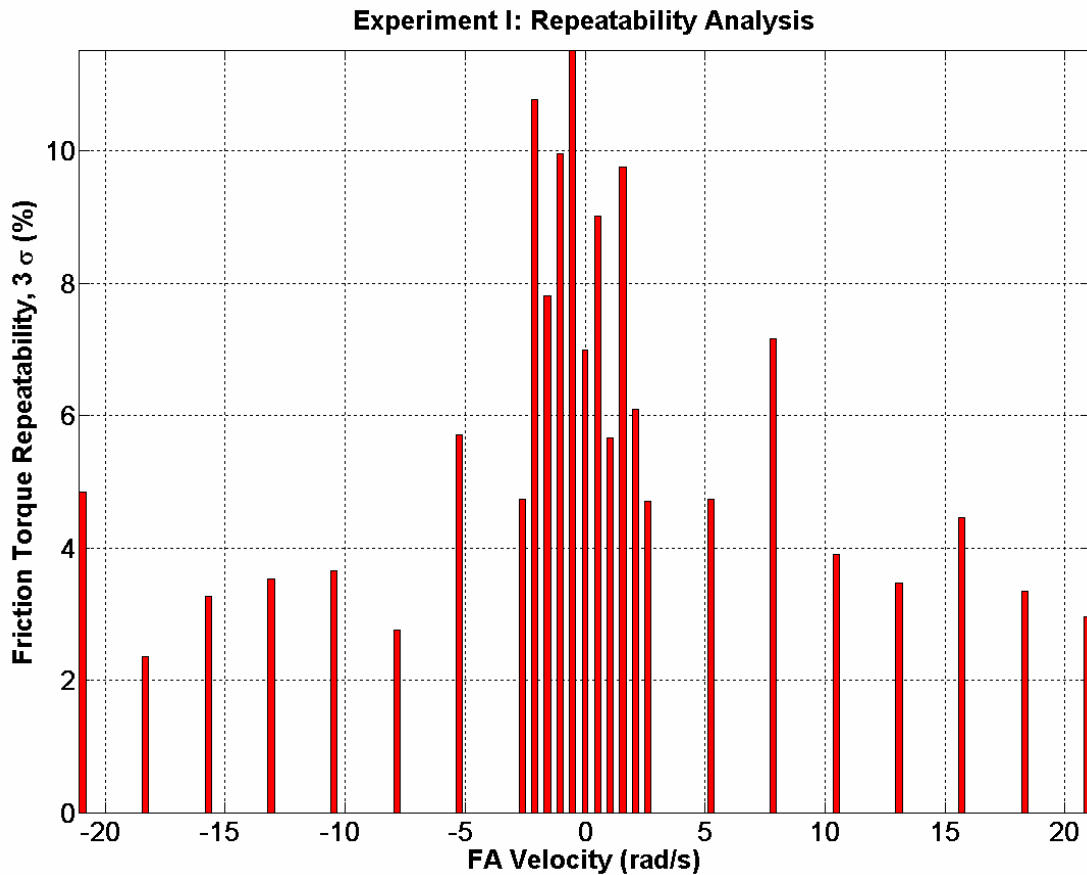


Figure 7.6. Results from repeatability analysis of our velocity-dependence experiments. The bars in this figure show the value of  $3\sigma$  in percentage for the experiment at every speed setting. Based on this bar chart, the average  $3\sigma$  for all experiments was 5.6% which indicates a relatively high repeatability.

This relatively lower repeatability at these lower velocities could be explained as follows: (i) friction has systematic and stochastic components (Armstrong-Hélouvy, 1991) and at low velocities the stochastic behavior might be predominant, (ii) the torques observed in these experiments are approximately 0.2% of the torque range of the sensor and, therefore, the sensor readings are relatively less precise, and (iii) the variance was calculated across a small sample (10 runs) and our expectation is that the repeatability would improve with a larger sample. Our main focus here was to lay out a systematic

method to characterize the velocity-dependent friction in the FA branch for very low velocities. We have only experimented with speeds as low as 25% of the rated speed of the FA motor. This is because the FA is expected to be in a low velocity zone for a significant portion of its operation (for instance, see example in Figure 6.18 from Chapter 6).

As mentioned earlier, the FFT analysis (see Figure 7.7) was performed on the filtered torque data expressed as a function of FA shaft position (Figure 7.8). The FFT was plotted using spatial frequency units (cycles/rev).

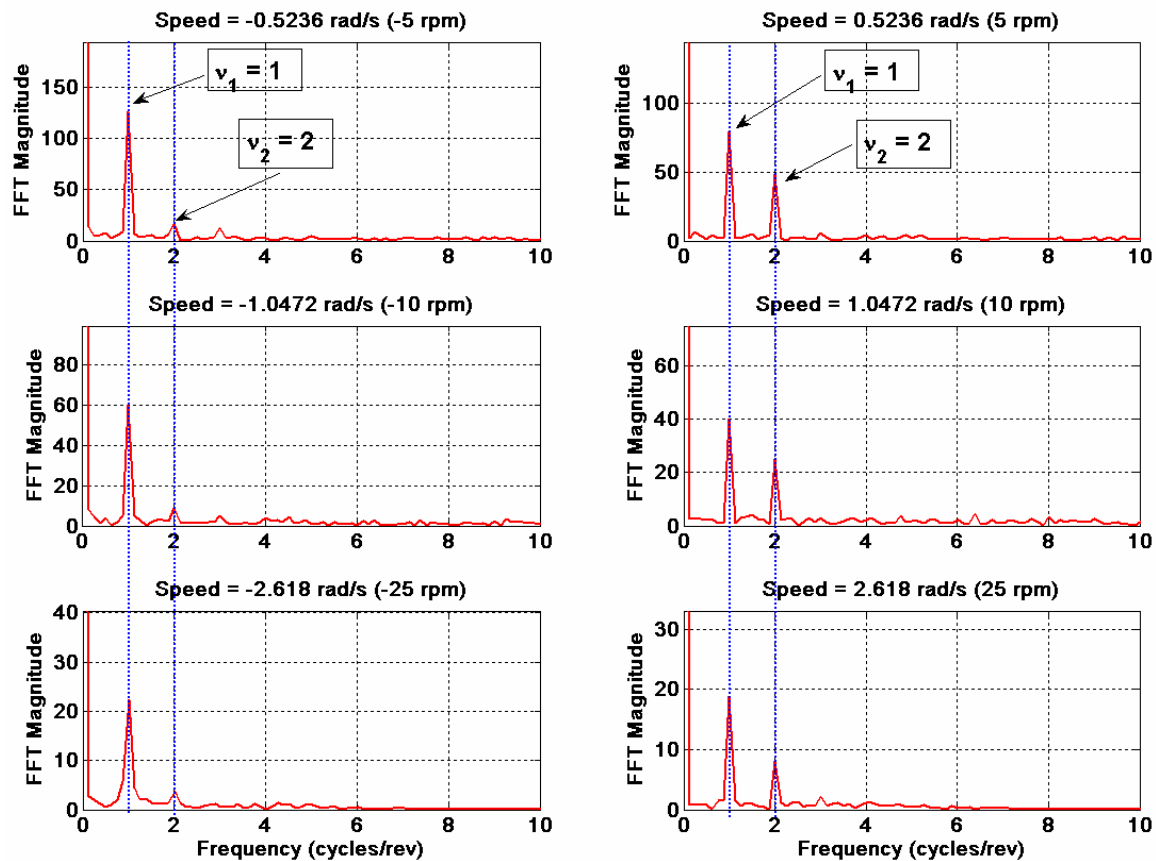


Figure 7.7. Results from FFT analysis of friction torque data as a function of FA shaft position during the experimental determination of position-dependence of friction. Note that the frequency units are cycles/rev to directly determine torque oscillation period as a multiple of FA shaft revolution.



The advantage of using these units is two-fold:

- The frequency of torque oscillation as a function of shaft revolution ( $\nu$ ) allows us to compare energy content in the torque data at various multiples of a rotation. A peak in the FFT magnitude at  $\nu = 1$  cycles/rev (fairly repeatably at various speed settings<sup>44</sup>) suggests that there is an oscillation of friction torque during every rotation of the FA shaft.
- Typically, if a peak is observed at a frequency  $\nu'$  other than  $\nu = 1$  (again, for various speed settings) then the ratio  $r_{\nu',\nu} = (\nu'/\nu)$  is indicative of torque oscillations caused due to another component which is rotating at the rate of  $r_{\nu',\nu}$  revolutions when the FA shaft rotates one revolution. In other words, it is possible to back out gear ratios in a system. For instance, in the above mentioned case,  $r_{\nu',\nu}$  could possibly be a gear ratio in the system. See (Garcia et al., 2002) for details.

In our FFT results shown Figure 7.7, we observed a peak frequency at  $\nu_1 = 1$  cycles/rev (first dashed blue line) with a  $3\sigma$  limit of 0.56%. This shows a very high repeatability of torque oscillation at the rate of rotation of the shaft. A second peak frequency of  $\nu_2 = 2$  cycles/rev (second dashed blue line) was observed with a  $3\sigma$  limit of 0.54%. This suggests that the rotation of a component at approximately 2 times the revolution of the FA shaft is causing this frequency of oscillation. Although the detailed design of the gear train, and thus the intermediate gear ratios, are not available to us, we suspect that this oscillation could be generated by a component in the differential gear train. In addition to the FFT plots, we have also included the plots of low-pass filtered torque data w.r.t. FA shaft position (see Figure 7.8) for the various speed settings experimented with and for 10 revolutions of the FA shaft. Torque oscillations can be caused due to many phenomena

---

<sup>44</sup> This requirement is inevitable to distinguish between torque oscillation frequencies arising due to position and those influenced by velocity or other sources.

such as the stress in the shaft-coupler and deflection in the bearing. Even gravity loading due to unbalanced masses could contribute to cyclic loading.

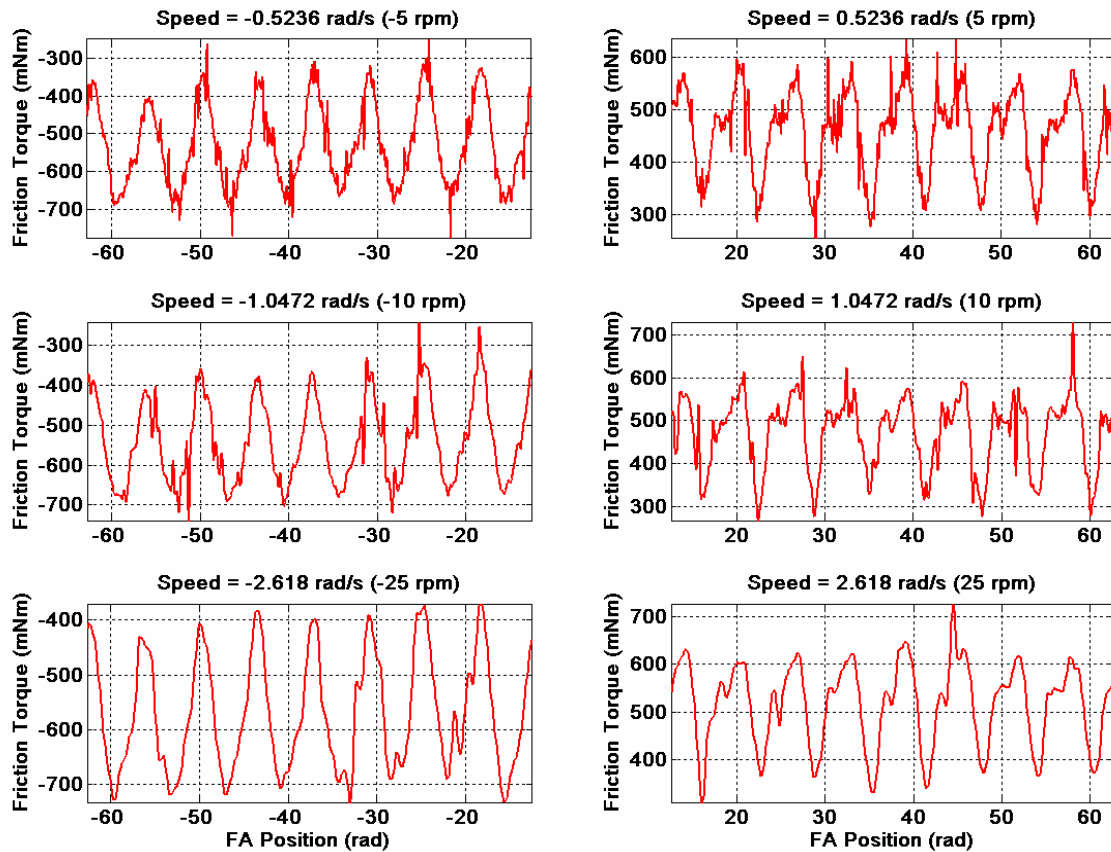


Figure 7.8. Torque data plotted with respect to FA shaft position for the six test speeds and for 10 revolutions. A low-pass second-order Butterworth filter was used with a cut-off frequency of 5 Hz.

In this section we have focussed on laying down a systematic procedure to experimentally characterize some of these position-dependent phenomena in a potential, and more refined, second prototype of the PFVA. The friction parameters identified using Experiment I have been summarized in Table 7.2.

Table 7.2 Summary of Identified Friction Parameters

	Positive	Negative
Stiction Torque (N-m)	$1.008 \pm 7\%$	$-0.9705 \pm 7\%$
Viscous Damping (N-m/rad/s)	0.002	0.0021
Viscous Damping Correlation	0.9883	0.9901
Critical Velocity (rad/s)	1.5708	-1.0472
Position-Dependent Torque Oscillation Frequencies (cycles/rev)	$\nu = 1, 2$	$\nu = 1, 2$

### 7.2.2. Experiment II: Identification of Dynamic Coupling

The focus of this experiment was to measure the dynamic coupling torque between the FA and VA. Knowledge of this coupling torque is essential to designing a control scheme for real-time operation of the PFVA. As this type of problem is unique to our actuator design (dual velocity-summing), to the best of the authors' knowledge, no experimental procedure was found in the literature to characterize such coupling between dual actuator inputs. Therefore, we believe that the experimental methodology laid out in this section to identify this phenomenon is an original contribution of this work.

#### ***THEORY AND PROCEDURE***

The theory behind this experiment follows from the model in Eq. (6.31) which can be re-written as two coupled differential equations:

$$\begin{aligned}
 I_{vv}\ddot{\phi}_v + I_{vf}\ddot{\phi}_f + {}^v\tau_F(\dot{\phi}_v, \dot{\phi}_f) + {}^v\tau_G(\phi_v, \phi_f) + g_t \left( \frac{1}{\tilde{\rho} + 1} \right) \tau_o &= \tau_{M_v} \\
 I_{vf}\ddot{\phi}_v + I_{ff}\ddot{\phi}_f + {}^f\tau_F(\dot{\phi}_v, \dot{\phi}_f) + {}^f\tau_G(\phi_v, \phi_f) + \frac{\tilde{\rho}}{\tilde{\rho} + 1} \tau_o &= \tau_{M_f}
 \end{aligned} \tag{7.1}$$

where  ${}^i\tau_F$  and  ${}^i\tau_G$  are the friction and gravitational torques reflected to input  $i \in \{v, f\}$ , respectively,  $g_t$  is the velocity ratio of the differential's casing relative to the VA motor shaft, introduced by the timing belt, and the other symbols have the meanings defined

earlier in Chapter 6 in Eq. (6.31). Now, consider the operating conditions and their modeling implications listed in Table 7.3.

Table 7.3 Conditions Imposed on PFVA in Experiment II and their Modeling Implications

Physical Condition	Mathematical Implication
The FA is controlled at zero velocity (holding position). Therefore, the friction torque due to its angular position or velocity does not exist.	$\phi_f = \dot{\phi}_f = \ddot{\phi}_f = 0$ , ${}^f\tau_F(\phi_f, \dot{\phi}_f) \approx 0$ , and ${}^v\tau_F(\phi_f, \dot{\phi}_f) \approx 0$
The output link and mass are removed and it is assumed that the gear components contribute negligible gravitational loading	${}^v\tau_G(\phi_v, \phi_f) = {}^f\tau_G(\phi_v, \phi_f) = 0$
The VA is controlled to track a particular time-varying velocity profile	$\phi_v(t), \dot{\phi}_v(t), \ddot{\phi}_v(t)$ are specified
No external loading is imposed on the system	$\tau_o = 0$

The resulting equations of motion for the PFVA after imposing those conditions are

$$\begin{aligned}
 I_{vv}\ddot{\phi}_v + {}^v\tau_F(\phi_v, \dot{\phi}_v) &= \tau_{M_v} \\
 I_{vf}\ddot{\phi}_v + {}^f\tau_F(\phi_v, \dot{\phi}_v) &= \tau_{M_f}
 \end{aligned}
 \tag{7.2}$$

The VA motor controller provides the torque  $\tau_{M_v}$  necessary to track the specified motion profile  $\phi_v(t), \dot{\phi}_v(t), \ddot{\phi}_v(t)$ . On the other hand, to ascertain that  $\phi_f = \dot{\phi}_f = \ddot{\phi}_f = 0$ , the FA motor controller provides just enough torque  $\tau_{M_f}$  to compensate the disturbance introduced by the VA. This disturbance torque is, therefore, measured by the torque sensor in the FA branch because the FA shaft is controlled to be at rest.

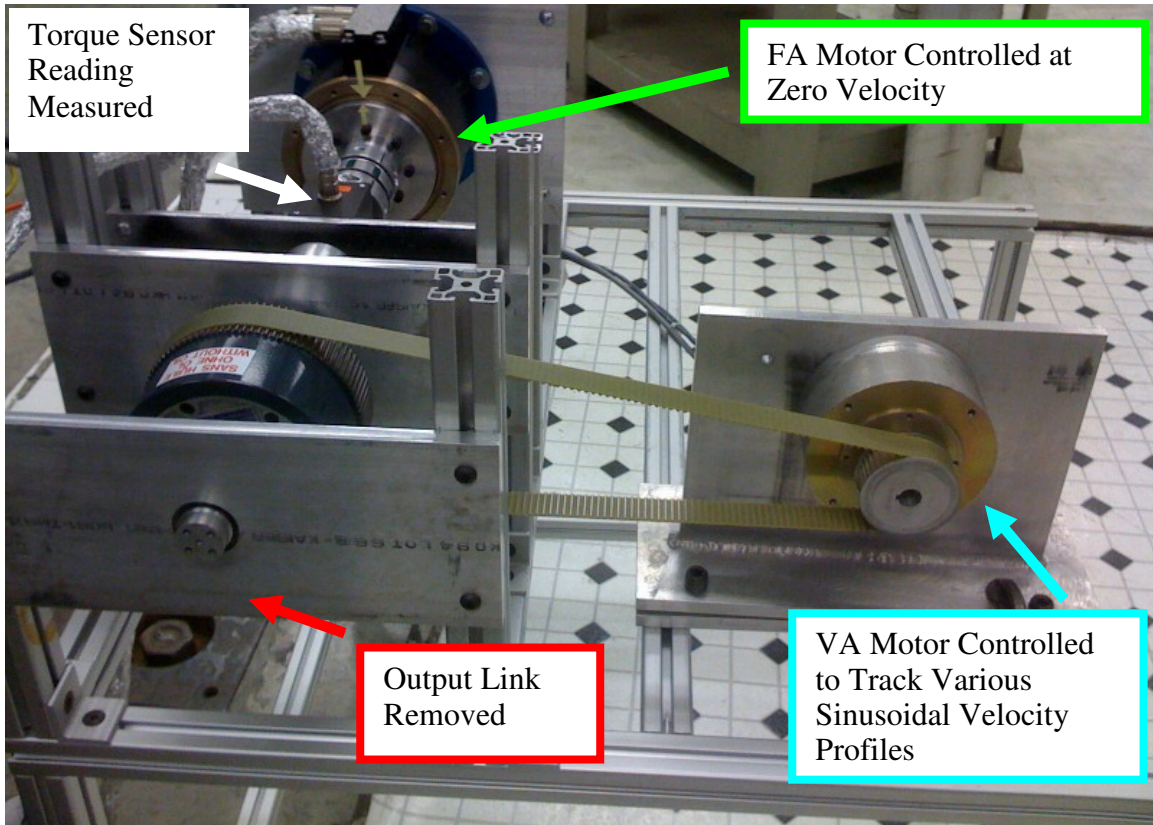


Figure 7.9. Conditions imposed on the PFVA testbed during the dynamic coupling experiment. FA motor was controlled at zero velocity, VA motor was controlled to track various velocity profiles and torque reading from the torque sensor was measured. Trends in torque reading were then correlated with the velocity profiles used.

Our methodology for this experiment follows from the above theory as explained below. The conditions imposed on the PFVA testbed for this experiment were similar to those listed in Table 7.3 (also see Figure 7.9):

- The output link was removed so that the effect of the gravity torque can be neglected.
- The VA was commanded to follow a sinusoidal velocity trajectory of varying frequencies (simple harmonic motion):

$$\dot{\phi}_v = \Omega \sin\left(\frac{2\pi t}{T} + \varphi\right) \quad (7.3)$$

where  $\Omega$  is the velocity amplitude,  $T$  is the time-period of oscillation, and  $\varphi$  is the phase-lag. It follows that

$$\phi_v = -\frac{\Omega T}{2\pi} \cos\left(\frac{2\pi t}{T} + \varphi\right) \text{ and } \ddot{\phi}_v = \left(\frac{2\pi\Omega}{T}\right) \cos\left(\frac{2\pi t}{T} + \varphi\right) \quad (7.4)$$

- The FA was commanded to hold position.

	1 Hz	0.5 Hz	0.25 Hz
50 rpm	5	2	6
100 rpm	7	4	1
200 rpm	3	8	9

- The measurement from the torque sensor under the above conditions approximately indicates a combination of (i) the inertial coupling torque on the FA motor due to the acceleration of the VA motor shaft, (ii) the coupling viscous friction torque on the FA motor due to the velocity of the VA (see Section 6.2.1), and, possibly, (iii) the disturbance on the FA dependent on the position of the VA. The FA and VA encoder values were used for velocity measurement. Acceleration was computed using finite differencing from the velocity measurements in LabVIEW. The position of the VA was measured using the encoder counts of the VA motor. The experiments were done for the speed and period combinations shown in Table 7.4. The numbers in the cells of this table suggest the randomized order in which these experiments were done.
- The coupling terms in the dynamic model in Eq. (7.1) were studied by determining the cross-correlation (Ingle and Proakis, 1997; Proakis and Manolakis, 2007) between three pairs of signals: (i) torque data and VA acceleration data, (ii) torque data and VA velocity measurements, and (iii) torque data and VA position measurements. Cross-correlation  $r_{xy}$  between two time-based signals  $x(t)$  and  $y(t)$  is given by

$$r_{xy}(\tau) = \int_{-\infty}^{\infty} x(t)y(t-\tau)dt \quad (7.5)$$

which, for discrete-time periodic signals with a common period  $N$ , reduces to

$$r_{xy}(m) = \frac{1}{N} \sum_{n=0}^{N-1} x(n)y(n-m) \quad (7.6)$$

The parameter  $m$  is called the time-shift or lag (Proakis and Manolakis, 2007) and the maximum lag introduced in our experiment for the frequencies 0.25 Hz, 0.5 Hz, and 1 Hz were 300, 200, and 100, respectively. In the notation in Eqs. (7.5) and (7.6), the order of the subscripts  $xy$  indicates that  $x$  is unshifted while  $y$  is shifted.

- Signal noise was filtered using a second-order forward-backward Butterworth filter. It is important to do both forward and backward filtering to eliminate the lag introduced by the filter. This lag would bias our cross-correlation results. Note that, however, forward-backward filtering can be performed only in off-line situations such as ours. Another filtering induced artifact is the transient at the beginning. Therefore, the experiment was run for exactly 12 oscillations for every amplitude and time-period combination, and the first and last time-periods were ignored during cross-correlation.

### ***DATA ANALYSIS AND RESULTS***

The time-domain plots of the position, velocity, and acceleration of the sinusoidal VA motion (see Figure 7.10) and the frequency-domain plot of the disturbance torque  $\tau_{vf}$

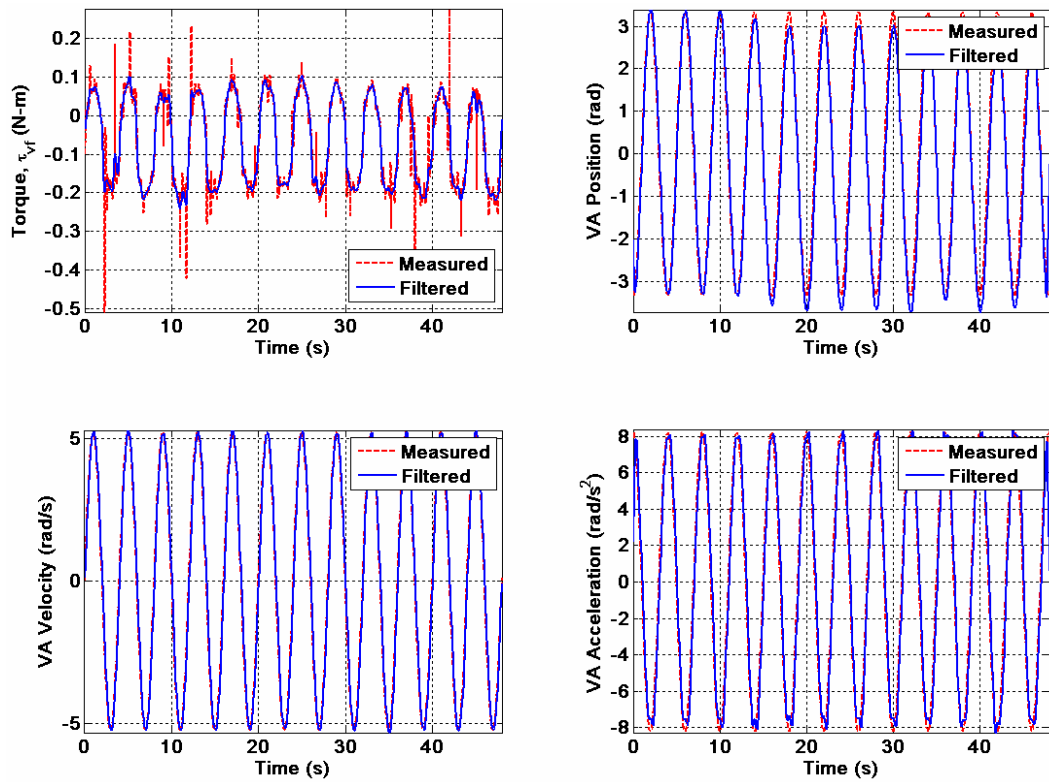


Figure 7.10. Torque sensor measurements and position, velocity, and acceleration data for Experiment II using 5.23 rad/s cycled at 0.25 Hz.

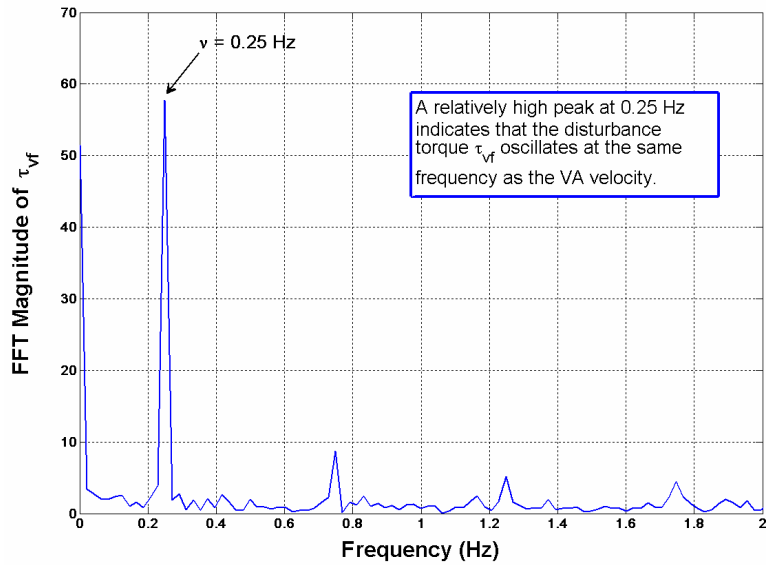


Figure 7.11. FFT of torque data for Experiment II using 5.23 rad/s cycled at 0.25 Hz.



(see Figure 7.11) confirmed that the disturbance felt by the FA motor follows the same frequency as the sinusoidal motion profile of the VA. As an example, for 50 rpm sinusoidal velocity amplitude and a frequency of 0.25 Hz, notice the relatively high peak in the FFT magnitude of the disturbance torque in Figure 7.11 at the same frequency. The corresponding time-domain plot is shown in Figure 7.10. Now, as  $\tau_{vf}$  and the VA motion have the same frequency of oscillation we can use the cross-correlation analysis for periodic signals discussed in Eq. (7.6).

### CROSS-CORRELATION FOR 50 RPM (5.23 RAD/S)

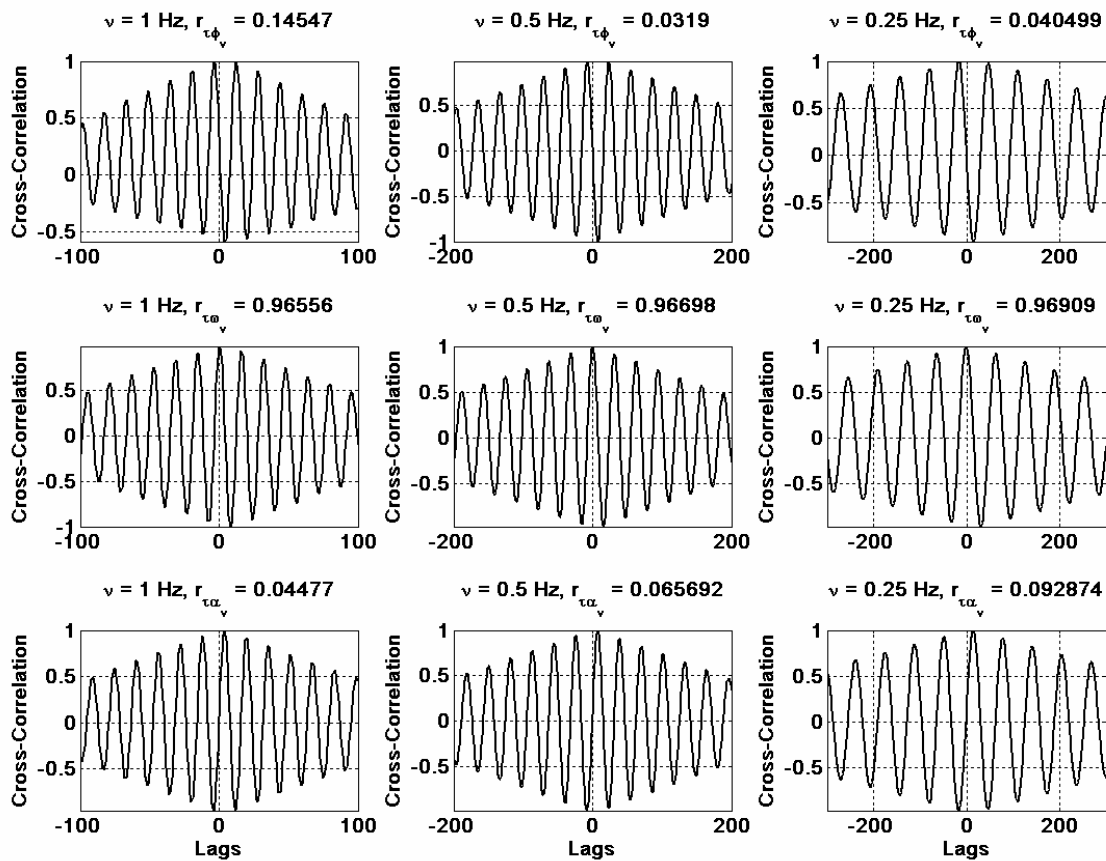


Figure 7.12. Cross-correlation results for 50 rpm (5.23 rad/s). The first, second, and third row represent correlations of the disturbance torque with VA position, velocity, and acceleration, respectively. The first, second, and third columns represent results for 1, 0.5, and 0.25 Hz, respectively.

As an example result, the cross-correlation function magnitudes for various lag values are shown in Figure 7.11. The first, second, and third rows in this figure correspond to correlation of  $\tau_{vf}$  with position, velocity, and acceleration of the VA, respectively. For instance, in the bottom right corner of this figure is shown the correlation magnitude ( $r_{\tau\alpha_v} \approx 0.093$ ) and cross-correlation results for 50 rpm and 0.25 Hz between  $\tau_{vf}$  and the VA acceleration for this setting. These results suggest that, for our experiment, the disturbance torque is strongly correlated (for example,  $r_{\tau\omega_v} \approx 0.965$  for 1 Hz) with the velocity of the VA and, at the same time, weakly correlated with the acceleration ( $r_{\tau\alpha_v} \approx 0.044$ ) and position signals ( $r_{\tau\phi_v} \approx 0.145$ ).

### CROSS-CORRELATION FOR 100 RPM (10.46 RAD/S)

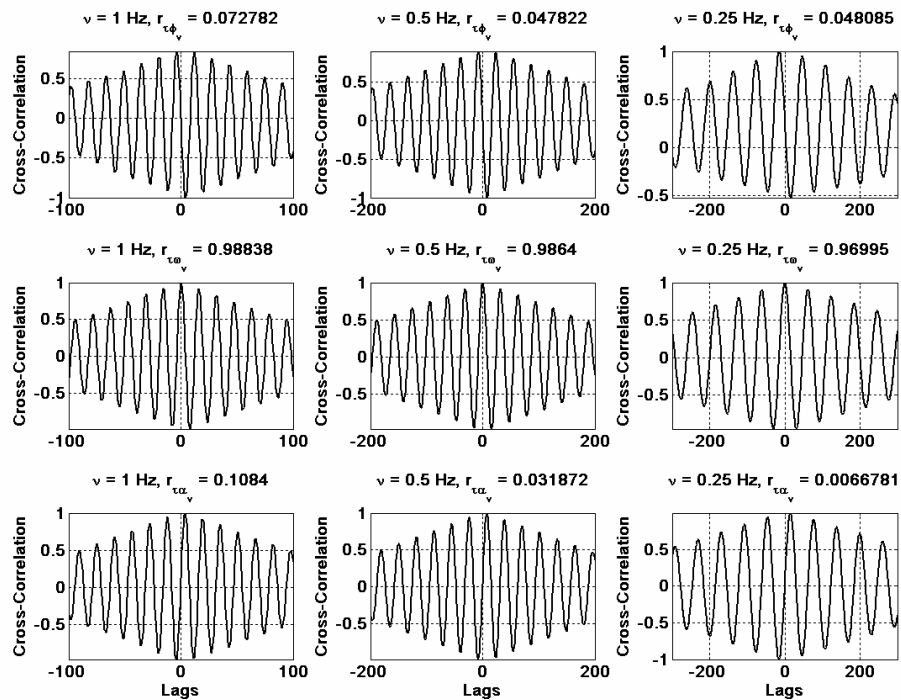


Figure 7.13. Cross-correlation results for 100 rpm (10.46 rad/s). The first, second, and third row represent correlations of the disturbance torque with VA position, velocity, and acceleration, respectively. The first, second, and third columns represent results for 1, 0.5, and 0.25 Hz, respectively.

### CROSS-CORRELATION FOR 200 RPM (20.93 RAD/S)

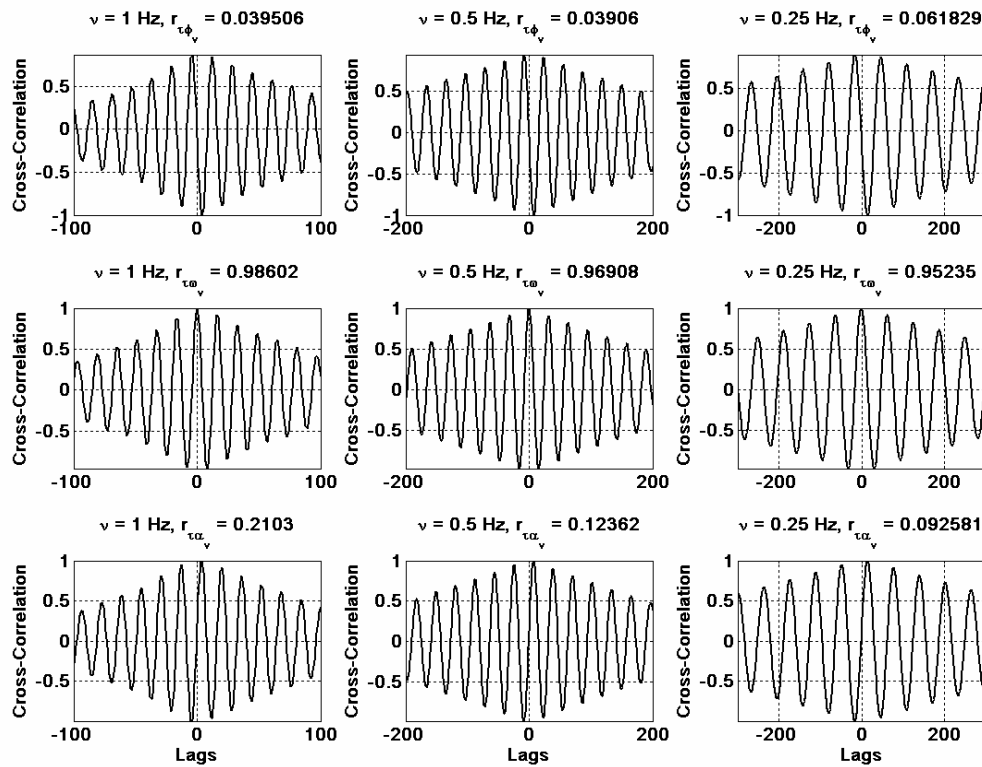


Figure 7.14. Cross-correlation results for 200 rpm (20.93 rad/s). The first, second, and third row represent correlations of the disturbance torque with VA position, velocity, and acceleration, respectively. The first, second, and third columns represent results for 1, 0.5, and 0.25 Hz, respectively.

Table 7.5 Cross-Correlation Analysis Summary

	Torque-Position	Torque-Velocity	Torque-Acceleration
Correlation	0.05855	0.972646	0.08631
Repeatability (Across 9 Readings)	60%	1.22%	70%

These results were also produced for the other speed settings as shown in Figure 7.13 and Figure 7.14. The cross-correlation data was tabulated (see Table 7.5) to examine the repeatability of this result. It was observed that the mean correlations (over the 9 settings listed in Table 7.4) for torque vs. position, velocity, and accelerations were, respectively, 0.05855 ( $\pm 60\%$ ), 0.972646 ( $\pm 1.22\%$ ), and 0.08631 ( $\pm 70\%$ ). There was poor repeatability in the position and acceleration correlations possibly due to a small sample of 9 readings. On the contrary, the torque to velocity correlation was very strong and repeatable in spite of the small sample size.

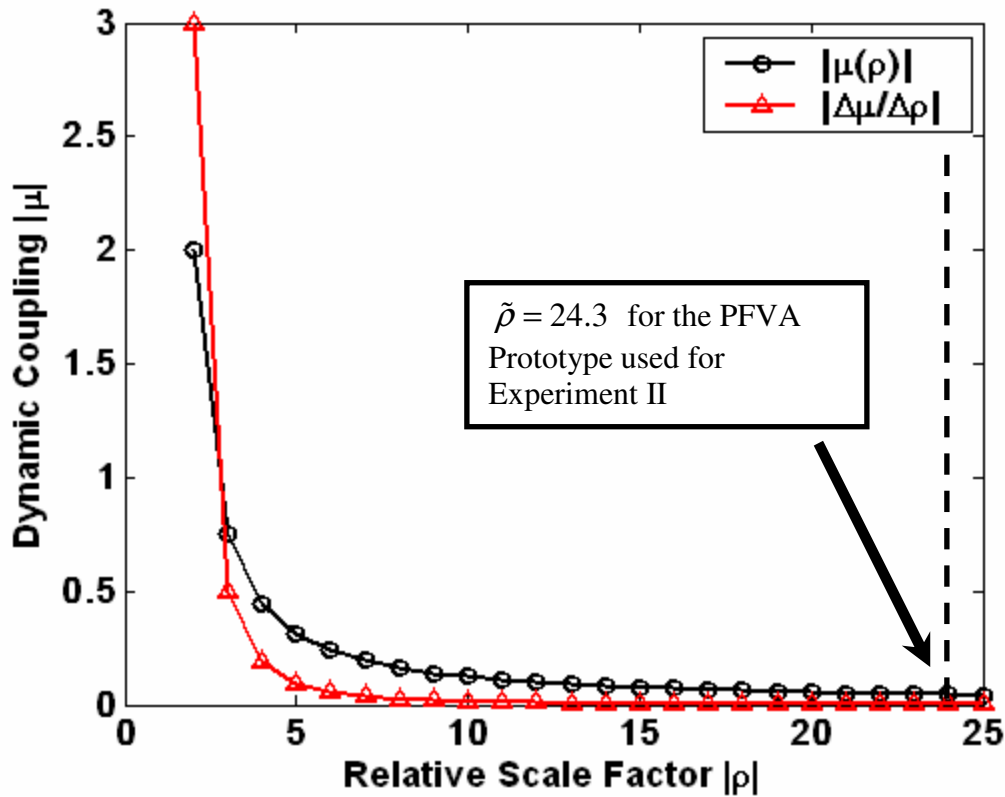


Figure 7.15. Variation of dynamic coupling factor<sup>45</sup> between the FA and VA, and its derivative as a function of the RSF. Note that as  $\tilde{\rho} \rightarrow \infty$ ,  $\tilde{\mu}, \tilde{\mu}' \rightarrow 0$ . This figure is adapted from (Rabindran and Tesar, 2007a, pp. 421)<sup>46</sup>.

<sup>45</sup> This term was introduced in Chapter 5 in Eq. (5.28)

<sup>46</sup> Note that the use of tilde in  $\tilde{\rho}$  and  $\tilde{\mu}$  is a notation we have adopted since the publication of (Rabindran and Tesar, 2007a) for dimensionless parameters.

The physical meaning of this result can be investigated by partitioning  $\tau_{vf}$  into various components<sup>47</sup> dependent on the acceleration, velocity, and the position of the VA:

$$\tau_{vf} = I_{vf} \ddot{\phi}_v + \tau_{vf}(\dot{\phi}_v) + \tau_{vf}(\phi_v) \quad (7.7)$$

Now, the first term on the right hand side of Eq. (7.7) is dependent on the inertial coupling between the two inputs which in turn is a function of the RSF  $\tilde{\rho}$  as shown in Figure 7.15 (Rabindran and Tesar, 2007a). In our testbed,  $\tilde{\rho} = 24.3$  which according to the model shown in Figure 7.15 corresponds to  $\tilde{\mu} \approx 0.038$ . This results in a very low disturbance torque component due to inertias. We hypothesize that this could be a prominent reason for the weak correlation between  $\tau_{vf}$  and VA acceleration. The weak correlation with position can be explained by the fact that there is neither gravity loading nor position-dependent friction from the FA branch. The strong correlation of the disturbance torque with velocity is probably because the FA motor's PID controller is reacting primarily to velocity-disturbances acting on the FA shaft more than any other kind of influence. Therefore the FA motor's active torque, and thus, the torque measured by the torque sensor both follow the trend of the VA velocity profile. This hypothesis can be easily tested by monitoring the current on the FA motor. Future experiments might benefit from the presence of an accelerometer in the FA branch and another torque sensor in the VA branch. In summary, the objective of this experiment was to achieve the following goals:

- Confirm the presence of a dynamic coupling phenomenon. This is a fairly intuitive behavior in a dual velocity-summing mechanism; however it was important for us to characterize it.
- Devise an experiment to measure this phenomenon. As explained earlier, due to the conditions imposed on the FA motor there is a good chance (98.77%) that the

---

<sup>47</sup> See Eq. (7.2) for a discussion on modeling the disturbance  $\tau_{vf}$ .

measured disturbance torque follows the same trend as the VA velocity due to the PID action of the FA motor. However, the methodology laid out in this section is a first step towards a more refined characterization of dynamic coupling.

- Compare the relative contributions of VA position, velocity, and acceleration to the torque disturbance on the FA branch. According to the results presented in Table 7.5, the VA velocity is approximately 2 orders of magnitude more correlated with the disturbance torque than the position or acceleration.

### 7.2.3. Experiment III: Utilizing Redundancy to Mitigate Low-Velocity Friction

In Experiment I we have shown that the PFVA drive can have high stiction in the FA branch which in turn can affect low-velocity performance of this device. In addition, although not demonstrated experimentally in our work, the stick-slip phenomenon (Armstrong-Hélouvry, 1991) is a performance diminishing effect which becomes dominant during low velocity motion. However the kinematic redundancy in the drive (as a result of dual inputs) can be exploited to mitigate these friction effects by using relatively high null space velocities. This was theoretically shown in Chapter 6 in Section 6.1.1. In Experiment III, our goal was to demonstrate this capability using the PFVA prototype. Similar work has been reported in the literature by Ontañón-Ruiz et al. (1998). In this experiment, we will build on the theoretical background developed by them and, additionally, study the influence of the RSF  $\tilde{\rho}$  on the capability of the PFVA to utilize its null space motion effectively.

#### ***THEORY AND PROCEDURE***

The theory behind this experiment was discussed in Section 6.1.1. For a velocity specification  $\dot{\phi}_{od}$  at the output, the pseudo-inverse based solution to determine the required VA and FA velocity commands ( $\dot{\phi}_{vd}$  and  $\dot{\phi}_{fd}$ ) was expressed in the following form in Section 6.1.1

$$\begin{aligned}\dot{\phi}_{vd} &= \left( \frac{\tilde{\rho}+1}{\tilde{\rho}^2+1} \right) \dot{\phi}_{od} + k \left( \frac{-\tilde{\rho}}{\tilde{\rho}^2+1} \right) \\ \dot{\phi}_{fd} &= \left( \frac{\tilde{\rho}(\tilde{\rho}+1)}{\tilde{\rho}^2+1} \right) \dot{\phi}_{od} + k \left( \frac{1}{\tilde{\rho}^2+1} \right)\end{aligned}\tag{7.8}$$

where  $k$  is a scaling factor to choose null-space velocities, and  $\tilde{\rho}$  is the RSF for the differential drive train. Note that in our prototype there is an additional reduction in the VA branch due to the timing belt with velocity ratio  $g_t$ . Therefore Eq. (7.8) needs to be modified to account for this addition transmission ratio. The complete transformation of the VA and FA motor velocities to the output can be written in the form

$$\dot{\phi}_o = \begin{bmatrix} 1 & \tilde{\rho} \\ \tilde{\rho}+1 & \tilde{\rho}+1 \end{bmatrix} G_b \begin{bmatrix} \dot{\phi}_v \\ \dot{\phi}_f \end{bmatrix}\tag{7.9}$$

where  $G_b \in R^{2 \times 2}$  is a diagonal matrix of ‘back-end’ velocity ratios<sup>48</sup>:

$$G_b = \begin{bmatrix} g_{v_b} & 0 \\ 0 & g_{f_b} \end{bmatrix}\tag{7.10}$$

In Eq. (7.9),  $g_{v_b}$  and  $g_{f_b}$  are the velocity ratios of transmissions that might exist between the differential train and the VA and FA motors, respectively. If no transmission exists then this velocity ratio will be unity. In our testbed,  $g_{v_b} = g_t$  the timing belt velocity ratio, and  $g_{f_b} = 1$  because the FA motor is directly connected to the differential. Now, comparing Eqs. (7.8) and (7.9) we have, in our case,

$$\begin{aligned}\dot{\phi}_{vd} &= \frac{1}{g_t} \left( \frac{\tilde{\rho}+1}{\tilde{\rho}^2+1} \right) \dot{\phi}_{od} + \frac{k}{g_t} \left( \frac{-\tilde{\rho}}{\tilde{\rho}^2+1} \right) \leq \dot{\phi}_{v\_max} \\ \dot{\phi}_{fd} &= \left( \frac{\tilde{\rho}(\tilde{\rho}+1)}{\tilde{\rho}^2+1} \right) \dot{\phi}_{od} + k \left( \frac{1}{\tilde{\rho}^2+1} \right) \leq \dot{\phi}_{f\_max}\end{aligned}\tag{7.11}$$

---

<sup>48</sup> In most of our models in this report, we have not considered transmission ratios that could potentially exist between the FA/VA motor and the differential drive. Equations (7.9) and (7.10) can as well be used with other models in this report to investigate the effect of a back-end velocity ratio. This is left as an exercise for the interested reader.

For this experiment, we chose  $\dot{\phi}_{v\_max} = \dot{\phi}_{f\_max} = 200$  rpm based on the capability of the VA and FA motors and considering a safe operating speed,  $\tilde{\rho} = 24.27$ , and  $g_t = 0.4383$ . This makes the gross ratio of the velocity ratios of the FA and VA approximately equal to 55.367. In our experiment we specified the output velocity to be a sinusoidal function with amplitude of 0.25 rpm and a period of 10 seconds (0.1 Hz). Using Eq. (7.11) we then determined the corresponding specifications of the VA and FA motor velocities. The ideal value of the null velocity scaling factor in order to maximize the null space velocities to avoid low velocity friction was  $k = 97$  (corresponding to VA null velocity of 200 rpm). However in this condition the VA motor velocity tracking was poor. Therefore, we reduced the scaling factor to  $k = 50$ . The output velocity was then computed based on the model in Eq. (7.9).

#### ***DATA ANALYSIS AND RESULTS***

The results from our experiment are shown in Figure 7.16 as velocity trajectories of the VA, FA, and the output. Consider the fact that to control a velocity of 0.25 rpm at the output in the absence of the other input, the VA and FA would have to be controlled at approximately 13.75 ( $\approx 55 \times 0.25$ ) rpm and 0.25 rpm, respectively. In our experiment, however, due to the use of null velocities of the FA and VA, they are both spinning at significantly higher speeds (approximately a factor of 10) than they would if they were the only input while maintaining the output velocity to be 0.25 rpm. This demonstrates how the PFVA can be used to increase the operational speeds of the inputs for very low specified output speeds. This mode of operation can be used to stay away from low-velocity friction zones. One disadvantage of using the drive in this mode is that each motor controller is now trying to reject the disturbance torque introduced by the other input. We suspect that this disturbance torque causes the poor tracking (RMS error of 2.6 rpm) of the VA velocity specification as evidenced in the second plot in Figure 7.18. At



the same, notice that this error in tracking does not significantly influence the tracking at the output due to the low velocity ratio of the VA (approx. 0.0174). In our dynamic coupling model (for example, Eqs. (5.31) and (5.32)) we have shown that the disturbance torque felt by both inputs are equal and opposite to one another. Therefore, when the VA feels the disturbance in the above case and tracks poorly, the FA is also feeling the same disturbance. However, in our testbed, the FA motor is much stronger than the VA motor (approximately an order of magnitude more continuous torque capability). So, the FA tracking performance is not affected as significantly as the VA tracking.

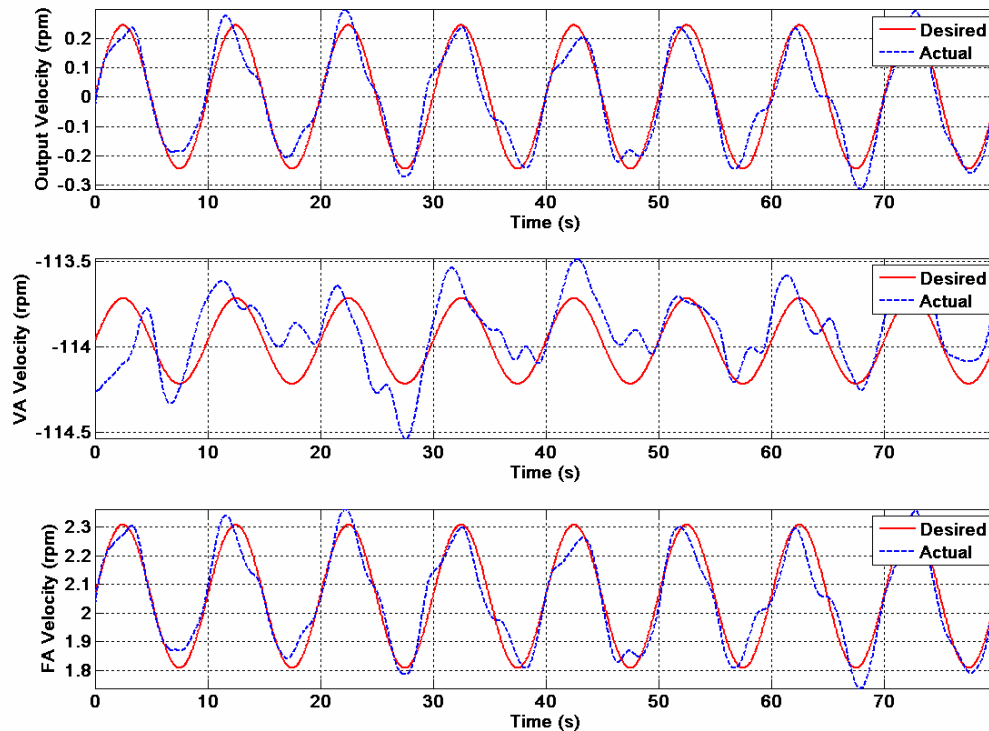


Figure 7.16. Velocity Trajectories of the VA, FA, and the Output During a Sinusoidal Trajectory Tracking Task by Utilizing Null Space Velocities to Stay Away from Low-Velocity Zones.

Another noteworthy observation from this experiment is the influence of RSF  $\tilde{\rho}$  on our choice of null-space velocities. In Figure 7.17 we show the vector space of the VA

and FA motor velocities. Note that in this figure, the pseudo-inverse solution (called the  $p$ -line) and null-space velocities (lying on the  $n$ -line) have already been mapped to the FA/VA motors using Eq. (7.11). Therefore, in the motor velocity space, the mapped pseudo-inverse and null sub-spaces will not be orthogonal as shown in Figure 6.1 due to the scaling factor  $g_t$ . The RSF and  $g_t$  determine the slopes of the  $p$ - and  $n$ - lines. In our case, for null-motion at the output, the maximum FA motor velocity is

$$\dot{\phi}_{f\_max} = \dot{\phi}_{v\_max} \left( \frac{g_t}{\tilde{\rho}} \right) = 200 \left( \frac{0.4483}{24.27} \right) = 3.61 \text{ rpm.}$$

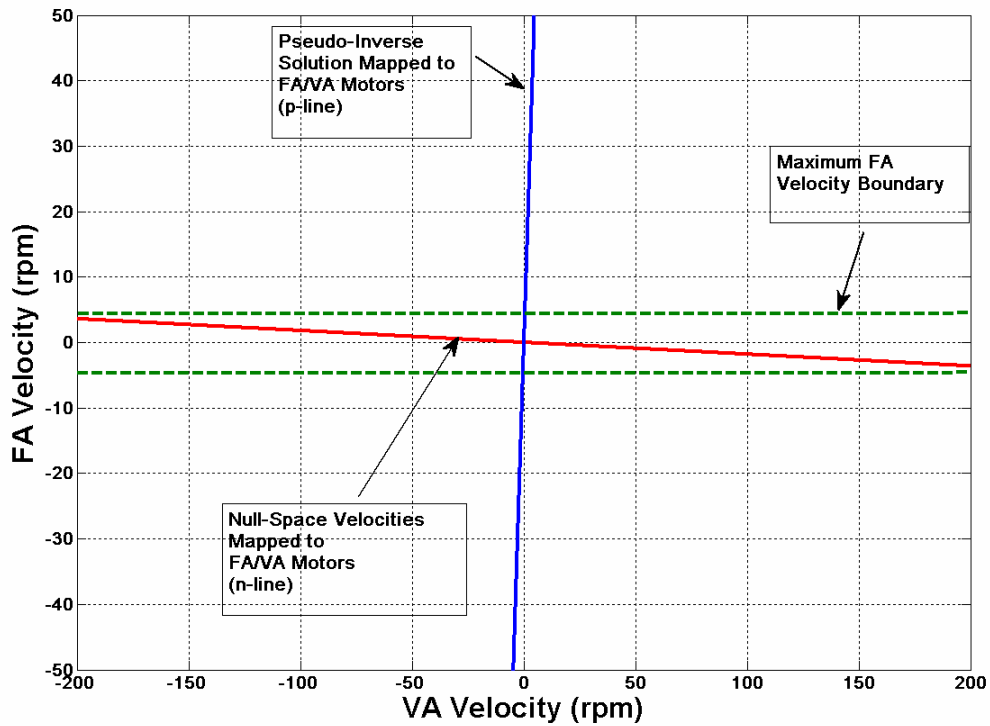


Figure 7.17. Velocity Trajectories of the VA, FA, and the Output During a Sinusoidal Trajectory Tracking Task by Utilizing Null Space Velocities to Stay Away from Low-Velocity Zones.

Therefore, as  $\tilde{\rho}$  increases, our choice of FA motor null-velocities diminishes because the  $n$ -line leans more toward the VA velocity axis. Note also that choosing non-zero specification for output velocity, the range of null-velocities for the FA diminishes

further. From this analysis, we believe it is very clear that the output velocity is predominantly dictated by the FA motor velocity ( $p$ -line leans more toward FA axis) and the null-motion is primarily dictated by the VA velocity ( $n$ -line leans more toward VA axis). In summary, our goals in Experiment III were to

- Demonstrate that the kinematic redundancy in the PFVA can be utilized to drive the FA and VA at much higher velocities than if they were single inputs. This mode of operation helps in operating away from low-velocity zones where stick-slip and stiction effects become dominant.
- Investigate the effect of RSF on the choice of null-space velocities. It was observed that with increasing RSF, the FA range of choices on the FA null velocity diminishes.

#### **7.2.4. Experiment IV: Safety to Collisions Using FA's Controlled Backdriveability**

In Experiments I and II we focused on identifying some relevant model parameters for the PFVA. In Experiment III we demonstrated the operational mode for the PFVA where the FA and VA are both under velocity control. We will now begin to study the dynamic response of the PFVA when the VA is commanded a velocity trajectory and the torque level on the FA is controlled to improve the safety of the device during collisions. Two types of collisions were experimented with: (i) slow collisions with approach velocities less than 0.5 m/s, and (ii) impulse loading.

##### ***Response to Slow Collisions***

The objective of this experiment was to demonstrate the safety feature of the PFVA when an obstacle resists the motion of the output link. This was made possible due to the controlled backdriveability of the FA input. The backdriveability of the FA was

controlled by setting a safe torque limit on its motor. The theory behind Experiment IV was discussed in great detail in Chapter 6 under Section 6.4.1 with dynamic simulations.

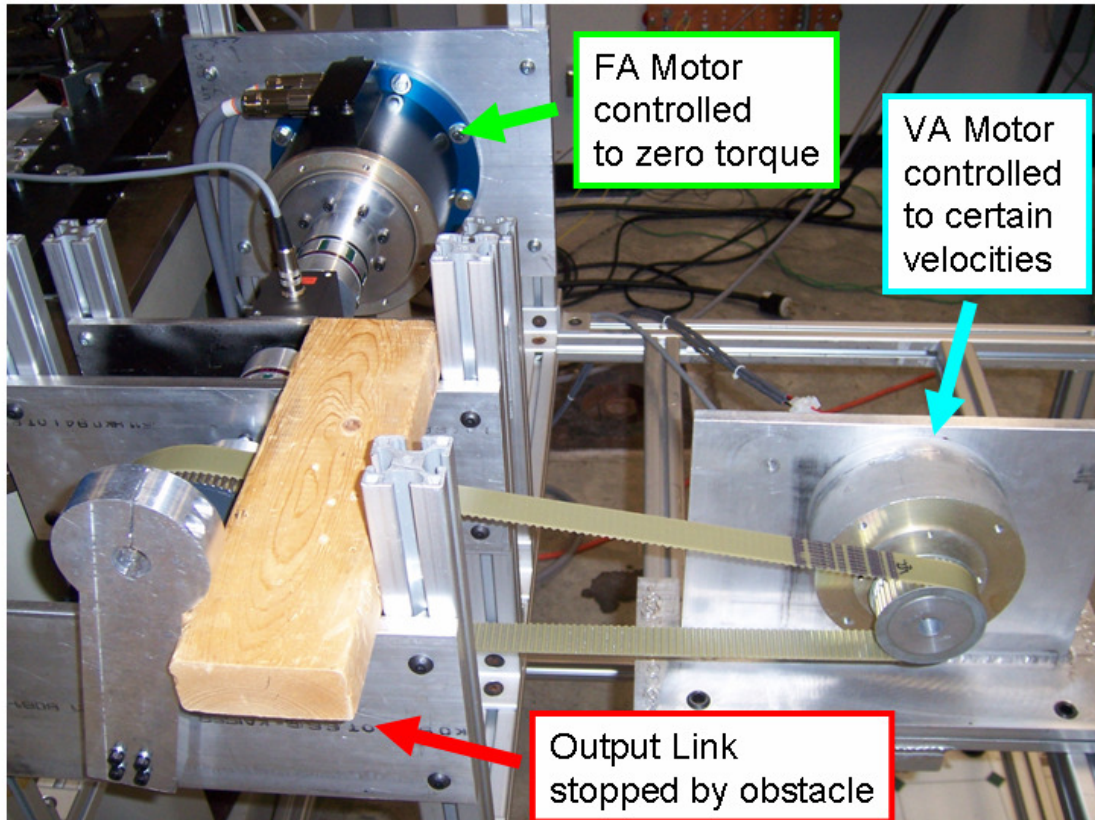


Figure 7.18. Conditions imposed on the PFVA testbed during Experiment IV for response to slow collisions.

**Procedure.** The FA motor was controlled at zero torque while the VA motor was running at a constant speed. The safety limit of the FA in this condition is zero. This is equivalent to the FA motor not present; however there is some torque resistance in this branch due to friction. Two sets of readings were taken by choosing two different VA velocities: 109.08 (11.417) and -150 (-15.7) rpm (rad/s). During the motion of the output link, an obstacle was placed in the link's path to resist its motion (see Figure 7.18). As long as the link made contact with the obstacle, the link was restricted from moving. Consequently, the

output branch of the differential develops a certain amount of torque, backdriving the FA motor while the VA velocity is not affected. Torque data was sampled at 20 Hz. Using a second-order low-pass forward-backward Butterworth filter the FA and VA velocity data, and the torque data were filtered with a cut-off frequency of 10 Hz. A certain time after the FA began backdriving, the obstacle was manually removed from the link's path, thus restoring the motion of the system to its state before the obstacle was introduced. This manual introduction and removal of the obstacle caused some transients in the torque and velocity readings, although not significant. To eliminate the signal artifacts due to forward-backward filtering, 10% of the total time from the beginning and the end was ignored for our data analysis. Although in this experiment the safety limit on the FA motor was set to zero, any other value can be potentially set.

**Results.** Our results for this experiment show plots (Figure 7.19 and Figure 7.20) of the velocities of the three shafts connected to the differential, namely VA ( $\dot{\phi}_v$ ), FA ( $\dot{\phi}_f$ ), and the output ( $\dot{\phi}_o$ ), and the torque measured by the torque sensor. Three distinct phases in these plots are notable: (i) free space motion of the output link, (ii) introduction of the obstacle (denoted by the green  $C_0$  line), and (iii) removal of the obstacle (denoted by the red  $C_n$  line). The results are shown for different runs of the experiment with varying speeds of the VA ( $\dot{\phi}_v$ ).

In Figure 7.19, notice that during the first phase of the motion (free-space), the specified constant velocity of the VA (109.08 rpm = 11.42 rad/s) results in a constant velocity of the output link. Although there is a disturbance torque acting on the FA input due to the VA motion (as shown in Experiment II in 7.2.2) and the FA is controlled at zero torque, the FA shaft is at rest because the disturbance is not greater than the static friction torque during this phase (see Experiment I in Section 7.2.1 for details on friction identification in the FA branch). At the first dashed-line  $C_0$  in Figure 7.19 (after

approximately  $t = 6.5\text{s}$ ), the link encounters a manually introduced stationary obstacle (wooden block shown in Figure 7.19) with an approach velocity of  $0.0326\text{ m/s}$  (computed based on the distance of  $0.158\text{m}$  between the point of collision on the link and its rotational center). This collision introduces a resisting torque in the direction opposite the link's commanded motion. This torque is reflected at the FA input according to its  $g_f$  function and is measured by the torque sensor. The FA motor shows minimal resistance to this resisting torque (dictated by the static friction and the motor controller loop-gains in this branch), since it is torque-controlled to maintain zero torque.

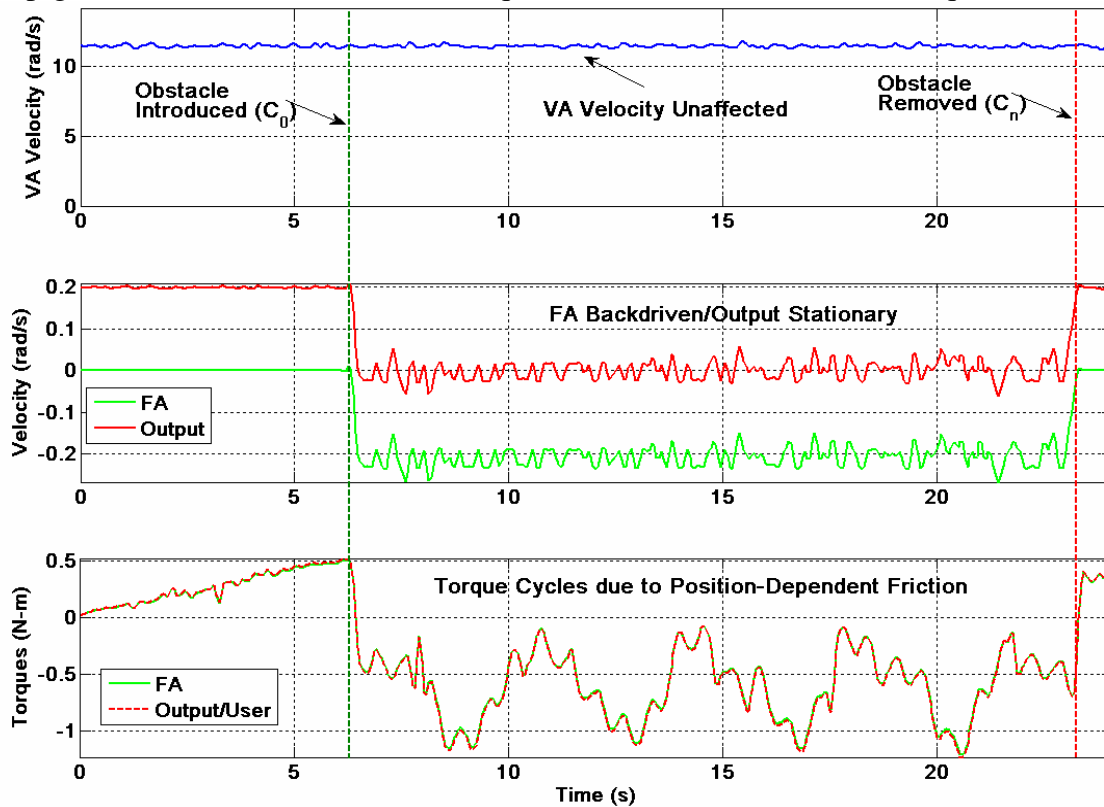


Figure 7.19. Results for Experiment IV when  $\dot{\phi}_v = 11.42\text{ rad/s}$  (link approach velocity =  $0.0326\text{ m/s}$ ). This experiment demonstrates the safety feature of the PFVA due to the backdriveability of the FA input. Three distinct phases are notable and separated by dashed-lines: (i) free space motion of the output link, (ii) introduction of the stationary obstacle ( $C_0$  line), and (iii) removal of the obstacle ( $C_n$  line).

Since the VA velocity was chosen as 2 times the relative scaling between the inputs (55.367), the velocity of the backdriven FA is approximately  $-0.2093$  rad/s (governed by the dynamics of this system modeled in Chapter 6 in Section 6.4.1 with  $\dot{\phi}_o = 0$ ). Therefore, the backdriving velocity of the FA motor depends on the relative scale factor  $\tilde{\rho}$  and the commanded VA velocity (governed by Eq. (7.9) in Experiment III discussed in Section 7.2.3 ). During this phase, the velocity of the VA is not affected because it is insensitive to disturbances at the output (owing to its relatively small velocity ratio  $g_v \approx 0.01736$ ).

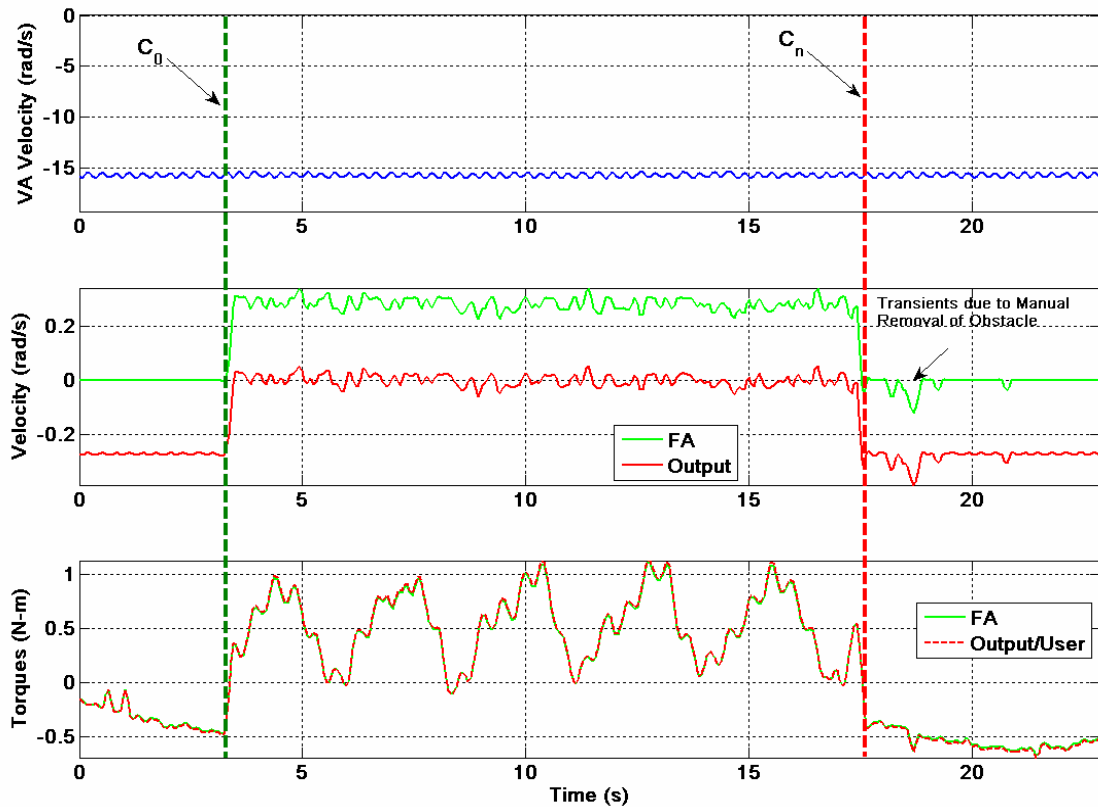


Figure 7.20. Results for Experiment IV repeated for  $\dot{\phi}_v = -15.7$  rad/s (link approach velocity = 0.0448 m/s).

Notice that when the FA shaft attains an approximately steady velocity of  $-0.2093$  rad/s, the torque reading cycles due to the position-dependent friction phenomenon discussed in

Experiment I. Figure 7.9 also shows the torque felt at the output link if a user interacts with the device. This torque was computed based on the torque sensor reading, a forward driving efficiency of 0.98 for the FA branch (Andantex, Inc, 2007), and the g-function of the FA  $g_f \approx 0.96$ . Notice that the user and FA feel the same torque due to the almost perfect efficiency and the near direct-drive nature of the FA. At approximately 17.5s, the obstacle was gradually (manually) removed. Consequently, the output link regains its originally specified speed and the FA motor stops rotating. Note that the non-zero torque readings before  $C_0$  and after  $C_n$  are due to the gravity load of the link.

The experiment was repeated with one other value for the VA velocity to produce a higher approach velocity of the link before colliding with the obstacle. Figure 7.20 shows the same behavior as presented for the first case shown in Figure 7.19. The commanded VA velocity in this case was -15.7 rad/s resulting in an approach velocity of 0.0448 m/s. The obstacle causes the FA motor to backdrive at approximately 0.287 rad/s.

### ***Safe Response to Impulse Loads***

The previous experiment with slow collisions was limited by the maximum speed of the VA motor to produce the approach velocity of the output link. Another experiment was done to examine the response of the PFVA to an impulsive force acting at the tip of the output link. The theory and procedure of this latter experiment is similar to those for the former one. The only difference is the frequency content in the loading condition. Impulse loads contain a broad spectrum of frequencies.

**Procedure.** To introduce the impulse the link was struck hard by a rubber hammer while the link was commanded to follow a constant velocity trajectory. Again, the torque of the FA motor was specified to be zero and a constant VA velocity of 11.42 rad/s was chosen. The torque sensor was sampled at 20 Hz. Due to high level of electromagnetic interference in our testbed we employ a 4 Hz cut-off hardware filter to the torque data



before we read it in our control program (LabVIEW application). Therefore we were limited by this cut-off frequency in seeing the broad spectrum of frequencies in an impulse.

**Results.** The results of this experiment show the VA and FA velocities and the torque in the force input branch measured by the torque sensor (which is indicative of the torque at the output link due to the FA's near-unity velocity ratio and near perfect backward driving efficiency). These are shown in Figure 7.21. Also shown in this figure is the FFT magnitude of the torque data to indicate the broad spectrum of frequencies due to impulse loading. In the beginning of the experiment the VA velocity of 11.42 rad/s results in an output velocity of 0.074 rad/s. Stiction keeps the FA motor from moving (similar to slow collision experiment). After about 2.5s the output link is hit by the wooden block. The applied impulse at the output is reflected to the FA branch, where the torque sensor detects a torque jump of approximately 2N-m for approximately 3 time-steps (0.06s). This means that the impulse is 0.12 N-ms. Since the FA is set at zero torque, it backdrives with minimal resistance, thus absorbing some of the energy from the impact. In doing so, the FA accelerates approximately up to -18.17 rad/s. The friction of the system dissipates the kinetic energy of the FA, bringing the FA motor back to rest less than 1s after the impact. Note that during such a motion, the FA motor acts like a generator. A circuit could be designed to store the energy that is dissipated. An interesting observation here was the noticeable vibratory response of the FA (boxed in Figure 7.21).

To study these oscillatory dynamics of the FA subsystem more carefully, we performed an additional test where the above experiment (impact experiment) was repeated but the FA was now commanded zero velocity rather than zero torque. Physically, the FA will act as a 'casing' and try to reject the disturbances it feels to maintain position (a mode similar to the dynamic coupling experiment in Section 7.2.2).

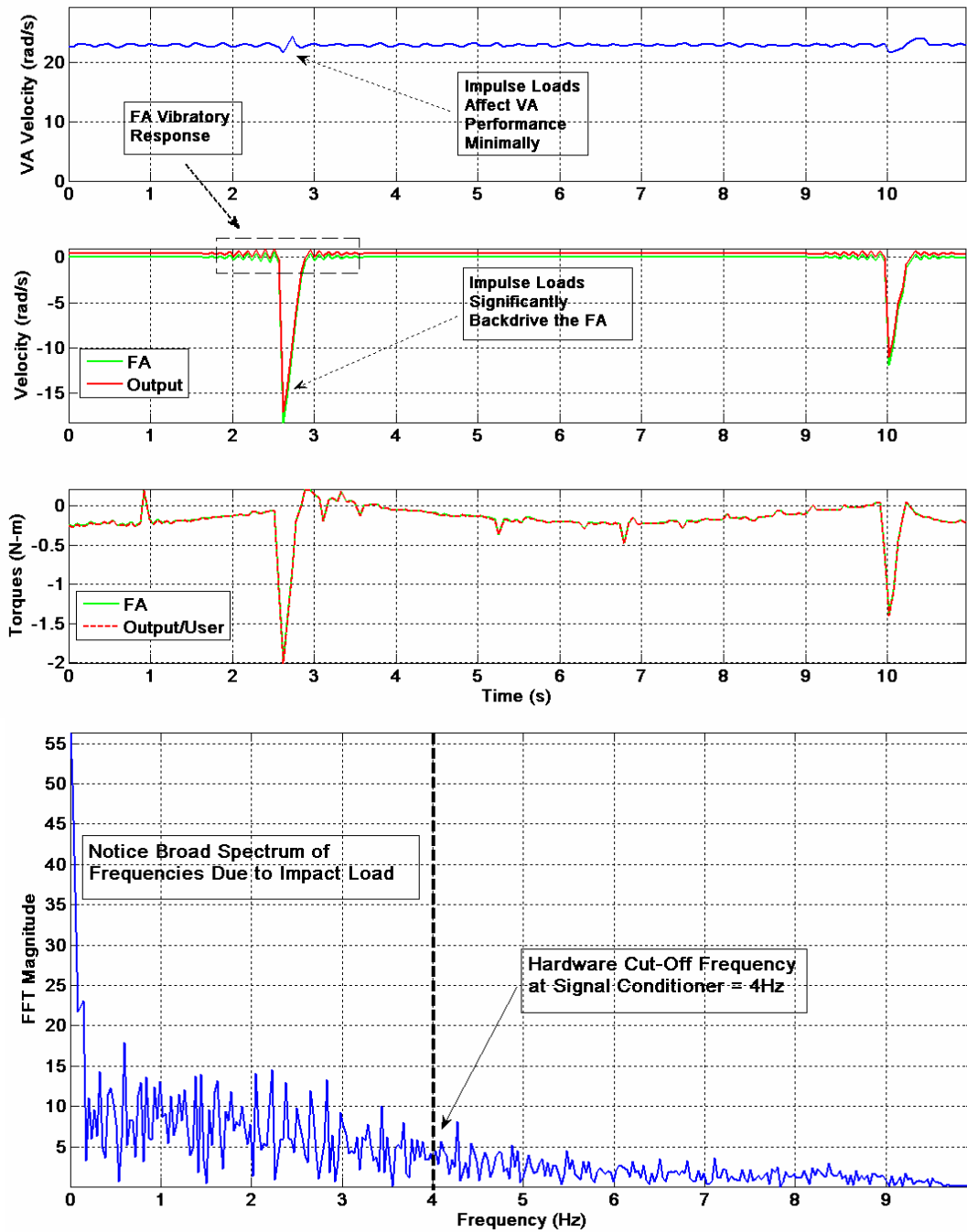


Figure 7.21. Experimental results of safe response to impact loads. (Top) Time-domain trajectories of FA and VA velocities, and torque data. (Bottom) FFT of torque data to show the broad spectrum of frequencies in an impulse.

In this mode, part of the impact energy is absorbed by the FA which now acts as a dynamic system with dominant spring-damper behavior due to its direct drive nature (this influence of the FA's dynamic behavior on the output dynamic behavior was discussed in Section 5.5.1 with specific reference to mechanical and electromagnetic stiffness), and dissipated during the vibratory response. Interestingly, from classical vibrations theory (Tse et al., 1963), this FA velocity decay (see Figure 7.22) can be used to determine the damping ratio and the natural frequency of the FA subsystem<sup>49</sup>.

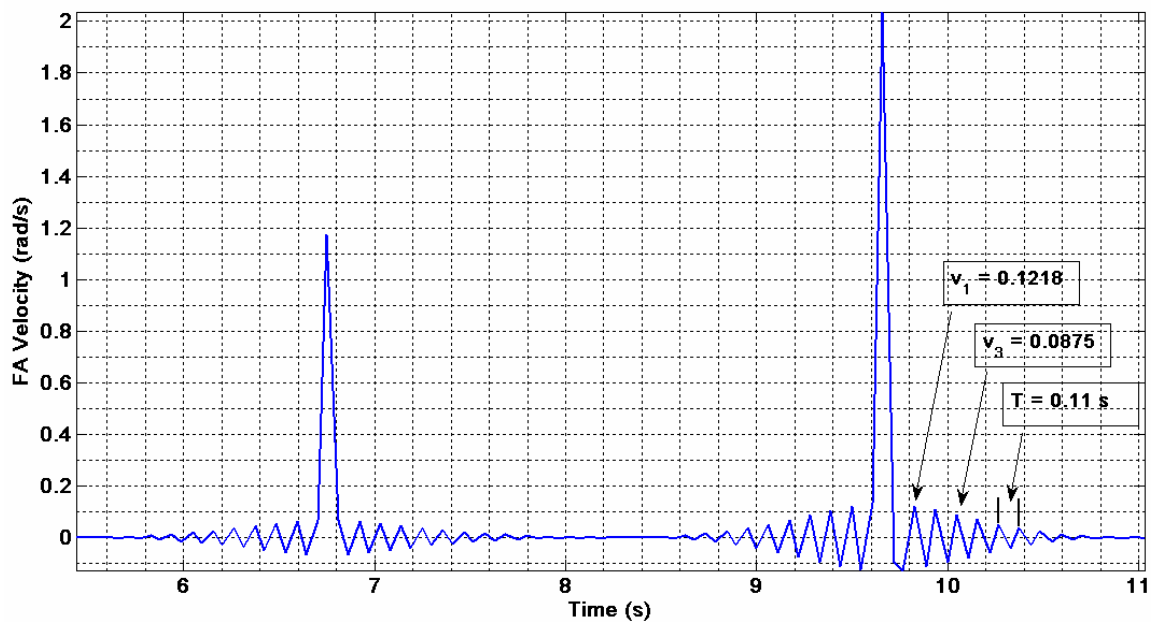


Figure 7.22. Experimental results of safe response to impact loads. (Top) Time-domain trajectories of FA and VA velocities, and torque data. (Bottom) FFT of torque data to show the broad spectrum of frequencies in an impulse.

One way to do this is using the logarithmic decrement method (Tse et al., 1963, p. 58). Consider two peaks  $v_1$  and  $v_3$  on the FA velocity decay plot in Figure 7.22 separated by 2 time-periods ( $T = 0.11\text{s}$ ). Now, the logarithmic decrement  $\delta$  can be determined:

<sup>49</sup> Note that in the decay shown in Figure 7.22, the first peak is much higher than the expected peak based on the logarithmic decrement ratio. This is probably because not all the energy from the impact is absorbed in the vibratory response. However with the known peaks, the expected peak can be determined by extrapolation.

$$\delta = \frac{1}{2} \ln \left( \frac{v_1}{v_3} \right) = 0.1654 \quad (7.12)$$

Knowing  $\delta$ , the damping ratio  $\zeta$  can be computed:

$$\zeta = \frac{1}{\sqrt{1 + \left( \frac{2\pi}{\delta} \right)^2}} = 0.0263 \quad (7.13)$$

The damped natural frequency of the FA system is

$$\omega_d = \frac{2\pi}{T} = 57.1199 \text{ rad/s} \quad (7.14)$$

Therefore, the natural frequency of this system is

$$\omega_n = \frac{\omega_d}{\sqrt{1 - \zeta^2}} = 57.1396 \text{ rad/s} (\approx 9.1 \text{ Hz}) \quad (7.15)$$

If we now determine the inertia content in the FA subsystem, then we can estimate the stiffness of the FA. The stiffness thus estimated would, however, include both mechanical stiffness and the stiffness introduced by other factors such as the electromagnetic characteristics of the FA prime-mover and the PID gains of the FA's controller. For a detailed discussion of these latter factors that contribute to apparent stiffness at the output, refer (Younkin, 2003).

In summary, our goal in Experiment IV was to demonstrate the safe response of the PFVA due to the FA's controlled backdriveability. We showed this response for both slow collisions (characterized by approach velocities  $< 0.5$  m/s) and for impact loading. For the latter case, the vibratory response of the FA to an impulse function was also experimentally characterized using the logarithmic decrement method.

### 7.3. CHAPTER SUMMARY

The focus of this chapter was to present experimental results from our work on a first generation prototype of a rotary PFVA. Our broad goals in this chapter were:

1. To describe the UTRRG PFVA prototype and the tesbed associated with it.

2. Identify two phenomena which are critical to the operation of the PFVA: friction in the FA branch and dynamic coupling between the FA and the VA.
3. Demonstrate two different operational modes of the PFVA: (i) utilizing the kinematic redundancy in the actuator to mitigate low-velocity friction effects and (ii) safe response of the actuator to collision and impact scenarios by controlling the FA's backdriveability. A secondary objective of this set of experiments was to partially characterize the dominant spring-damper dynamics of the FA by determining its damping ratio and natural frequency.

A summary of these experiments and major results are listed in Table 7.6.

Table 7.6 Summary of Experiments and Major Results

Experiment	Significant Results/Conclusions	Major References
<b>PARAMETER IDENTIFICATION</b>		
Identification of Friction Phenomena (Section 7.2.1)	<ul style="list-style-type: none"> <li>• Velocity-dependent friction phenomena, such as stiction, Stribeck effect, and viscous damping were identified.</li> <li>• Position-dependent friction was characterized using spatial spectral analysis.</li> </ul>	(Armstrong-Hélouvy, 1991; Garcia et al., 2002)
Identification of Dynamic Coupling (Section 7.2.2)	<ul style="list-style-type: none"> <li>• An experimental methodology was proposed and demonstrated to characterize dynamic coupling torques between the FA and VA.</li> <li>• In our testbed, the coupling torque correlated almost entirely with velocity.</li> </ul>	No major references found
<b>PERFORMANCE TESTING</b>		
Utilizing Kinematic Redundancy to Mitigate Low Velocity Friction (Section 7.2.3)	<ul style="list-style-type: none"> <li>• One mode of operation was demonstrated where the kinematic redundancy in the actuator was effectively utilized to avoid low-velocity zones.</li> </ul>	(Ontanon Ruiz, 2003)
Mechanical Safety through Controlled Backdriveability of FA (Section 7.2.4)	<ul style="list-style-type: none"> <li>• A mechanically safe mode of operation was demonstrated via the controlled backdriveability of the FA input. Two specific loading conditions were imposed: (i) slow collisions and (ii) impulse loading.</li> <li>• The damping ratio and natural frequency of the FA subsystem were determined based on logarithmic decrement method and an impulse response.</li> </ul>	(Tse et al., 1963) for vibration response theory.

## SYSTEM LEVEL ANALYTIC FORMULATION

### Chapter 8. Generalized Dynamic Modeling of PFVA-Driven Serial Manipulators

In Chapters 4 and 5 we have presented the parametric design of the PFVA. In Chapters 6 and 7 we presented simulations and experimental testing of the PFVA's dynamic performance. In this chapter we will extend that actuator-level work and develop an analytic formulation to model  $n$ -DOF serial robot manipulators that incorporate PFVA-type inputs at its joints. The motivation for performing this analysis is threefold:

- To gain physical insight into the design and operation of PFVA-driven  $n$ -DOF systems. For example, such insight can assist in answering questions related to dynamic coupling, mutual disturbance conflicts among inputs, etc.
- To create a tool to simulate the system response for a given set of inputs.
- To formulate system-level performance metrics that can assist in comparing PFVA-driven systems to conventional serial manipulators that use one input per joint. Additionally, these metrics could also be used to compare various PFVA-driven manipulator systems.

The system-level dynamic model in this chapter only entails a change of coordinates<sup>50</sup> of the manipulator equations of motion to the actuator (or PFVA) space; however, we will perform the analysis from first principles to gain physical insight. The generalized coordinates for our dynamic model will be the positions of the two sets of actuators (FA

---

<sup>50</sup> Refer (Freeman and Tesar, 1988) for a formal discussion on change of generalized coordinates, given the controlling equations of motion of the system using one set of generalized coordinates. We used that work to confirm our models based on the first principles.

and VA), and the generalized velocities would be the prime-mover velocities of these actuators.

The notation used in the following development is from the work on serial chain dynamic modeling by Thomas and Tesar (1982). In general, a vector is represented in lower-case bold-face and a matrix is represented in upper-case bold-face. A post subscript refers to the number of a link or the element of a vector.

### 8.1. CONFIGURATION SPACES

Before the analytical framework is developed for a PFVA-driven manipulator, we will first lay out the configurations spaces of interest. Generally, there are three of these (see Figure 8.1) that we are interested in: (i) PFVA space, (ii) joint space, and (iii) operational or End-Effector (EEF) space.

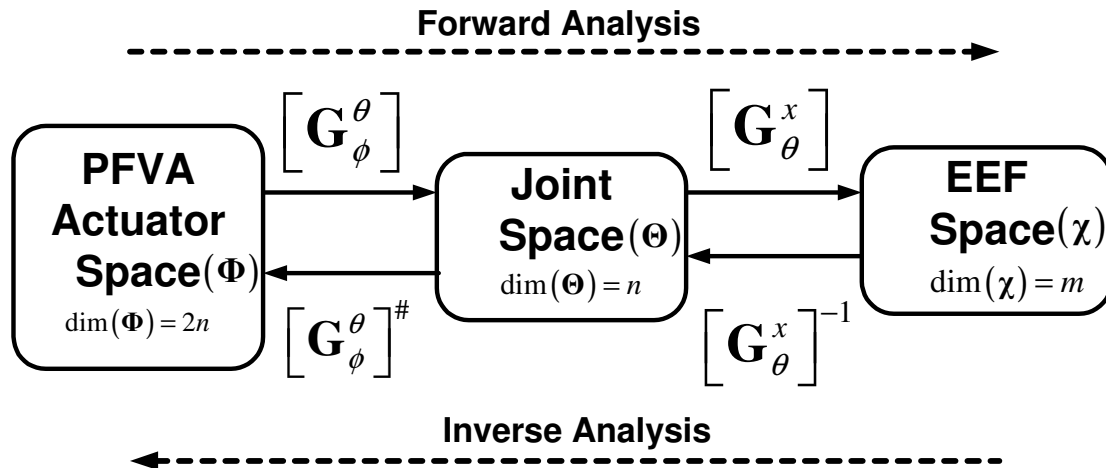


Figure 8.1. Configuration spaces of interest in a PFVA-driven serial robot manipulator (adapted from Chen and Tsai, 1993).

In general, for a serial manipulator with  $n$  joints each having two velocity-summing inputs, VA and FA, the dimension of the actuator space ( $\Phi$ ) is

$$\dim(\Phi) = 2n \quad (8.1)$$

We can now consider two subspaces,  $\Phi_1$  and  $\Phi_2$ , of  $\Phi$  each having a dimension  $n$  and representing<sup>51</sup> the VA and FA inputs to the manipulator, respectively:

$$\begin{aligned}\Phi_i &\subset \Phi, i \in \{1, 2\} \\ \dim(\Phi_i) &= n \forall i\end{aligned}\tag{8.2}$$

Therefore, for a PFVA-driven manipulator

$$\begin{aligned}\phi_1 &\in \Phi_1 \text{ (represents VA)}, \\ \phi_2 &\in \Phi_2 \text{ (represents FA)}\end{aligned}\tag{8.3}$$

The dimension of the joint space ( $\Theta$ ), which typically equals the motion Degrees of Freedom (DOF), is  $n$ :

$$\dim(\Theta) = n\tag{8.4}$$

The dimension of the EEF space ( $\chi$ ) has a dimension equal to the number of task coordinates  $m$  that completely specifies the manipulator's task:

$$\dim(\chi) = m \leq 6\tag{8.5}$$

## 8.2. GENERALIZED KINEMATICS

There are well-defined kinematic mappings among the configurations defined in the previous (see Figure 8.1) as will be shown in this section. These kinematic mappings are fundamental to analyzing both the kinematics and dynamics of the system.

### 8.2.1. Generalized Velocity Analysis

The velocity mapping between the PFVA space ( $\Phi$ ) and the joint space ( $\Theta$ ) can be written as

$$\dot{\theta} = \begin{bmatrix} \mathbf{G}_{\phi_1}^\theta \end{bmatrix} \dot{\phi}_1 + \begin{bmatrix} \mathbf{G}_{\phi_2}^\theta \end{bmatrix} \dot{\phi}_2\tag{8.6}$$

where  $\dot{\theta} \in \Theta$  is the vector of manipulator joint velocities,  $\phi_i \in \Phi_i$   $i \in \{1, 2\}$  are vectors representing the prime-mover velocities at VA and FA inputs of the PFVA,  $\begin{bmatrix} \mathbf{G}_{\phi_i}^\theta \end{bmatrix}$  ( $i = 1, 2$ ) are constant matrices of velocity ratios for the two inputs. We chose to use two

---

<sup>51</sup> We have not used the obvious subscripts of  $v$  and  $f$  for the VA and FA, respectively, for convenience in using indices in summations.



different matrices  $\begin{bmatrix} \mathbf{G}_{\phi_i}^\theta \end{bmatrix} \in R^{n \times n}$  incorporating the velocity ratios instead of one non-square matrix<sup>52</sup>  $\mathbf{G}_\phi^\theta \in R^{n \times 2n}$  (see Figure 8.1)

$$\mathbf{G}_\phi^\theta = \begin{bmatrix} \mathbf{G}_{\phi_1}^\theta & \mathbf{G}_{\phi_2}^\theta \end{bmatrix} \quad (8.7)$$

to explicitly represent the contribution from each input set. This choice lends better physical insight into our modeling problem.

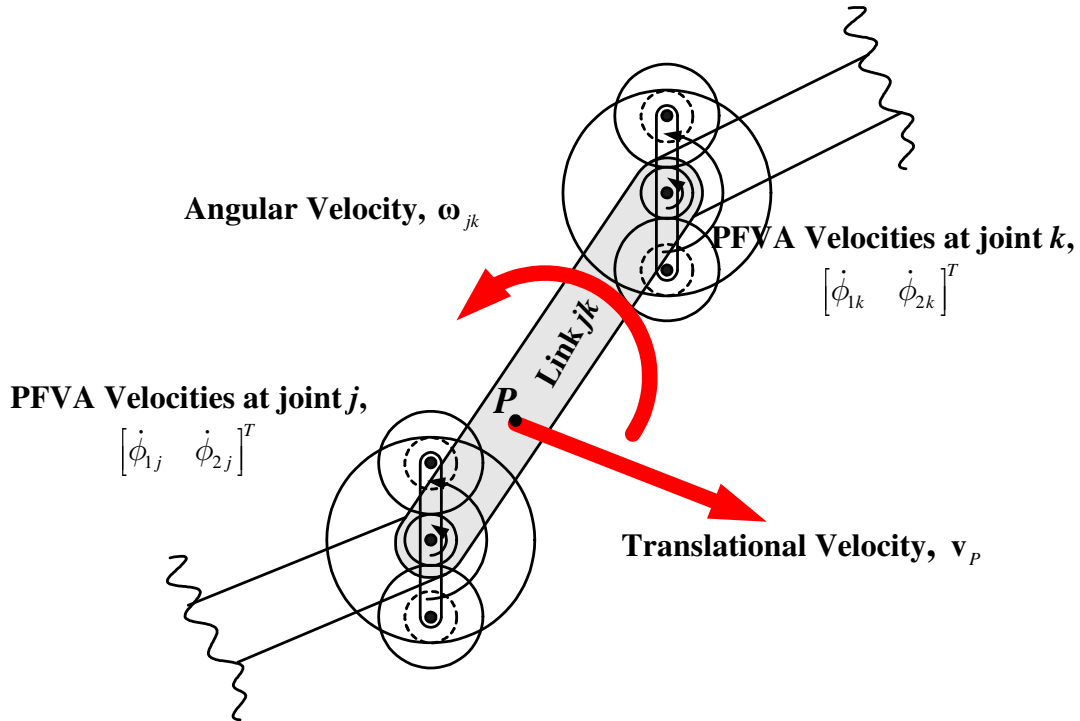


Figure 8.2. Conceptual sketch of the velocity kinematics of a generalized link  $jk$  on a PFVA-driven manipulator.

In the PFVA, which is realized by a differential, these velocity-ratio matrices  $\begin{bmatrix} \mathbf{G}_{\phi_i}^\theta \end{bmatrix}$  are constant and functions of the Relative Scale Factor (RSF) matrix  $\tilde{\mathbf{p}} \in R^{n \times n}$  which is diagonal:

<sup>52</sup> Chen and Tsai (1993) call a matrix of this type that incorporates the gear train transmission ratios as the *structure matrix*.

$$\tilde{\boldsymbol{\rho}} = \begin{bmatrix} \tilde{\rho}_1 & \dots & \dots & 0 \\ 0 & \tilde{\rho}_2 & \dots & 0 \\ \dots & \dots & \dots & \dots \\ 0 & \dots & \dots & \tilde{\rho}_n \end{bmatrix} \quad (8.8)$$

In Eq. (8.8)  $\tilde{\boldsymbol{\rho}}(i,i) = \tilde{\rho}_i$  is the RSF corresponding to the PFVA at joint  $i$ . Now, if input 1 is assumed to be the VA input, the FA sub-system is input 2, and  $\mathbf{I} \in R^{n \times n}$  is the identity matrix, then

$$\begin{bmatrix} \mathbf{G}_{\phi_1}^\theta \end{bmatrix} = (\mathbf{I} + \tilde{\boldsymbol{\rho}})^{-1} \quad (8.9)$$

$$\begin{bmatrix} \mathbf{G}_{\phi_2}^\theta \end{bmatrix} = \tilde{\boldsymbol{\rho}}(\mathbf{I} + \tilde{\boldsymbol{\rho}})^{-1} \quad (8.10)$$

In general, the velocity state of a link  $jk$  in a PFVA-driven manipulator can be expressed as the translational velocity  $\mathbf{v}_p \in R^3$  of a generic point P on this link and the angular velocity  $\boldsymbol{\omega}_{jk} \in R^3$  of the link (as shown in Figure 8.2):

$$\mathbf{v}_p = \begin{bmatrix} \mathbf{G}_p \end{bmatrix} \dot{\boldsymbol{\theta}} \quad (8.11)$$

$$\boldsymbol{\omega}_{jk} = \begin{bmatrix} \mathbf{G}_{jk} \end{bmatrix} \dot{\boldsymbol{\theta}} \quad (8.12)$$

where  $\begin{bmatrix} \mathbf{G}_p \end{bmatrix} \in R^{3 \times n}$  and  $\begin{bmatrix} \mathbf{G}_{jk} \end{bmatrix} \in R^{3 \times n}$  are the first-order translational KIC associated with point  $P$  and rotational KIC associated with link  $jk$ , respectively (Thomas and Tesar, 1982). We can now determine the velocity mapping between the joint space ( $\boldsymbol{\Theta}$ ) and the End-Effector (EEF) space ( $\mathbf{X}$ ):

$$\dot{\mathbf{x}} = \begin{bmatrix} \mathbf{G}_\theta^x \end{bmatrix} \dot{\boldsymbol{\theta}} \quad (8.13)$$

where  $\dot{\mathbf{x}} \in \boldsymbol{\chi}$  is the vector of end-effector velocities and  $\begin{bmatrix} \mathbf{G}_\theta^x \end{bmatrix} \in R^{m \times n}$  is the configuration-dependent manipulator Jacobian such that

$$\begin{bmatrix} \mathbf{G}_\theta^x \end{bmatrix} = \begin{bmatrix} \mathbf{G}_E \\ \text{-----} \\ \mathbf{G}_{n(n+1)} \end{bmatrix} \quad (8.14)$$

The point  $E$  is a point of interest on the end-effector and  $n$  is the number of links<sup>53</sup> in the serial chain. Substituting Eqs. (8.6) and Eqs. (8.9)-(8.10) in Eq. (8.13) we have

$$\begin{aligned}\dot{\mathbf{x}} &= [\mathbf{G}_\theta^x] \{ [\mathbf{G}_{\phi_1}^\theta] \dot{\phi}_1 + [\mathbf{G}_{\phi_2}^\theta] \dot{\phi}_2 \} \\ \dot{\mathbf{x}} &= [\mathbf{G}_\theta^x] \{ (\mathbf{I} + \tilde{\rho})^{-1} \dot{\phi}_1 + \tilde{\rho} (\mathbf{I} + \tilde{\rho})^{-1} \dot{\phi}_2 \}\end{aligned}\quad (8.15)$$

In Eq. (8.15),  $[\mathbf{G}_\theta^x][\mathbf{G}_{\phi_i}^\theta] = [\mathbf{G}_{\phi_i}^x] \in R^{m \times n}$  can be regarded as a *linearly-scaled* manipulator Jacobian. From Eq. (8.15) the PFVA-driven manipulator can be visualized as the velocity-summing combination of two kinematically distinct manipulators: a VA- and an FA-based manipulator. This combination is shown in Figure 8.3.

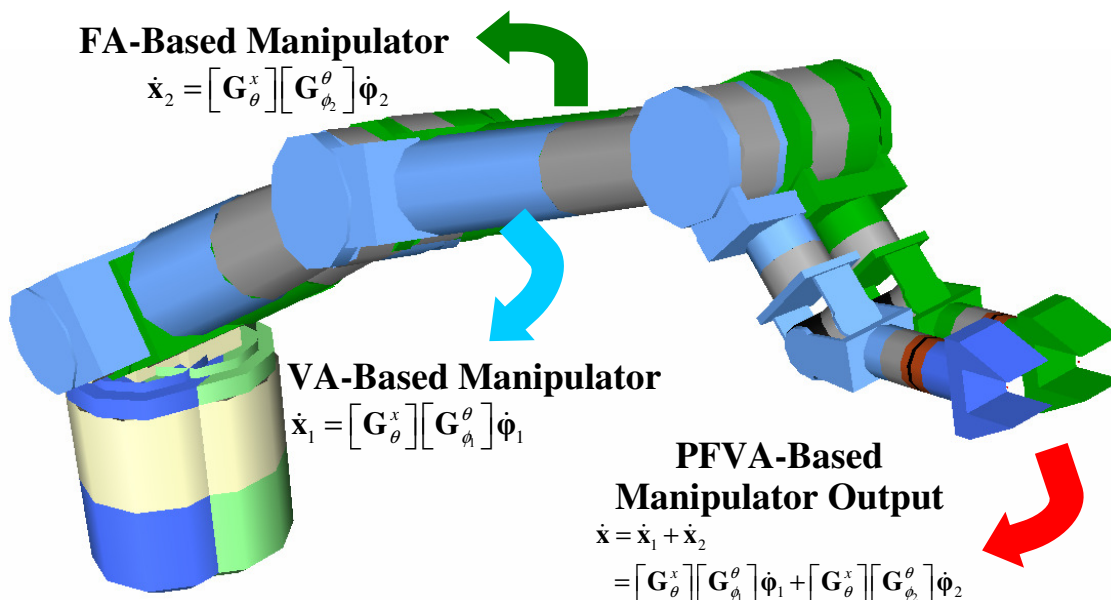


Figure 8.3. A PFVA-driven manipulator's output may be visualized as the velocity-summed combination of two constituent manipulators (with the same joint space and link configuration) driven by dual inputs at joints: (i) FAs, and (ii) VAs.

In the light of the visualization of a PFVA-driven manipulator as the superposition of a FA- and a VA-based manipulator, a distinction has to now be made between multiple coordinating manipulators (for example, dual arms (Cox et al., 1995)) and the PFVA-

<sup>53</sup> The end-effector or tool of an  $n$ -link serial manipulator is frequently regarded as link  $(n+1)$ .

driven robot. The former case involves force-summing, i.e. the end-point velocities of the two coordinating manipulators are constrained by the desired velocity of the manipulated object while the sum of their end-point wrenches is the resultant wrench acting on the manipulated object. The latter case (PFVA-driven combination) involves velocity-summing of the FA- and VA-driven robots (velocities sum and forces are distributed).

### ***Inverse Velocity Analysis***

The inverse velocity kinematics problem deals with determining the required velocities at the different sets of inputs  $\dot{\phi}_i$  for a specified EEF velocity  $\dot{\mathbf{x}}$ . To characterize the two sets of inputs, we can now analyze Eq. (8.15) in terms of two distinct velocity inverses:

$$(\mathbf{I} + \tilde{\boldsymbol{\rho}}) [\mathbf{G}_\theta^x]^{-1} \dot{\mathbf{x}} = \dot{\phi}_1 \quad (8.16)$$

$$(\mathbf{I} + \tilde{\boldsymbol{\rho}}) \tilde{\boldsymbol{\rho}}^{-1} [\mathbf{G}_\theta^x]^{-1} \dot{\mathbf{x}} = \dot{\phi}_2 \quad (8.17)$$

If we consider  $\dot{\phi}_2 = \mathbf{0}$  (FA is stationary), then the velocity inverse solution for  $\dot{\phi}_1$  (VA velocity), given a target  $\dot{\mathbf{x}}$ , is as shown in Eq. (8.16). On the contrary, considering  $\dot{\phi}_1 = \mathbf{0}$  (VA is stationary) and solving the inverse velocity problem for the FA results in Eq. (8.17). Both inverses exist if and only if two conditions are met: (i) the manipulator is not in a singularity i.e.  $[\mathbf{G}_\theta^x]^{-1}$  exists, and (b)  $\tilde{\boldsymbol{\rho}}$  is not ill-conditioned, which is always true by the design of the PFVA.

By definition of the RSF,  $|\tilde{\rho}(i,i)| > 1 \forall i$  and, therefore, from the two distinct inverses in Eqs. (8.16)-(8.17), we notice that the velocities required from the VA inputs are much higher than those required from the FA inputs. If we examine the mapping from the PFVA space to the joint space (Figure 8.4), there is a null-space due to the duality between the inputs. We will now derive the complete solution of the inverse kinematics problem. In doing so, we have retained the explicit contributions from the VA and FA.

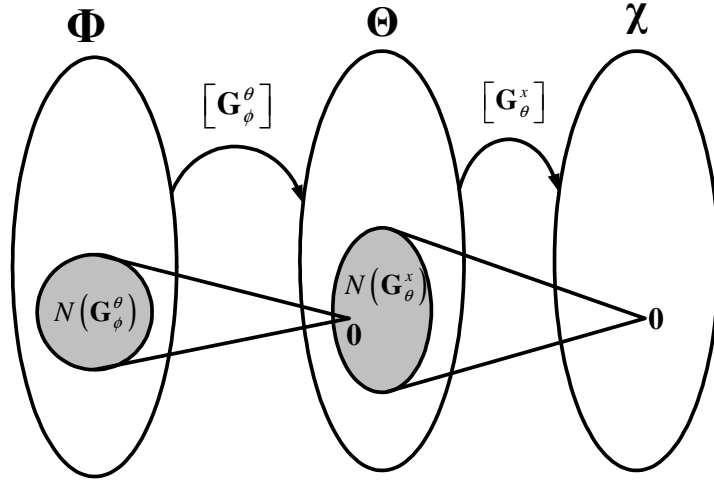


Figure 8.4. Conceptual picture of the null space velocities in the actuator space of the PFVA-driven manipulator that result in zero joint velocities. In addition, if the manipulator is kinematically redundant (i.e.  $n > m$ ), then there are also null-space velocities in the joint space that contribute to zero EEF velocity.

Examining the partitioned form of Eq. (8.15) and using variable substitutions for the coefficient matrices, we have

$$\begin{aligned} [\mathbf{G}_\theta^x]^{-1} \dot{\mathbf{x}} &= [\mathbf{A} \quad \mathbf{B}] \begin{bmatrix} \dot{\phi}_1 \\ \dot{\phi}_2 \end{bmatrix}, \\ \mathbf{A} &= [\mathbf{G}_{\phi_1}^\theta] \quad \text{and} \quad \mathbf{B} = [\mathbf{G}_{\phi_2}^\theta] \end{aligned} \quad (8.18)$$

In Eq. (8.18), it is assumed that the inverse of the manipulator Jacobian exists because this is a well-studied problem. In the case where the manipulator is kinematically redundant, the term  $[\mathbf{G}_\theta^x]^{-1}$  in Eq. (8.18) can be replaced by its generalized inverse (Ben-Israel and Greville, 1974). In Eq. (8.18) we have reduced the problem of inverse velocity analysis to the problem of determining the pseudo-inverse  $[\mathbf{A} \quad \mathbf{B}]^\#$  such that

$$\begin{bmatrix} \dot{\phi}_1 \\ \dot{\phi}_2 \end{bmatrix} = [\mathbf{A} \quad \mathbf{B}]^\# [\mathbf{G}_\theta^x]^{-1} \dot{\mathbf{x}} \quad (8.19)$$

The right pseudo-inverse which is typically used for underconstrained systems (Sciavicco and Siciliano, 2001) such as the one in Eq. (8.15) is used:

$$[\mathbf{A} \ \mathbf{B}]^\# = [\mathbf{A} \ \mathbf{B}]^T \left( [\mathbf{A} \ \mathbf{B}] [\mathbf{A} \ \mathbf{B}]^T \right)^{-1} \quad (8.20)$$

Simplifying,

$$[\mathbf{A} \ \mathbf{B}]^\# = \begin{bmatrix} \mathbf{A}^T \\ \mathbf{B}^T \end{bmatrix} (\mathbf{A}\mathbf{A}^T + \mathbf{B}\mathbf{B}^T)^{-1} \quad (8.21)$$

Using the Woodbury matrix identity (Woodbury, 1950) for the special case of two matrices, say  $\mathbf{X}$  and  $\mathbf{Y}$ , of equal dimension

$$(\mathbf{X} + \mathbf{Y})^{-1} = \mathbf{X}^{-1} - \mathbf{X}^{-1}\mathbf{Y}(\mathbf{Y} + \mathbf{Y}\mathbf{X}^{-1}\mathbf{Y})^{-1}\mathbf{Y}\mathbf{X}^{-1} \quad (8.22)$$

and realizing that  $\mathbf{A}$  and  $\mathbf{B}$  are diagonal, Eq. (8.21) can be reduced to

$$[\mathbf{A} \ \mathbf{B}]^\# = \begin{bmatrix} \mathbf{A} \\ \mathbf{B} \end{bmatrix} (\mathbf{A}^2 + \mathbf{B}^2)^{-1} \quad (8.23)$$

Substitute  $\mathbf{A} = (\mathbf{I} + \tilde{\rho})^{-1}$  and  $\mathbf{B} = \tilde{\rho}(\mathbf{I} + \tilde{\rho})^{-1}$  from Eq. (8.15) in Eq. (8.23)

$$[\mathbf{A} \ \mathbf{B}]^\# = \begin{bmatrix} (\mathbf{I} + \tilde{\rho})^{-1} \\ \tilde{\rho}(\mathbf{I} + \tilde{\rho})^{-1} \end{bmatrix} \left( \left\{ (\mathbf{I} + \tilde{\rho})^{-1} \right\}^2 + \left\{ \tilde{\rho}(\mathbf{I} + \tilde{\rho})^{-1} \right\}^2 \right)^{-1} \quad (8.24)$$

which can then be simplified to

$$[\mathbf{A} \ \mathbf{B}]^\# = \begin{bmatrix} \mathbf{I} \\ \tilde{\rho} \end{bmatrix} (\mathbf{I} + \tilde{\rho}^2)^{-1} (\mathbf{I} + \tilde{\rho}) \quad (8.25)$$

This is directly comparable to the scalar form of this expression discussed in Chapter 6 in Eq. (6.4) for a 1-DOF PFVA drive. That expression is repeated for the reader's convenience:

$$\mathbf{G}^\# = \begin{bmatrix} \left( \frac{\tilde{\rho} + 1}{\tilde{\rho}^2 + 1} \right) \\ \tilde{\rho} \left( \frac{\tilde{\rho} + 1}{\tilde{\rho}^2 + 1} \right) \end{bmatrix} \quad (8.26)$$

Substituting Eq. (8.34) in Eq. (8.27), the pseudo-inverse solution for the inverse velocity kinematics problem for a PFVA-driven manipulator can now be determined:

$$\begin{bmatrix} \dot{\phi}_1 \\ \dot{\phi}_2 \end{bmatrix} = \begin{bmatrix} \mathbf{I} \\ \tilde{\rho} \end{bmatrix} (\mathbf{I} + \tilde{\rho}^2)^{-1} (\mathbf{I} + \tilde{\rho}) [\mathbf{G}_\theta^x]^{-1} \dot{\mathbf{x}} \quad (8.27)$$

This solution provides the specified EEF velocity  $\dot{\mathbf{x}}$  by minimizing the norm of  $\begin{bmatrix} \dot{\phi}_1^T & \dot{\phi}_2^T \end{bmatrix}^T$ . By examining Eq. (8.15) it can be seen that the null-space projection matrix is  $\begin{bmatrix} \mathbf{I} & -\tilde{\rho}^T \end{bmatrix}^T$ . Therefore, the complete solution of the inverse kinematics problem is

$$\begin{bmatrix} \dot{\phi}_1 \\ \dot{\phi}_2 \end{bmatrix} = \begin{bmatrix} \mathbf{I} \\ \tilde{\rho} \end{bmatrix} (\mathbf{I} + \tilde{\rho}^2)^{-1} (\mathbf{I} + \tilde{\rho}) [\mathbf{G}_\theta^x]^{-1} \dot{\mathbf{x}} + \begin{bmatrix} \mathbf{I} \\ -\tilde{\rho} \end{bmatrix} \begin{bmatrix} \dot{\phi}_1 \\ \dot{\phi}_2 \end{bmatrix}_{null} \quad (8.28)$$

where the first term is the pseudo-inverse that minimizes the velocity norms. The second term in Eq. (8.28) contains the null-space input velocities  $\begin{bmatrix} \dot{\phi}_1^T & \dot{\phi}_2^T \end{bmatrix}_{null}^T$  which can be chosen appropriately to optimize a secondary criterion such as minimizing backlash or low-velocity friction. See Section. 6.1.1 in Chapter 6 for a discussion on the physical relevance of this result.

### 8.2.2. Generalized Acceleration Analysis

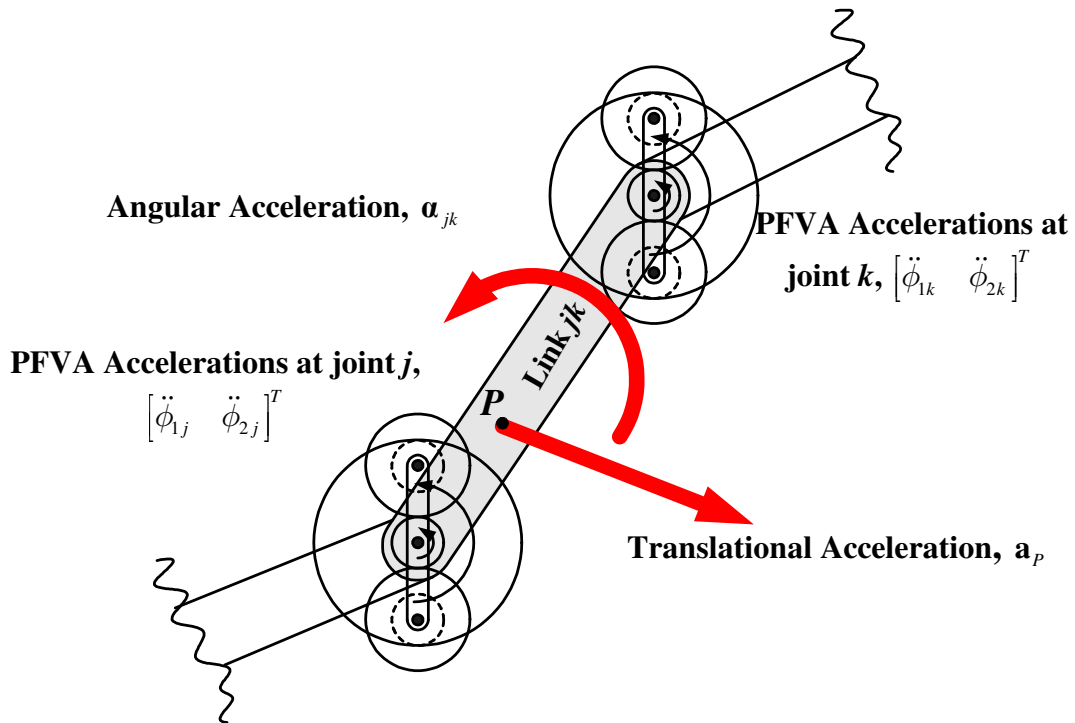


Figure 8.5. Conceptual sketch of the acceleration kinematics of a generalized link  $jk$  on a PFVA-driven manipulator.

Similar to our development of velocity kinematics, the acceleration state of a link  $jk$  in a PFVA-driven manipulator can be expressed as the translational acceleration  $\mathbf{a}_P \in R^3$  of a generic point  $P$  on this link and the angular acceleration  $\boldsymbol{\alpha}_{jk} \in R^3$  of the link (as shown in Figure 8.5) (Thomas and Tesar, 1982):

$$\mathbf{a}_P = \dot{\boldsymbol{\theta}}^T [\mathbf{H}_P] \dot{\boldsymbol{\theta}} + [\mathbf{G}_P] \ddot{\boldsymbol{\theta}} \quad (8.29)$$

$$\boldsymbol{\alpha}_{jk} = \dot{\boldsymbol{\theta}}^T [\mathbf{H}_{jk}] \dot{\boldsymbol{\theta}} + [\mathbf{G}_{jk}] \ddot{\boldsymbol{\theta}} \quad (8.30)$$

where  $[\mathbf{H}_P] \in R^{3 \times n}$  and  $[\mathbf{H}_{jk}] \in R^{3 \times n}$  are the second-order translational KIC associated with point  $P$  and rotational KIC associated with link  $jk$ , respectively (Thomas and Tesar, 1982). We can now determine the acceleration mapping between the joint space ( $\Theta$ ) and the End-Effector (EEF) space ( $\mathbf{X}$ ):

$$\ddot{\mathbf{x}} = \dot{\boldsymbol{\theta}}^T [\mathbf{H}_{\theta\theta}^x] \dot{\boldsymbol{\theta}} + [\mathbf{G}_\theta^x] \ddot{\boldsymbol{\theta}} \quad (8.31)$$

where  $\ddot{\mathbf{x}} \in R^m$  is the vector of end-effector velocities and  $[\mathbf{H}_{\theta\theta}^x] \in R^{m \times n \times n}$  is the Hessian array and consists of  $m$  planes of symmetric matrices that are of the same dimension as the manipulator Jacobian  $[\mathbf{G}_\theta^x] \in R^{m \times n}$ . The first term in Eq. (8.13) can be partitioned into the translational and angular components as follows (Thomas and Tesar, 1982):

$$\dot{\boldsymbol{\theta}}^T [\mathbf{H}_{\theta\theta}^x] \dot{\boldsymbol{\theta}} = \begin{bmatrix} \dot{\boldsymbol{\theta}}^T [\mathbf{H}_E] \dot{\boldsymbol{\theta}} \\ \text{-----} \\ \dot{\boldsymbol{\theta}}^T [\mathbf{H}_{n(n+1)}] \dot{\boldsymbol{\theta}} \end{bmatrix} \quad (8.32)$$

Combining Eqns. (8.6) and (8.31), we can determine the EEF acceleration state as a function of the PFVA input accelerations:

$$\ddot{\mathbf{x}} = \sum_{i=1}^2 \left\{ \dot{\boldsymbol{\phi}}_i^T [\mathbf{G}_{\phi_i}^\theta]^T [\mathbf{H}_{\theta\theta}^x] [\mathbf{G}_{\phi_i}^\theta] \dot{\boldsymbol{\phi}}_i + [\mathbf{G}_\theta^x] [\mathbf{G}_{\phi_i}^\theta] \ddot{\boldsymbol{\phi}}_i \right\} \quad (8.33)$$

Substituting Eqns. (8.9)-(8.10) in Eq. (8.33) we get

$$\begin{aligned} \ddot{\mathbf{x}} &= \ddot{\mathbf{x}}_C + \ddot{\mathbf{x}}_N \\ \ddot{\mathbf{x}}_C &= \dot{\boldsymbol{\phi}}_1^T (\mathbf{I} + \tilde{\boldsymbol{\rho}})^{-1} [\mathbf{H}_{\theta\theta}^x] (\mathbf{I} + \tilde{\boldsymbol{\rho}})^{-1} \dot{\boldsymbol{\phi}}_1 + \dot{\boldsymbol{\phi}}_2^T (\mathbf{I} + \tilde{\boldsymbol{\rho}})^{-1} \tilde{\boldsymbol{\rho}} [\mathbf{H}_{\theta\theta}^x] \tilde{\boldsymbol{\rho}} (\mathbf{I} + \tilde{\boldsymbol{\rho}})^{-1} \dot{\boldsymbol{\phi}}_2 \\ \ddot{\mathbf{x}}_N &= [\mathbf{G}_\theta^x] (\mathbf{I} + \tilde{\boldsymbol{\rho}})^{-1} \{ \ddot{\boldsymbol{\phi}}_1 + \tilde{\boldsymbol{\rho}} \ddot{\boldsymbol{\phi}}_2 \} \end{aligned} \quad (8.34)$$



where  $\ddot{\mathbf{x}}_C$  and  $\ddot{\mathbf{x}}_N$  are the centripetal/Coriolis and the other acceleration components, respectively. Note that  $(\mathbf{I} + \tilde{\boldsymbol{\rho}})^{-T} = (\mathbf{I} + \tilde{\boldsymbol{\rho}})^{-1}$  and  $\tilde{\boldsymbol{\rho}}^T = \tilde{\boldsymbol{\rho}}$  because these are diagonal matrices.

### ***Inverse Acceleration Analysis***

In the inverse acceleration problem, the configuration of the manipulator and its velocity state are both given and the task is to determine the required accelerations at the VA and FA inputs,  $\ddot{\boldsymbol{\phi}}_1$  and  $\ddot{\boldsymbol{\phi}}_2$ , to support a desired EEF acceleration  $\ddot{\mathbf{x}}$ . The solution to this problem can be approached in a manner similar to the inverse velocity problem. By re-arranging the terms in Eq. (8.34) we get

$$\left[ \mathbf{G}_\theta^x \right]^{-1} (\ddot{\mathbf{x}} - \ddot{\mathbf{x}}_C) = \begin{bmatrix} \mathbf{I} \\ \tilde{\boldsymbol{\rho}} \end{bmatrix} (\mathbf{I} + \tilde{\boldsymbol{\rho}})^{-1} \begin{bmatrix} \ddot{\boldsymbol{\phi}}_1 \\ \ddot{\boldsymbol{\phi}}_2 \end{bmatrix} \quad (8.35)$$

Note that knowing the velocity state of the manipulator, we know the centripetal/Coriolis accelerations  $\ddot{\mathbf{x}}_C$ . Now using the result in Eq. (8.39) we can express the complete solution of the inverse acceleration problem for a PFVA-driven manipulator as

$$\begin{bmatrix} \ddot{\boldsymbol{\phi}}_1 \\ \ddot{\boldsymbol{\phi}}_2 \end{bmatrix} = \begin{bmatrix} \mathbf{I} \\ \tilde{\boldsymbol{\rho}} \end{bmatrix} (\mathbf{I} + \tilde{\boldsymbol{\rho}}^2)^{-1} (\mathbf{I} + \tilde{\boldsymbol{\rho}}) \left[ \mathbf{G}_\theta^x \right]^{-1} (\ddot{\mathbf{x}} - \ddot{\mathbf{x}}_C) + \begin{bmatrix} \mathbf{I} \\ -\tilde{\boldsymbol{\rho}} \end{bmatrix} \begin{bmatrix} \ddot{\boldsymbol{\phi}}_1 \\ \ddot{\boldsymbol{\phi}}_2 \end{bmatrix}_{null} \quad (8.36)$$

where  $\begin{bmatrix} \ddot{\boldsymbol{\phi}}_1^T & \ddot{\boldsymbol{\phi}}_2^T \end{bmatrix}_{null}$  are the null-space accelerations.

### ***Discussion on Acceleration Responsiveness***

In Chapter 6 we have introduced the concept of acceleration responsiveness as a design criterion. The acceleration responsiveness of each PFVA input in a manipulator depends on its maximum torque capability and the total system inertia reflected to it. Since the system inertia is a function of the configuration of the manipulator, the acceleration responsiveness also depends on the configuration.

### 8.3. GENERALIZED STATIC LOAD TORQUES

Consider a force  $\mathbf{f}_p$  at point P and a moment  $\mathbf{m}_{jk}$  acting on a link  $jk$  of a PFVA-driven manipulator as shown in Figure 8.6. Our goal in this section is to reflect these applied loads to the PFVA inputs of the system.

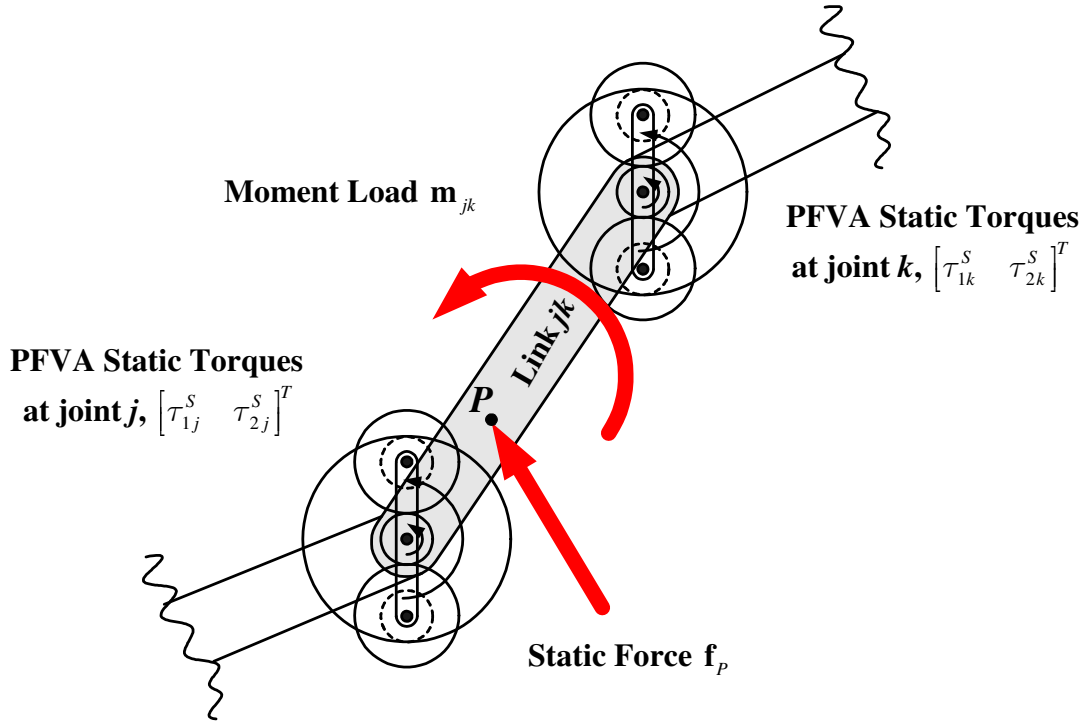


Figure 8.6. Conceptual sketch of an applied static force  $\mathbf{f}_p$  at point P and moment  $\mathbf{m}_{jk}$  on link  $jk$  of a PFVA-driven manipulator.

For a virtual time interval  $\delta t$  the virtual work done by these applied loads is

$$\delta W = \left( \sum_{P=1}^{P=N_f} \mathbf{v}_P^T \mathbf{f}_P \right) \delta t + \left( \sum_{j=1}^{j=n} \boldsymbol{\omega}_{jk}^T \mathbf{m}_{jk} \right) \delta t \quad (8.37)$$

where  $\mathbf{v}_P \delta t$  and  $\boldsymbol{\omega}_{jk} \delta t$  are the virtual displacements associated with the force  $\mathbf{f}_P$  and moment  $\mathbf{m}_{jk}$ , respectively (Thomas and Tesar, 1982). In general, the virtual work done

by the PFVA inputs to support these applied loads is

$$\delta W = \sum_{i=1}^2 (\boldsymbol{\phi}_i^T \boldsymbol{\Gamma}_i^S) \delta t \quad (8.38)$$

If there are no losses in the transfer of virtual work between the load and the inputs, then from Eqs. (8.37)-(8.38)

$$\left( \sum_{p=1}^{P=N_f} \mathbf{v}_p^T \mathbf{f}_p \right) \delta t + \left( \sum_{j=1}^{j=n} \boldsymbol{\omega}_{jk}^T \mathbf{m}_{jk} \right) \delta t = \sum_{i=1}^2 (\dot{\boldsymbol{\phi}}_i^T \boldsymbol{\Gamma}_i^S) \delta t \quad (8.39)$$

Substituting Eqs. (8.6), (8.11), and (8.12) in Eq. (8.39) and canceling  $\delta t \neq 0$  from both sides we have

$$\left( \sum_{p=1}^{P=N_f} \left( \sum_{i=1}^{i=2} \dot{\boldsymbol{\phi}}_i^T [\mathbf{G}_{\phi_i}^\theta]^T [\mathbf{G}_p]^T \right) \mathbf{f}_p \right) + \left( \sum_{j=1}^{j=n} \left( \sum_{i=1}^{i=2} \dot{\boldsymbol{\phi}}_i^T [\mathbf{G}_{\phi_i}^\theta]^T [\mathbf{G}_{jk}]^T \right) \mathbf{m}_{jk} \right) = \sum_{i=1}^2 (\dot{\boldsymbol{\phi}}_i^T \boldsymbol{\Gamma}_i^S) \quad (8.40)$$

By re-ordering the summations, Eq. (8.40) can be rewritten as

$$\left( \sum_{i=1}^{i=2} \dot{\boldsymbol{\phi}}_i^T [\mathbf{G}_{\phi_i}^\theta]^T \left( \sum_{p=1}^{P=N_f} [\mathbf{G}_p]^T \mathbf{f}_p \right) \right) + \left( \sum_{i=1}^{i=2} \dot{\boldsymbol{\phi}}_i^T [\mathbf{G}_{\phi_i}^\theta]^T \left( \sum_{j=1}^{j=n} [\mathbf{G}_{jk}]^T \mathbf{m}_{jk} \right) \right) = \sum_{i=1}^2 \dot{\boldsymbol{\phi}}_i^T (\boldsymbol{\Gamma}_i^S) \quad (8.41)$$

It follows from Eq. (8.41) that

$$\boldsymbol{\Gamma}_i^S = [\mathbf{G}_{\phi_i}^\theta]^T \left( \sum_{p=1}^{P=N_f} [\mathbf{G}_p]^T \mathbf{f}_p \right) + [\mathbf{G}_{\phi_i}^\theta]^T \left( \sum_{j=1}^{j=n} [\mathbf{G}_{jk}]^T \mathbf{m}_{jk} \right) \quad (8.42)$$

This implies that the static loads applied on the body of the manipulator are distributed among the different PFVA inputs based on the first-order KICs. For the special case of input reflected static loads due to an applied load  $\mathbf{F} = [\mathbf{f}_E^T \quad \mathbf{m}_{n(n+1)}^T]^T$  at the EEF

$$\begin{aligned} \boldsymbol{\Gamma}_1^S &= (\mathbf{I} + \tilde{\boldsymbol{\rho}})^{-T} \mathbf{F} \\ \boldsymbol{\Gamma}_2^S &= (\mathbf{I} + \tilde{\boldsymbol{\rho}})^{-T} \tilde{\boldsymbol{\rho}}^T \mathbf{F} \end{aligned} \quad (8.43)$$

If the backdriving efficiency matrices (efficiency of power transfer from the load to the PFVA inputs) are  $\boldsymbol{\eta}_{bi}$  ( $i = 1, 2$ )

$$\boldsymbol{\eta}_{bi} = \begin{bmatrix} \eta_{b1i} & \dots & \dots & \dots & 0 \\ \dots & \dots & \dots & \dots & \dots \\ 0 & \dots & \eta_{bji} & \dots & 0 \\ \dots & \dots & \dots & \dots & \dots \\ 0 & \dots & \dots & \dots & \eta_{bni} \end{bmatrix} \quad (8.44)$$

where  $\eta_{bji}$  is the backdriving efficiency of input  $i$  at joint  $j$  then

$$\begin{aligned}
\Gamma_1^S &= \boldsymbol{\eta}_{b1} (\mathbf{I} + \tilde{\boldsymbol{\rho}})^{-T} \mathbf{F} && \text{(For VA Input Set)} \\
\Gamma_2^S &= \boldsymbol{\eta}_{b2} (\mathbf{I} + \tilde{\boldsymbol{\rho}})^{-T} \tilde{\boldsymbol{\rho}}^T \mathbf{F} && \text{(For FA Input Set)}
\end{aligned}
\tag{8.45}$$

We can visualize the EEF load  $\mathbf{F}$  as being shared by two constituent manipulators: VA- and FA-based robots as shown in Figure 8.7.

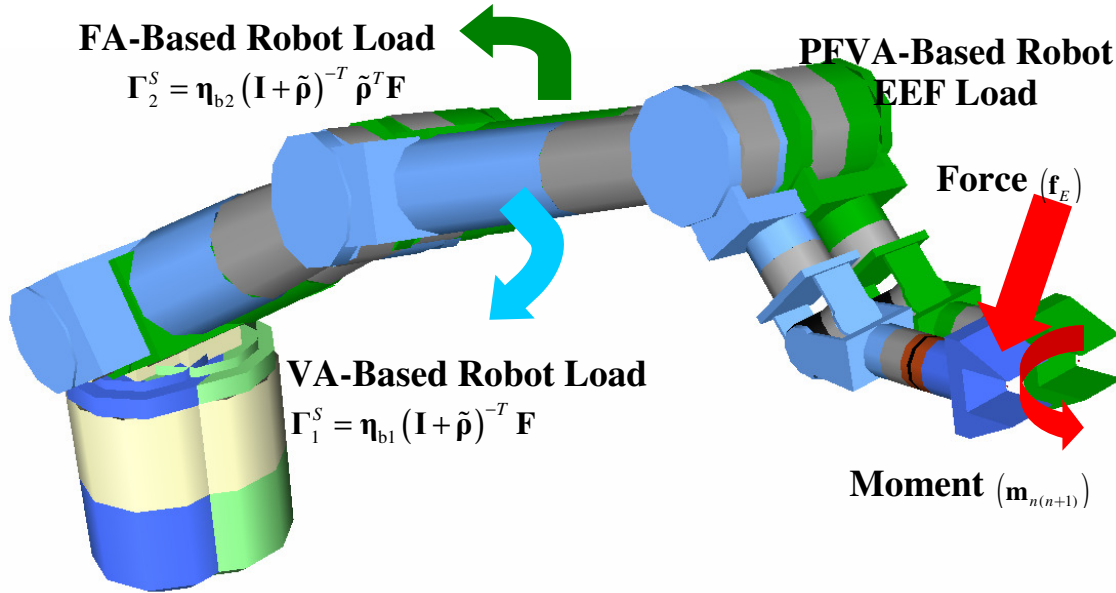


Figure 8.7. A PFVA-driven manipulator's EEF load may be visualized as being shared by two constituent manipulators (with the same joint space and link configuration) driven by dual inputs at joints: (i) FAs, and (ii) VAs.

This completes our analysis of static torques. Note that gravity torques are included as unique load forces in this development. We will now perform a similar analysis for torques due to the system's dynamic state (position, velocity, and acceleration).

#### 8.4. GENERALIZED INERTIAL TORQUES

In this section we will derive the expressions for generalized inertia torques at the PFVA inputs for a given motion state (position, velocity, and acceleration) of the manipulator. Before we do that, we will discuss the concepts of input dynamic coupling matrix and input-reflected manipulator inertia matrix.

### 8.4.1. Input Dynamic Coupling Matrix

The input dynamic coupling matrix ( $\mathbf{\Pi}_M$ ) includes the inertias of all the gear train, prime-mover, and actuator components in the PFVA-driven manipulator. This is the generalization of the  $\mathbf{I}_M$  matrix introduced in Appendix C (see Eq. (C4)):

$$\mathbf{\Pi}_M = \mathbf{\Pi}_I + \mathbf{\Pi}_C \quad (8.46)$$

where  $\mathbf{\Pi}_I \in R^{(2n) \times (2n)}$  is a constant  $(2 \times 2)$  diagonal matrix of  $(n \times n)$  diagonal sub-matrices consisting of the prime-mover inertias at all joints:

$$[\mathbf{\Pi}_I]_{ll} = \begin{bmatrix} I_{ll1}^p & 0 & \dots & 0 & 0 \\ 0 & I_{ll1}^p & \dots & \dots & 0 \\ \dots & \dots & \dots & \dots & \dots \\ 0 & \dots & \dots & I_{ll(n-1)}^p & 0 \\ 0 & 0 & \dots & 0 & I_{lln}^p \end{bmatrix} \quad (8.47)$$

In Eq. (8.47)  $[\mathbf{\Pi}_I]_{ll}$  is the diagonal sub-matrix at position  $(l, l)$  of  $\mathbf{\Pi}_I$  and  $I_{llk}^p$  is the inertia of the prime-mover for input  $l$  at joint  $k$ . Similarly,  $\mathbf{\Pi}_C \in R^{(2n) \times (2n)}$  is a constant  $(2 \times 2)$  matrix of  $(n \times n)$  matrices consisting of the actuator component inertias such that

$$[\mathbf{\Pi}_C]_{lm} = \begin{bmatrix} I_{lm1} & 0 & \dots & 0 & 0 \\ 0 & I_{lm2} & \dots & \dots & 0 \\ \dots & \dots & \dots & \dots & \dots \\ 0 & \dots & \dots & I_{lm(n-1)} & 0 \\ 0 & 0 & \dots & 0 & I_{lmn} \end{bmatrix} \quad (8.48)$$

where  $[\mathbf{\Pi}_C]_{lm}$  is the diagonal sub-matrix at position  $(l, m)$  of  $\mathbf{\Pi}_C$  and  $I_{lmk}$  represents the dynamic coupling between inputs  $l$  and  $m$  at joint  $k$ . Note that  $\mathbf{\Pi}_M$  is positive definite and symmetric.

### 8.4.2. Kinetic Energy

Consider the motion state of link  $jk$  in a PFVA-driven manipulator as shown in Figure 8.8. Let the center of gravity of this link be at  $C_j$ , its inertia matrix about the center of gravity be  $\mathbf{\Pi}_{jk}^{C_j}$ , its mass be  $M_{jk}$ , its translational (at  $C_j$ ) and angular velocity

be  $\mathbf{v}_{C_j}$  and  $\boldsymbol{\omega}_{jk}$ , respectively, and its translational and angular accelerations be  $\mathbf{a}_{C_j}$  and  $\mathbf{a}_{jk}$ , respectively.

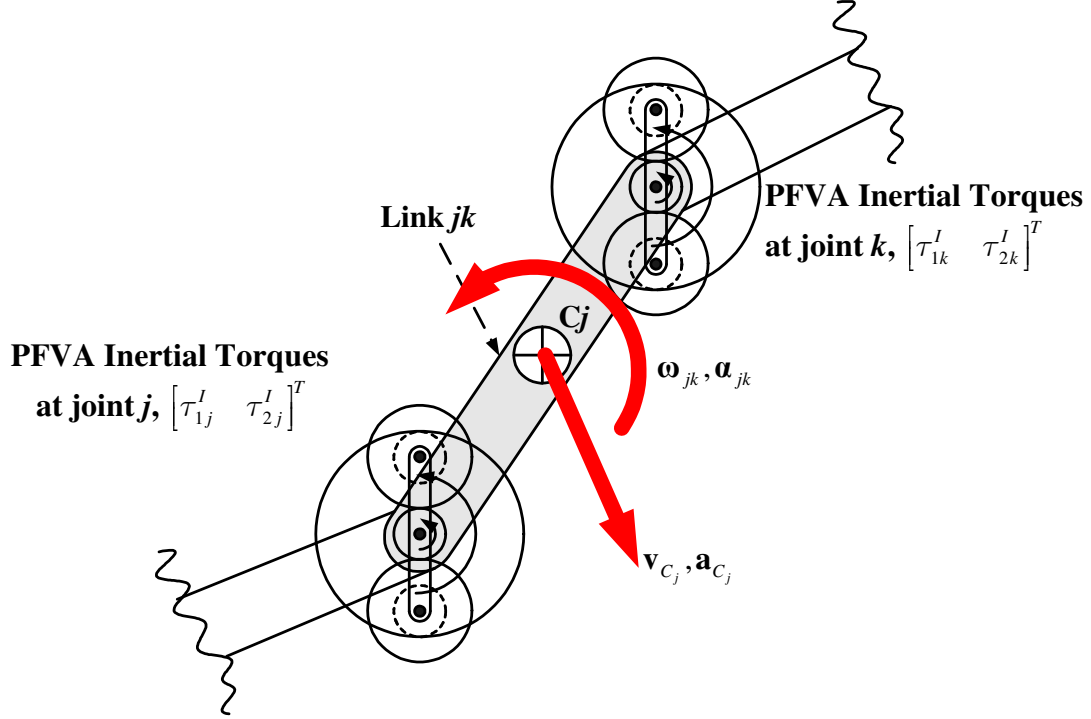


Figure 8.8. Conceptual sketch of inertial loads to due to the acceleration of link  $jk$  in a PFVA-driven manipulator.  $C_j$  represents the Center of Gravity (COG) of the link.

The total kinetic energy of the manipulator can be expressed as<sup>54</sup>

$$E_k = \frac{1}{2} \left\{ \sum_{j=1}^n M_{jk} \mathbf{v}_{C_j}^T \mathbf{v}_{C_j} + \boldsymbol{\omega}_{jk}^T \boldsymbol{\Pi}_{jk} \boldsymbol{\omega}_{jk} \right\} + \frac{1}{2} \sum_{l=1}^2 \sum_{m=1}^2 \dot{\phi}_l^T [\boldsymbol{\Pi}_M]_{lm} \dot{\phi}_m \quad (8.49)$$

where the first two terms have been introduced in (Thomas and Tesar, 1982) and the third term represents the kinetic energy contribution due to the PFVA inputs (i.e. prime mover, gear train, and actuator components). In Eq. (8.49)  $\boldsymbol{\Pi}_{jk} = [\mathbf{R}_j][\boldsymbol{\Pi}_{jk}^{C_j}][\mathbf{R}_j]^T$  where  $\mathbf{R}_j$  is a rotation matrix relating the body fixed frame  $j$  of link  $jk$  to a coordinate frame parallel

<sup>54</sup> Note that the subscript  $k$  in  $E_k$  denotes kinetic energy (versus potential energy) and is distinct from the link index  $k$ .

to the robot world frame and origin coincident with the origin of frame  $j$  (Thomas and Tesar, 1982).

Using the velocity transformations presented in Eqs. (8.6), (8.11), and (8.12) we can rewrite Eq. (8.49) as

$$\begin{aligned}
E_k = & \frac{1}{2} \left\{ \sum_{j=1}^n M_{jk} \left\{ \sum_{l=1}^2 \dot{\phi}_l^T [\mathbf{G}_{\phi_l}^\theta]^T [\mathbf{G}_{C_j}]^T \right\} \left\{ \sum_{m=1}^2 [\mathbf{G}_{C_j}] [\mathbf{G}_{\phi_m}^\theta] \dot{\phi}_m \right\} \right\} \\
& + \frac{1}{2} \left\{ \sum_{j=1}^n \left\{ \sum_{l=1}^2 \dot{\phi}_l^T [\mathbf{G}_{\phi_l}^\theta]^T [\mathbf{G}_{jk}]^T \right\} \mathbf{\Pi}_{jk} \left\{ \sum_{m=1}^2 [\mathbf{G}_{jk}] [\mathbf{G}_{\phi_m}^\theta] \dot{\phi}_m \right\} \right\} \\
& + \frac{1}{2} \sum_{l=1}^2 \sum_{m=1}^2 \dot{\phi}_l^T [\mathbf{\Pi}_M]_{lm} \dot{\phi}_m
\end{aligned} \tag{8.50}$$

which may then be simplified by reordering the summations as

$$E_k = \frac{1}{2} \sum_{l=1}^2 \sum_{m=1}^2 \dot{\phi}_l^T \left\{ [\mathbf{G}_{\phi_l}^\theta]^T \mathbf{\Pi}_{\theta\theta}^* [\mathbf{G}_{\phi_m}^\theta] + [\mathbf{\Pi}_M]_{lm} \right\} \dot{\phi}_m \tag{8.51}$$

where

$$\mathbf{\Pi}_{\theta\theta}^* = \sum_{j=1}^n \left\{ [\mathbf{G}_{C_j}]^T M_{jk} [\mathbf{G}_{C_j}] + [\mathbf{G}_{jk}]^T \mathbf{\Pi}_{jk} [\mathbf{G}_{jk}] \right\} \tag{8.52}$$

In Eq. (8.52),  $\mathbf{\Pi}_{\theta\theta}^*$  is the total inertia of the manipulator links scaled to the joint space (Thomas and Tesar, 1982). Also, the total inertia of the whole manipulator can now be scaled to the PFVA space ( $\Phi$ ). This reflected inertia matrix  $[\mathbf{I}_{\phi\phi}^*] \in R^{(2n) \times (2n)}$  can be partitioned into a  $(2 \times 2)$  grid of sub-matrices of size  $(n \times n)$  such that

$$[\mathbf{I}_{\phi\phi}^*]_{lm} = [\mathbf{G}_{\phi_l}^\theta]^T \mathbf{\Pi}_{\theta\theta}^* [\mathbf{G}_{\phi_m}^\theta] + [\mathbf{\Pi}_M]_{lm}, \quad l, m \in \{1, 2\} \tag{8.53}$$

and the manipulator's kinetic energy can then be expressed in a further simplified form:

$$E_k = \frac{1}{2} \sum_{l=1}^2 \sum_{m=1}^2 \dot{\phi}_l^T [\mathbf{I}_{\phi\phi}^*]_{lm} \dot{\phi}_m \tag{8.54}$$

Having determined the kinetic energy we can now proceed to calculate the generalized inertia torques required at the PFVA-inputs to support a motion state of the manipulator. Note that  $[\mathbf{I}_{\phi\phi}^*]$  is necessarily positive definite and symmetric because  $\mathbf{\Pi}_{\theta\theta}^*$  and  $\mathbf{\Pi}_M$  are so. In the following derivation, we will use the short-hand  $\mathbf{\Pi}_{\theta\theta}^* = \mathbf{\Pi}^*$  for brevity.

### 8.4.3. Calculation of Generalized Inertia Torques

The generalized inertia torque<sup>55</sup>  $\mathbf{\Gamma}_{m^*}^I \in R^n$  for the input set<sup>56</sup>  $m^* \in \{1, 2\}$  can be determined based on the kinetic energy expression in Eq. (8.54) and the Lagrangian equations of motion as also presented by Thomas and Tesar (1982):

$$\left(\mathbf{\Gamma}_{m^*}^I\right)^T = \frac{d}{dt} \left( \frac{\partial E_k}{\partial \dot{\boldsymbol{\phi}}_{m^*}} \right) - \frac{\partial E_k}{\partial \boldsymbol{\phi}_{m^*}} \quad (8.55)$$

The first term in Eq. (8.55) can be further simplified as

$$\frac{d}{dt} \left( \frac{\partial E_k}{\partial \dot{\boldsymbol{\phi}}_{m^*}} \right) = \sum_{i=1}^2 \left\{ \dot{\boldsymbol{\phi}}_i^T \left[ \mathbf{I}_{\phi\phi}^* \right]_{im^*} \right\} + \sum_{i=1}^2 \left\{ \dot{\boldsymbol{\phi}}_i^T \frac{d \left[ \mathbf{I}_{\phi\phi}^* \right]_{im^*}}{dt} \right\} \quad (8.56)$$

Using Eq. (8.53), the second term in Eq. (8.56) can be simplified as

$$\sum_{i=1}^2 \left\{ \dot{\boldsymbol{\phi}}_i^T \frac{d \left[ \mathbf{I}_{\phi\phi}^* \right]_{im^*}}{dt} \right\} = \sum_{i=1}^2 \left\{ \dot{\boldsymbol{\phi}}_i^T \frac{d}{dt} \left( \left[ \mathbf{G}_{\phi_i}^\theta \right]^T \boldsymbol{\Pi}^* \left[ \mathbf{G}_{\phi_{m^*}}^\theta \right] + \left[ \boldsymbol{\Pi}_M \right]_{im^*} \right) \right\} \quad (8.57)$$

or

$$\sum_{i=1}^2 \left\{ \dot{\boldsymbol{\phi}}_i^T \frac{d \left[ \mathbf{I}_{\phi\phi}^* \right]_{im^*}}{dt} \right\} = \sum_{i=1}^2 \left\{ \dot{\boldsymbol{\phi}}_i^T \left[ \mathbf{G}_{\phi_i}^\theta \right]^T \frac{d \boldsymbol{\Pi}^*}{dt} \left[ \mathbf{G}_{\phi_{m^*}}^\theta \right] \right\} \quad (8.58)$$

because  $\left[ \mathbf{G}_{\phi_i}^\theta \right]$  and  $\left[ \boldsymbol{\Pi}_M \right]_{ij}$  are constant matrices w.r.t. time for all  $i$  and  $j$ . Now, the time derivative of the joint space manipulator inertia matrix  $\boldsymbol{\Pi}^*$  can be determined (Nakamura, 1994, pp. 23-24):

$$\frac{d \boldsymbol{\Pi}^*}{dt} = \begin{pmatrix} \frac{\partial \boldsymbol{\Pi}_{:1}^*}{\partial \boldsymbol{\theta}} \dot{\boldsymbol{\theta}} & \frac{\partial \boldsymbol{\Pi}_{:2}^*}{\partial \boldsymbol{\theta}} \dot{\boldsymbol{\theta}} & \dots & \frac{\partial \boldsymbol{\Pi}_{:n}^*}{\partial \boldsymbol{\theta}} \dot{\boldsymbol{\theta}} \end{pmatrix} \quad (8.59)$$

where  $\boldsymbol{\Pi}_{:k}^*$  is the  $k$ -th column of  $\boldsymbol{\Pi}^*$ . Substituting Eq. (8.59) in Eq. (8.58)

$$\sum_{i=1}^2 \left\{ \dot{\boldsymbol{\phi}}_i^T \frac{d \left[ \mathbf{I}_{\phi\phi}^* \right]_{im^*}}{dt} \right\} = \sum_{i=1}^2 \left\{ \dot{\boldsymbol{\phi}}_i^T \left[ \mathbf{G}_{\phi_i}^\theta \right]^T \left( \frac{\partial \boldsymbol{\Pi}_{:1}^*}{\partial \boldsymbol{\theta}} \dot{\boldsymbol{\theta}} \quad \frac{\partial \boldsymbol{\Pi}_{:2}^*}{\partial \boldsymbol{\theta}} \dot{\boldsymbol{\theta}} \quad \dots \quad \frac{\partial \boldsymbol{\Pi}_{:n}^*}{\partial \boldsymbol{\theta}} \dot{\boldsymbol{\theta}} \right) \left[ \mathbf{G}_{\phi_{m^*}}^\theta \right] \right\} \quad (8.60)$$

<sup>55</sup> The convention used in this section is that the gradient of a scalar function w.r.t. a column vector is a row vector. This notation has been previously used in many works related to serial manipulator modeling (Thomas and Tesar, 1982; Nakamura, 1991; Sciavicco and Siciliano, 2001). For a primer on multivariable calculus for robotics applications refer (Nakamura, 1991; Sciavicco and Siciliano, 2001; Angeles, 2007).

<sup>56</sup> The notation  $m^*$  distinguishes the input that we are particularly interested in from the other inputs. For example, if the goal is to determine the inertial torques at the VA inputs, then  $m^* = 1$ .



and recognizing the terms independent of index  $i$ , Eq. (8.60) can also be expressed as

$$\begin{aligned} \sum_{i=1}^2 \left\{ \dot{\boldsymbol{\phi}}_i^T \frac{d[\mathbf{I}_{\phi\phi}^*]_{im^*}}{dt} \right\} &= \sum_{i=1}^2 \left\{ \dot{\boldsymbol{\phi}}_i^T [\mathbf{G}_{\phi_i}^\theta]^T \right\} \left( \frac{\partial \Pi_{:1}^*}{\partial \boldsymbol{\theta}} \dot{\boldsymbol{\theta}} \quad \frac{\partial \Pi_{:2}^*}{\partial \boldsymbol{\theta}} \dot{\boldsymbol{\theta}} \quad \dots \quad \frac{\partial \Pi_{:n}^*}{\partial \boldsymbol{\theta}} \dot{\boldsymbol{\theta}} \right) [\mathbf{G}_{\phi_{m^*}}^\theta] \\ &= \left( \dot{\boldsymbol{\theta}}^T \frac{\partial \Pi_{:1}^*}{\partial \boldsymbol{\theta}} \dot{\boldsymbol{\theta}} \quad \dot{\boldsymbol{\theta}}^T \frac{\partial \Pi_{:2}^*}{\partial \boldsymbol{\theta}} \dot{\boldsymbol{\theta}} \quad \dots \quad \dot{\boldsymbol{\theta}}^T \frac{\partial \Pi_{:n}^*}{\partial \boldsymbol{\theta}} \dot{\boldsymbol{\theta}} \right) [\mathbf{G}_{\phi_{m^*}}^\theta] \end{aligned} \quad (8.61)$$

Now the second term in Eq. (8.55) can be simplified as

$$\frac{\partial E_k}{\partial \boldsymbol{\phi}_{m^*}} = \frac{1}{2} \sum_{i=1}^2 \sum_{j=1}^2 \dot{\boldsymbol{\phi}}_i^T \frac{\partial [\mathbf{I}_{\phi\phi}^*]_{ij}}{\partial \boldsymbol{\phi}_{m^*}} \dot{\boldsymbol{\phi}}_j \quad (8.62)$$

Substituting Eq. (8.53) in Eq. (8.62)

$$\frac{\partial E_k}{\partial \boldsymbol{\phi}_{m^*}} = \frac{1}{2} \sum_{i=1}^2 \sum_{j=1}^2 \left\{ \dot{\boldsymbol{\phi}}_i^T \frac{\partial}{\partial \boldsymbol{\phi}_{m^*}} \left( [\mathbf{G}_{\phi_i}^\theta]^T \boldsymbol{\Pi}^* [\mathbf{G}_{\phi_j}^\theta] + [\boldsymbol{\Pi}_M]_{ij} \right) \dot{\boldsymbol{\phi}}_j \right\} \quad (8.63)$$

Eq. (8.63) can be reduced to

$$\frac{\partial E_k}{\partial \boldsymbol{\phi}_{m^*}} = \frac{1}{2} \sum_{i=1}^2 \sum_{j=1}^2 \left\{ \dot{\boldsymbol{\phi}}_i^T [\mathbf{G}_{\phi_i}^\theta]^T \frac{\partial \boldsymbol{\Pi}^*}{\partial \boldsymbol{\phi}_{m^*}} [\mathbf{G}_{\phi_j}^\theta] \dot{\boldsymbol{\phi}}_j \right\} \quad (8.64)$$

because  $[\boldsymbol{\Pi}_M]_{ij}$  is a constant matrix. Now the derivative can be determined as follows:

$$\mathbf{Y} = \begin{pmatrix} \frac{\partial \boldsymbol{\Pi}^*}{\partial \boldsymbol{\phi}_{m^*1}} & \frac{\partial \boldsymbol{\Pi}^*}{\partial \boldsymbol{\phi}_{m^*2}} & \dots & \frac{\partial \boldsymbol{\Pi}^*}{\partial \boldsymbol{\phi}_{m^*n}} \end{pmatrix} \quad (8.65)$$

where  $\boldsymbol{\phi}_{m^*k}$  refers to the  $k$ -th element in  $\boldsymbol{\phi}_{m^*}$ . Considering that  $\boldsymbol{\Pi}^*$  is a function of  $\boldsymbol{\theta}$ ,

using the chain rule of partial differentiation, Eq. (8.65) can be expanded as

$$\mathbf{Y} = \begin{pmatrix} \sum_{r=1}^n \frac{\partial \boldsymbol{\Pi}^*}{\partial \theta_r} \frac{\partial \theta_r}{\partial \boldsymbol{\phi}_{m^*1}} & \sum_{r=1}^n \frac{\partial \boldsymbol{\Pi}^*}{\partial \theta_r} \frac{\partial \theta_r}{\partial \boldsymbol{\phi}_{m^*2}} & \dots & \sum_{r=1}^n \frac{\partial \boldsymbol{\Pi}^*}{\partial \theta_r} \frac{\partial \theta_r}{\partial \boldsymbol{\phi}_{m^*n}} \end{pmatrix} \quad (8.66)$$

Substituting Eq. (8.66) in Eq. (8.64) results in a row vector

$$\frac{\partial E_k}{\partial \boldsymbol{\phi}_{m^*}} = \frac{1}{2} \sum_{i=1}^2 \sum_{j=1}^2 \left\{ \dot{\boldsymbol{\phi}}_i^T [\mathbf{G}_{\phi_i}^\theta]^T \mathbf{Y} [\mathbf{G}_{\phi_j}^\theta] \dot{\boldsymbol{\phi}}_j \right\} = \boldsymbol{\gamma}^T \quad (8.67)$$

whose  $c$ -th column  $\gamma_c$  can be expressed as

$$\gamma_c = \frac{1}{2} \sum_{i=1}^2 \sum_{j=1}^2 \left\{ \dot{\boldsymbol{\phi}}_i^T [\mathbf{G}_{\phi_i}^\theta]^T \left( \sum_{r=1}^n \frac{\partial \boldsymbol{\Pi}^*}{\partial \theta_r} \frac{\partial \theta_r}{\partial \boldsymbol{\phi}_{m^*c}} \right) [\mathbf{G}_{\phi_j}^\theta] \dot{\boldsymbol{\phi}}_j \right\} \quad (8.68)$$

or

$$\gamma_c = \frac{1}{2} \sum_{i=1}^2 \sum_{j=1}^2 \left\{ \dot{\phi}_i^T [\mathbf{G}_{\phi_i}^\theta]^T \left( \sum_{r=1}^n \frac{\partial \Pi^*}{\partial \theta_r} [\mathbf{G}_{\phi_{m^*}}^\theta]_{cr} \right) [\mathbf{G}_{\phi_j}^\theta] \dot{\phi}_j \right\} \quad (8.69)$$

or, re-ordering the summations

$$\gamma_c = \frac{1}{2} \sum_{r=1}^n \left( \sum_{i=1}^n \sum_{j=1}^n \dot{\phi}_i^T [\mathbf{G}_{\phi_i}^\theta]^T \frac{\partial \Pi^*}{\partial \theta_r} [\mathbf{G}_{\phi_{m^*}}^\theta]_{cr} [\mathbf{G}_{\phi_j}^\theta] \dot{\phi}_j \right) \quad (8.70)$$

Equation (8.70) can be further simplified as

$$\gamma_c = \frac{1}{2} \sum_{r=1}^n \left( \sum_{i=1}^n \sum_{j=1}^n \dot{\phi}_i^T [\mathbf{G}_{\phi_i}^\theta]^T \frac{\partial \Pi^*}{\partial \theta_r} [\mathbf{G}_{\phi_j}^\theta] \dot{\phi}_j \right) [\mathbf{G}_{\phi_{m^*}}^\theta]_{cr} \quad (8.71)$$

or

$$\gamma_c = \frac{1}{2} \left( \sum_{i=1}^n \sum_{j=1}^n \dot{\phi}_i^T [\mathbf{G}_{\phi_i}^\theta]^T \frac{\partial \Pi^*}{\partial \theta} [\mathbf{G}_{\phi_j}^\theta] \dot{\phi}_j \right) [\mathbf{G}_{\phi_{m^*}}^\theta]_{:c} \quad (8.72)$$

Using Eq. (8.72) to populate all columns of  $\gamma^T$  in Eq. (8.67)

$$\gamma^T = \frac{1}{2} \left( \sum_{i=1}^n \sum_{j=1}^n \dot{\phi}_i^T [\mathbf{G}_{\phi_i}^\theta]^T \frac{\partial \Pi^*}{\partial \theta} [\mathbf{G}_{\phi_j}^\theta] \dot{\phi}_j \right) [\mathbf{G}_{\phi_{m^*}}^\theta] \quad (8.73)$$

Similar to Eq. (8.61), Eq. (8.73) can now be expressed as

$$\frac{\partial E_k}{\partial \phi_{m^*}} = \frac{1}{2} \left( \dot{\theta}^T \frac{\partial \Pi^*}{\partial \theta_1} \dot{\theta} \quad \dot{\theta}^T \frac{\partial \Pi^*}{\partial \theta_2} \dot{\theta} \quad \dots \quad \dot{\theta}^T \frac{\partial \Pi^*}{\partial \theta_n} \dot{\theta} \right) [\mathbf{G}_{\phi_{m^*}}^\theta] \quad (8.74)$$

To determine the inertia torque demand at input set  $m^*$  we will combine Eqs. (8.56),

(8.61), and (8.74):

$$\begin{aligned} (\Gamma_{m^*}^I)^T &= \sum_{i=1}^2 \left\{ \ddot{\phi}_i^T [\mathbf{I}_{\phi\phi}^*]_{im^*} \right\} \\ &+ \left\{ \dot{\theta}^T \left( \frac{\partial \Pi_{:1}^*}{\partial \theta} - \frac{\partial \Pi^*}{\partial \theta_1} \right) \dot{\theta} \quad \dot{\theta}^T \left( \frac{\partial \Pi_{:2}^*}{\partial \theta} - \frac{\partial \Pi^*}{\partial \theta_2} \right) \dot{\theta} \quad \dots \quad \dot{\theta}^T \left( \frac{\partial \Pi_{:n}^*}{\partial \theta} - \frac{\partial \Pi^*}{\partial \theta_n} \right) \dot{\theta} \right\} [\mathbf{G}_{\phi_{m^*}}^\theta] \end{aligned} \quad (8.75)$$

Performing a matrix transpose operation on both sides of Eq. (8.75) we get

$$\Gamma_{m^*}^I = \sum_{i=1}^2 \left\{ [\mathbf{I}_{\phi\phi}^*]_{im^*} \ddot{\phi}_i \right\} + [\mathbf{G}_{\phi_{m^*}}^\theta]^T \dot{\theta}^T [\mathbf{P}_{\theta\theta}^*] \dot{\theta} \quad (8.76)$$

where

$$[\mathbf{P}_{\theta\theta}^*] = \left( \frac{\partial \Pi_{:1}^*}{\partial \theta} - \frac{\partial \Pi^*}{\partial \theta_1} \quad \frac{\partial \Pi_{:2}^*}{\partial \theta} - \frac{\partial \Pi^*}{\partial \theta_2} \quad \dots \quad \frac{\partial \Pi_{:n}^*}{\partial \theta} - \frac{\partial \Pi^*}{\partial \theta_n} \right)^T \quad (8.77)$$

is an  $n \times n \times n$  tensor called the inertia power array (Thomas and Tesar, 1982).

Substituting the velocity transformation from Eq. (8.6) into Eq. (8.76)

$$\Gamma_{m^*}^I = \sum_{i=1}^2 \left\{ \left[ \mathbf{I}_{\phi\phi}^* \right]_{im^*} \ddot{\phi}_i \right\} + \left[ \mathbf{G}_{\phi_{m^*}}^\theta \right]^T \sum_{i=1}^n \sum_{j=1}^n \left( \dot{\phi}_i^T \left[ \mathbf{G}_{\phi_i}^\theta \right]^T \left[ \mathbf{P}_{\theta\theta\theta}^* \right] \left[ \mathbf{G}_{\phi_j}^\theta \right] \dot{\phi}_j \right) \quad (8.78)$$

We can now explicitly write down the inertial torque demand on the VA input set:

$$\Gamma_1^I = \sum_{i=1}^2 \left\{ \left[ \mathbf{I}_{\phi\phi}^* \right]_{i1} \ddot{\phi}_i \right\} + \left[ \mathbf{G}_{\phi_1}^\theta \right]^T \sum_{i=1}^n \sum_{j=1}^n \left( \dot{\phi}_i^T \left[ \mathbf{G}_{\phi_i}^\theta \right]^T \left[ \mathbf{P}_{\theta\theta\theta}^* \right] \left[ \mathbf{G}_{\phi_j}^\theta \right] \dot{\phi}_j \right) \quad (8.79)$$

Similarly, the inertial torque demand on the FA input set is

$$\Gamma_2^I = \sum_{i=1}^2 \left\{ \left[ \mathbf{I}_{\phi\phi}^* \right]_{i2} \ddot{\phi}_i \right\} + \left[ \mathbf{G}_{\phi_2}^\theta \right]^T \sum_{i=1}^n \sum_{j=1}^n \left( \dot{\phi}_i^T \left[ \mathbf{G}_{\phi_i}^\theta \right]^T \left[ \mathbf{P}_{\theta\theta\theta}^* \right] \left[ \mathbf{G}_{\phi_j}^\theta \right] \dot{\phi}_j \right) \quad (8.80)$$

The total inertial torque demands on the inputs of the PFVA-driven manipulator can be visualized as being shared by VA- and FA-based manipulators as shown in Figure 8.10. It is important to understand the physical meaning of the terms in Eqs. (8.79)-(8.80). This has been shown in Figure 8.9 for  $m^*=1$  (i.e. VA input) and can be extended to the other input.

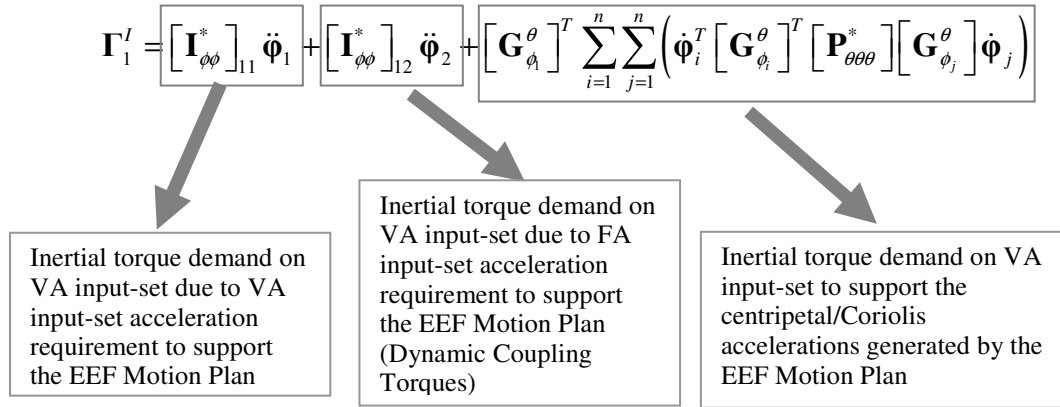
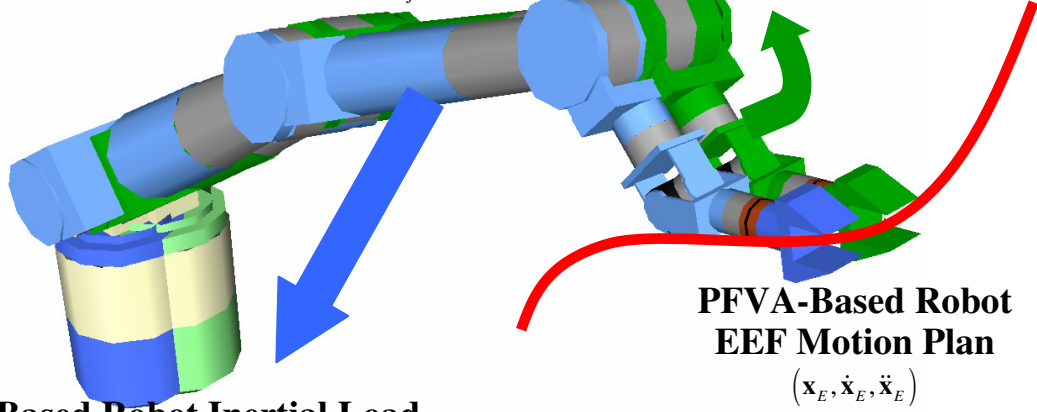


Figure 8.9. Physical meaning of inertial torque terms from Eq. (8.79) explained with regard to the VA input-set.

### FA-Based Robot Inertial Load

$$\Gamma_2^I = \sum_{i=1}^2 \left\{ \left[ \mathbf{I}_{\phi\phi}^* \right]_{i2} \ddot{\phi}_i \right\} + \left[ \mathbf{G}_{\phi_2}^\theta \right]^T \sum_{i=1}^n \sum_{j=1}^n \left( \dot{\phi}_i^T \left[ \mathbf{G}_{\phi_i}^\theta \right]^T \left[ \mathbf{P}_{\theta\theta\theta}^* \right] \left[ \mathbf{G}_{\phi_j}^\theta \right] \dot{\phi}_j \right)$$



### VA-Based Robot Inertial Load

$$\Gamma_1^I = \sum_{i=1}^2 \left\{ \left[ \mathbf{I}_{\phi\phi}^* \right]_{i1} \ddot{\phi}_i \right\} + \left[ \mathbf{G}_{\phi_1}^\theta \right]^T \sum_{i=1}^n \sum_{j=1}^n \left( \dot{\phi}_i^T \left[ \mathbf{G}_{\phi_i}^\theta \right]^T \left[ \mathbf{P}_{\theta\theta\theta}^* \right] \left[ \mathbf{G}_{\phi_j}^\theta \right] \dot{\phi}_j \right)$$

Figure 8.10. A PFVA-driven manipulator's inertial torque demand due to an EEF motion plan may be visualized as being shared by two constituent manipulators (with the same joint space and link configuration) driven by dual inputs at joints: (i) FAs, and (ii) VAs.

We have now determined the inertial torque demand on each input set (FA and VA) of the PFVA-driven manipulator. The next step is to develop the controlling equations of motion for the manipulator based on all types of torque demands.

## 8.5. CONTROLLING EQUATIONS OF MOTION FOR PFVA-DRIVEN MANIPULATOR

In this section we will consolidate the results from Sections 8.2-8.4 to develop the Equations of the Motion (EOM) for the PFVA-driven manipulator. The uniqueness of our development thus far has been that the input demands have been partitioned into the FA and VA input sets. We will do the same for the EOM as well. The EOM for the input set  $m^* \in \{1, 2\}$  can be developed using D'Alembert's principle (Lanczos, 1986, Chapter IV):

$$\left( \Gamma_{m^*}^A + \Gamma_{m^*}^S + \Gamma_{m^*}^F \right) - \left( \Gamma_{m^*}^I \right) = \mathbf{0}, \text{ or} \quad (8.81)$$

$$\mathbf{\Gamma}_{m^*}^I - (\mathbf{\Gamma}_{m^*}^S + \mathbf{\Gamma}_{m^*}^F) = \mathbf{\Gamma}_{m^*}^A$$

where

$\mathbf{\Gamma}_{m^*}^A$  = Actuator torque provided at input set  $m^*$ ,

$\mathbf{\Gamma}_{m^*}^I$  = Inertial torque demand on input set  $m^*$ ,

$\mathbf{\Gamma}_{m^*}^S$  = Static load torque demand (including gravity loads) on input set  $m^*$ , and

$\mathbf{\Gamma}_{m^*}^F$  = Friction torque demand on input set  $m^*$ , the development for which has not been explicitly presented in this chapter. However, this term can be added depending on the friction model used. A frequently used model is the Stribeck friction model (Armstrong-Hélouvy, 1991; Majd and Simaan, 1995).

Substituting previously developed expressions for  $\mathbf{\Gamma}_{m^*}^I$  and  $\mathbf{\Gamma}_{m^*}^S$  from Eqs. (8.45) and (8.79)-(8.80), respectively, in Eq. (8.81) we have two sets of coupled EOM for the VA and FA as shown below. In these expressions, the subscripts 1 and 2 have been replaced with  $v$  and  $f$ , respectively, for easily recognizing terms associated with the VA and FA.

EOM FOR VA-INPUT SET

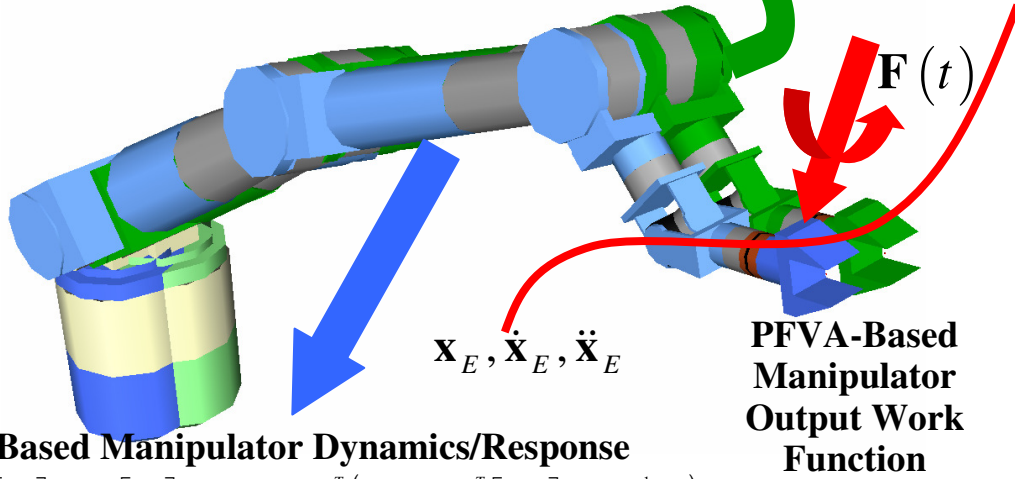
$$\begin{aligned} \mathbf{\Gamma}_v^A = & \left[ \mathbf{I}_{\phi\phi}^* \right]_{vv} \ddot{\phi}_v + \left[ \mathbf{I}_{\phi\phi}^* \right]_{vf} \ddot{\phi}_f + (\mathbf{I} + \tilde{\rho})^{-T} \left( \dot{\phi}_v^T (\mathbf{I} + \tilde{\rho})^{-T} \left[ \mathbf{P}_{\theta\theta}^* \right] (\mathbf{I} + \tilde{\rho})^{-1} \dot{\phi}_f \right) \\ & + (\mathbf{I} + \tilde{\rho})^{-T} \left( \dot{\phi}_v^T (\mathbf{I} + \tilde{\rho})^{-T} \left[ \mathbf{P}_{\theta\theta}^* \right] \tilde{\rho} (\mathbf{I} + \tilde{\rho})^{-1} \dot{\phi}_f \right) + (\mathbf{I} + \tilde{\rho})^{-T} \left( \dot{\phi}_f^T (\mathbf{I} + \tilde{\rho})^{-T} \tilde{\rho}^T \left[ \mathbf{P}_{\theta\theta}^* \right] (\mathbf{I} + \tilde{\rho})^{-1} \dot{\phi}_v \right) \\ & + (\mathbf{I} + \tilde{\rho})^{-T} \left( \dot{\phi}_f^T (\mathbf{I} + \tilde{\rho})^{-T} \tilde{\rho}^T \left[ \mathbf{P}_{\theta\theta}^* \right] \tilde{\rho} (\mathbf{I} + \tilde{\rho})^{-1} \dot{\phi}_f \right) + \mathbf{n}_{bv} (\mathbf{I} + \tilde{\rho})^{-T} \mathbf{F} + \mathbf{\Gamma}_v^F \end{aligned} \quad (8.82)$$

EOM FOR FA-INPUT SET

$$\begin{aligned} \mathbf{\Gamma}_f^A = & \left[ \mathbf{I}_{\phi\phi}^* \right]_{ff} \ddot{\phi}_f + \left[ \mathbf{I}_{\phi\phi}^* \right]_{fv} \ddot{\phi}_v + (\mathbf{I} + \tilde{\rho})^{-T} \tilde{\rho}^T \left( \dot{\phi}_1^T (\mathbf{I} + \tilde{\rho})^{-T} \left[ \mathbf{P}_{\theta\theta}^* \right] (\mathbf{I} + \tilde{\rho})^{-1} \dot{\phi}_1 \right) \\ & + (\mathbf{I} + \tilde{\rho})^{-T} \tilde{\rho}^T \left( \dot{\phi}_1^T (\mathbf{I} + \tilde{\rho})^{-T} \left[ \mathbf{P}_{\theta\theta}^* \right] \tilde{\rho} (\mathbf{I} + \tilde{\rho})^{-1} \dot{\phi}_2 \right) + (\mathbf{I} + \tilde{\rho})^{-T} \tilde{\rho}^T \left( \dot{\phi}_2^T (\mathbf{I} + \tilde{\rho})^{-T} \tilde{\rho}^T \left[ \mathbf{P}_{\theta\theta}^* \right] (\mathbf{I} + \tilde{\rho})^{-1} \dot{\phi}_1 \right) \\ & + (\mathbf{I} + \tilde{\rho})^{-T} \tilde{\rho}^T \left( \dot{\phi}_2^T (\mathbf{I} + \tilde{\rho})^{-T} \tilde{\rho}^T \left[ \mathbf{P}_{\theta\theta}^* \right] \tilde{\rho} (\mathbf{I} + \tilde{\rho})^{-1} \dot{\phi}_2 \right) + \mathbf{n}_{bf} (\mathbf{I} + \tilde{\rho})^{-T} \tilde{\rho}^T \mathbf{F} + \mathbf{\Gamma}_f^F \end{aligned} \quad (8.83)$$

### FA-Based Manipulator Dynamics/Response

$$\begin{aligned} \Gamma_f^A = & [\mathbf{I}_{\phi\phi}^*]_{ff} \ddot{\phi}_f + [\mathbf{I}_{\phi\phi}^*]_{fv} \ddot{\phi}_v + (\mathbf{I} + \tilde{\rho})^{-T} \tilde{\rho}^T \left( \dot{\phi}_1^T (\mathbf{I} + \tilde{\rho})^{-T} [\mathbf{P}_{\theta\theta}^*] (\mathbf{I} + \tilde{\rho})^{-1} \dot{\phi}_1 \right) \\ & + (\mathbf{I} + \tilde{\rho})^{-T} \tilde{\rho}^T \left( \dot{\phi}_1^T (\mathbf{I} + \tilde{\rho})^{-T} [\mathbf{P}_{\theta\theta}^*] \tilde{\rho} (\mathbf{I} + \tilde{\rho})^{-1} \dot{\phi}_2 \right) + (\mathbf{I} + \tilde{\rho})^{-T} \tilde{\rho}^T \left( \dot{\phi}_2^T (\mathbf{I} + \tilde{\rho})^{-T} \tilde{\rho}^T [\mathbf{P}_{\theta\theta}^*] (\mathbf{I} + \tilde{\rho})^{-1} \dot{\phi}_1 \right) \\ & + (\mathbf{I} + \tilde{\rho})^{-T} \tilde{\rho}^T \left( \dot{\phi}_2^T (\mathbf{I} + \tilde{\rho})^{-T} \tilde{\rho}^T [\mathbf{P}_{\theta\theta}^*] \tilde{\rho} (\mathbf{I} + \tilde{\rho})^{-1} \dot{\phi}_2 \right) + \eta_{bf} (\mathbf{I} + \tilde{\rho})^{-T} \tilde{\rho}^T \mathbf{F} + \Gamma_f^F \end{aligned}$$



### VA-Based Manipulator Dynamics/Response

$$\begin{aligned} \Gamma_v^A = & [\mathbf{I}_{\phi\phi}^*]_{vv} \ddot{\phi}_v + [\mathbf{I}_{\phi\phi}^*]_{vf} \ddot{\phi}_f + (\mathbf{I} + \tilde{\rho})^{-T} \left( \dot{\phi}_v^T (\mathbf{I} + \tilde{\rho})^{-T} [\mathbf{P}_{\theta\theta}^*] (\mathbf{I} + \tilde{\rho})^{-1} \dot{\phi}_f \right) \\ & + (\mathbf{I} + \tilde{\rho})^{-T} \left( \dot{\phi}_v^T (\mathbf{I} + \tilde{\rho})^{-T} [\mathbf{P}_{\theta\theta}^*] \tilde{\rho} (\mathbf{I} + \tilde{\rho})^{-1} \dot{\phi}_f \right) + (\mathbf{I} + \tilde{\rho})^{-T} \left( \dot{\phi}_f^T (\mathbf{I} + \tilde{\rho})^{-T} \tilde{\rho}^T [\mathbf{P}_{\theta\theta}^*] (\mathbf{I} + \tilde{\rho})^{-1} \dot{\phi}_v \right) \\ & + (\mathbf{I} + \tilde{\rho})^{-T} \left( \dot{\phi}_f^T (\mathbf{I} + \tilde{\rho})^{-T} \tilde{\rho}^T [\mathbf{P}_{\theta\theta}^*] \tilde{\rho} (\mathbf{I} + \tilde{\rho})^{-1} \dot{\phi}_f \right) + \eta_{bv} (\mathbf{I} + \tilde{\rho})^{-T} \mathbf{F} + \Gamma_v^F \end{aligned}$$

Figure 8.11. A PFVA-driven manipulator's total torque demand due to an EEF motion plan and contact force may be visualized as being shared by two constituent manipulators (with the same joint space and link configuration) driven by dual inputs at joints: (i) FAs, and (ii) VAs.

where  $\tilde{\rho}$  is the RSF matrix defined earlier in Eq. (8.8). The individual dynamics of each input-set can be visualized as shown in Figure 8.11. Notice that Eqs. (8.82)-(8.83) are a coupled set of differential equations and have to be evaluated (for the inverse dynamics problem) and/or solved (for the forward dynamic problem) together for a complete understanding of the PFVA-driven manipulator's dynamics. The unique representation we have followed in this chapter – isolating the demands for each input set, VA and FA – is for convenience of understanding the dynamic effects at these two distinctive coupled

inputs at each joint. This representation is particularly useful for designing PFVA-driven manipulators.

### 8.6. 3R PLANAR PFVA-DRIVEN MANIPULATOR EXAMPLE: PARAMETER STUDY

In this section we will demonstrate the models we have developed in the previous sections through simulations using a planar PFVA-driven manipulator with all rotary joints. The kinematic and dynamic parameters of this manipulator, and those of the PFVAs used in its joints are listed in Appendix D. One of our motivations in developing the generalized dynamic model for PFVA-driven robot manipulators was to perform parameter studies to compare various designs. In this section we will present such a study using various RSF values at the PFVA joints of the 3R robot.

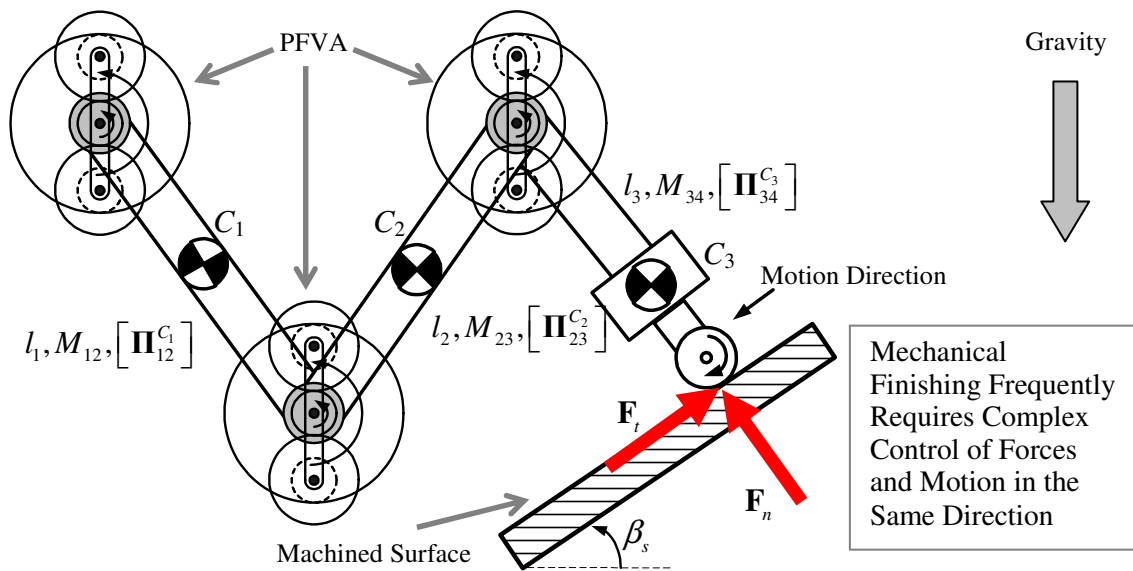


Figure 8.12. Conceptual representation of a planar 3R PFVA-driven manipulator performing a finishing operation on a part surface. The centers of mass of the links are also shown.

### 8.6.1. Methodology

To model the work function acting on the 3R planar robot manipulator (Figure 8.12), a contact task is considered where a grinding tool attached to the manipulator end-point is performing a mechanical finishing operation on an inclined planar surface. In addition, the manipulator is in a gravity field. The geometric stability of force control based on previous work at the Robotics Research Group by Yi et al. (1988) was considered in choosing the direction of motion of the grinding wheel with respect to the surface (Figure 8.12). The details regarding the contact task are listed in Appendix D. This task results in distinct loading conditions at the VA and FA input-sets depending on the choice of the RSF matrix  $\tilde{\rho}$ . Our parameter study in this section is a first step in the direction of developing guidelines for this choice.

Before we explain the methodology used for the parameter study, it is important to understand the physical implications of choosing  $\tilde{\rho} = \text{diag}(\tilde{\rho}_i)$ . For a given total maximum load requirement  $\tau_{\max}$  at a joint  $j$  based on the manipulator design, the FA and VA in this joint both have to be designed to support  $\tau_{\max}$ . This follows from the velocity-summing property of the PFVA, due to which the joint load is shared by both input sets. Now, based on the determined total load requirement at the FA and VA, choosing a RSF  $\tilde{\rho}$  for this joint in turn determines four important parameters among others: (i) velocity-ratios for each input, (ii) inertia content in the transmission, (iii) inertia content in the prime-movers, and (iv) backdriving efficiencies of the two inputs. For example, if the total joint load requirement was 100 N-m and we choose  $\tilde{\rho} = 9$ . This implies that  $g_v = 0.1$  and  $g_f = 0.9$ . Based on these velocity ratios, the VA and FA have to be designed for a maximum rating of 10 and 90 N-m, respectively. The velocity ratios and the torque capacities will now determine the differential gear train and the VA and FA



prime-movers. Therefore, the inertia content in the prime-movers and the backdriving efficiency of each input are governed by these requirements.

For this study, we will consider only the parameter variation of the RSF values ( $\tilde{\rho}$ ). In addition, we will restrict these RSF values to the set  $\{255.4, 24.3, 1.0\}$  which are three distinct designs (approximately equispaced on log-scale) chosen from the SR product range offered by Andantex, Inc (2007). This product was used in the PFVA prototype ( $\tilde{\rho} = 24.3$ ) described in Chapter 7 and the parameters from this product range were used in Chapters 4-6 as well. Based on the above set of RSF values and the DOF of the robot, the design space for RSF can be represented as shown in Figure 8.13.

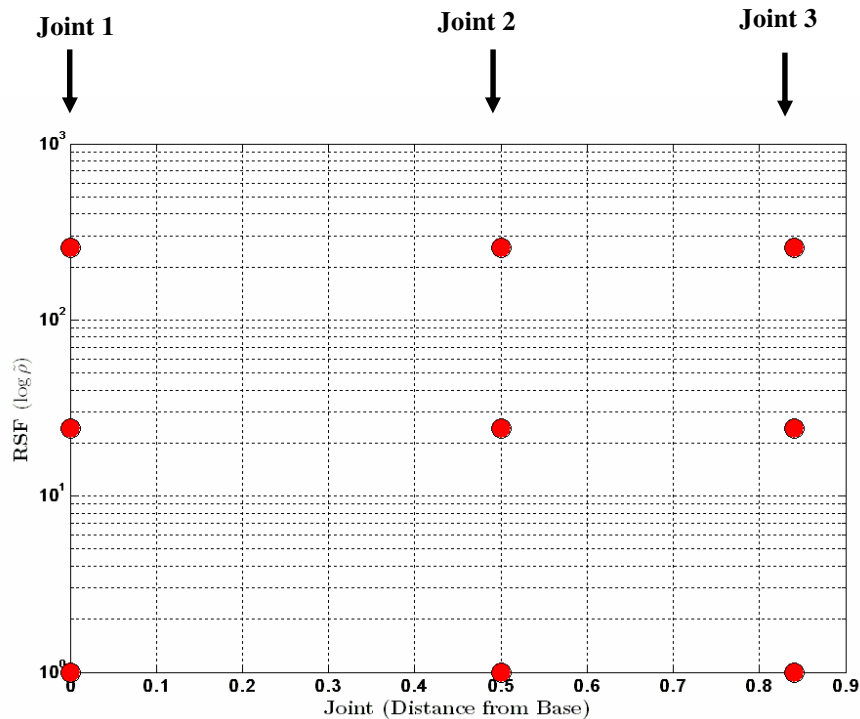


Figure 8.13. Design space for choosing RSF values for the 3R PFVA-driven Robot.

In this design space we will study three cases, the trends for which are shown in Figure 8.14. In Case (1) we will look at the effect of a constant large RSF = 255.4 for all joints in the 3R robot. In Case (2) we will analyze the effect of a constant small RSF = 1.0 for

all joints, and in Case (3) we will consider a decreasing trend of RSF as we move from the first joint to the most distal joint ( $\tilde{\rho}_1 = 255.4$ ,  $\tilde{\rho}_2 = 24.3$ , and  $\tilde{\rho}_3 = 1.0$ ).

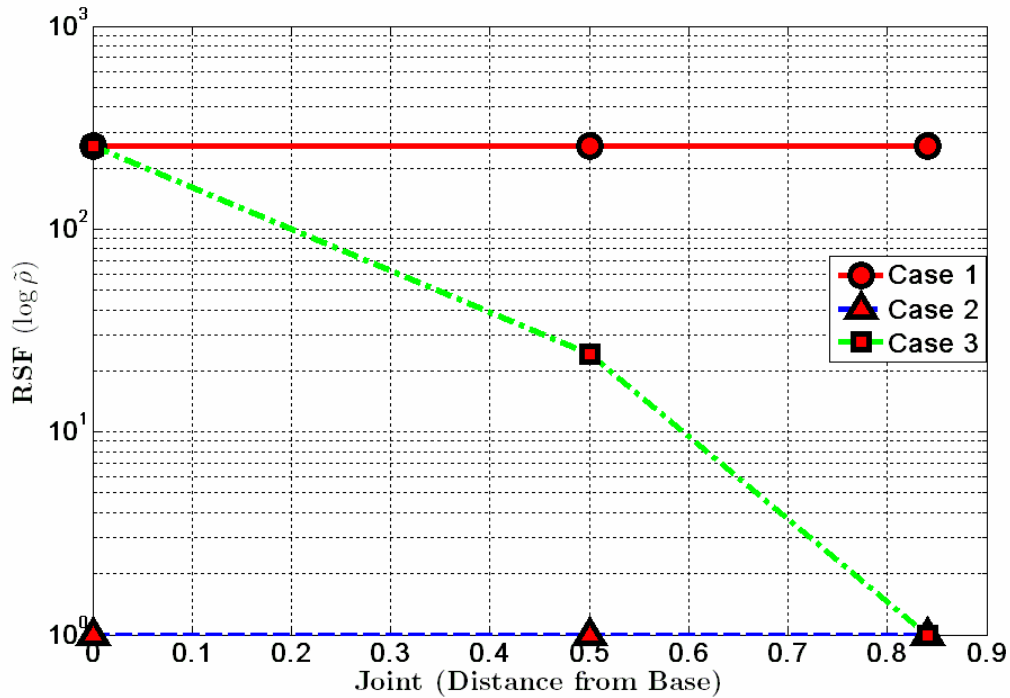


Figure 8.14. Design cases considered in the RSF-based parameter study.

For each of the above mentioned cases, we will study the distribution of each type of load, i.e. acceleration torques, Coriolis/centripetal torques, static load torques, and gravity torques, on the VA and FA input sets. Conclusions will be drawn about these specific design cases based on the sensitivity of an input to an external disturbance acting at the EEF and the resulting inertial load on an input due to the RSF choice.

### 8.6.2. Implementation

The C++ software library called Operational Software Components for Advanced Robotics (OSCAR) (OSCAR Reference, 2008) was used for this implementation. This software architecture was developed at the Robotics Research Group (Kapoor and Tesar,

1996). OSCAR is an object-oriented library that can be used for both operation and design of serial manipulators. It was designed to be generalized, modular, re-usable, and extensible. Among others, OSCAR includes operational software libraries for kinematics, dynamics, performance criteria, motion planning, and controls. The RSF-based parameter study entailed the computation of inverse dynamics for the serial 3R planar robot in the PFVA space. The Newton-Euler component from OSCAR's dynamics library was used to compute the inverse dynamics solution in the joint space. This result was then transformed<sup>57-58</sup> to the PFVA space using the generalized model developed earlier in this chapter in Eqs. (8.82)-(8.83). This procedure is relatively convenient for the computation of inverse dynamics; however it is not as straight-forward to dynamically simulate the PFVA-driven robot (i.e. forward dynamics) because the two coupled sets of EOMs for the VA and FA have to be integrated simultaneously. In our parameter study only the computation of inverse dynamics was necessary.

### 8.6.3. Results

Before we performed the design case studies the total joint torque requirement for the 3R robot during the contact task was analyzed (Figure 8.15). As the task performed by the robot is a low-velocity contact task, the acceleration and velocity related torques are much lower (1 and 3 orders of magnitude for the acceleration and velocity torques, respectively) when compared to the gravity and load torques. Based on this joint torque requirement, the design torques for J1, J2, and J3 (i.e. joints 1, 2, and 3) were determined to be 150, 100, and 40 N-m, respectively. The sum of the different torque components was used to arrive at these estimates. The prime-mover and gear train inertias for each

---

<sup>57</sup> As mentioned before, this transformation of generalized coordinates can also be done using the method suggested by Freeman and Tesar (1988).

<sup>58</sup> To transform the acceleration torques from the joint space to the PFVA space, pseudo-inverse based accelerations were used for the FA and VA inputs (see Eq. (8.36) for details) with zero null-accelerations.

joint, and the backdriving efficiencies for the drive trains were then determined based on these torque requirements (see Appendix D for details).

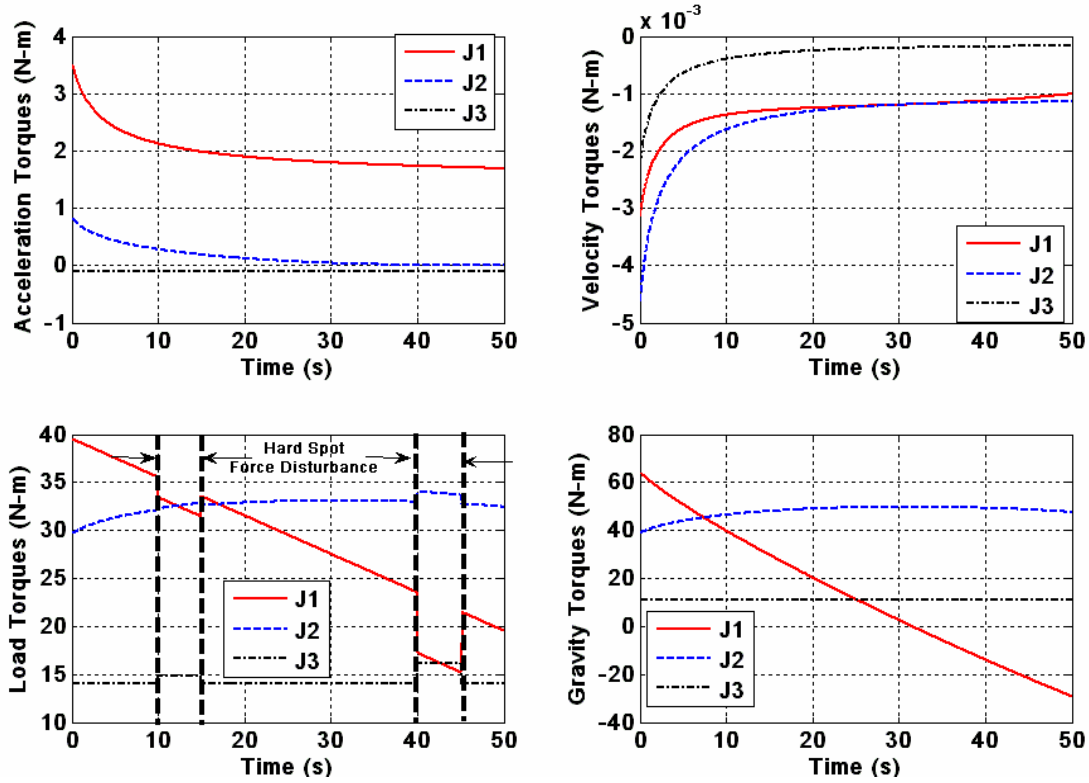


Figure 8.15. Joint torques for the finishing task performed by a 3R planar manipulator (see Appendix D for details).

We will now systematically present the results from the three case studies.

**Case 1** ( $\tilde{\rho}_1 = \tilde{\rho}_2 = \tilde{\rho}_3 = 255.4$ ). The results from this case are shown in Figure 8.16. In this figure, the different torque components, i.e. acceleration, velocity (centripetal/Coriolis), load, and gravity torques, acting on the VA and FA inputs at the three joints (J1, J2, and J3) are shown for the entire task. These torque components were determined based on the joint torque requirements shown in Figure 8.15.

### DESIGN CASE 1

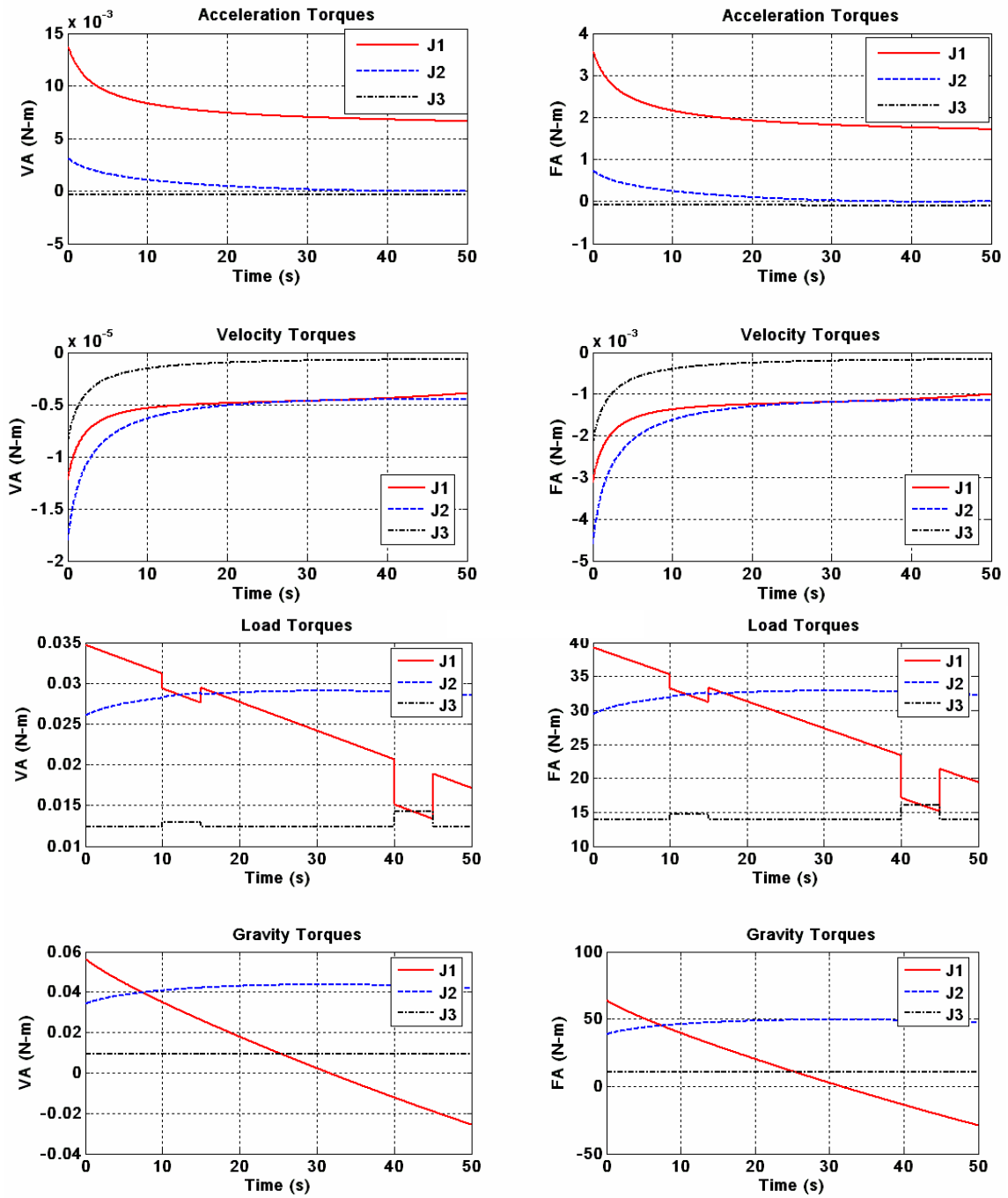


Figure 8.16. Distribution of torque requirement between VA and FA input sets of the 3R manipulator for Design Case 1 ( $\tilde{\rho}_1 = \tilde{\rho}_2 = \tilde{\rho}_3 = 255.4$ ).

In this design case, the FA at every joint is approximately equivalent to a direct drive actuator (i.e.  $g_f = 0.9961$ ). Consequently, almost all the load at the joint is required to be supported by the FA input set. The average total (sum of all components at all joints) torque requirement at the FA inputs is approximately 3 orders of magnitude greater than that at the VA inputs. Due to this high torque requirement, the mass content in the FA input set is on the average approximately 4 orders of magnitude greater than that at the VA input set. This remarkable distinction in mass content can be observed as a marked difference in the acceleration torque distribution between the two input sets shown in Figure 8.16. Another metric we introduced and defined in Chapter 5 is the dynamic coupling factor  $\tilde{\mu} = \tilde{\rho} / (\tilde{\rho} + 1)^2$  which indicates the extent of inertial disturbance between the two inputs. In this case study  $\tilde{\mu} = 0.4\%$  for all joints, or in other words, the coupling inertia between the FA and VA at every joint is only 0.4% of the joint reflected inertia at the joint. Therefore, the two input sets in this design are essentially decoupled. Now, the backdriving efficiency of the FA input set is 99.7% and that for the VA set is 22.5%. Considering also the high RSF value of 255.4, this means that the load and gravity torques at the joints will be reflected at the FA input set almost entirely. Observe that the FA input set sees a change of approximately 8 N-m at  $t = 40s$  at J1, while, at the same instant, the VA sees a change of only 0.007 N-m (a factor of  $255.4 \times (99.7 / 22.5) \approx 1131$ ). If the torque at the FA input set is limited to a safe threshold then this torque limitation together with the high sensitivity of the FA input set can be utilized to safely respond to collisions (as experimentally demonstrated for a 1-DOF PFVA in Chapter 7) or to sense and respond to force disturbances. Comparison of mean values in this case study is justified because the RSF values are equal at all joints. This is true for the next design case as well which will now be discussed.

DESIGN CASE 2

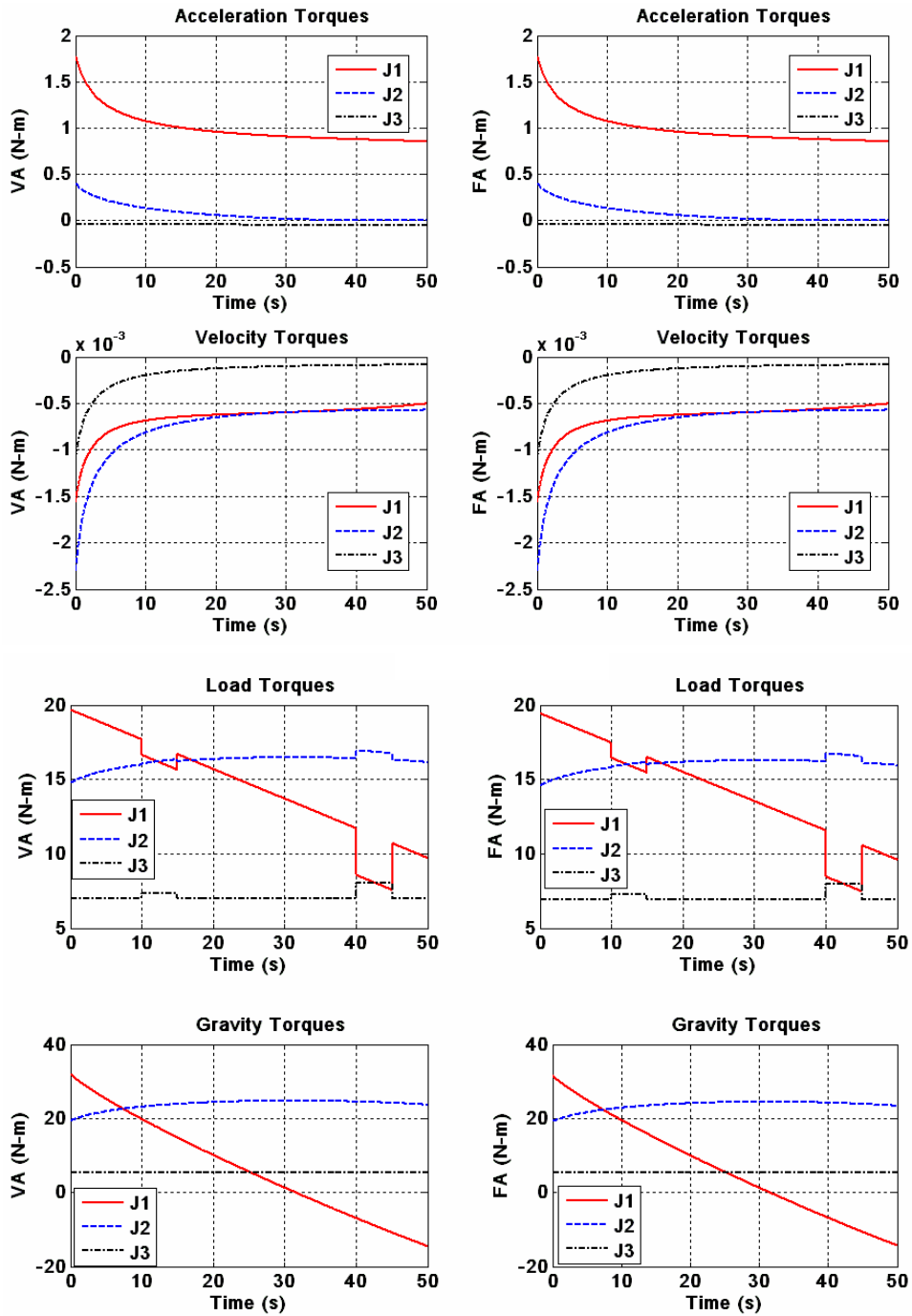


Figure 8.17. Distribution of torque requirement between VA and FA input sets of the 3R manipulator for Design Case 2 ( $\tilde{\rho}_1 = \tilde{\rho}_2 = \tilde{\rho}_3 = 1$ ).

DESIGN CASE 3

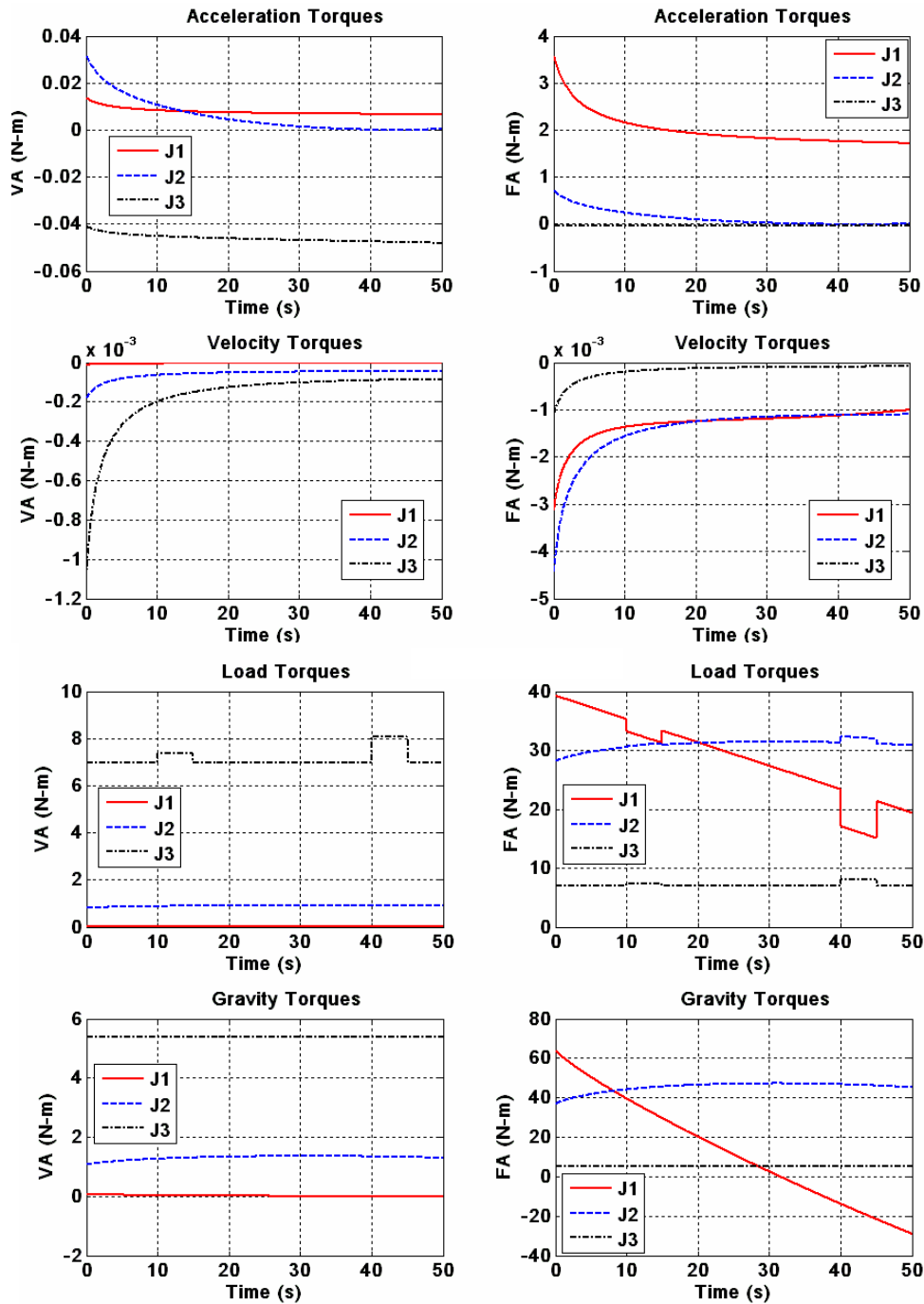


Figure 8.18. Distribution of torque requirement between VA and FA input sets of the 3R manipulator for Design Case 3 ( $\tilde{\rho}_1 = 255.4$ ,  $\tilde{\rho}_2 = 24.3$ ,  $\tilde{\rho}_3 = 1$ ).



**Case 2** ( $\tilde{\rho}_1 = \tilde{\rho}_2 = \tilde{\rho}_3 = 1$ ). The results from this case are shown in Figure 8.17. In this case study, the joint torque requirements are, as expected, equally distributed between the two inputs. This is a classical example of Level I fault-tolerance (Tesar et al., 1990; Sreevijayan et al., 1994) where velocity-summing equal dual inputs drive the output. This type of design ( $\tilde{\rho} = 1$ ) was used by Wu et al. (1993) to develop a differential based fault tolerant actuator for a remote manipulator on a space shuttle. This design case is ideal for fault tolerance because the two input sets are essentially equivalents and can potentially replace each other in the event of a fault. This is a good design for utilizing the kinematic redundancy in the dual drive actuator because higher null-space velocities result. For example, if  $\tilde{\rho} = 200$  and the VA's maximum velocity is 400 rpm, then the maximum velocity at which the FA can be rotated to obtain null output motion is only -2 rpm. Typically, electrical motors do not provide precise velocity control at such low speeds. Now, if the RSF is reduced to  $\tilde{\rho} = 1$ , then, for the above example, the FA can now be rotated at -200 (which is significantly higher and precisely achievable) to produce a zero output velocity.

On the contrary, from a dynamics point of view, such a design is energetically inefficient because the dynamic coupling factor is approximately  $\tilde{\mu} = 25\%$  (its maximum<sup>59</sup> value). Physically, this means that if both inputs are driving the output, then each input spends half of its effort to fight the dynamic disturbance due to the other input. In Figure 8.17, observe the equal distribution (for example, approximately 1.75 N-m for J1 at initial condition) of joint acceleration torque requirement between the two input sets. Now, half of this torque produced by each input (i.e. 0.875 N-m) is used to fight the inertial disturbance of the other input.

---

<sup>59</sup> See Eq. (14) and Fig. 4 in (Rabindran and Tesar, 2007a) to determine this maximum.

**Case 3** ( $\tilde{\rho}_1 = 255.4$ ,  $\tilde{\rho}_2 = 24.3$ ,  $\tilde{\rho}_3 = 1$ ). Results from this case are shown in Figure 8.18. This design case was chosen to understand the effect of unequal distribution of RSFs along the serial chain. Based on lessons learned in the design cases (1) and (2) discussed earlier, a decreasing RSF trend was used. A high value of RSF  $\tilde{\rho}_1 = 255.4$  at the base joint concentrates most of the mass content there. This proximal mass content in a serial chain manipulator is relatively more tractable from an operational point of view. At the same time, the effort on the FAs at distal joints can be reduced by choosing a lower value of RSF for them. For J3, the lowest possible value (considering only positive-ratio drive trains) was chosen ( $\tilde{\rho}_3 = 1$ ). The design requirement for J2 was 100 N-m which closely matched that of the PFVA testbed described in the previous chapter. Therefore,  $\tilde{\rho}_2 = 24.3$  (same as the RSF for the experimental prototype) was chosen for J2.

In this ‘mixed’ case, the distribution of different torque components among the FA and VA at J1 is similar to case (1) and the distribution at J3 is similar to case (2). For J2, the dynamic coupling factor is  $\tilde{\mu} = 3.8\%$  which indicates almost 10 times *more* coupling than at J1 and approximately 7 times *less* coupling than at J3. Also, J1 is the most sensitive to output torque disturbances because of two reasons: (i) it is the farthest from the tool point where the tool-part interaction takes place, and (ii) it has the largest RSF. This can be concluded from Figure 8.18 by comparing the change in FA load torque in J1 (6.2940 Nm) at  $t = 40s$  (force disturbance due to hard spot in the machined part) to those in J2 (1.0083 Nm) and J3 (1.06 Nm) at the same instant. Physically this means that J1 will be most sensitive to the force disturbance at the EEF.

#### **8.6.4. Discussion on RSF Based Parameter Study**

The RSF based parameter study presented in this section is preliminary work in exploring the available design space. For the chosen set of actuators, we have explored only 3 out of 9 possible combinations (see Figure 8.13 and Figure 8.14) because these are

the physically meaningful and worthwhile to pursue based on the work of Rios and Tesar (2009). For discussion purposes, if a set of  $p$  PFVA designs (or, equivalently, RSF values) are considered for an  $n$ -DOF serial manipulator ( $p \geq n$ ), then there are  $\binom{p}{n}$  possible configurations. In this section we have pointed to some metrics (for example, dynamic coupling factor) which can be used to explore this design space. However, a detailed design methodology is yet to be laid out to choose an optimal RSF set for a manipulator with a given kinematic configuration and task parameters.

It was observed in our design case studies that due to the force sensitivity of the FA inputs (due to high RSF values) these inputs can be made backdriveable by limiting the torque on them. This observation now raises an intriguing question: where on the serial manipulator is backdriveability more relevant? For example, in a 6-DOF manipulator with a PUMA configuration, is it more useful to have backdriveability in the regional structure (3 inboard joints) or the orientation structure (wrist joints)? Through our parameter study we have shown that such a question can be answered only by concurrently designing the manipulator and the backdriveable actuator (for example, PFVA).

## **8.7. INTRODUCTION TO PFVA-DRIVEN MANIPULATOR PERFORMANCE CRITERIA**

Having developed a complete model for PFVA-driven manipulators, we can now begin to leverage past work on performance criteria for serial manipulators (Tisius et al., 2004; Tisius et al., 2009) and develop similar criteria for PFVA-driven serial manipulators. This section presents introductory work toward that goal. Two performance criteria are developed: (i) partition value of kinetic energy to measure the distribution of kinetic energy in a PFVA-driven manipulator between the FA and VA input sets, and (ii) generalized relative scale factor which is an extension of the RSF concept for a PFVA to a PFVA-manipulator.

### 8.7.1. Partition Value of Kinetic Energy

The total kinetic energy of the PFVA-driven manipulator was developed in Section 8.4.2 in Eq. (8.54):

$$E_k = \frac{1}{2} \sum_{l=1}^2 \sum_{m=1}^2 \dot{\phi}_l^T [\mathbf{I}_{\phi\phi}^*]_{lm} \dot{\phi}_m \quad (8.84)$$

The Partition Value of Kinetic Energy (PVKE)<sup>60</sup> for a particular input set  $m^*$  can now be determined as

$$\mathcal{E}_{m^*} = \frac{\frac{1}{2} \sum_{l=1}^2 \dot{\phi}_l^T [\mathbf{I}_{\phi\phi}^*]_{lm^*} \dot{\phi}_{m^*}}{\frac{1}{2} \sum_{l=1}^2 \sum_{m=1}^2 \dot{\phi}_l^T [\mathbf{I}_{\phi\phi}^*]_{lm} \dot{\phi}_m} \quad (8.85)$$

For example, the PVKE for the VA input set in the PFVA-driven manipulator can be expressed as (using subscripts  $v$  and  $f$  instead of 1 and 2, respectively)

$$\mathcal{E}_v = \frac{\dot{\phi}_v^T [\mathbf{I}_{\phi\phi}^*]_{vv} \dot{\phi}_v + \dot{\phi}_v^T [\mathbf{I}_{\phi\phi}^*]_{vf} \dot{\phi}_f}{\dot{\phi}_v^T [\mathbf{I}_{\phi\phi}^*]_{vv} \dot{\phi}_v + \dot{\phi}_v^T [\mathbf{I}_{\phi\phi}^*]_{vf} \dot{\phi}_f + \dot{\phi}_f^T [\mathbf{I}_{\phi\phi}^*]_{ff} \dot{\phi}_f + \dot{\phi}_f^T [\mathbf{I}_{\phi\phi}^*]_{fv} \dot{\phi}_v} \quad (8.86)$$

Similarly, the PVKE for the FA input set is

$$\mathcal{E}_f = \frac{\dot{\phi}_f^T [\mathbf{I}_{\phi\phi}^*]_{ff} \dot{\phi}_f + \dot{\phi}_f^T [\mathbf{I}_{\phi\phi}^*]_{fv} \dot{\phi}_v}{\dot{\phi}_v^T [\mathbf{I}_{\phi\phi}^*]_{vv} \dot{\phi}_v + \dot{\phi}_v^T [\mathbf{I}_{\phi\phi}^*]_{vf} \dot{\phi}_f + \dot{\phi}_f^T [\mathbf{I}_{\phi\phi}^*]_{ff} \dot{\phi}_f + \dot{\phi}_f^T [\mathbf{I}_{\phi\phi}^*]_{fv} \dot{\phi}_v} \quad (8.87)$$

### 8.7.2. Generalized Relative Scale Factor

The velocity ratio and mechanical advantage are significant criteria to analyze the performance of a mechanical system (Chen and Tsai, 1993). These criteria have been generalized for mechanical systems (for example, linkages and manipulators) in the form of Kinematic Influence Coefficients (KICs) (Benedict and Tesar, 1978; Hall, 1992). Several scalar KIC measures have been proposed to indicate the influence of the inputs on the outputs in a multi-input-multi-output system such as an  $n$ -DOF serial robot

---

<sup>60</sup> See Chapter 5 in (Rios and Tesar, 2008) for a detailed literature statement and concept description of PVKEs.

manipulator. Chen and Tsai (1993) suggested a measure called generalized velocity ratio. We will use this measure and derive a new measure for PFVA-type (i.e. velocity-summing) manipulators called Generalized Relative Scale Factor (GRSF). RSF was introduced in Chapter 3 and has been extensively used in this work. Therefore we thought it relevant to generalize this concept, in the form of GSRF, for the PFVA-driven manipulator. GSRF is defined as the ratio of the generalized velocity ratios of the FA and VA inputs.

We will define a weighted norm  $\|\dot{\mathbf{x}}\|: \chi \rightarrow R$  of the EEF velocity vector  $\dot{\mathbf{x}}$  as (Chen and Tsai, 1993)

$$\|\dot{\mathbf{x}}\|^2 = \dot{\mathbf{x}}^T \mathbf{W}_x \dot{\mathbf{x}} \quad (8.88)$$

where  $\mathbf{W}_x \in R^{m \times m}$  is an appropriate positive-definite weighting matrix that accounts for the unit inconsistency among the elements<sup>61</sup> of  $\dot{\mathbf{x}}$ . Similarly, the norm  $\|\dot{\phi}_i\|: \Phi \rightarrow R$  ( $i \in \{1, 2\}$ ) of the velocity of the input set  $i$  can be defined as

$$\|\dot{\phi}_i\|^2 = \dot{\phi}_i^T \mathbf{W}_\phi \dot{\phi}_i \quad (8.89)$$

where  $\mathbf{W}_\phi \in R^{n \times n}$  is an appropriate positive-definite weighting matrix. Assuming that only the input set  $i$  is active in the manipulator and the other input is controlled at zero velocity, the generalized velocity ratio  ${}^i \kappa_v$  corresponding to input  $i$  is defined as

$${}^i \kappa_v^2 = \frac{\|\dot{\mathbf{x}}\|^2}{\|\dot{\phi}_i\|^2} \quad (8.90)$$

Substituting Eqs. (8.88)-(8.89) in Eq. (8.90)

$${}^i \kappa_v^2 = \frac{\dot{\mathbf{x}}^T \mathbf{W}_x \dot{\mathbf{x}}}{\dot{\phi}_i^T \mathbf{W}_\phi \dot{\phi}_i} \quad (8.91)$$

Using Eq. (8.15) in Eq. (8.90) and assuming only input set  $i$  to be controlled with non-zero velocity (the other being controlled at zero velocity), we have

---

<sup>61</sup> The first three components of  $\dot{\mathbf{x}}$  represent translational velocities with units of, for example, m/s and the last three elements represent rotational velocities with units of, say, rad/s.

$${}^i\kappa_v^2 = \frac{\dot{\boldsymbol{\phi}}_i^T [\mathbf{G}_{\phi_i}^\theta]^T [\mathbf{G}_\theta^x]^T \mathbf{W}_x [\mathbf{G}_\theta^x] [\mathbf{G}_{\phi_i}^\theta] \dot{\boldsymbol{\phi}}_i}{\dot{\boldsymbol{\phi}}_i^T \mathbf{W}_\phi \dot{\boldsymbol{\phi}}_i} \quad (8.92)$$

Now consider the following generalized eigenvalue problem:

$$\left\{ [\mathbf{G}_{\phi_i}^\theta]^T [\mathbf{G}_\theta^x]^T \mathbf{W}_x [\mathbf{G}_\theta^x] [\mathbf{G}_{\phi_i}^\theta] \right\} \dot{\boldsymbol{\phi}}_i = \{ {}^i\lambda \mathbf{W}_\phi \} \dot{\boldsymbol{\phi}}_i \quad (8.93)$$

Recognize that the ratio in Eq. (8.92) is the *Rayleigh quotient* (Strang, 1988, pp. 347-352) and, therefore, the square-root of the eigenvalues of Eq. (8.93) represents the extreme values of  ${}^i\kappa_v$ . Substituting Eqs. (8.9)-(8.10) in Eq. (8.93) we can determine the

generalized velocity ratios for the VA and FA inputs:

$$\begin{aligned} \left\{ (\mathbf{I} + \tilde{\boldsymbol{\rho}})^{-T} [\mathbf{G}_\theta^x]^T \mathbf{W}_x [\mathbf{G}_\theta^x] (\mathbf{I} + \tilde{\boldsymbol{\rho}})^{-1} \right\} \dot{\boldsymbol{\phi}}_1 &= \{ {}^1\lambda \mathbf{W}_\phi \} \dot{\boldsymbol{\phi}}_1 \text{ (corresponding to VA)} \\ \left\{ (\mathbf{I} + \tilde{\boldsymbol{\rho}})^{-1} \tilde{\boldsymbol{\rho}} [\mathbf{G}_\theta^x]^T \mathbf{W}_x [\mathbf{G}_\theta^x] \tilde{\boldsymbol{\rho}} (\mathbf{I} + \tilde{\boldsymbol{\rho}})^{-1} \right\} \dot{\boldsymbol{\phi}}_2 &= \{ {}^2\lambda \mathbf{W}_\phi \} \dot{\boldsymbol{\phi}}_2 \text{ (corresponding to FA)} \end{aligned} \quad (8.94)$$

Note that the generalized eigenvalue problems in Eq. (8.93) each has  $n$  solutions  ${}^i\lambda_r$  ( $i \in \{1, 2\}$  represents the VA and FA inputs, and  $r \in \{1, 2, \dots, n\}$  represents the solutions). The generalized velocity ratios for each input  $i$  are bounded by the square root of the minimum and maximum eigenvalues of Eq. (8.94):

$$\sqrt{{}^i\lambda_1} \leq {}^i\kappa_v \leq \sqrt{{}^i\lambda_n} \quad (8.95)$$

Equation (8.95) assumes that the eigenvalues  ${}^i\lambda_r$  are arranged in ascending order with  ${}^i\lambda_1$  being the minimum value and  ${}^i\lambda_n$  being the maximum value. The GSRF  $\tilde{\kappa}_v$  for a PFVA-driven manipulator can now be defined as the ratio of the generalized velocity ratios of the two inputs:

$$\tilde{\kappa}_v = \frac{{}^2\kappa_v}{{}^1\kappa_v} \quad (8.96)$$

## 8.8. CHAPTER SUMMARY

This chapter was focused on the analytic formulation at the system level for PFVA-driven serial robot manipulators. Specifically, three tasks were accomplished:

- A generalized dynamic model for PFVA-driven serial robots was developed with a focus on determining the contribution of each input set (FA and VA) to different types of output loads: acceleration, velocity (centripetal/Coriolis), static load, gravity, and friction torques. This effort resulted in 2 sets of equations of motion, one each for the VA and FA input set (see Sections 8.1-8.5 for details).
- Based on the above developed model, a design study was conducted to analyze the effect of different RSF distributions among the serial manipulator joints. For this study a 3R planar robot and a low-velocity contact task were considered. Three design cases were considered, (i)  $\tilde{\rho}_1 = \tilde{\rho}_2 = \tilde{\rho}_3 = 255.4$ , (ii)  $\tilde{\rho}_1 = \tilde{\rho}_2 = \tilde{\rho}_3 = 1$ , and (iii)  $\tilde{\rho}_1 = 255.4$ ,  $\tilde{\rho}_2 = 24.3$ ,  $\tilde{\rho}_3 = 1$ . The distribution of various torque components between the VA and FA input sets was determined for all three cases with the goal of analyzing the dynamic coupling, among other factors, between these inputs (see Sections 8.6 for details).
- Preliminary work was presented that leveraged prior work in performance criteria for serial robots and developed two criteria for PFVA-driven serial manipulators: (i) partition value of kinetic energy to measure the distribution of kinetic energy in a PFVA-driven manipulator between the FA and VA input sets and (ii) generalized relative scale factor which is an extension of the RSF concept for a PFVA to a PFVA-manipulator (see Sections 8.7 for details).

# DISSERTATION SUMMARY

## Chapter 9. Conclusions and Discussion

This chapter provides an executive summary of the research work presented in Chapters 1-8. It is organized in the following manner:

- **Research Objectives and Contributions.** The goals of this dissertation and the primary research contributions from this work will be listed.
- **Summary of Reviewed Literature.** The key references that are relevant to our work from both academic and patent literatures will be summarized.
- **Research Results.** This work constitutes analytical as well as experimental results which are pertinent to both designing and operating Parallel Force/Velocity Actuators (PFVAs). Additionally, results from the analytical formulation at the system level will be discussed.
- **Major Recommendations.** Based on the understanding of PFVAs gained through this work, we will outline our recommendations for the design and operation of these actuators.
- **Key Questions Raised.** During the course of this work, some research questions have been raised which will be listed.
- **Suggested Future Work.** Based on our results and recommendations, a research roadmap including a list of short-term and long-term research topics and a plan will be laid down.

### 9.1. RESEARCH OBJECTIVES AND CONTRIBUTIONS

The objective of this research work was to propose and develop the PFVA concept through analysis and experiments. A PFVA combines a Force Actuator (FA) and



a Velocity Actuator (VA) using a 2-DOF differential gear train (Figure 9.1). The FA is a high velocity ratio (near direct-drive) input which is an ideal candidate for force control. The VA is a low velocity ratio (high gear reduction) input which is an ideal velocity source. There are primarily two goals for this design: (i) to provide at least one backdriveable input in this dual-input actuator by introducing a near direct-drive subsystem that can be responsive to output force disturbances, and (ii) to enhance the dynamic range of velocities of the combination actuator in comparison to its constituent sub-systems. The first goal translates to improved mechanical safety of a PFVA-driven manipulator and the second goal addresses the requirement to expand the choices available at the actuator-level.

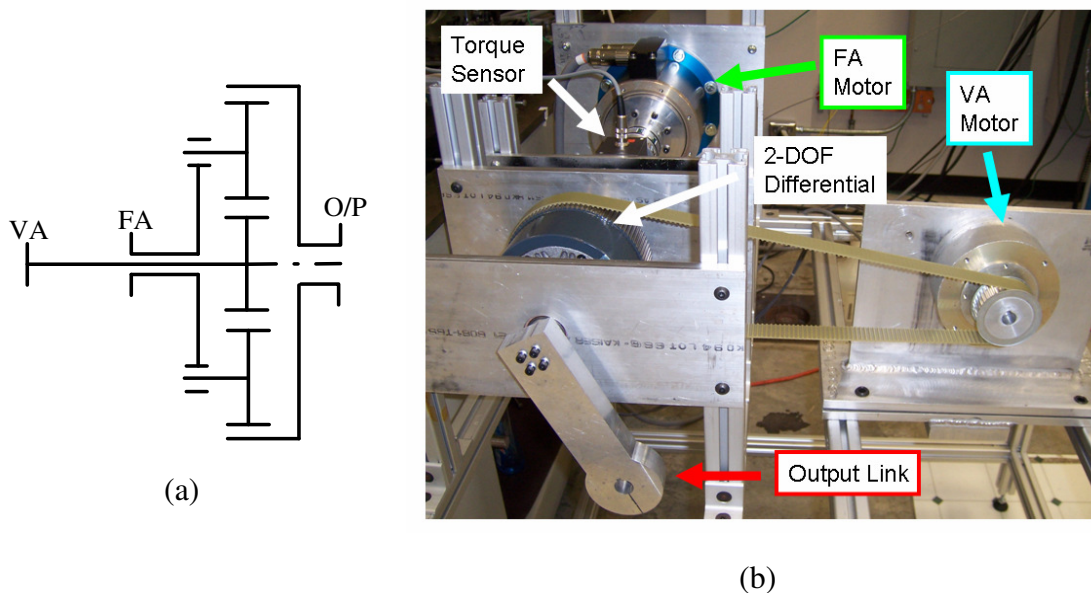


Figure 9.1. Parallel Force/Velocity Actuation concept. (a) Schematic, (b) Laboratory Prototype.

Our focus was primarily at the actuator level where power-flow, force distribution, and dynamic response were studied. Additionally, the objective was to

develop an analytical formulation for serial robot systems driven by PFVA-type actuators. Some contributions from this work are listed in Table 9.1.

Table 9.1 Summary of Contributions (Section 1.4)

Contributions (Section References)
PARAMETRIC DESIGN OF PFVAS
<ul style="list-style-type: none"> <li>• Dimensionless and scalable parametric analysis of PFVA design and operation based on approximately six new fundamental design parameters of the actuator. (See Sections 3.1, 4.1-4.3, and 5.2-5.5)</li> <li>• Over ten design and five operational guidelines based on parametric analysis. (See Sections 4.4 and 5.7)</li> <li>• Above guidelines used to design a single-joint PFVA testbed for experimental work (See Section 5.6).</li> <li>• Identification of the purely geometric RSF <math>\tilde{\rho}</math> as a dimensionless and dominant parameter in the PFVA-type devices is extensible to other differential-based mechanisms. (See Section 3.1)</li> </ul>
ANALYTICAL AND EXPERIMENTAL CHARACTERIZATION OF PFVA DYNAMIC RESPONSE
<ul style="list-style-type: none"> <li>• Analytical model and experimental demonstration was presented for a method to resolve the kinematic redundancy in the PFVA to meet a velocity specification at the output while optimizing for secondary criteria. (See Sections 6.1.1 and 7.2.3)</li> <li>• Two performance limiting physical phenomena (friction and dynamic coupling) were experimentally identified and compared either with existing models in the literature or with analytical models developed in this work. (See Sections 5.4.2, 6.4.1, 7.2.1, and 7.2.2)</li> <li>• An experimental methodology to measure dynamic coupling in PFVA-type actuators. (See Section 7.2.2)</li> <li>• Analytical model and experimental demonstration of the mechanical safety feature of the PFVA. (See Section 7.2.4)</li> <li>• Identification of the FA-side damping ratio and natural frequency including the servo-system dynamic properties in addition to the mechanical properties. (See Section 7.2.4)</li> </ul>
GENERALIZED ANALYTICAL FORMULATION FOR PFVA-DRIVEN SERIAL MANIPULATORS
<ul style="list-style-type: none"> <li>• The analytical formulation for serial robot manipulators driven by PFVA-type inputs. (See Sections 8.2-8.5)</li> <li>• Model development with focus on partitioning of manipulator work function requirements at each input.</li> <li>• Three design case studies for distribution of RSF among joints of a 3R PFVA-robot. (See Section 8.6)</li> </ul>

## 9.2. LITERATURE SUMMARY

Related work in both academic and patent literature relevant to dual-actuators, mechanical safety, and model formulations for systems with dual actuators was reviewed.

Table 9.2 Summary of Selected Literature (Section 2.2)

Reference	Description	Relevance to PFVA Work
(Chang and Tsai, 1993)	<ul style="list-style-type: none"> <li>• Developed a torque summing redundant drive for backlash-free robots</li> <li>• Presented analytical model and design criteria for manipulators with dual torque summing actuators</li> </ul>	<ul style="list-style-type: none"> <li>• Analytical model developed for dual actuators is of importance in our work on modeling of serial chains with PFVAs (Chapter 8)</li> </ul>
(Cho, Tesar, and Freeman, 1989)	<ul style="list-style-type: none"> <li>• Proposed an antagonistic elbow module</li> <li>• Presented an analytical framework for modeling the response of manipulators with antagonistic dual actuators</li> </ul>	<ul style="list-style-type: none"> <li>• The analytical development using kinematic influence coefficients to model serial chains with dual actuators is relevant to work in Chapter 7.</li> <li>• The antagonistic stiffness modeling might be relevant to analyzing the effective stiffness of a PFVA manipulator.</li> </ul>
(Kim et al., 2007)	<ul style="list-style-type: none"> <li>• Developed a dual input actuator for simultaneous control of position and stiffness</li> <li>• Used a differential gear train to mix actuator inputs</li> <li>• Primary goal was to employ the drive to sense collisions and forces</li> </ul>	<ul style="list-style-type: none"> <li>• Design of this actuator is very similar to the PFVA – dual inputs with differential summing.</li> </ul>
(Lauria et al., 2008)	<ul style="list-style-type: none"> <li>• Proposed a differential elastic actuator based on series elasticity and differential mechanics</li> <li>• Also developed a 3-DOF manipulator incorporating DEAs</li> </ul>	<ul style="list-style-type: none"> <li>• Design of this actuator is very similar to the PFVA – dual inputs with differential summing.</li> <li>• The difference is in the presence of a passive compliant element in the DEA.</li> </ul>
(Pratt and Williamson, 1995a)	<ul style="list-style-type: none"> <li>• Introduced the idea of intentionally added compliance between actuator and load for better force control in unstructured environments</li> </ul>	<ul style="list-style-type: none"> <li>• The PFVA can be regarded as an active SEA. Similarly, we can also think of the DEA as a particular case of the PFVA with one input being replaced by a passive spring.</li> </ul>
(Tesar, 1985; 1999; 2003)	<ul style="list-style-type: none"> <li>• Proposed the control-in-the-small concept based on which the layered control actuator was developed</li> <li>• Proposed the force/motion control actuator</li> </ul>	<ul style="list-style-type: none"> <li>• Current work in PFVA builds on this past work at UTRRG.</li> <li>• The original name for the PFVA was FMCA when the latter was proposed in the EMAA in 2003.</li> </ul>
(Zinn et al., 2004)	<ul style="list-style-type: none"> <li>• Layered torque control with inclusion of compliance and appropriate placement of actuators near the base of the robot.</li> <li>• Performed studies on a manipulator safety index to evaluate the safety of robots around humans.</li> </ul>	<ul style="list-style-type: none"> <li>• The similarity between Zinn’s work and our work is the layering of two controlled inputs. In our case we layer velocity inputs.</li> </ul>

The major references from the academic and patent literatures are listed in Table 9.2 and Table 9.3, respectively.

Table 9.3 Summary of US Patent Literature on Dual Actuators (Section 2.2.4)

Actuation Concept	Patent Number (Year), Inventor(s) (Company/Institution Lab)
Control-in-the-Small	4505166 (1985), D. Tesar (University of Florida, Gainesville)
Fault-Tolerant Rotary Actuator	7122926 (2006), D. Tesar (The University of Texas at Austin)
Force/Motion Control Actuator	Provisional Patent, D. Tesar (The University of Texas at Austin) The focus area of this report, PFVA, is based on the FMCA concept.
High Performance Differential Actuator	Patent Application 11/694123 (2007), Lauria et al. (University of Sherbrooke, Canada)
Hybrid Drive System	5875691 (1999), H. Hata, S. Kubo, Y. Taga, and R. Ibaraki (Toyota)
NEXXT Drive	UK Patent Number Unavailable (NexxtDrive Ltd., London, UK)
NuVinci Continuously Variable Transmission	6945903 (2005), D. Miller (Fallbrook Technologies, Inc.)
Series Elastic Actuator	5650704 (1995), G. Pratt and M. Williamson (Yobotics, Inc.)
Solomon Electric Wheel Drive	11/552207 (2006), R.A. Pesiridis and A.J. Christian (Solomon Technologies, Inc.)

### 9.3. SIGNIFICANT RESULTS

The major results from this work have been organized into two categories in this section: analytical and experimental results. These have been summarized below.

#### 9.3.1. Key Analytical Results

Our actuator-level analytical modeling effort focused on identifying relevant parameters and criteria for the design and operation PFVAs. The most fundamental and relevant parameter that emerged from our analysis was the ratio of velocity ratios of the FA and VA, called the relative scale factor (RSF). This parameter physically depends on the geometry of the device (i.e., it is time independent).

Table 9.4 Summary of PFVA Actuator-Level Parameters, Criteria, and Models

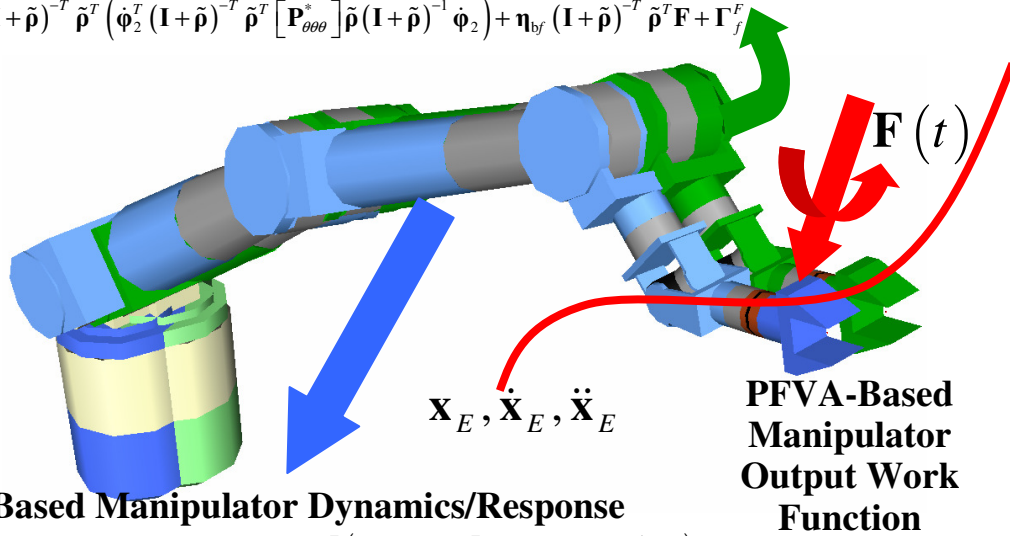
Design and Operation Issues	Parameter Dependencies (Notation)	Physical Dependencies	Criteria and Mathematical Model
External Power Flow (Section 4.1)	RSF ( $\tilde{\rho}$ ) FA and VA Efficiencies ( $\eta_{f \rightarrow o}, \eta_{v \rightarrow o}$ ) Velocity Mixing Ratio ( $\tilde{\lambda}$ )	<ul style="list-style-type: none"> <li>Meshing friction losses</li> <li>Operating velocities of VA and FA</li> </ul>	Overall Mechanical Efficiency ( $\eta$ ) $\eta = \frac{\tilde{\lambda} + \tilde{\rho}}{\frac{\tilde{\lambda}}{\eta_{v \rightarrow o}} + \frac{\tilde{\rho}}{\eta_{f \rightarrow o}}} \text{ (Eq. (4.12))}$
Internal Power Flow (Section 4.2)	RSF ( $\tilde{\rho}$ ) Velocity Mixing Ratio ( $\tilde{\lambda}$ )	<ul style="list-style-type: none"> <li>Operating velocities of VA and FA</li> <li>Torques acting on PFVA shafts</li> </ul>	Futile Power Ratio ( $\tilde{\nu}$ ) $\tilde{\nu} = P_{futile} P_o^{-1} \text{ (Eq. (4.24)-(4.25))}$ where $P_{futile} = \min\{ P_{R,v \rightarrow o} ,  P_{C,v \rightarrow o} \}$
Effective Inertia (Section 4.3)	RSF ( $\tilde{\rho}$ ) Velocity Mixing Ratio ( $\tilde{\lambda}$ ) Coupling Inertia Ratio ( $\tilde{I}_{vf}$ ) Prime-Mover Inertia Ratio ( $\tilde{I}_M$ )	<ul style="list-style-type: none"> <li>Operating velocities of the VA and FA</li> <li>Inertia content in prime-mover and gear train components</li> </ul>	Effective Inertia Ratio ( $\tilde{I}_{eff}$ ) $\tilde{I}_{eff} = \frac{(\tilde{\lambda}^2 + 2\tilde{I}_{vf}\tilde{\lambda} + \tilde{I}_M)(\tilde{\rho} + 1)^2}{(\tilde{\lambda} + \tilde{\rho})^2} \text{ (Eq. (4.31))}$
Position Uncertainty (Section 5.2)	RSF ( $\tilde{\rho}$ ) Relative Accuracy Factor ( $\tilde{\alpha}_f^v$ )	<ul style="list-style-type: none"> <li>Operating velocities of the VA and FA</li> <li>FA and VA prime-mover position inaccuracies</li> <li>FA- and VA-side lost motion and backlash</li> </ul>	Relative Accuracy Factor ( $\tilde{\alpha}_f^j$ ) $\tilde{\alpha}_f^j = \sqrt{\left[\frac{\tilde{\alpha}_f^v}{\tilde{\rho} + 1}\right]^2 + \left[\frac{\tilde{\rho}}{\tilde{\rho} + 1}\right]^2} \text{ (Eq. (5.5))}$
Static Torque Distribution (Section 5.4.1)	RSF ( $\tilde{\rho}$ ) Relative Efficiency Ratio ( $\tilde{\eta}$ )	<ul style="list-style-type: none"> <li>Meshing friction losses</li> </ul>	Static Torque Distribution Ratio ( $\tilde{\tau}^s$ ) $\tilde{\tau}^s = \frac{\tilde{\rho}}{\tilde{\eta}}$ (Eq. (5.22))
Inertial Torque Distribution (Section 5.4.2)	RSF ( $\tilde{\rho}$ ) Output-to-VA Inertia Ratio ( $\tilde{I}_j^*$ ) Acceleration Mixing Ratio ( $\tilde{\phi}$ ) Prime-Mover Inertia Ratio ( $\tilde{I}_M$ )	<ul style="list-style-type: none"> <li>Output inertia</li> <li>Inertia content in the gear train</li> <li>Inertia content in the actuator components on FA- and VA-sides</li> </ul>	Inertia Torque Distribution Ratio ( $\tilde{\tau}^l$ ) $\tilde{\tau}^l = \frac{\left(\tilde{I}_{vf} + \tilde{I}_j^* \frac{\tilde{\rho}}{(\tilde{\rho} + 1)^2}\right) + \left(\tilde{I}_M + \tilde{I}_j^* \frac{\tilde{\rho}^2}{(\tilde{\rho} + 1)^2}\right) \tilde{\phi}}{\left(1 + \tilde{I}_j^* \frac{1}{(\tilde{\rho} + 1)^2}\right) + \left(\tilde{I}_{vf} + \tilde{I}_j^* \frac{\tilde{\rho}}{(\tilde{\rho} + 1)^2}\right) \tilde{\phi}}$

			Dynamic Coupling Factor ( $\tilde{\mu}$ ) $\tilde{\mu} = \frac{\tilde{\rho}}{(\tilde{\rho}+1)^2}$ (Eqs. (5.28) and (5.38))
Acceleration Responsiveness (Section 5.4.3)	Relative Motor Torque Ratio ( $\tilde{\tau}_{Mr}$ ) Prime-Mover Inertia Ratio ( $\tilde{I}_M$ ), and Output-to-VA Inertia Ratio ( $\tilde{I}_j^*$ ), RSF ( $\tilde{\rho}$ )	<ul style="list-style-type: none"> <li>• Torque capacities of the FA and VA prime-movers</li> <li>• Inertia content in the output machine, the gear train, and the actuator components on FA- and VA-sides of the PFVA</li> <li>• Type of prime-movers (electro-mechanical, hydraulic, etc.) used for VA and FA and torque density of these prime-movers</li> </ul>	Relative Acceleration Responsiveness ( $\tilde{\xi}$ ) $\tilde{\xi} = \frac{-\left[\tilde{I}_{vf} + \tilde{I}_j^* \frac{\tilde{\rho}}{(\tilde{\rho}+1)^2}\right] + \left[1 + \tilde{I}_j^* \frac{1}{(\tilde{\rho}+1)^2}\right] \tilde{\tau}_{Mr}}{\left[\tilde{I}_M + \tilde{I}_j^* \frac{\tilde{\rho}^2}{(\tilde{\rho}+1)^2}\right] - \left[\tilde{I}_{vf} + \tilde{I}_j^* \frac{\tilde{\rho}}{(\tilde{\rho}+1)^2}\right] \tilde{\tau}_{Mr}}$ (Eq. (5.45))
Effective Mechanical Stiffness (Section 5.5.1)	Relative Stiffness ( $\tilde{K}$ ), Relative Backdriving Efficiency ( $\tilde{\eta}_b$ ), RSF ( $\tilde{\rho}$ )	<ul style="list-style-type: none"> <li>• Meshing friction losses for reverse power-flow (output to input)</li> <li>• <i>Mechanical</i> compliances of VA and FA actuator components, and that of the differential's gear meshes</li> </ul>	Relative Joint Stiffness ( $\tilde{K}_j$ ) $\tilde{K}_j = \frac{1}{\eta_{j \rightarrow v}} \left( \frac{\tilde{K} (\tilde{\rho}+1)^2}{\tilde{K} + \tilde{\eta}_b \tilde{\rho}^2} \right)$ (Eq. (5.53))
Kinematic Redundancy (Section 6.1.1)	RSF ( $\tilde{\rho}$ ) Specified Output Velocity ( $\dot{\phi}_{od}$ )	<ul style="list-style-type: none"> <li>• Diameters of the component gears</li> <li>• Velocity capabilities of VA and FA</li> <li>• Motor and motor controller selection</li> </ul>	Inverse velocity solutions for VA and FA ( $\dot{\phi}_{vd}, \dot{\phi}_{fd}$ ) $\begin{bmatrix} \dot{\phi}_{vd} \\ \dot{\phi}_{fd} \end{bmatrix} = \begin{bmatrix} \frac{\tilde{\rho}+1}{\tilde{\rho}^2+1} \\ \frac{\tilde{\rho}(\tilde{\rho}+1)}{\tilde{\rho}^2+1} \end{bmatrix} \dot{\phi}_{od} + k \begin{bmatrix} -\tilde{\rho} \\ 1 \end{bmatrix}$ (Eq. (6.3))
Dynamic Response (Section 6.4.1)	Input reflected inertia matrix ( $\mathbf{I}$ ), System geometry ( $\mathbf{G}$ ), Friction torque parameters ( $b, \tau_c, \dot{\phi}_c, \tau_s$ ), Gravity ( $g$ )	<ul style="list-style-type: none"> <li>• Diameters of the component gears</li> <li>• Meshing friction losses</li> <li>• Motor selection</li> </ul>	$\mathbf{I}\ddot{\phi} + \tau_F(\dot{\phi}) + \tau_G(\phi) + \tau_S = \tau_M$ (Eq. (6.31))

For example, in a rotary PFVA, the RSF depends on the diameters of the component gears in the differential train. Other parameters and criteria are summarized in Table 9.4. The key analytical result from our system-level modeling effort consisted of the equations of motion for a PFVA-driven serial manipulator focusing on the partitioning of different types of loads (inverse dynamics) between the FA and VA input-sets due to a given work-function at the manipulator output (Figure 9.2). For details, see Eqs. (8.82) and (8.83) in Section 8.5.

### FA-Based Manipulator Dynamics/Response

$$\begin{aligned} \Gamma_f^A = & [\mathbf{I}_{\phi\phi}^*]_{ff} \ddot{\phi}_f + [\mathbf{I}_{\phi\phi}^*]_{fv} \ddot{\phi}_v + (\mathbf{I} + \tilde{\rho})^{-T} \tilde{\rho}^T \left( \dot{\phi}_1^T (\mathbf{I} + \tilde{\rho})^{-T} [\mathbf{P}_{\theta\theta}^*] (\mathbf{I} + \tilde{\rho})^{-1} \dot{\phi}_1 \right) \\ & + (\mathbf{I} + \tilde{\rho})^{-T} \tilde{\rho}^T \left( \dot{\phi}_1^T (\mathbf{I} + \tilde{\rho})^{-T} [\mathbf{P}_{\theta\theta}^*] \tilde{\rho} (\mathbf{I} + \tilde{\rho})^{-1} \dot{\phi}_2 \right) + (\mathbf{I} + \tilde{\rho})^{-T} \tilde{\rho}^T \left( \dot{\phi}_2^T (\mathbf{I} + \tilde{\rho})^{-T} \tilde{\rho}^T [\mathbf{P}_{\theta\theta}^*] (\mathbf{I} + \tilde{\rho})^{-1} \dot{\phi}_1 \right) \\ & + (\mathbf{I} + \tilde{\rho})^{-T} \tilde{\rho}^T \left( \dot{\phi}_2^T (\mathbf{I} + \tilde{\rho})^{-T} \tilde{\rho}^T [\mathbf{P}_{\theta\theta}^*] \tilde{\rho} (\mathbf{I} + \tilde{\rho})^{-1} \dot{\phi}_2 \right) + \eta_{bf} (\mathbf{I} + \tilde{\rho})^{-T} \tilde{\rho}^T \mathbf{F} + \Gamma_f^F \end{aligned}$$



### VA-Based Manipulator Dynamics/Response

$$\begin{aligned} \Gamma_v^A = & [\mathbf{I}_{\phi\phi}^*]_{vv} \ddot{\phi}_v + [\mathbf{I}_{\phi\phi}^*]_{vf} \ddot{\phi}_f + (\mathbf{I} + \tilde{\rho})^{-T} \left( \dot{\phi}_v^T (\mathbf{I} + \tilde{\rho})^{-T} [\mathbf{P}_{\theta\theta}^*] (\mathbf{I} + \tilde{\rho})^{-1} \dot{\phi}_f \right) \\ & + (\mathbf{I} + \tilde{\rho})^{-T} \left( \dot{\phi}_v^T (\mathbf{I} + \tilde{\rho})^{-T} [\mathbf{P}_{\theta\theta}^*] \tilde{\rho} (\mathbf{I} + \tilde{\rho})^{-1} \dot{\phi}_f \right) + (\mathbf{I} + \tilde{\rho})^{-T} \left( \dot{\phi}_f^T (\mathbf{I} + \tilde{\rho})^{-T} \tilde{\rho}^T [\mathbf{P}_{\theta\theta}^*] (\mathbf{I} + \tilde{\rho})^{-1} \dot{\phi}_v \right) \\ & + (\mathbf{I} + \tilde{\rho})^{-T} \left( \dot{\phi}_f^T (\mathbf{I} + \tilde{\rho})^{-T} \tilde{\rho}^T [\mathbf{P}_{\theta\theta}^*] \tilde{\rho} (\mathbf{I} + \tilde{\rho})^{-1} \dot{\phi}_f \right) + \eta_{bv} (\mathbf{I} + \tilde{\rho})^{-T} \mathbf{F} + \Gamma_v^F \end{aligned}$$

Figure 9.2. A PFVA-driven manipulator's total torque demand due to an EEF motion plan and contact force may be visualized as being shared by two constituent manipulators (with the same joint space and link configuration) driven by dual inputs at joints: (i) FAs, and (ii) VAs.

### 9.3.2. Key Experimental Results

The results from our experimental work with a single-joint PFVA prototype is summarized in Table 9.5. This work involved two categories of experiments: (i) parameter identification and (ii) performance testing.

Table 9.5 Summary of Experiments and Major Results

Experiment	Significant Results/Conclusions	Major References
PARAMETER IDENTIFICATION		
Identification of Friction Phenomena (Section 7.2.1)	<ul style="list-style-type: none"> <li>• Velocity-dependent friction phenomena, such as stiction, Stribeck effect, and viscous damping were identified.</li> <li>• Position-dependent friction was characterized using spatial spectral analysis.</li> </ul>	(Armstrong-Hélouvy, 1991; Garcia et al., 2002)
Identification of Dynamic Coupling (Section 7.2.2)	<ul style="list-style-type: none"> <li>• An experimental methodology was proposed and demonstrated to characterize dynamic coupling torques between the FA and VA.</li> <li>• In our testbed, the coupling torque correlated almost entirely with velocity.</li> </ul>	No major references found
PERFORMANCE TESTING		
Utilizing Kinematic Redundancy to Mitigate Low Velocity Friction (Section 7.2.3)	<ul style="list-style-type: none"> <li>• One mode of operation was demonstrated where the kinematic redundancy in the actuator was effectively utilized to avoid low-velocity zones.</li> </ul>	(Ontanon Ruiz, 2003)
Mechanical Safety through Controlled Backdriveability of FA (Section 7.2.4)	<ul style="list-style-type: none"> <li>• A mechanically safe mode of operation was demonstrated via the controlled backdriveability of the FA input. Two specific loading conditions were imposed: (i) slow collisions and (ii) impulse loading.</li> <li>• The damping ratio and natural frequency of the FA subsystem were determined based on logarithmic decrement method and an impulse response.</li> </ul>	(Tse et al., 1963) for vibration response theory.

In parameter identification experiments two performance-limiting factors were studied, namely friction (position- and velocity-dependent) in the FA branch, and dynamic coupling between the FA and VA. In performance testing experiments two modes of operation were demonstrated: (i) velocity control with kinematic redundancy resolution to determine FA/VA velocities and (ii) PFVA response to slow collisions and impulse loads.



#### 9.4. GUIDELINES FOR THE PFVA DESIGNER

Our parametric analysis in Chapters 3-6 has allowed us to recommend guidelines for a PFVA designer. These guidelines were further categorized into those for design and operation of PFVAs which are summarized in Table 9.6 and Table 9.7, respectively.

Table 9.6 Summary of Design Guidelines

DG-1.	The basic efficiency of the inverted train in a PFVA reduces as increases, i.e., the FA and VA become more and more distinct kinematically.
DG-2.	In the normal operational mode, the overall mechanical efficiency of a positive-ratio PFVA decreases when two conditions simultaneously occur, viz., (i) the FA and VA become significantly distinct from each other in terms of their velocity ratios, and (ii) when the VA actuator is spinning significantly faster than the FA.
DG-3.	The input to output inertia of a PFVA system is bounded by the VA and FA SISO effective inertias, $[I_{eff}]_{FA} \leq [I_{eff}]_{PFVA} \leq [I_{eff}]_{VA}$ , if we exclude the special case of $\tilde{\lambda} \rightarrow -\tilde{\rho}$ , which corresponds to an unbounded effective inertia.
DG-4.	To reduce the effective inertia of a PFVA system it is thus necessary to drive it as closely as possible to a SISO FA, i.e., $\tilde{\lambda} \rightarrow 0$ .
DG-5.	In considering the influence of the input motor accuracies on the output (or ) joint accuracy, as the gear ratios in a PFVA approach their theoretical limit ( $\tilde{\rho} \rightarrow \infty$ ), the output position accuracy will be entirely dictated by the accuracy of the FA actuator's prime-mover.
DG-6.	As the two inputs in a PFVA become more and more distinct, and approach their theoretical limits ( $\tilde{\rho} \rightarrow \infty$ ), the entire static load requirement is only on the FA. Consequently, in this scenario, the two inputs are decoupled in terms of static torque demand.
DG-7.	As the two inputs in a PFVA become more and more distinct, and approach their theoretical limits ( $\tilde{\rho} \rightarrow \infty$ ), the entire output inertial load requirement is only on the FA. Consequently, in this scenario, the two inputs are decoupled in terms of inertial torque demand.
DG-8.	As the two inputs in a PFVA become more and more distinct, and approach their theoretical limits ( $\tilde{\rho} \rightarrow \infty$ ), the FA has much more acceleration capability than the VA.
DG-9.	When the two inputs to the PFVA approach an ideal FA and VA, the relative joint stiffness of the actuator is entirely governed by the relative stiffness and the backdriving efficiency of the FA alone. When the backdriving efficiency of the FA approaches zero as the two inputs become very distinct, the PFVA stiffness approaches infinity (i.e. a very large stiffness which usually will lead to non-backdriveability).
DG-10.	The effective compliance of the PFVA increases when the compliance of the FA increases. The system essentially behaves as a system of series spring with different displacement influence coefficients to the output.

Table 9.7 Summary of Operational Guidelines

OG-1.	There are always infinitely many combinations of input velocities that can meet a specified output velocity requirement for the PFVA. The infinite combinations of input velocities that result in a null output motion are such that they bear a constant ratio equal to $-\tilde{\rho}$ .
OG-2.	If the torque on one of the connected shafts in a PFVA is specified, then the (magnitude and direction of) torques on the other two shafts are automatically fixed based on the geometry and basic efficiency of the gear train. Consequently, a torque sensor on one of the three connected shafts suffices to reasonably estimate the magnitude and direction of the other two shaft torques.
OG-3.	Futile power ratio becomes a relevant dimensionless operational criterion for PFVAs based on positive velocity ratio simple revolving epicyclic drives. Futile power flow exists only when one of the partial power flows between the VA and the machine (or PFVA output) is in the opposite direction of the effective power flow between the same two shafts.

### 9.5. KEY QUESTIONS RAISED

Several questions were raised that have directed the course of this work. Here we raise some of the relevant questions again and, if available, provide short answers to them with pointers to sections in the document where they were addressed in detail.

- An important question that was raised during our review of the literature was: where should the research emphasis be to enhance the safety of robot systems around humans? Specifically, should it be on the fundamentally different mechanical design of actuators or on leveraging improvements in control methodologies (and associated sensing technologies) to improve the system's situational awareness and responsiveness? The simple answer to this question was that a mechanical/control co-design approach is best suited. Additionally, the significance of safety across all sub-systems of a HRI system was emphasized in Chapter 2. See Section 2.1.3 for details.
- We began our parametric analysis for PFVA design based on a series of questions which are listed below:

- What is the dynamic coupling between the two inputs? How much do the two inputs disturb each other? We have modeled this dynamic coupling and disturbance torque arising due to it in Sections 5.4.2 and 4.3. This term was experimentally quantified in Section 7.2.2.
- How do we mix the contributions from each input to best satisfy the task requirements, etc? This is a control question and has not been completely answered in this work because we emphasized on design and modeling. However, a preliminary dynamic simulation was shown in Section 6.4.1 that demonstrates utilization of both inputs to transition from free-space motion to force controlled mode after detecting a collision. The mixing of velocities via kinematic redundancy resolution was shown analytically in Section 6.1.1 and experimentally in Section 7.2.3.
- There were similar questions we desired answers to in the larger context of serial manipulator systems driven by PFVAs:
  - How much expansion do we obtain in achievable dynamic responses? This is an advanced question and was out of the scope of this work. However our dynamic modeling effort in Chapter 8 and recent work by Rios and Tesar (2009) are steps toward answering this question.
  - In what manner do we partition the torque and velocity requirements at the joint (or output) among the two inputs? The work on performance criteria for PFVA-driven manipulators was initiated in Section 8.7. This work will lead to guidelines for mixing the contributions from the two input-sets. The analytical formulation for mixing of velocities of the FA and VA input-sets in a PFVA-driven robot based on specified EEF velocity was discussed in Section 8.2.1.

- Can the PFVA-based system provide mechanical safety (via backdriveability of one input) while maintaining performance? This feature of the PFVA was experimentally demonstrated in Section 7.2.4.
- An intriguing question was raised during the design case study in Chapter 8: where on the serial manipulator is backdriveability more relevant? For example, in a 6-DOF manipulator with a PUMA configuration, is it more useful to have backdriveability in the regional structure (3 inboard joints) or the orientation structure (wrist joints)? Although we have not answered this question in the current work, through our parameter study (Section 8.6.4) we have shown that such a question can be answered only by concurrently designing the manipulator and the backdriveable actuator (for example, PFVA).

## **9.6. ROADMAP FOR FUTURE WORK**

In this section we will discuss some directions for future work which are organized into two categories: (i) short-term work (1-2 years) which includes tasks that immediately extend from the current work and (ii) long-term work (2-5 years) that would draw from the current and previous research at the RRG and move forward this research thread on expansion of the actuation capability for robots.

### **9.6.1. Short-Term Future Work (1-2 Years)**

The short-term future work will be organized into the three principal areas of research in the current report: (i) parametric design of PFVAs, (ii) analytical and experimental study of the PFVA's dynamic response, and (iii) system-level dynamic model formulation. These are discussed below.

**Parametric Design of PFVAs.** One important issue that has not been addressed in this work is the packaging of the PFVA. A packaged version of the PFVA concept, called the

Force/Motion Control Actuator (FMCA) was initially proposed by Tesar (2003) which is now protected by a provisional patent. Embedding the prime-movers, differential, brakes, and controls into a PFVA module is a topic that needs to be pursued in the near future. In Chapter 4 we presented the analytical results for power flow modes within the PFVA (Sections 4.1 and 4.2). These modes (especially futile power) need to be evaluated experimentally. Furthermore, if a feedback loop exists between the FA and VA, then circulating power becomes a relevant phenomenon (Tesar, 1972; Müller, 1982) and needs to be studied in more detail. Although the analysis in this work has been generalized, most examples have used positive-ratio drives and simple differential drive designs (one or two stages, and one or two inputs). Work needs to be done to evaluate the implication of using negative-ratio drives as well as complex differential gear trains that might have more than two compound stages and possibly more than two inputs. Performance-limiting phenomena in differential gear-trains, such as self-locking (Müller, 1982), should be explored.

**Analytical and Experimental Study of PFVA's Response.** In both our analysis and experimental testing we have shown that a limiting phenomenon in PFVA-type dual actuator combinations is the dynamic coupling between the two inputs. We have shown models and an experimental methodology to identify dynamic coupling (Section 7.2.2). This coupling needs to be completely characterized using further testing. For instance, we currently have a reasonably accurate model for friction in the FA branch based on the Stribeck friction identification experiments (Section 7.2.1). However the coupling matrix for viscous friction reflected to the PFVA inputs (Section 6.2.1) should be determined based on a testing procedure similar to that for dynamic coupling (Section 7.2.2). To accomplish this, we propose re-doing the friction experiments for the FA branch while controlling the VA input at different non-zero velocities (positive and negative).

In the area of performance modeling and testing, a significant effort in the next two years should concentrate on demonstrating the advantages of the PFVA using different modes of operation some of which are listed below:

- Performing admittance control at the PFVA output by using the kinematic redundancy to spin the inputs reasonably fast while, at the same time, limiting the torque on the FA branch to provide safety to collisions.
- Including a mass at the PFVA output to determine the payload capability of the actuator in various operational scenarios.
- Performing a force-controlled task in an unmodeled collision scenario. This mode was shown using a dynamic simulation in Section 6.4.1, but needs to be experimentally demonstrated.

The damped and natural frequencies of the FA branch were determined in Section 7.2.4; however this result can be extended to characterize the servo-stiffness of the FA completely (including the stiffness of the motor controller in addition to mechanical stiffness). Additionally, analytical, and possibly experimental, comparison of the PFVA with other actuator architectures (Cho, Tesar, and Freeman, 1989; Pratt and Williamson, 1995a; Zinn, et al., 2004; Kim, et al., 2007, Lauria et al., 2008 [See Table 9.2]) should be done. While doing so, possible application areas for the PFVA should be explored.

Some work has been done in modeling of actuators by equally emphasizing forward- and backward- power-flow modes. For instance, (Wu et al., 1993) at NASA JSC on a fault-tolerant actuator presents a model that includes both forward-driving and backward driving scenarios; (Abba and Chaillet, 1999) presents a power-flow based dynamic modeling approach for serial robots. However, it is our opinion that the property of

*backdriveability*<sup>62</sup>, although very relevant to the current work and related work on human-safe intelligent mechanical systems, has not been rigorously studied, analytically or experimentally, in the literature. For a physical HRI system, we think the backdriving mode (reverse power-flow) should be analyzed with the same rigor (dynamic response studies, responsiveness, etc.) as the forward-driving (and the more common) operational mode.

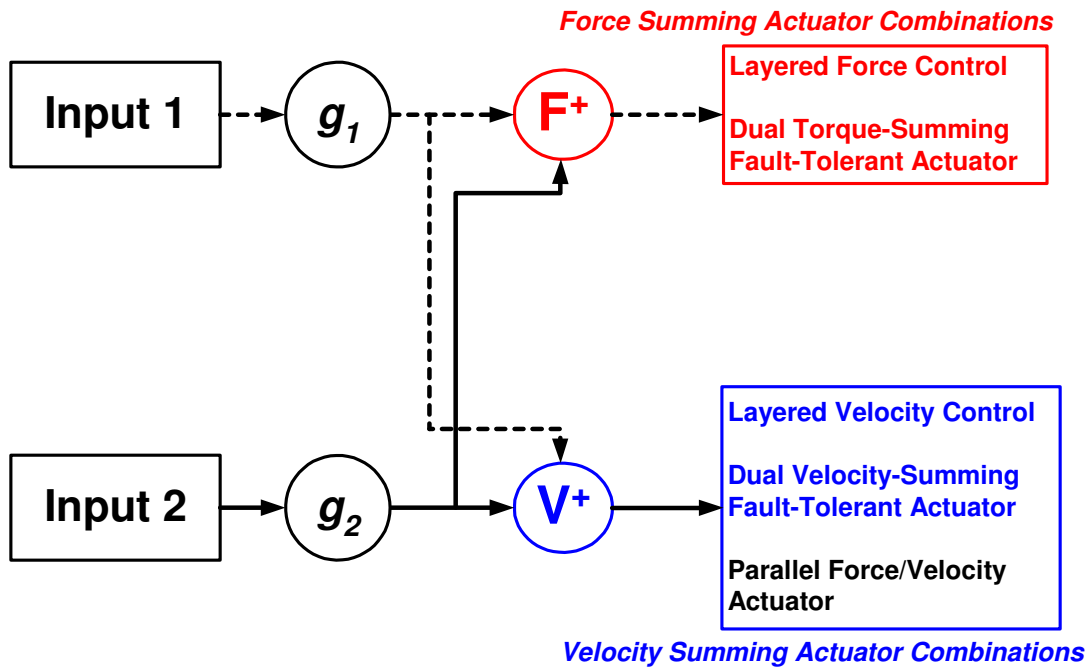
**System-Level Dynamic Model Formulation.** The short-term work in this area should draw from the current analytical framework and focus on performing experiments. It is expected that our current model (Sections 8.6.1-8.6.3) can be leveraged to design and build a 2- or 3-DOF planar 3R PFVA-driven serial robot, and to perform preliminary performance testing on this device. An important area that needs to be addressed is the development of performance criteria with sound physical meaning for PFVA-driven robots. Preliminary work in this topic was presented in Section 8.7; however a significant follow-up effort is important for the design and operation of PFVA-robots. This effort is made possible by the generalized development laid out in Chapter 8 and previous work by Tisius et al. (2004, 2009).

### **9.6.2. Long-Term Future Work (5 Year Roadmap)**

In the long-term, the planar 3R PFVA-driven robot testbed proposed in Section 9.6.1 can be used for advanced testing on a real application where a forgiving response might be relevant (example, fettling using a look-ahead sensor) or where safety might be important (example, human rehabilitation). The far-reaching goal at the system-level in that research thread is to experimentally test a spatial serial robot driven by PFVAs.

---

<sup>62</sup> We have shown to some extent in Section 7.2.4 that this property might not be purely mechanical and could depend on non-mechanical properties such as servo-stiffness in direct-drive applications, for instance.



Note: This architecture can be further expanded by varying the combination ratio  $\tilde{\rho} = \frac{g_1}{g_2}$ .

Figure 9.3. Conceptual picture of force- and velocity-summing actuator combinations. We studied the PFVA case in this report.

Several actuator combinations have been proposed by Tesar over the last four decades which are summarized in the Electromechanical Actuator Architecture report (Tesar, 2003). Special reference to force- and velocity-summing dual actuator combinations in this architecture was made by Rabindran and Tesar (2004). These are conceptually shown in Figure 9.3. The PFVA is a special case of this set of dual actuators where velocity summing of two kinematically distinct (i.e., distinct  $g_1$  and  $g_2$ ) inputs was used. In the current work, our methodology to understand the parametric design (based on power-flow and load distributions) and the dynamic response (analytical and experimental), and to finally extend this study at the actuator-level to  $n$ -DOF serial robot systems, has been developed in a fairly generalized manner. We have thus laid down a generalized approach to study other elements of the dual-actuator set (Figure 9.3),



although our specific models and experimental methodology might have been developed for PFVA-type velocity-summing actuators. For example, the RSF parameter can be used to characterize the kinematic distinction between the inputs regardless of the type of combination (force- or velocity-summing).

Based on the approach used in the current work and the lessons learned, we can now study torque-summing actuators to implement layered force-control (see previous work by Zinn et al. (2004), and Morell and Salisbury (1995)). An actuator design to accomplish torque-summing was proposed at the RRG (Sreevijayan, Price, and Tesar, 1994; Tesar, 2003) for fault-tolerance and by Chang and Tsai (1993) for backlash-free mechanisms (Figure 9.4).

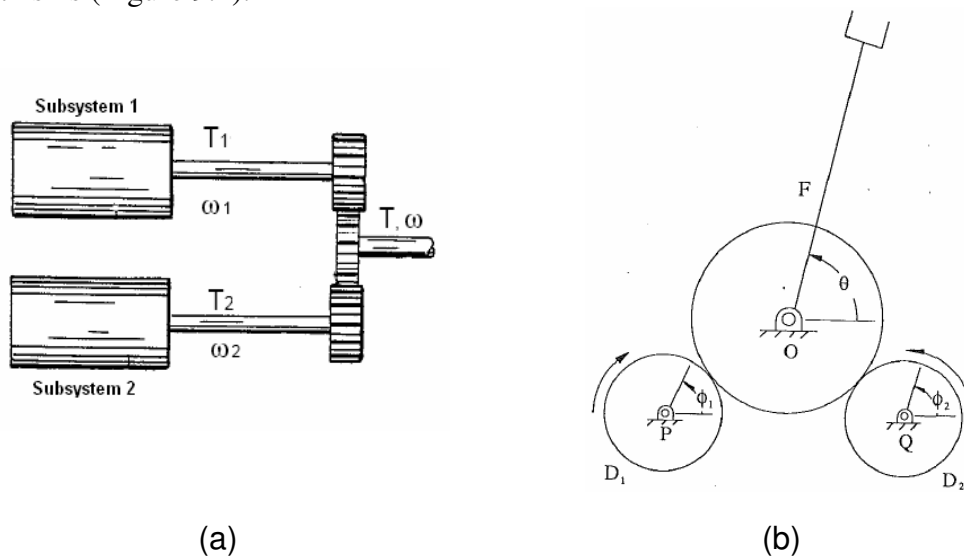


Figure 9.4. Torque-summing combinations of two inputs. (a) (Sreevijayan et al., 1994; Tesar, 2003) (b) (Chang and Tsai, 1993).

Now, considering that force and velocity are power-conjugate variables, parallels can be drawn between force-summing and velocity-summing designs. For example, the redundancy available for velocity selection available in a velocity-summing PFVA-type device (see Section 6.1.1) translates to torque-redundancy in its force-summing

counterpart (see Eqs. (2) and (3) on p.248 of (Chang and Tsai, 1993)). A foreseeable challenge to implement torque-summing actuators is as follows. From Section 2.2.1 we know that the velocities of the sub-systems in a force-summing actuator should bear a constant ratio (see Figure 2.3). To ascertain this kinematic requirement is a mechanical design challenge. For instance, in Figure 9.4 (b), achieving torque-summing while maintaining a constant ratio between  $\phi_1$  and  $\phi_2$  is limited by manufacturing/assembly tolerances and velocity errors introduced by the motor-controller.

In the current work we have introduced a dimensionless parameter, RSF  $\tilde{\rho}$ , for dual-input systems which is similar to the gear ratio for a single-input system. Extensive work has been done (Thomas et al., 1985; Bowling and Khatib, 2005; Rios and Tesar, 2009) on the influence of actuator parameters at the output of a robot system. Similarly, in the context of dual-actuator driven systems, the influence of RSF at the output of the robot system is largely an unexplored topic. Furthermore, an analytical formulation for serial robots that is based on power-flow and that can model the behavior of the robot in both forward-driving and backdriving modes is now becoming increasingly important due to the research thrust in the area of human-centric systems. Another important and budding research area in human-safe robots is *safety* itself. Although some work (Bicchi and Tonietti, 2004; Zinn et al., 2004; Alami et al., 2006) has been done in understanding and defining safety principles for physical HRI, there are immense opportunities and challenges in this area. For instance, the current robot safety literature uses metrics such as the Head Injury Criterion (HIC) borrowed from the automobile safety literature which might not be relevant to robotics (Haddadin et al., 2007). Applications such as robotic surgery, human rehabilitation, and prosthetics are application areas which might benefit from safety-related research. Our short- and long-term goals have been tabulated in Table 9.8.

Table 9.8 Five-Year Research Plan in Dual Actuators and Mechanical Safety

Timeline	Research Tasks
<i>YEAR 1</i>	<ul style="list-style-type: none"> <li>• PFVA packaging</li> <li>• Experimental testing of power-flow modes within the PFVA (see Sections 4.1 and 4.2)</li> <li>• Analysis of PFVAs with negative-ratio drive trains that have multiple stages</li> <li>• Analytical and experimental study of performance-limiting phenomena such as self-locking and circulating power (Müller, 1982) in the differential train</li> <li>• Further characterization of dynamic coupling (see Section 7.2.2) between FA and VA by including cross-coupling viscous friction effects</li> </ul>
<i>YEAR 2</i>	<ul style="list-style-type: none"> <li>• Experimental demonstration of additional operational modes of the PFVA: force-controlled task in unmodelled collision scenario, forgiving response in the presence of payload, utilization of kinematic redundancy to perform admittance control while limiting the torque in the FA branch.</li> <li>• Complete experimental identification of the servo-system dynamics of the FA (with emphasis on servo-stiffness during direct-drive applications where this characterization becomes more relevant)</li> <li>• Analytical and experimental comparison of the PFVA with other actuator architectures from the literature (example, Cho, Tesar, and Freeman, 1989; SEA by Pratt and Williamson, 1995)</li> <li>• In-depth study of backdriveability with focus on a power-flow based modeling approach that distinguishes between forward-driving and backdriving modes (for example, Wu et al., 1993)</li> </ul>
<i>YEAR 3</i>	<ul style="list-style-type: none"> <li>• Survey of application areas for PFVAs (for example, mechanical finishing tasks and human rehabilitation)</li> <li>• Designing and building of a planar 3R PFVA-driven serial robot testbed for performance evaluation and testing</li> <li>• Development of performance criteria for PFVA-driven manipulators (see Section 8.7.1 and past work by Tisius et al. (2004, 2009))</li> <li>• Parametric design of torque-summing actuator for layered force-control leading to prototype design</li> </ul>
<i>YEAR 4</i>	<ul style="list-style-type: none"> <li>• Actuator-level analysis of dynamic-response for torque-summing actuators</li> <li>• Experimental testing of laboratory prototype of torque-summing dual-actuators</li> <li>• Study of influence of RSF <math>\bar{\rho}</math> on the performance capabilities at the robot system output (see past work including (Thomas et al., 1985), (Bowling and Khatib, 2005), and (Rios and Tesar, 2009))</li> </ul>
<i>YEAR 5</i>	<ul style="list-style-type: none"> <li>• Analytical study of serial manipulator systems driven by torque-summing actuators</li> <li>• Dynamic models for single- and dual-input serial robot arms to analyze forward-driving and backdriving performance</li> <li>• Characterization of safety for physical human-robot interaction (see past work by (Zinn et al., 2004) and (Haddadin et al., 2007))</li> </ul>

## 9.7. CONCLUDING REMARKS

This research began with the broad objective of expanding the science-base for dual-input actuators. The effort that followed studied a differential-based velocity-summing actuator called PFVA. The PFVA concept was investigated both analytically and experimentally. Furthermore, the implication of this actuation paradigm on the design of a serial robot manipulator was modeled. One important feature of this novel dual-actuator design was emphasized – mechanical safety. This feature was analytically modeled and experimentally demonstrated on a single-joint PFVA prototype. Additionally, the kinematic redundancy offered by PFVAs was understood with generalized analysis and experimental testing. At the system-level, generalized dynamic models for PFVA-driven robot systems were developed with emphasis on explicitly accounting for the partitioning of output requirements (static load, inertia torques, gravity torques, etc.) between the dual input sets (VA and FA) of the PFVA-robot.

Significant actuator research effort at UTRRG has emphasized on expanding the choices in EMAs. The current research builds on that work and investigates a new design for velocity summing dual actuators with unequal sub-systems – PFVA. We believe that our approach to the study of PFVA is extensible to other types of dual-actuators (for example, torque-summing actuators for layered force-control). The focus in this research thread is on developing the underlying analytical and experimental tools to evaluate such multi-input actuators. In this concluding chapter, we have laid out a roadmap for continuing research in this area. It is our belief that this research effort will open the door to intriguing scientific questions regarding dual-actuators and challenging applications in physical HRI.

## SUPPLEMENTARY MATERIAL

### Appendix A. Differential Mechanisms: A Review

This appendix draws from several references (Macmillan, 1961; Tesar, 1972; Uicker, Pennock, and Shigley, 2003) and serves as a review on differential mechanisms for the interested reader.

Table A.1 A List of Rotary and Linear Differential Mechanisms (Adapted from Macmillan, 1961)

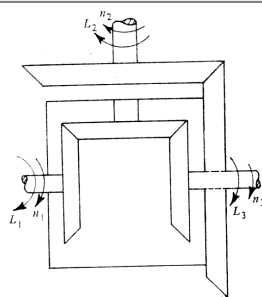
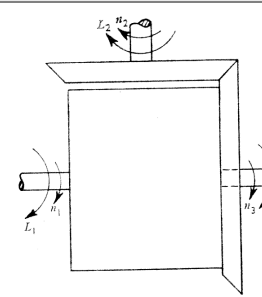
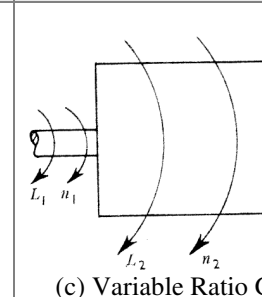
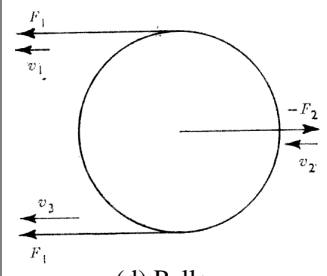
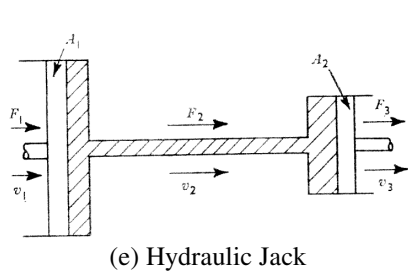
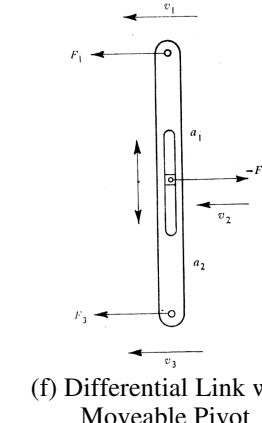
	Fixed Ratio	Constant Ratio	Variable Ratio
<b>Rotary</b>	 <p>(a) Bevel Gear</p>	 <p>(b) Epicyclic Gear</p>	 <p>(c) Variable Ratio Gear</p>
<b>Linear</b>	 <p>(d) Pulley</p>	 <p>(e) Hydraulic Jack</p>	 <p>(f) Differential Link with Moveable Pivot</p>

Table A.1 (Macmillan, 1961) lists a variety of linear and rotary differential mechanisms. These mechanisms are used as summers in mechanical control systems such as the automobile differential (Uicker, Pennock, and Shigley, 2003, pp. 323-328).

The following development (Sections A.1-A.3) has been transcribed from (Tesar, 1972) with permission. The objective of that early work (part of a lecture series at the University of Florida at Gainesville) was to delineate some of the basic laws of differential systems in terms of the concept of influence coefficients (Benedict and Tesar, 1978; Hall, 1992). In (Tesar, 1972), the elementary differential gear system was used as a basic tool to then interpret a more complex epicyclic differential system.

### A.1. DIFFERENTIAL LINK

To elaborate on the basic principles of a differential, let us consider the differential link shown in Table A.1(f). This mechanism is shown in more detail diagrammatically in Figure A.1.

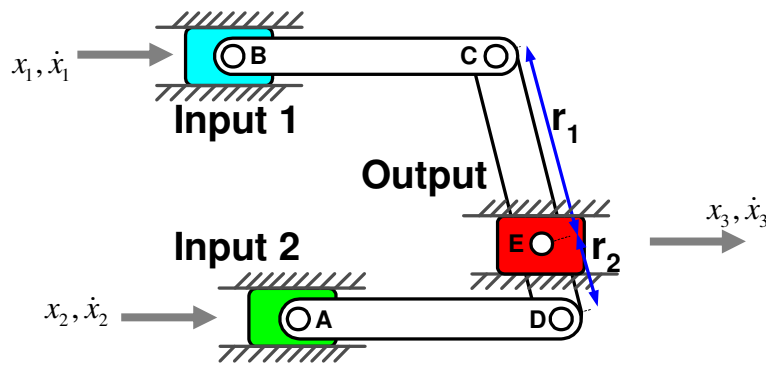


Figure A.1. Differential Link Mechanism. Note in this example  $r_1 > r_2$ .

The velocity of the output (E) is a sum of the component velocities (of A and B), i.e.,  $\dot{x}_3 = f(\dot{x}_1, \dot{x}_2)$  such that

$$\dot{x}_3 = g_{3/1}^0 \dot{x}_1 + g_{3/2}^0 \dot{x}_2 \quad (A1)$$

where

$$g_{3/1}^0 = \dot{x}_3 \Big|_{\substack{\dot{x}_1=1 \\ \dot{x}_2=0}}, \text{ and} \quad (A2)$$

$$g_{3/2}^0 = \dot{x}_3 \Big|_{\substack{\dot{x}_1=0 \\ \dot{x}_2=1}}$$

are the constant kinematic influence coefficients or  $g$ -functions for inputs 1 and 2. Furthermore, these  $g$ -functions can be expressed in terms of the geometry of the mechanism:

$$g_{3/1}^0 = \frac{r_2}{r_1 + r_2} \text{ and } g_{3/2}^0 = \frac{r_1}{r_1 + r_2} \quad (\text{A3})$$

Note that  $g_{3/1}^0 + g_{3/2}^0 = 1$ . To perhaps clarify this further, let  $x_{10}$ ,  $x_{20}$ , and  $x_{30}$  be the initial position of the reference variables  $x_1$ ,  $x_2$ , and  $x_3$ , respectively. Then the total displacement  $x_3$  by direct geometrical evaluation following from Eq. (A1) is

$$x_3 = g_{3/1}^0 (x_1 - x_{10}) + g_{3/2}^0 (x_2 - x_{20}) = f(x_1, x_2) \quad (\text{A4})$$

Note that

$$\frac{\partial x_3}{\partial x_1} = g_{3/1}^0, \frac{\partial x_3}{\partial x_2} = g_{3/2}^0 \quad (\text{A5})$$

are both constants and not functions of the system motion. It follows that

$$\frac{\partial^2 x_3}{\partial x_1 x_2} = \frac{\partial^2 x_3}{\partial x_2 x_1} = 0 \quad (\text{A6})$$

which means that the geometry does not connect the inputs by higher order properties. This ensures that  $x_1$  and  $x_2$  are indeed independent which is the basis for the concept of parallel inputs.

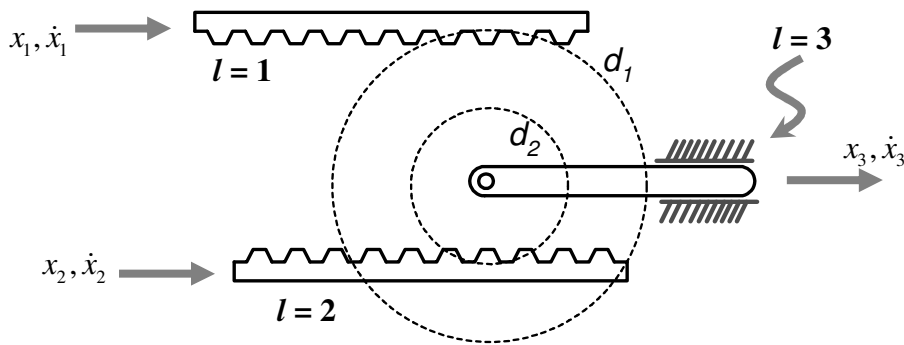


Figure A.2. Differential Gear Mechanism. The outer and inner gears have diameters  $d_1$  and  $d_2$ , respectively (i.e.,  $d_1 > d_2$ ).

## A.2. DIFFERENTIAL GEAR

In Figure A.2 is shown a system similar to the differential link mechanism in that the inputs are independent with the result that

$$\dot{x}_3 = \bar{g}_{3/1}^0 \dot{x}_1 + \bar{g}_{3/2}^0 \dot{x}_2 \quad (\text{A7})$$

with

$$\bar{g}_{3/1}^0 = \frac{d_2}{d_1 + d_2} \quad \text{and} \quad \bar{g}_{3/2}^0 = \frac{d_1}{d_1 + d_2} \quad (\text{A8})$$

Consider a system similar to Figure A.2 but with a feedback link as shown in Figure A.3.

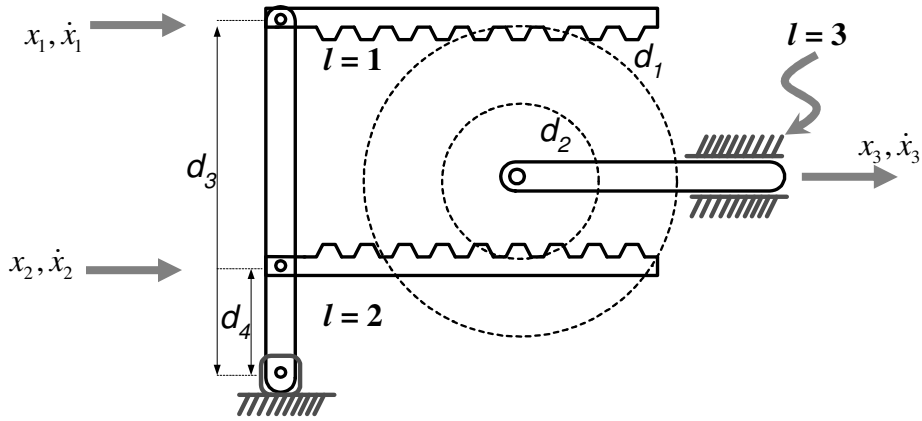


Figure A.3. Differential Gear Mechanism with Mechanical Feedback.

As with the epicyclic gear, we temporarily ignore the feedback system and fix the arm, which in this case is link 3. This allows the use of the formula

$$\frac{\dot{x}_{2/3}}{\dot{x}_{1/3}} = \frac{\dot{x}_2 - \dot{x}_3}{\dot{x}_1 - \dot{x}_3} = g_{2/1} = -\frac{d_2}{d_1} \quad (\text{A9})$$

We now wish to find  $\bar{g}_{3/1}^0$  and  $\bar{g}_{3/2}^0$  which can be determined by

$$\bar{g}_{3/1}^0 = \left. \frac{\dot{x}_3}{\dot{x}_1} \right|_{\dot{x}_2=0} = \left. \frac{g_{2/1} \dot{x}_1 - \dot{x}_2}{\dot{x}_1} \right|_{\dot{x}_2=0} = \frac{g_{2/1}}{g_{2/1} - 1} = \frac{(-d_2/d_1)}{(-d_2/d_1) - 1} = \frac{d_2}{d_1 + d_2} \quad (\text{A10})$$



$$\bar{g}_{3/2}^0 = \frac{\dot{x}_3}{\dot{x}_2} \Big|_{\dot{x}_1=0} = \frac{1 - g_{2/1}' \dot{x}_1}{1 - g_{2/1}'} \Big|_{\dot{x}_1=0} = \frac{1}{1 - g_{2/1}'} = \frac{1}{1 + (d_2/d_1)} = \frac{d_1}{d_1 + d_2} \quad (\text{A11})$$

The feedback constraint between  $\dot{x}_1$  and  $\dot{x}_2$  is given by

$$\bar{g}_f = \bar{g}_{2/1} = \frac{\dot{x}_2}{\dot{x}_1} = \frac{d_4}{d_3} \quad (\text{A12})$$

This results in the total influence coefficient as due to the following

$$\begin{aligned} dx_3 &= \frac{\partial x_3}{\partial x_1} dx_1 + \frac{\partial x_3}{\partial x_2} dx_2 \\ \Rightarrow \frac{dx_3}{dx_1} &= \frac{\partial x_3}{\partial x_1} + \frac{\partial x_3}{\partial x_2} \frac{dx_2}{dx_1} \end{aligned} \quad (\text{A13})$$

which may be interpreted as

$$\bar{g}_{3/1} = \bar{g}_{3/1}^0 + g_f \bar{g}_{3/2}^0 = \frac{1}{d_1 + d_2} \left( d_2 + d_1 \frac{d_4}{d_3} \right) \quad (\text{A14})$$

### A.3. FORCE BALANCE IN DIFFERENTIALS

First consider the differential gear system without mechanical feedback as being without springs, dashpots, mass, and operated on by one load  $\bar{F}_3$  only (Figure A.4).

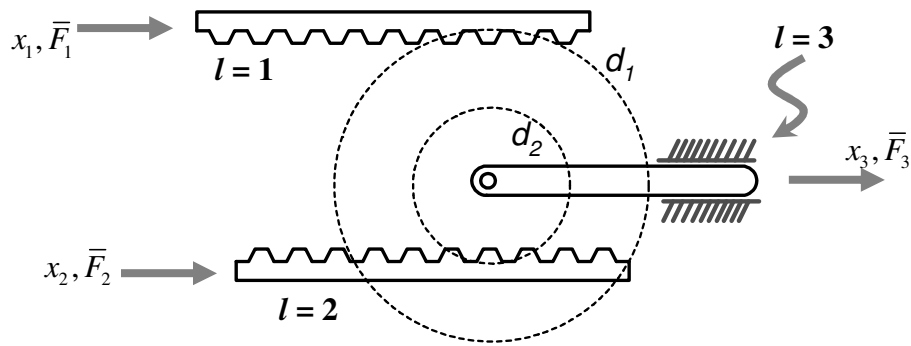


Figure A.4. Differential Gear Mechanism without Mechanical Feedback and with Pure Static Loads.

The virtual work done by this system must be zero if it is in equilibrium, hence

$$\bar{F}_3(dx_3) + \bar{F}_1(dx_1) + \bar{F}_2(dx_2) = 0 \quad (\text{A15})$$

If it is assumed that all the  $dx_i$  are positive then  $\bar{F}_3$  must be a negative value to maintain static equilibrium. This leads to

$$\bar{F}_3 = -\left(\bar{F}_1 \frac{dx_1}{dx_3} + \bar{F}_2 \frac{dx_2}{dx_3}\right) = -\left(\bar{F}_1 \frac{1}{\bar{g}_{3/1}^0} + \bar{F}_2 \frac{1}{\bar{g}_{3/2}^0}\right) \quad (\text{A16})$$

as a result of Eq. (A2). Now consider the differential gear with mechanical feedback. The forces in the system (Figure A.5) are  $\bar{F}_1$  and  $\bar{F}_3$  (that are external) and  $f_1$  and  $f_2$  (that are internal).

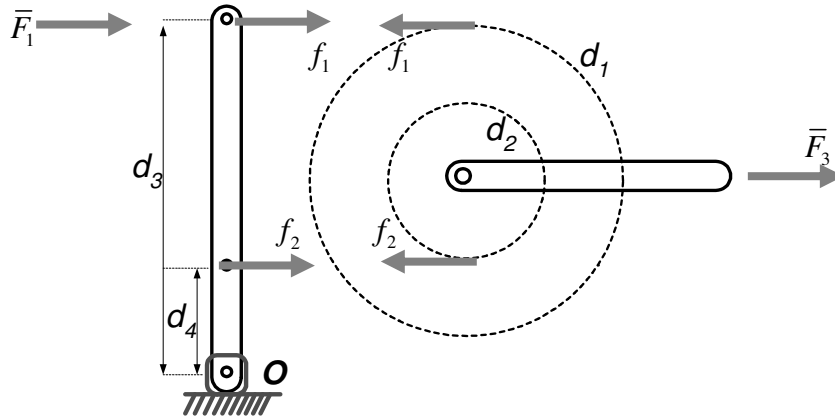


Figure A.5. Free-Body Diagram of Differential Gear Mechanism with Mechanical Feedback.

The feedback  $g$ -function between  $\dot{x}_1$  and  $\dot{x}_2$  is

$$g_f = \bar{g}_{2/1} = \frac{\dot{x}_2}{\dot{x}_1} = \frac{d_4}{d_3} \quad (\text{A17})$$

By definition, the equivalent force  $F_3$  for external load  $\bar{F}_3$  is given by

$$F_3 = \bar{g}_{3/1} \bar{F}_3 \quad (\text{A18})$$

If the system is momentarily in static equilibrium, then

$$\bar{F}_1 = -F_3 = -\bar{g}_{3/1} \bar{F}_3 \quad (\text{A19})$$

Further, summing the moments about point  $O$  gives

$$(f_1 + \bar{F}_1)d_3 + f_2d_4 = 0 \quad (\text{A20})$$

Finally, summing forces on the differential gear yields

$$\bar{F}_3 = f_1 + f_2 \quad (\text{A21})$$

This gives three relations, Eqs. (A19)-(A21), in terms of the three unknowns  $\bar{F}_3, f_1, f_2$  assuming  $\bar{F}_1$  is known. Solving this system of equations we get

$$f_1 = \frac{\bar{F}_1 (\bar{g}_{2/1} - \bar{g}_{3/1})}{\bar{g}_{3/1} (1 - \bar{g}_{2/1})} = \frac{\bar{F}_1 (g_f - \bar{g}_{3/1})}{\bar{g}_{3/1} (1 - g_f)} \quad (\text{A22})$$

$$f_2 = -\frac{\bar{F}_1 (1 - \bar{g}_{3/1})}{\bar{g}_{3/1} (1 - \bar{g}_{2/1})} = \frac{\bar{F}_1 (\bar{g}_{3/1} - 1)}{\bar{g}_{3/1} (1 - g_f)} \quad (\text{A23})$$

An important question results in comparing transmitted power with the circulating power.

The transmitted power is

$$P_{TR} = \bar{F}_1 \dot{x}_1 \quad (\text{A24})$$

while circulating power is

$$P_{cir} = f_2 \dot{x}_2 \quad (\text{A25})$$

The ratio  $\gamma$  of the circulating power to the transmitted power is an important concept in differential systems, i.e.

$$\gamma = \frac{P_{cir}}{P_{TR}} = \frac{f_2 \dot{x}_2}{\bar{F}_1 \dot{x}_1} \quad (\text{A26})$$

This becomes

$$\begin{aligned} \gamma &= -\frac{(1 - g_{3/1}) \bar{F}_1 \dot{x}_2}{g_{3/1} (1 - g_f) \bar{F}_1 \dot{x}_1} = \frac{-g_f (1 - g_{3/1})}{g_{3/1} (1 - g_f)}, \text{ or} \\ \gamma &= -\frac{\left(1 - \frac{1}{g_{3/1}}\right)}{\left(1 - \frac{1}{g_f}\right)} = -\frac{(1 - \bar{m}_{3/1})}{(1 - \bar{m}_{2/1})} \end{aligned} \quad (\text{A27})$$

where  $m$  is the mechanical advantage. Hence

$$\gamma = -\left\{ \frac{1 - (m \text{ for the total train})}{1 - (m \text{ for the circuit loop})} \right\} \quad (\text{A28})$$

This is a general concept for all parallel systems having a feedback loop. Note that for systems in series, the force relationship is

$$F_{out} = (m_1 m_2 \dots m_n) F_{in} \quad (A29)$$

and for systems in parallel

$$F_{out} = m_1 F_1 + m_2 F_2 + \dots + m_n F_n \quad (A30)$$

The analogy with electrical systems in terms of their force (or voltage) is evident.

## Appendix B. Sample PFVA Designs for Effective Inertia Analysis

Three sample PFVA designs were considered in Chapter 4 (Example 4.3) to numerically demonstrate the concepts related to the effective inertia of the PFVA. These designs were based on a requirement of given torque (150 N-m) and speed (40 rpm) at the PFVA output. The gear train considered for these designs were the type SA planetary drives from Andantex Inc. (2007). The prime-movers were Emoteq (2007) and Kollmorgen (2007) motors. The design components and parameters are listed in the table below.

Table B.1 Actuator Design Parameters used in Example 4.3

Design#	1	2	3
Gear Train	Andantex SR 20	Andantex SR 20	Andantex SR 20
RSF, $\bar{\rho}$	66.85	24.27	3.7
VA Motor	Emoteq HT07000	Kollmorgen RBE-03001-A50	Danaher Motion DH063M-22-1310
FA Motor	Danaher Motion DH063M-22-1310	Danaher Motion DH063M-22-1310	Danaher Motion DH063M-22-1310
$I_{M_f}$ (Kg-m <sup>2</sup> )	$2.24 \times 10^{-2}$	$2.11 \times 10^{-2}$	$1.48 \times 10^{-2}$
$I_{M_v}$ (Kg-m <sup>2</sup> )	$1.6 \times 10^{-3}$	$9 \times 10^{-4}$	$1.04 \times 10^{-2}$
$I_{vf}$ (Kg-m <sup>2</sup> )	$4 \times 10^{-4}$	$1 \times 10^{-3}$	$3.3 \times 10^{-3}$

## Appendix C. Calculation of Reflected Inertia Terms

In this appendix we will illustrate the method to calculate the terms  $\mathbf{I}_M$ , which is the prime-mover inertia matrix, and  $\mathbf{I}^*$ , which is the output to input reflected inertia matrix. Consider a four-bar linkage driven by a PFVA as shown in Figure C.1.

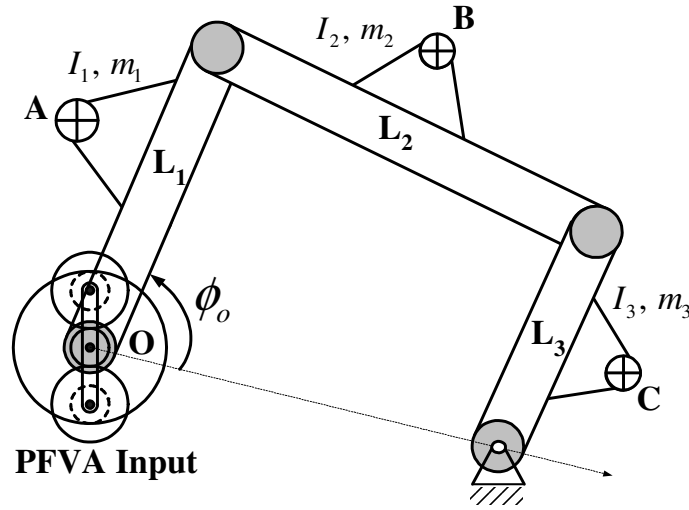


Figure C.1. Planar four-bar linkage driven by a PFVA

The inertia properties of the various links  $L_1$ - $L_3$  are also shown in Figure C.1. This 1-DOF system can be represented as an equivalent link (Benedict and Tesar, 1978) with inertia  $I(\phi_o)$  at the machine input O as shown in Figure C.2.

$$I(\phi_o) = \sum_{i=1}^{N_L} \left[ I_i (g_i)^2 + m_i (g_i^x)^2 + m_i (g_i^y)^2 \right] \quad (C1)$$

In Eqn. (C1),  $N_L$  is the total number of links in the mechanism and

$$g_i = \frac{\dot{\phi}_i}{\dot{\phi}_o}, \quad g_i^x = \frac{\dot{x}_i}{\dot{\phi}_o}, \quad g_i^y = \frac{\dot{y}_i}{\dot{\phi}_o} \quad (C2)$$

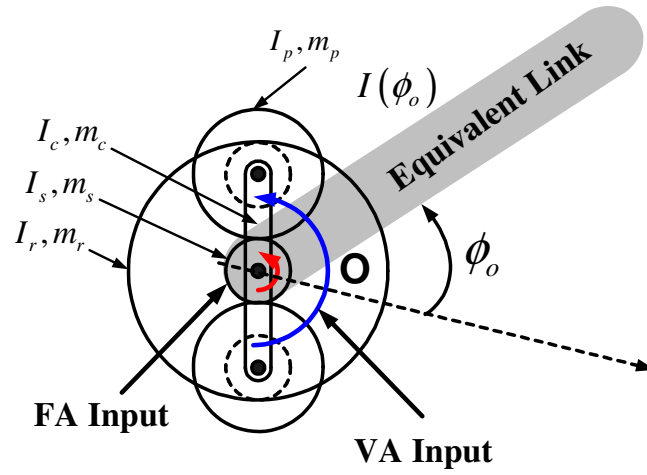


Figure C.2. Equivalent link representation of the four-bar linkage (Rabindran and Tesar, 2007a)

Now if the relative scale factor  $\tilde{\rho}$  for the PFVA is known, then the reflected inertia matrix  $\mathbf{I}^*$  at the PFVA inputs can be determined (Rabindran and Tesar, 2007a):

$$\mathbf{I}^* = \frac{I}{(\tilde{\rho}+1)^2} \begin{bmatrix} 1 & \tilde{\rho} \\ \tilde{\rho} & \tilde{\rho}^2 \end{bmatrix} \quad (\text{C3})$$

In a similar manner, the inertia of a gear train component can be reflected to the PFVA inputs. For example, consider the simple gear train shown in Figure C.2. The inertia properties of the various gear components are shown in this figure. The total inertia  $\mathbf{I}_M$  seen by the PFVA inputs due to the components of the gear train and the prime-mover can now be determined:

$$\mathbf{I}_M = \mathbf{I}_I + \sum_{j=1}^{N_C} (I_j^* + {}^x m_j^* + {}^y m_j^*) \quad (\text{C4})$$

where

$$I_j^* = \begin{bmatrix} g_v^j \\ g_f^j \end{bmatrix} I_j \begin{bmatrix} g_v^j & g_f^j \end{bmatrix} \quad (\text{C5})$$

$${}^x m_j^* = \begin{bmatrix} {}^x g_v^j \\ {}^x g_f^j \end{bmatrix} m_j \begin{bmatrix} {}^x g_v^j & {}^x g_f^j \end{bmatrix} \quad (\text{C6})$$

$${}^y m_j^* = \begin{bmatrix} {}^y g_v^j \\ {}^y g_f^j \end{bmatrix} m_j \begin{bmatrix} {}^y g_v^j & {}^y g_f^j \end{bmatrix} \quad (C7)$$

are the reflected inertias for component  $j$  in the principal directions and

$$g_i^j = \frac{\dot{\phi}_j}{\dot{\phi}_i}, \quad {}^x g_i^j = \frac{\dot{x}_j}{\dot{\phi}_i}, \quad {}^y g_i^j = \frac{\dot{y}_j}{\dot{\phi}_i}, \quad i \in \{v, f\} \quad (C8)$$

are the kinematic influence coefficients for component  $j$  w.r.t. the input  $i$  in the principal directions. Also, in Eqn. (C4),  $I_r$  is a diagonal matrix of motor inertias:

$$\mathbf{I}_r = \begin{bmatrix} I_v & 0 \\ 0 & I_f \end{bmatrix} \quad (C9)$$

In Eq. (C4)  $N_c$  is the total number of components in the gear train and the prime-mover.

This appendix only demonstrates the methodology to calculate the inertia terms for a planar mechanism. However, this procedure can be extended to spatial systems.



## Appendix D. Simulation Parameters for 3R PFVA-Driven Robot

### D.1. KINEMATIC AND DYNAMIC PARAMETERS

The manipulator used in Chapter 8 is a planar 3R PFVA-driven manipulator (Figure D.1). The Denavit-Hartenberg (D-H) frame assignment (Craig, 1989) for this robot is shown in Figure D.1. Note that in the robot's world frame  $X_0Y_0Z_0$ , the gravity force vector is  $(0, -g, 0)$  where  $g$  is the magnitude of the acceleration due to gravity.

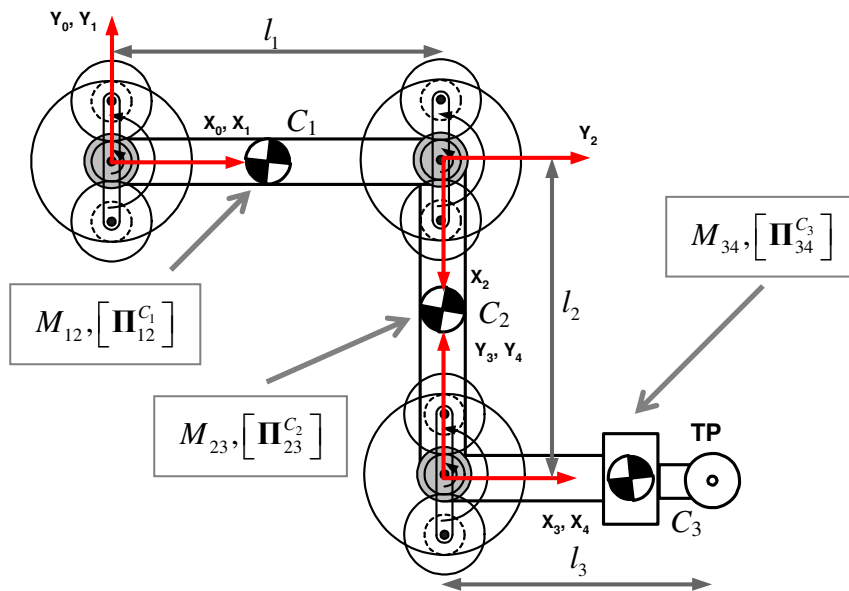


Figure D.1. Conceptual representation of the planar 3R PFVA-driven manipulator used in Chapter 8. The Tool Point (TP) is also shown.

Table D.1 D-H Parameters for the 3R Planar PFVA-Manipulator				
$i$	$a_{i-1}$ (m)	$\alpha_{i-1}$ (rad)	$d_i$ (m)	$\theta_i^{63}$ (rad)
1	0	0	0	$\theta_1 = 0$
2	$l_1 = 0.5$	0	0	$\theta_2 = -\pi/2$
3	$l_2 = 0.5$	0	0	$\theta_3 = \pi/2$
TP = $(l_3, 0, 0)$ in $X_3Y_3Z_3$ , $l_3 = 0.34$ m.				

<sup>63</sup> This value is for the configuration shown in Figure D.1.

The D-H parameters based on the above frame assignment are listed in Table D.1. The dynamic parameters for the manipulator, i.e. Center of Mass (COM), lumped masses, and inertia tensors for the links in their local frames about their COMs, are listed in Table D.2. Notation used is from Thomas and Tesar (1982) which is also used in Chapter 8.

Table D.2 Dynamic Parameters for the 3R Planar PFVA-Manipulator			
Link ( $j$ )	COM in Local Link Frame ( $C_j$ ) (m)	Link Mass ( $M_{jk}$ ) (kg)	Inertia Tensor about $C_j$ in Local Link Frame ( $\mathbf{I}_{jk}^{C_j}$ ) <sup>64</sup> (kg-m <sup>2</sup> )
1	$C_1 \equiv \left(\frac{l_1}{2}, 0, 0\right)$	$M_{12} = 10$	$\left(\mathbf{I}_{12}^{C_1}\right)_{zz} = 2.5 \times 10^{-3}$
2	$C_2 \equiv \left(\frac{l_2}{2}, 0, 0\right)$	$M_{23} = 10$	$\left(\mathbf{I}_{23}^{C_2}\right)_{zz} = 2.5 \times 10^{-3}$
3	$C_3 \equiv \left(\frac{2l_3}{3}, 0, 0\right)$	$M_{34} = 5$	$\left(\mathbf{I}_{34}^{C_3}\right)_{zz} = 1.0 \times 10^{-3}$

We will now list (Table D.3) the kinematic and dynamic parameters for the PFVAs in the 3R robot for the three design case studies presented in Section 8.6. In Table D.3 the parameters have been separately listed for the three design cases. Based on the design torque at each joint, the design torque for the VA and FA input sets were determined based on the RSF values for each design case. The backdriving efficiency for the drive train was assumed to be equal to the forward driving efficiency. The forward driving efficiencies of the two inputs were determined using the RSF values and the SISO efficiency plot shown in Figure 4.1. The gear train inertia for the Andantex drives is approximately constant (0.0146 kg-m<sup>2</sup>) across the RSF values we have considered for this simulation. However, the gear train inertias reflected to each input will be proportional to the square of this input's velocity ratio (see Table D.3). The prime-mover inertias were determined by considering a set of high torque brushless DC motors from

<sup>64</sup> All components other than  $I_{zz}$  are assumed to be zero.

Emoteq (with known torque rating and rotor inertia for each motor). The inertias required for the simulation were then determined by interpolating between the inertia values in this set for a given torque.

Table D.3 Kinematic and Dynamic Parameters for the PFVAs of the 3R Robot			
Parameter	Joint 1	Joint 2	Joint 3
Design Torque (N-m)	150	100	40
<b>DESIGN CASE 1</b>			
RSF, $\tilde{\rho}$	255.4	255.4	255.4
VA Velocity Ratio, $g_1$	0.0039	0.0039	0.0039
FA Velocity Ratio, $g_2$	0.9961	0.9961	0.9961
VA Design Torque (N-m)	0.5850	0.39	0.156
FA Design Torque	149.415	99.61	39.844
VA Backdriving Efficiency, $\eta_{b1}$	0.225	0.225	0.225
FA Backdriving Efficiency, $\eta_{b2}$	0.997	0.997	0.997
VA-Side Gear Train Inertia, $I_{11}$ (kg-m <sup>2</sup> )	$2.226 \times 10^{-7}$	$2.226 \times 10^{-7}$	$2.226 \times 10^{-7}$
FA-Side Gear Train Inertia, $I_{22}$ (kg-m <sup>2</sup> )	0.0145	0.0145	0.0145
Gear Train Coupling Inertia, $I_{12} = I_{21}$ (kg-m <sup>2</sup> )	$5.686 \times 10^{-5}$	$5.686 \times 10^{-5}$	$5.686 \times 10^{-5}$
VA Prime-Mover Inertia, $I_{11}^p$ (kg-m <sup>2</sup> )	$9.2436 \times 10^{-7}$	$4.624 \times 10^{-7}$	$1.261 \times 10^{-7}$
FA Prime-Mover Inertia, $I_{22}^p$ (kg-m <sup>2</sup> )	0.0641	0.0306	0.0014
<b>DESIGN CASE 2</b>			
RSF, $\tilde{\rho}$	1.0	1.0	1.0
VA Velocity Ratio, $g_1$	0.5	0.5	0.5
FA Velocity Ratio, $g_2$	0.5	0.5	0.5

VA Design Torque (N-m)	75	50	20
FA Design Torque	75	50	20
VA Backdriving Efficiency, $\eta_{b1}$	0.995	0.995	0.995
FA Backdriving Efficiency, $\eta_{b2}$	0.983	0.983	0.983
VA-Side Gear Train Inertia, $I_{11}$ (kg-m <sup>2</sup> )	0.0037	0.0037	0.0037
FA-Side Gear Train Inertia, $I_{22}$ (kg-m <sup>2</sup> )	0.0037	0.0037	0.0037
Gear Train Coupling Inertia, $I_{12} = I_{21}$ (kg-m <sup>2</sup> )	0.0037	0.0037	0.0037
VA Prime-Mover Inertia, $I_{11}^p$ (kg-m <sup>2</sup> )	0.0141	0.0018	0.0006
FA Prime-Mover Inertia, $I_{22}^p$ (kg-m <sup>2</sup> )	0.0141	0.0018	0.0006
<b>DESIGN CASE 3</b>			
RSF, $\tilde{\rho}$	255.4	24.3	1.0
VA Velocity Ratio, $g_1$	0.0039	0.0395	0.5
FA Velocity Ratio, $g_2$	0.9961	0.9605	0.5
VA Design Torque (N-m)	0.5850	3.9526	20
FA Design Torque	149.415	96.047	20
VA Backdriving Efficiency, $\eta_{b1}$	0.225	0.69	0.995
FA Backdriving Efficiency, $\eta_{b2}$	0.997	0.988	0.983
VA-Side Gear Train Inertia, $I_{11}$ (kg-m <sup>2</sup> )	$2.226 \times 10^{-7}$	$2.286 \times 10^{-5}$	0.0037
FA-Side Gear Train Inertia, $I_{22}$ (kg-m <sup>2</sup> )	0.0145	0.0135	0.0037
Gear Train Coupling Inertia, $I_{12} = I_{21}$ (kg-m <sup>2</sup> )	$5.6864 \times 10^{-5}$	$5.5567 \times 10^{-4}$	0.0037
VA Prime-Mover Inertia, $I_{11}^p$ (kg-m <sup>2</sup> )	$9.2436 \times 10^{-7}$	$4.6496 \times 10^{-5}$	0.0006
FA Prime-Mover Inertia, $I_{22}^p$ (kg-m <sup>2</sup> )	0.0641	0.0282	0.0006

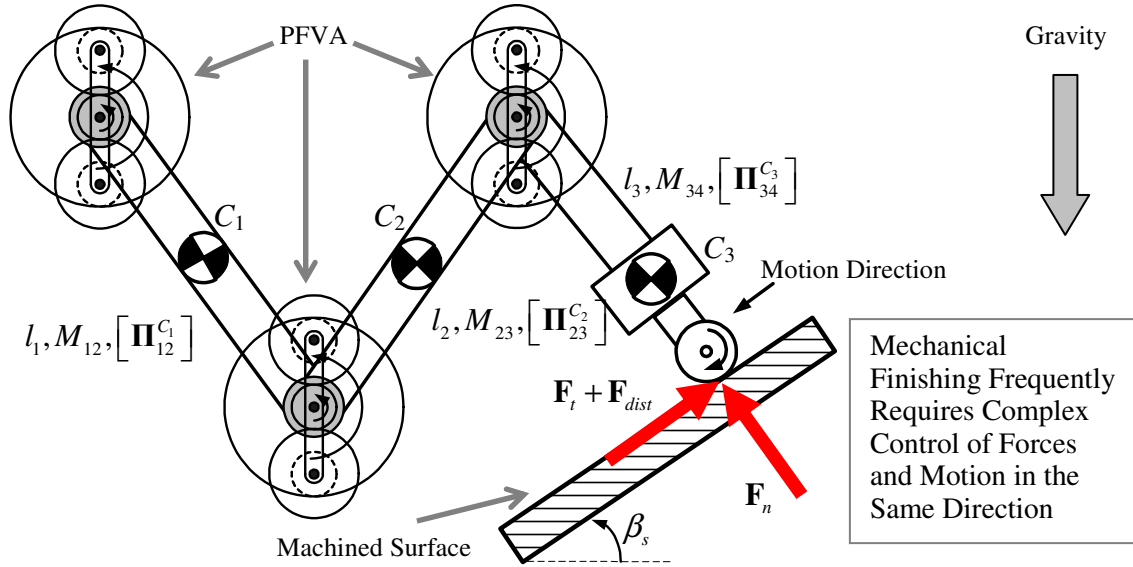


Figure D.2. Conceptual representation of a planar 3R PFVA-driven manipulator performing a finishing operation on a planar part.

## D.2. TASK PARAMETERS

The contact task considered for this simulation was mechanical finishing (Figure D.2). This task required finishing a planar inclined surface at an angle  $\beta_s = 30^\circ$ . The initial configuration of the robot was chosen to be  $\theta = [75^\circ \quad -20^\circ \quad -50^\circ]^T$  and the task required moving downward along the planar surface by a distance of 0.5m at the rate of 10 mm/s by maintaining a constant orientation of the tool frame with respect to the part. This orientation is determined from the initial configuration. The VA and FA input set velocities and accelerations were determined via inverse kinematics from Eqs. (8.27) and (8.36).

The contact forces acting on the tool were resolved into the normal force  $\mathbf{F}_n$ , tangential force  $\mathbf{F}_t$ , and the moment  $\mathbf{M}$ :

$$\|\mathbf{F}_n\| = 40 \text{ N}, \quad \|\mathbf{F}_t\| = \mu_s \mathbf{F}_n, \quad \mu_s = 0.3 \quad (\text{D1})$$

where  $\mu_s$  is the coefficient of friction between the tool and the part. The viscous friction disturbance force  $\mathbf{F}_{dist}$  was used to model hard-spots in the part arising from material impurities:

$$\mathbf{F}_{dist} = -B_s \mathbf{v}_t$$
$$B_s = \begin{cases} 0.5 & 10s \leq t \leq 15s \\ 1.5 & 40s \leq t \leq 45s \end{cases} \text{ (N-m/s)} \quad (\text{D2})$$

where  $B_s$  is the viscous friction coefficient and  $\mathbf{v}_t$  is the tangential velocity of the contact point along the surface.

## Appendix E. PFVA Testbed Details

The mechanical components used in the PFVA testbed (discussed in Chapter 7) are shown in Figure E.1 and are listed in Table E.1.

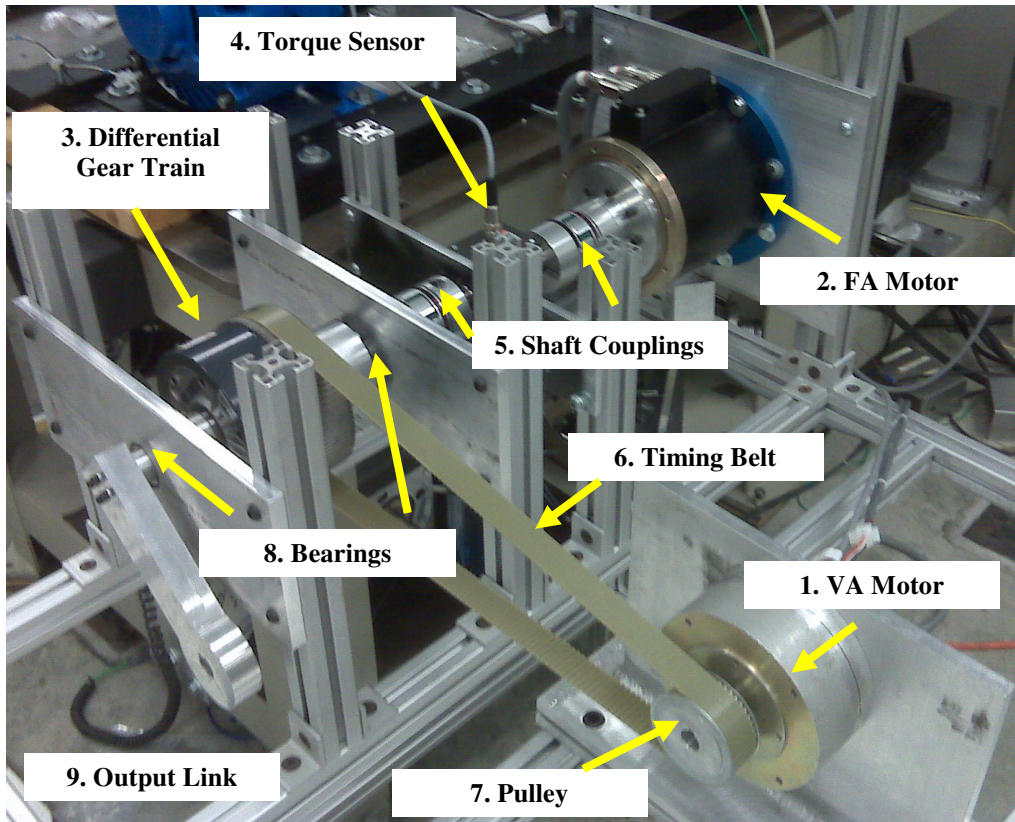


Figure E.1. PFVA Experimental Testbed Layout with Labeled Parts.

The control system hardware layout of the PFVA testbed is shown in Figure E.2. The host PC was a Windows XP Pro machine (Intel Pentium D and 1 GB RAM) with two software applications primarily used for the control of our testbed: (i) National Instruments (NI) LabVIEW 8.0 and (ii) Kollmorgen's S-DRIVE 600 v. 5.53.

Table E.1 List of Components in the PFVA Testbed

Part (Figure E.1)	Components	Manufacturer and Model	Relevant Specifications
1	VA Motor (Framed)	Kollmorgen RBE-03001-A50 (Permanent Magnet Synchronous Motor)	Peak Torque = 28.9 N-m, Max. Speed = 281 rpm, Rotor Inertia = $7.8 \times 10^{-4}$ kg-m <sup>2</sup> Encoder Counts Per Rev = 8192
2	FA Motor (Framed)	Kollmorgen Goldline DDR DH063M-22-1310 (Brushless DC Motor)	Peak Torque = 150 N-m, Max. Speed = 800 rpm, Rotor Inertia = $8.6 \times 10^{-3}$ kg-m <sup>2</sup> Encoder Counts Per Rev = 8192
3	2-DOF Differential (Oil Lubricated)	Andantex SR-20 Unit	Rated Torque = 150 N-m, Relative Scaling Factor = 24.27, VA Forward Efficiency = 69%, FA Forward Efficiency = 98%
4	Torque Sensor	Honeywell Lebow 1703-1NM	Torque Range = $\pm 200$ N-m, Accuracy = $\pm 0.25\%$ , Rise Time = 2 ms, Bandwidth (3dB) = 200 Hz, Voltage Output = $\pm 10$ V
5	Shaft Couplings	R+W America EK2/150/B/26/26 (Elastomer Coupling)	Material = Aluminum, Max. Speed = 500 rpm, Max. Torque = 200 N-m.
6	Timing Belt	Speed Control Inc. T5/1280/25	Length = 1280 mm, Teeth = T5, Width = 25 mm, Material = Steel Reinforced Urethane
7	Timing Belt Pulley	American Metric Corp. 36T5/42-2, 5/8 Bore Keyway	Pitch Diameter = 67 mm, Teeth = T5, Width = 36 mm
8	Bearings	Control Bearings, MB542DD (Torque Tube Type)	Inner Dia = 1.3125 in, Outer Dia = 1.75 in Inner Width = 0.2810 in, Outer Width = 0.25 in
9	Output Link	Fabricated In-house (Aluminum)	Material = Aluminum, Length = 0.158 m

A NI-PXI-7358 motion controller was used with a UMI-7774 interface board for VA and FA motor control using NI-Motion 7.5 (Table E.2). The torque sensor was connected to an NI SCXI-1313 terminal block and an SCXI-1325 signal conditioning module, and then interfaced to the host PC via a NI-PXI-6251 M-Series DAQ Card. The servo amplifiers associated with the VA and FA motors were Advanced Motion Control (AMC) SE30A40 and Kollmorgen S640, respectively. The NI Measurement and Automation Explorer (MAX) utility was used to configure the settings for NI-Motion and to define a global DAQ channel for the torque sensor. See (Yoo and Tesar, 2004; Janardhan and Tesar, 2008; and Donner, 2009) for more detailed specifications.



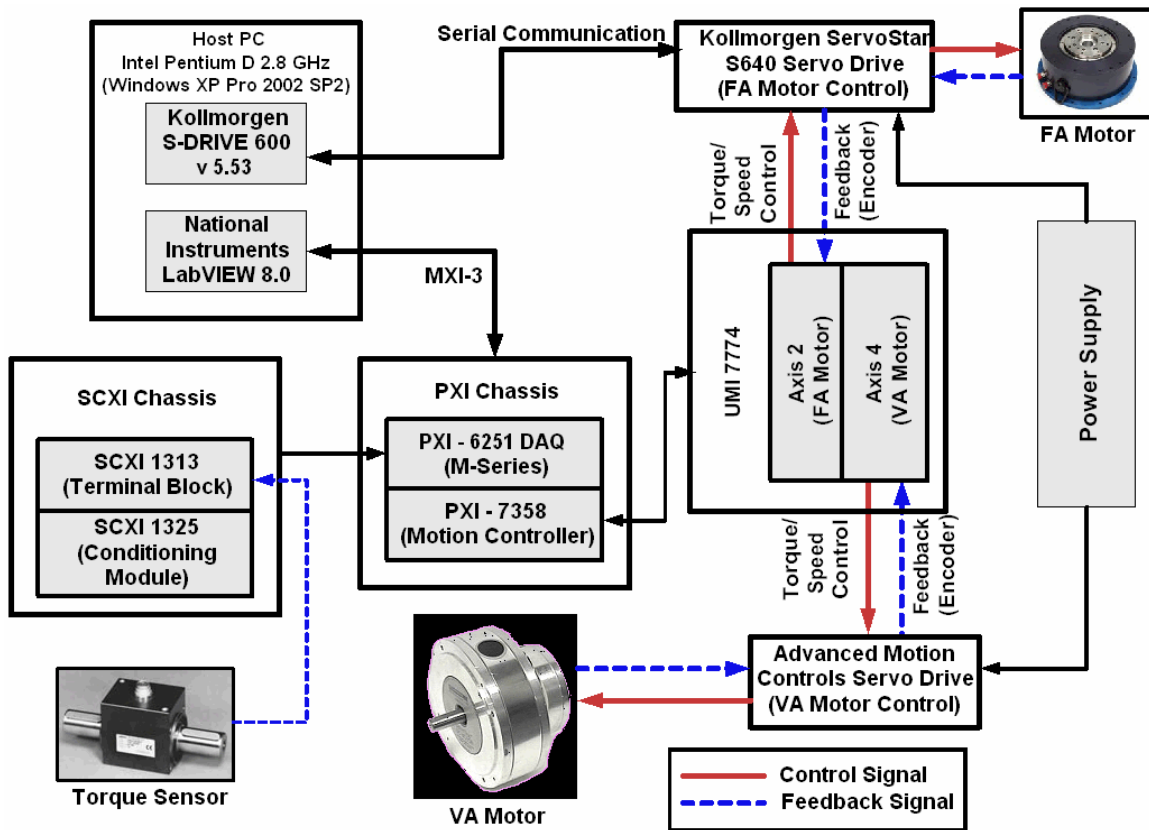


Figure E.2. Block Diagram Representing the System Layout of the PFVA Testbed

Table E.2 List of Principal Control System Components in the PFVA Testbed

Components	Manufacturer and Model	Relevant Specifications
VA Motor Amplifier	AMC SE30A40	Peak Current = 30 A, Continuous Current = 15 A, AC Supply Voltage = 45-270 VAC
FA Motor Amplifier	Kollmorgen Servostar S640	Nominal Current = 40A AC Supply Voltage = 230-480 VAC
Motion Controller (Yoo and Tesar, 2004)	NI-PXI-7358	8-Axis Brushless Motor Controller ( Sinusoidal Commutation) System Processor: Motorola 32 bit $\mu$ P, DSP, and FPGA Communication Interface: PXI with Bi-Directional FIFO, Analog I/O: 8 channel multiplexed, 16-bit ADC Minimum Servoloop Update Rate: 62.5 $\mu$ s

## References

- Abba, G. and Chaillet, N., 1999, "Robot Dynamic Modeling Using a Power Flow Approach with Application to Biped Locomotion," *Autonomous Robots*, **6**(1), pp. 39-52.
- Alami, et al., 2006, "Safe and Dependable Physical Human-Robot Interaction in Anthropic Domains: State of the Art and Challenges," Workshop on Physical Human-Robot Interaction, *Proceedings of the IEEE International Conference on Intelligent Robot Systems (IROS)*, Beijing, China.
- Albu-Schäeffler, A., Bicchi, A., and Vanderborght, (Organizers), 2008, Workshop on the Design and Control of Variable Impedance Actuators for Physical Interaction of Robots with Humans and their Environments, *Robotics Science and Systems IV (RSS)*, ETH Zurich, Switzerland.
- Albu-Schäffer, A., Eiberger, O., Grebenstein, M., Haddadin, S., Ott, C., Wimböck, T., Wolf, S., Hirzinger, G., 2008, "Soft Robotics: From Torque-Feedback Controlled Light-Weight Robots to Intrinsically Compliant Systems," *IEEE Robotics and Automation Magazine*, **15**(3), pp. 20-30.
- Andantex Inc., USA, 2007, "Differential Gearbox Series SA – Standard Range," Product Catalog; see also <http://www.andantex.com/sa.html/>.
- Angeles, J., 2007, *Fundamentals of Robotic Mechanical Systems: Theory, Methods, and Algorithms*, Springer, Third Edition.
- Armstrong-Hélouvry, B., 1991, *Control of Machines with Friction*, Kluwer Academic Publishers, Boston, MA.
- Asada, H., Kanade, T., and Takeyama, I., 1983, "Control of a Direct-Drive Arm," *ASME Journal of Dynamic Systems, Measurement, and Control*, Vol. 105, pp. 136-142.
- Asada, H., and Youcef-Toumi, K., 1987, *Direct-Drive Robots*, MIT Press.
- Aydin, M., Huang, S., and Lipo, T.A., 2006, "Torque Quality and Comparison of Internal and External Rotor Axial Flux Surface-Magnet Disc Machines," *IEEE Transactions on Industrial Electronics*, **53**(3), pp. 822-830.
- Barr, R.E and Chan, E.K., 1986, "Design and Implementation of Digital Filters for Biomedical Signal Processing," *Journal of Electrophysiological Techniques*, **13**(2), pp. 73-93.

- Bekey, G., Ambrose, R., Kumar, V., Sanderson, A., Wilcox, B., and Zheng, Y., 2006, "International Assessment of Research and Development in Robotics," World Technology Evaluation Center Panel Report; see also <http://www.wtec.org/robotics/report/screen-robotics-final-report.pdf>.
- Benedict, C.E., and Tesar, D., 1971, "Dynamic Response Analysis of Quasi-Rigid Mechanical System Using Kinematic Influence Coefficients," *ASME Journal of Mechanisms*, **6**(4), pp. 383-389.
- Benedict, C.E., and Tesar, D., 1978, "Model Formulation of Complex Mechanisms with Multiple Inputs," *ASME Journal of Mechanical Design*, **100**(4), pp. 747-754.
- Ben-Israel, A. and Greville, T., 1974, *Generalized Inverses: Theory and Applications*, John Wiley and Sons, New York.
- Bicchi, A., and Tonietti, G., 2004, "Fast and Soft Arm Tactics: Dealing with the Safety-Performance Tradeoff in Robot Arms Design and Control," *IEEE Robotics and Automation Magazine*, Special Issue on "Safety Among Us," **11**(2), pp. 22-33.
- Bonsignorio, F., Halam, J., and del Pobil, Angel, P. (Eds.), 2008, "Good Experimental Methodology Guidelines," Report of the Special Interest Group on Good Experimental Methodology and Benchmarking, European Robotics Research Network (EURON).
- Bowling, A. and Khatib, O., 2005, "The Dynamic Capability Equations: A New Tool for Analyzing Robot Manipulator Performance," *IEEE Transactions on Robotics*, **21**(1), pp. 115-123.
- Chang, S-L., and Tsai, L-W, 1993, "On the Redundant-Drive Backlash-Free Robotic Mechanisms," *ASME Journal of Mechanical Design*, **115**(2), pp. 247-254.
- Chen, C. and Angeles, J., 2007, "Virtual-Power Flow and Mechanical Gear-Mesh Power Losses of Epicyclic Gear Trains," *Journal of Mechanical Design*, **129**(1), pp. 107-113.
- Chen, D-Z and Tsai, L-W, 1993, "Kinematic and Dynamic Synthesis of Geared Robotic Mechanisms," *Journal of Mechanical Design*, **115**(2), pp. 241-246.
- Cho, W., Tesar, D., and Freeman, R.A., 1989, "The Dynamic and Stiffness Modeling of General Robotic Manipulator Systems with Antagonistic Actuation," *Proceedings of the International Conference on Robotics and Automation (ICRA)*, Scottsdale, AZ, pp. 1380-1387.
- Cox, D., Rackers, K., and Tesar, D., 1995, "Cooperative Manipulation Experiments Using a Dual Arm Robot," *Proceedings of the IEEE International Conference on Industrial Electronics, Control, and Instrumentation*, Orlando, FL, pp. 104-109.

- Craig, J.J., 1989, *Introduction to Robotics: Mechanics and Control*, Addison-Wesley Longman Publishing Co., Inc., Boston, MA, Second Edition.
- De Santis, A., Siciliano, B., De Luca, A., and Bicchi, A., 2008, "An Atlas of Physical Human-Robot Interaction," *Mechanism and Machine Theory*, **43**(3), pp. 253-270.
- Devore, J.L., 1999, *Probability and Statistics for Engineering and the Sciences*, Duxbury Thomson Learning, Pacific Grove, CA, Fifth Edition.
- Donner, P., 2009, "Construction and Experimental Evaluation of a Parallel Force/Velocity Actuator," Semestrarbeit, TU, München.
- Emoteq Inc., USA, 2007, "High Torque and High Speed Series Brushless DC Motors," Product Catalogs; see also <http://www.emoteq.com/>.
- Eppinger, S.D. and Seering, W.P., 1992, "Three Dynamic Problems in Robot Force Control," *IEEE Trans. Robotics and Automation*, **8**(6), pp. 751-758.
- Freeman, R.A., and Tesar, D., 1988, "Dynamic Modeling of Serial and Parallel Mechanisms/Robotic Systems: Part I – Methodology, Part II – Applications," *Proceedings of the ASME Biennial Mechanisms Conference, Trends and Developments in Mechanisms, Machines, and Robotics*, **15**(3), pp. 7-27.
- Garcia, E., de Santos, P.G., and de Wit, C.C., 2002, "Velocity Dependence in Cyclic Friction," *The International Journal of Robotics Research*, **21**(9), pp. 761-771.
- Haddadin, S., Albu-Schäffer, and Hirzinger, G., 2007, "Safety Evaluation of Physical Human-Robot Interaction via Crash-Testing," Burgard, W., Brock, O., and Stachniss, C. (Eds.), *Robotics Science and Systems III*, pp. 217-224, The MIT Press, Cambridge, MA.
- Hall, A.S. Jr., 1992, "A Note on the History of Kinematic Influence Coefficients," *Mechanism and Machine Theory*, **27**(3), p. 367.
- Harden, T., and Tesar, D., 2002, "Minimum Distance Influence Coefficients for Obstacle Avoidance in Manipulator Motion Planning," Ph.D. Dissertation, Mechanical Engineering Department, The University of Texas at Austin, Austin, TX.
- Hata, H., Kubo, S., Taga, Y., and Ibaraki, R., 1999, "Hybrid Drive System," United States Patent No. 5875691.
- Hill, A.V., 1970, *First and Last Experiments in Muscle Mechanics*, Cambridge University Press.
- Hogan, N., 1985, "Impedance Control: An Approach to Manipulation," Parts I-III, *Journal of Dynamic Systems, Measurement, and Control*, **107**(1), pp. 1-24.

- Hollerbach, J.M., Hunter, I.W., and Ballantyne, J., 1992, "A Comparative Analysis of Actuator Technologies for Robotics," In *Robotics Review 2*, Khatib, O., Craig, J.J., and Lozano-Perez, T., eds., MIT Press, Cambridge, Massachusetts, pp. 299-342.
- Hooper, R., and Tesar, D., "Multi-Criteria Inverse Kinematics for General Serial Robots," Ph.D. Dissertation, The University of Texas at Austin, Austin, TX.
- Hurst, J.W., Chestnutt, J., Rizzi, A., 2007, "Design and Philosophy of the BiMASC, a Highly Dynamic Biped," *Proceedings of the International Conference on Robotics and Automation*, Roma, Italy, pp. 1863-1868.
- Hyde, J.M., and Cutkosky, M.R., 1994, "Controlling Contact Transition," *IEEE Control Systems Magazine*, **14**(1), pp. 25-30.
- Ingle, V. and Proakis, J., 1997, *Digital Signal Processing Using MATLAB*, PWS Publishing Co., Boston.
- Janardhan, J. and Tesar, D., 2008, "Test Methodology for Electromechanical Actuators," Ph.D. Dissertation, Mechanical Engineering Department, The University of Texas at Austin, Austin, TX.
- Kahraman, A., 1994, "Planetary Gear Train Dynamics," *ASME Journal of Mechanical Design*, **116**(3), pp. 713-720.
- Kapoor, C. and Tesar, D., 1996, "A Reusable Operational Software Architecture for Advanced Robotics," Ph.D. Dissertation, Mechanical Engineering Department, The University of Texas at Austin, Austin, TX.
- Kapoor, C., Cetin, M., and Tesar, D., 1998, "Performance-Based Redundancy Resolution with Multiple Criteria," Proc. ASME Design Engineering and Technical Conferences (DETC), Atlanta, Georgia. Paper No: DETC98/MECH-5864
- Kim, B-S, Park, J-J, and Song, J-B, April 2007, "Double Actuator Unit with Planetary Gear Train for a Safe Manipulator," *Proceedings of the IEEE International Conference on Robotics and Automation*, pp. 1146-1151, Roma, Italy.
- Kollmorgen, 2007, "Direct Drive DC Torque Motors," Product Catalog; see also [http://www.motionvillage.com/products/product\\_literature/product\\_brochure/pdfs/KOL1154.pdf](http://www.motionvillage.com/products/product_literature/product_brochure/pdfs/KOL1154.pdf).
- Lanczos, C., 1986, *The Variational Principles of Mechanics*, Courier Dover Publications, Fourth Edition.

- Lauria, M., Legault, M.A., Lavoie, M.A., Michaud, F., 2008, "Differential Elastic Actuator for Robotic Interaction Tasks," *Proceedings of the IEEE International Conference on Robotics and Automation (ICRA)*, Pasadena, CA, pp. 3606-3611.
- Lauria, M., Legault, M.A., Lavoie, M.A., Giguere, P., Ganon, F., and Michaud, F., (Application: March 31, 2007), "High Performance Differential Elastic Actuator for Robotic Interaction Tasks," United States Patent Application 11/694123.
- Legault, M-A., Lavoie, M-A., Cabana, F., Jacob-Gordreau, Ph., Létourneau, D., Michaud, F., and Lauria, M., 2008, "Admittance Control of a Human-Centered 3-DOF Robotic Arm using Differential Elastic Actuators," *Proceedings of the International Conference on Intelligent Robot Systems (IROS)*, Nice, France, pp. 4143-4144.
- Litvin, F.L., Fuentes, A., Vecciato, D., and Gonzalez-Perez., I., 2004, "New Design and Improvement of Planetary Gear Trains," NASA Glenn Research Center, Technical Report No. NASA/CR-2004-213101.
- Luh, J.Y.S., Fisher, W.D., and Paul, R.C., 1983, "Joint Torque Control by a Direct Feedback for Industrial Robots," *IEEE Trans. Automatic Control*, **AC-28**(2), pp. 153-161.
- Macmillan, R.H., 1961, "Power Flow and Loss in Differential Mechanisms," *Journal of Mechanical Engineering Science*, **3**(1), pp. 37-41.
- Majd, V.J. and Simaan, M.A., 1995, "A Continuous Friction Model for Servo Systems with Stiction," *Proceedings of the IEEE Conference on Control Applications*, Albany, NY, USA, pp. 296-301.
- Mantriota, G. and Pennestri, E., May 2003, "Theoretical and Experimental Efficiency Analysis of Multi-Degrees-of-Freedom Epicyclic Gear Trains," *Multibody System Dynamics*, **9**(4), pp. 389-407.
- McNatt, B.S. and Tesar, D., 1993, "The Design of an Advanced Actuator Transmission for a Modular Robotic Manipulator," MSE Thesis, Mechanical Engineering Department, University of Texas at Austin, Austin, Texas.
- Medin, C., 2003, "Modeling of a Planetary Gear Train for Simulation of a Power Split Hybrid Vehicle," MSE Thesis, Signals and Systems Department, Chalmers University of Technology.
- Migliore, S.A., Brown, E.A., DeWeerth, S.P., 2005, "Biologically Inspired Joint Stiffness Control," *Proceedings of the International Conference on Robotics and Automation (ICRA)*, Barcelona, Spain, pp. 4508-4513.

- Miller, D.C., 2005, "Continuously Variable Transmission," United States Patent No. 6945903.
- Morel, G., Iagnemma, K., and Dubowsky, S., 2000, "Precise Control of Manipulators with High Joint Friction using Base Force/Torque Sensing," *Automatica*, Vol. 36, pp. 931-941.
- Morrell, J.B. and Salisbury, J.K., 1998, "Parallel Coupled Micro-Macro Actuators," *The International Journal of Robotics Research*, **17**(7), pp. 773-791.
- Mruthyunjaya, T.S., 1972, "Synthesis of Plane Linkages to Generate Functions of Two Variables Using Position-Position Reduction, Part 1: Rotary Inputs and Output," *Mechanism and Machine Theory*, **7**(3), pp. 363-370.
- Müller, H.W., 1982<sup>65</sup>, *Epicyclic Drive Trains: Analysis, Synthesis, and Applications*, Wayne State University Press, Detroit, Michigan.
- Nakamura, Y., 1991, *Advanced Robotics: Redundancy and Optimization*, Addison Wesley, USA.
- NEXXTDrive, London, United Kingdom, Accessed 04/10/2009; see also <http://www.nexxtdrive.com/>.
- Ontañón-Ruiz, J., Daniel, R.W., and McAree, P.R., 1998, "On the Use of Differential Drives for Overcoming Transmission Nonlinearities," *Journal of Robotic Systems*, **15**(11), pp. 641-660.
- Operation Software Components for Advanced Robotics (OSCAR), Version 2.0 Online Reference Manual; see also <http://www.robotics.utexas.edu/rrg/research/oscarv.2/>
- Pennestri, E. and Freudenstein, F., September 1993, "The Mechanical Efficiency of Epicyclic Gear Trains," *Journal of Mechanical Design*, **115**(3), pp. 645-651.
- Pennestri, E., and Valentini, P.P., 2003, "A Review of Formulas for the Mechanical Efficiency Analysis of Two Degrees-of-Freedom Epicyclic Gear Trains," *Journal of Mechanical Design*, **125**(3), pp. 602-608.
- Pennington, C.B. and Tesar, D., 1991, "The Design of Epicyclic Spur Gear Transmissions for Robotic Actuators," MSE Thesis, Mechanical Engineering Department, University of Texas at Austin, Austin, Texas.
- Pesiridis, R.A. and Christian, A.J., 2006, "Multi-Input Dual Output Electric Differential Motor," United States Application No. 11/552207.

---

<sup>65</sup> Originally published as *Die Umlaufgetriebe*, Springer-Verlag, Berlin-Heidelberg, 1971.

- Pratt, G.A., and Williamson, M.M., 1995a, "Series Elastic Actuators," *Proc. IEEE Conf. Intelligent Robot Systems (IROS)*, pp. 399-406.
- Pratt, G.A., and Williamson, M.M., 1995b, "Elastic Actuator for Precise Force Control," United States Patent No. 5650704.
- Proakis, J.G. and Manolakis, D.G., 2007, *Digital Signal Processing: Principles, Algorithms, and Applications*, Prentice Hall of India Pvt. Ltd., Fourth Edition (Eastern Economy Edition), Chapter 2.
- Rabindran, D., and Tesar, D., 2004, "Preliminary Studies in Force/Motion Control of Intelligent Mechanical Systems," Masters Thesis, Mechanical Engineering Department, The University of Texas at Austin, Austin, TX.
- Rabindran, D., and Tesar, D., Sept. 2007a, "Study of the Dynamic Coupling Term ( $\mu$ ) in Parallel Force/Velocity Actuated Systems," *Proceedings of the Third Annual IEEE Conference on Automation Science and Engineering*, Scottsdale, Arizona, pp. 418-423.
- Rabindran, D., and Tesar, D., Nov. 2007b, "Dynamic Analysis and Simulation of a 1-DOF Mechanism Driven by a Parallel Force/Velocity Actuator (PFVA)," *Proceedings of the International Mechanical Engineering Congress and Exposition (IMECE)*, Seattle, Washington. Paper Number: IMECE2007-44004.
- Rabindran, D., and Tesar, D., 2007c, "Analytical Formulation for Dual Actuator Driven Serial Robot Manipulators," White Paper, Robotics Research Group, The University of Texas at Austin, Austin, TX.
- Rabindran, D. and Tesar, D., Aug. 2008a, "Analysis of Power Flow in Parallel Force/Velocity Actuators: Theory and Simulations," *Proceedings of the Thirty Second Conference on Mechanisms and Robotics, ASME International Design Engineering Technical Conferences (IDETC)*, Brooklyn, New York. Paper Number: DETC2008-49164.
- Rabindran, D. and Tesar, D., Oct. 2008b, "Parametric Analysis of Parallel Force/Velocity Actuators (PFVA): Force Balance Analysis," *Proceedings of the First ASME Dynamic Systems and Control Conference (DSCC)*, Ann Arbor, Michigan.
- Rabindran, D. and Tesar, D., Feb. 2009, "Parametric Design and Power Flow Analysis of Parallel Force/Velocity Actuators," *ASME J. Mechanisms and Robotics* **1**(1), pp. 011007: 1-10.
- Radzimovsky, E.I., 1956, "A Simplified Approach for Determining Power Losses and Efficiency of Planetary Gear Drives," *Machine Design*, **28**(3), pp. 101-110.



- Raibert, M., and Craig, J.J., 1981, "Hybrid Position/Force Control of Manipulators," *ASME Journal of Dynamic Systems, Measurement, and Control*, Vol. 102, pp. 126-133.
- Rios, O., and Tesar, D., August 2008, "Influence of Actuator Parameters on the Performance Capability of Serial Robotic Manipulator Systems," Ph.D. Dissertation, Mechanical Engineering Department, The University of Texas at Austin, Austin, TX.
- Rios, O., and Tesar, D., February 2009, "Actuator Gain Distributions to Analytically Meet Specified Performance Capabilities in Serial Robot Manipulators," *ASME Journal of Mechanical Design*, **131**(2), pp. 021010: 1:9.
- Rivin, E.I., 1980, "Role of Induction Driving Motor in Transmission Dynamics," *Proceedings of the ASME Design Engineering Technical Conference*, Beverly Hills, CA, 10 p. Paper Number: 80-DET-96.
- Rivin, E.I., 1999, *Stiffness and Damping in Mechanical Design*, Marcel Dekker Inc., New York City, NY, pp. 200-271.
- Roberts, R.K., 1984, "The Compliance of End-Effector Force Sensors for Robot Manipulator Control," Ph.D. Thesis, Purdue University, West Lafayette, IN.
- Russell, R.A., 1987, "Compliant-Skin Tactile Sensor," *Proceedings of the IEEE Conference on Robotics and Automation*, pp. 1645-1648.
- Schempf, H. and Yoerger, D.R., 1993, "Study of Dominant Performance Characteristics in Robot Transmissions," *ASME Journal of Mechanical Design*, **115**(3), pp. 472-482.
- Schultz, M., 2004, "Circulating Mechanical Power in a Power-Split Hybrid Electric Vehicle Transmission," *Journal of Automobile Engineering (Proc. IMechE)*, **218**(D), pp. 1419-1425.
- Sciavicco, L. and Siciliano, B., 2001, *Modeling and Control of Robot Manipulators*, Springer.
- Spencer, A., Pryor, M., Kapoor, C., and Tesar, D., 2008, "Collision Avoidance Techniques for Teleoperated and Autonomous Manipulators in Overlapping Workspaces," *Proceedings of the IEEE International Conference on Robotics and Automation*, Pasadena, CA, pp. 2910-2915.
- Sreevijayan, D., Tosunoglu, S., and Tesar, D., 1994, "Architectures for Fault-Tolerant Mechanical Systems," *Proceedings of the Seventh Mediterranean Electrotechnical Conference*, Vol. 3, pp. 1029-1033.

- Steinfeld, B., and Tesar, D., 2009 (In Progress), “Criteria Based Evaluation of Stopping Trajectories in Serial Manipulators,” MSE Thesis, Mechanical Engineering Department, The University of Texas at Austin, Austin, TX.
- Strang, G., 1988, *Linear Algebra and its Applications*, Harcourt Brace Jovanovich College Publishers, Orlando, FL, Third Edition.
- Sulzer, J. S., Peshkin, M. A., and Patton, J. L., 2005, “MARIONET: An Exotendon-Driven Series Elastic Actuator for Exerting Joint Torque,” *Proceedings of the Ninth International Conference on Rehabilitation Robotics*, Chicago, IL, pp. 103–108.
- Sun, L., Gao, H., Song, Q., and Nei, J., 2002, “Measurement of Torque Ripple in PM Brushless Motors,” *Proceedings of the IEEE Industry Applications Conference, Thirty Seventh Annual IAS Meeting*, pp. 2567-2571.
- Swint, E., and Tesar, D., 2005, “Collision Detection and Obstacle Avoidance for Robotic Manipulators,” MSE Thesis, Mechanical Engineering Department, The University of Texas at Austin, Austin, TX.
- Tal, J. and Kahne, S., 1972, “The Selection of Variable Gear for Minimum Energy,” *IEEE Transactions on Automatic Control*, **17**(3), pp. 353-358.
- Tesar, D., Oct. 1972, “Differential Systems,” Lecture Series, Department of Mechanical Engineering, University of Florida, Gainesville.
- Tesar, D., 1985, “Control-In-The-Small for Precision, Under Load Control of Robot Manipulator,” United States Patent No. 4,505,166.
- Tesar, D., 1989, “Thirty Year Forecast: The Concept of a Fifth-Generation of Robotics – The Super Robot,” *ASME Manufacturing Review*, **2**(1), pp. 16-25.
- Tesar, D. et al, 1999, “Compact Hybrid Actuation for Maximum Performance (CHAMP),” Proposal to DARPA by University of Texas at Austin, Rockwell Science Center, ARM Automation Inc. and the Naval Surface Warfare Center.
- Tesar, D., 2003<sup>66</sup>, “Electromechanical Actuator Architecture (EMAA),” Robotics Research Group, University of Texas at Austin, Technical Report No. MR06-2003.
- Tesar, D., 2004, “Fault-Tolerant Linear Actuator,” United States Patent No. 6,791,215.

---

<sup>66</sup> This is a continuously evolving report that comprehensively describes the accomplishments in actuator research within UTRRG. The origin of the PFVA concept is described under “Force/Motion Control Actuator” in the 2003 version of this report.

- Tesar, D., 2006a, “The Dominant Importance of the Gear Train Reduction Ratio for Electromechanical Actuators,” Technical Report, Robotics Research Group, The University of Texas at Austin.
- Tesar, D., March, 2006b, “Dual Input Actuator Drive System Concepts,” Technical Report, Robotics Research Group, The University of Texas at Austin.
- Tesar, D., 2006c, “Fault-Tolerant Rotary Actuator,” United States Patent No. 7,122,926.
- Tesar, D., 2006d, “Dual Input Actuator Drive System Concepts,” White Paper, Robotics Research Group, The University of Texas at Austin.
- Tesar, D. and Matthew, G.K., 1976, *The Dynamic Synthesis, Analysis, and Design of Modeled Cam Systems*, Lexington Books, MA.
- Tesar, D., Sreevijayan, D., and Price, C., 1990, “Four-Level Fault Tolerance in Manipulator Design for Space Operations,” *Proceedings of the First International Symposium on Measurement and Control in Robotics*, Houston, Texas.
- Tesar, D. and Geisinger, J.W., 1998, “Where is the Field of Robotics Going?,” University of Texas Discovery Magazine, **15**(1); see also <http://www.utexas.edu/opa/pubs/discovery/disc1998v15n1/disc-tesar.html>.
- Thomas, M. and Tesar, D., 1982, “Dynamic Modeling of Serial Manipulator Arms,” *ASME Journal of Dynamic Systems, Measurement, and Control*, **104**(3), pp. 218-227.
- Thomas, M., Yuan-Chou, H. C., and Tesar, D., 1985, “Optimal Actuator Sizing for Robotic Manipulators Based on Local Dynamic Criteria,” *ASME Journal of Mechanisms, Transmissions, and Automation Design*, 107, pp. 163–169.
- Tisius, M., Kapoor, C., and Tesar, D., 2004, “An Empirical Approach to Performance Criteria and Redundancy Resolution,” Masters Thesis, Department of Mechanical Engineering, The University of Texas at Austin, Austin, TX.
- Tisius, M., Pryor, M., Kapoor, C., and Tesar, D., 2009, “An Empirical Approach to Performance Criteria for Manipulation,” *ASME Journal of Mechanisms and Robotics*. (In Press)
- Tokuz, L.C. and Jones, J.R., 1991, “Programmable Modulation of Motion using Hybrid Machines,” *Proceedings of the Institute of Mechanical Engineers (IMechE)*.
- Townsend, W.T. and Salisbury, J.K., 1988, “Effect of Transmission Design on Force-Controlled Manipulator Performance,” Ph.D. Thesis, Department of Mechanical Engineering, Massachusetts Institute of Technology.

- Tse, F.S., Morse, I.E., and Hinkle, R.T., 1963, *Mechanical Vibrations*, Allyn and Bacon, Inc., Boston.
- Tuplin, W.A., 1957, "Designing Compound Epicyclic Gear Trains for Maximum Efficiency at High Velocity Ratios," *Machine Design*, **29**(7), pp. 100-104.
- Uicker, J.J., Pennock, G.R., and Shigley, J.E., 2003, *Theory of Machines and Mechanisms*, Oxford University Press, Third Edition.
- Vaculik, S. and Tesar, D., 2008, "Electro-Mechanical Actuator Design and Scaling Rule Development," Ph.D. Dissertation, Mechanical Engineering Department, University of Texas at Austin, Austin, TX.
- Vanderborght, B., Ham, R.V., Lefeber, D., Sugar, T.G., and Hollander, K.W., January 2009, "Comparison of Mechanical Design and Energy Consumption of Adaptable, Passive-Compliant Actuators," *The International Journal of Robotics Research*, **28**(1), pp. 90-103.
- Vanderborght, B., Sugar, T.G., and Lefeber, D., eds., 2008, *Adaptable Compliance*, Special Issue of the *IEEE Robotics and Automation Magazine*, **15**(3).
- Waldron, K.J. and Kumar, A., 1979, "Development of a Theory of Errors for Manipulators," *Proceedings Fifth World Congress on Theory of Machines and Mechanisms*, pp. 821-826.
- Welch, G. and Bishop, G., August 12–17, 2001 "An Introduction to the Kalman Filter," SIGGRAPH 2001 Course 8. In *Computer Graphics, Annual Conference on Computer Graphics & Interactive Techniques*. ACM Press, Addison-Wesley, Los Angeles, CA, USA. SIGGRAPH 2001 Course Pack Edition.
- West, J.C. and Leonard, J.L., 1955, "The Necessary Torque Requirements for a Servo-Motor," *Journal of Scientific Instruments*, **32**(1), pp. 30-32.
- Woodbury, M.A., 1950, "Inverting Modified Matrices," Memorandum Report 42, Statistical Research Group, Princeton, NJ.
- Whitney, D.E., 1982, "Quasi-Static Assembly of Compliantly Supported Rigid Parts," *ASME Journal of Dynamic Systems, Measurement and Control*, Vol. 104, pp. 65-77.
- Willis, R., 1870, *Principles of Mechanism*, Longman's, Green, and Co., London, UK, Second Edition.
- Wu, E.C., Hwang, J.C., and Chladek, J.T., 1993, "Fault-Tolerant Joint Development for the Space Shuttle Remote Manipulator System: Analysis and Experiment," *IEEE Transactions on Robotics and Automation*, **9**(5), pp. 675-684.

- Yi, B-J, Walker, I.D., Tesar, D., and Freeman, R.A., 1991, "Geometric Stability in Force Control," *Proceedings of the International Conference on Robotics and Automation (ICRA)*, Sacramento, CA, pp. 281-286.
- Yoo, J.G. and Tesar, D., 2004, "Actuator Performance Map through Nonlinear Test Bed," Ph.D. Dissertation, Mechanical Engineering Department, The University of Texas at Austin, Austin, TX.
- Younkin, G.W., 2003, *Industrial Servo Control Systems: Fundamentals and Applications*, Marcel Dekker, Inc., New York City, NY, Second Edition.
- Zhou, W., Chew, C-M, and Hong, G-S, May 2009, "Design of Series Damper Actuators," *Robotica*, **27**(3), pp. 379-387.
- Zinn, M., Roth, B., Khatib, O., and Salisbury, J.K., 2004, "A New Actuation Approach for Human Friendly Robot Design," *The International Journal of Robotics Research*, **23**(4/5), pp. 379-398.

## Vita

Dinesh Rabindran was born in Manjeri, Kerala, India on October 15, 1978 the third son of Kizheettil Pisharath Rabindran and Cherukara Vilasini Rabindran. After completing high school at the Central School in Ottapalam, he entered the National Institute of Technology Calicut, where he received the B.Tech degree with honors in Production Engineering and Management in 2000. He worked with Bajaj Auto Ltd., Waluj, India, as a Graduate Trainee Engineer from 2000-2001. In the fall of 2001, Dinesh entered the Mechanical Engineering (ME) Department at The University of Texas at Austin (UT) for graduate studies in Mechanical Systems and Design. He received the M.S.E. degree in ME in 2004 and is currently a PhD candidate at the Robotics Research Group (RRG) in the ME department. He has been the team leader for the Systems Software and Operations team at the RRG since 2004. His current research interests are in manipulation, contact robotics, actuation, and rehabilitation robotics. He received the Graduate Student Professional Award in 2007 and an honorable mention for the 2008 IEEE Robotics and Automation Society Fellowship, and is the ME department's nominee for the 2009 Michael H. Granof Outstanding Graduate Student Award instituted by UT's Graduate School.

Permanent address: “Mangalasree (*Nalukettu*),” Eravimangalam P.O  
(via) Perintalmanna, Malappuram District  
Kerala – 679 340, INDIA

This dissertation was typed by the author.